Magnetic Excitations in Transport Measurements of Novel Quantum Materials

by

Jennifer A. Reid

A thesis
presented to the University of Waterloo
in fulfillment of the
thesis requirement for the degree of
Doctor of Philosophy
in
Physics

Waterloo, Ontario, Canada, 2023

© Jennifer A. Reid 2023

Examining Committee Membership

The following served on the Examining Committee for this thesis. The decision of the Examining Committee is by majority vote.

External Examiner:	Stephen Julian Professor, Dept. of Physics, University of Toronto
Supervisor:	Robert Hill Professor, Dept. of Physics and Astronomy, University of Waterloo
Internal Member:	Michel Gingras Professor, Dept. of Physics and Astronomy, University of Waterloo
Internal Member:	Roger Melko Professor, Dept. of Physics and Astronomy, University of Waterloo
Internal-External Member:	Adam Wei Tsen Professor, Dept. of Chemistry, University of Waterloo

Author's Declaration

I hereby declare that I am the sole author of this thesis. This is a true copy of the thesis, including any required final revisions, as accepted by my examiners.

I understand that my thesis may be made electronically available to the public.

Abstract

Quantum materials offer rich possibilities for quasiparticles that can revolutionalize our technology. The discovery of novel delocalized magnetic excitations in transport measurements implies that such quasiparticles are mobile, which may lead to technology applications that take advantage of the magnetic or charge properties of the collective excitations. Importantly, testing theoretical predictions of such quasiparticles allows us to understand how to realize such predictions in real materials.

The purpose of this thesis is to investigate novel magnetic excitations in quantum materials, primarily by using thermal transport measurements. We investigate the origin of experimentally reported novel charge-neutral quasiparticles in the topological Kondo insulator candidate SmB_6 to address seemingly contradictory analyses of experimental data and motivate theoretical models. Then we test the theoretical prediction of heat-conducting photon excitations in the quantum spin ice candidate $Pr_2Hf_2O_7$.

We primarily use thermal transport to investigate these magnetic excitations. Our standard steady state setup has a directional dependence that is optimized to investigate any anisotropic effects in single crystals by orienting the magnetic field and heat current directions along high-symmetry crystallographic directions, such as when investigating a spin ice anisotropy in the quantum spin ice candidate. After obtaining our data, a careful analysis of thermal conductivity allows us to distinguish the heat conduction of novel quasiparticles from that of more conventional heat carriers, such as phonons and conduction electrons. We also introduce magnetostriction measurements, which is a bulk thermodynamic measurement that is used to detect quantum oscillations in SmB_6.

While the search for novel quasiparticles in quantum materials underlies the methods and analysis in this thesis, the materials themselves are unrelated and hence are covered in separate sections. We first summarize theoretical predictions and experimental evidence on the topological Kondo insulator candidate SmB_6 to motivate our investigation of charge-neutral quasiparticles in the bulk of the material. Then we report evidence that charge-neutral excitations are most easily distinguished in the thermal transport of samples with minimal bulk disorder, which can be quantified between different samples using thermal conductivity analysis. Having addressed conflicting interpretations of thermal conductivity in differing samples, we further investigate the field anisotropy and quantum oscillations in the magnetostriction to gain more information about the underlying properties of bulk charge-neutral excitations.

After discussing our results for SmB_6, we introduce spin ice materials and the predicted excitations of the U(1) quantum spin liquid theory as applied to pyrochlore spin ices. Then

we motivate the search for such excitations in the quantum spin ice candidate $Pr_2Hf_2O_7$ with a particular emphasis on the gapless, linearly dispersive photon excitation that has yet to be unambiguously realized in real materials. Instead, we report a lack of a heat-conducting photon excitation in thermal conductivity, which places limits on the realization of the U(1) quantum spin liquid state in this material. Nonetheless, we also explore the temperature and field dependence of a suppressed thermal conductivity that suggests strong phonon scattering with an Ising anisotropy that could be related to strong spin fluctuations interacting with phonons.

Our results investigating magnetic quasiparticles experimentally through thermal transport test theoretical predictions and motivate the continued study of these materials. Importantly, we corroborate evidence that charge-neutral, heat-conducting excitations and bulk quantum oscillations are present in high quality samples of SmB_6 in spite of its insulating bulk state, which require further testing of theoretical motivations to uncover the mechanism behind this phenomena. Then, in $Pr_2Hf_2O_7$, despite expectations of a U(1) quantum spin liquid ground state with heat-conducting photon excitations, we instead observe a thermal conductivity that is most consistent with conventional phonon excitations as the sole heat carriers. Such experimental tests of theoretical predictions are important to understand the realization of novel phases of matter in real materials in order to use such materials in technological applications.

Acknowledgements

I would like to extend my gratitude to the mentors who helped me complete this research. Dr. Robert Hill has been instrumental at teaching me the methods and analytical approaches needed for scientific research and giving timely, detailed feedback. The members of the examining committee provided invaluable feedback to refine my communication and understanding of our results. Discussions with Dr. Michel Gingras helped me understand spin ice theories. Dr. Roger Melko's early assistance on python programming gave me something to build on when creating the programs used for fitting and modeling our thermal conductivity results. Dr. Adam Wei-Tsen and Dr. Stephen Julian's external perspectives led to a more well-rounded thesis. Additionally, Dr. David Hawthorn and Dr. Jan Kycia have been great mentors throughout my graduate program, including by providing feedback on experimental approaches and sharing equipment.

I would also like to thank our collaborators who grew and characterized our samples. Dr. Geetha Balakrishnan's group at the University of Warwick grew the SmB_6 samples and Dr. Bella Lake's group at the Helmholtz-Zentrum Berlin grew the $Pr_2Hf_2O_7$ samples. Dr. Michael Sutherland's group at the University of Cambridge electropolished the SmB_6 samples. We are indebted to their generosity and assistance with this research. Funding from the Natural Sciences and Engineering Research Council of Canada also helped support my graduate program and the research reported in this thesis.

I also extend my gratitude to the support staff and graduate students in the department. Hiruy Haile and the team at Science Technical Services stepped in to help us fix instrumentation or create new parts. Dr. William Toews introduced me to the low temperature techniques needed to operate our refrigerators and assisted with research on SmB_6 that is continued in this thesis. Finally, I am grateful for the company of the other graduate and undergraduate students our laboratory, who stepped in to help operate or fix equipment or asked thought-provoking questions that helped me learn from them throughout my graduate degree.

Dedication

For Joseph,
who encourages me to climb higher.

Table of Contents

List of Tables xiii

List of Figures xiv

List of Symbols xxvi

Introduction 1

I Experimental techniques 5

1 Cryogenic refrigeration 6

1.1 Pumped helium 4 cryostat 6

1.2 Helium 3-helium 4 dilution refrigerator 8

1.3 Temperature stability 9

1.4 Superconducting field 11

2 Thermal conductivity 13

2.1 Introduction to thermal transport 13

2.2 Thermal conductivity measurement 14

2.2.1 Thermometry 15

2.2.2 Error propagation and reduction 16

2.2.3 Sample error propagation calculations 17

3 Magnetostriction **19**

3.1 Quantum oscillations in magnetostriction 22

3.2 Capacitive dilatometer 26

3.3 Error analysis in magnetostriction 26

3.3.1 Improving precision 28

II Topological Kondo insulators **31**

4 Topological Kondo Insulators: Literature Review **32**

4.1 Early theories of TKI candidates 32

4.1.1 Kondo insulators 32

4.2 Topological insulators 35

4.3 Topological Kondo insulators 38

4.4 Experimental observations in SmB_6 38

4.4.1 Kondo insulator 38

4.4.2 Topological surface states 39

4.4.3 Exotic insulating bulk 41

4.5 Theories of anomalous dHvA oscillations 45

4.6 Sample growth and disorder 48

5 SmB_6 experimental results **54**

5.1 Sample information 54

5.2 Thermal conductivity results 57

5.2.1 Phonon conductivity in high quality samples 57

5.2.2 Signatures of bulk sample disorder 63

5.2.3 Field-induced excitations 66

5.2.4 Fermionic contributions to thermal conductivity 69

5.2.5 Comparison of results among identical samples 78

5.3 Magnetostriction . . . 79
5.3.1 Dilatometer setup . . . 79
5.3.2 Quantum oscillations in magnetostriction . . . 81
5.3.3 Characterizing quasiparticles in SmB_6 . . . 86
5.4 Summary of SmB_6 results . . . 89

III Quantum spin ice **91**

6 Quantum spin ice literature **92**
6.1 Classical spin ice . . . 93
6.1.1 Ice rules . . . 93
6.1.2 Dipolar spin ice model . . . 96
6.1.3 Signatures of spin ice physics . . . 101
6.1.4 CSI experimental results . . . 104
6.2 Quantum spin ice . . . 110
6.2.1 U(1) quantum spin liquid . . . 110
6.2.2 Kramers versus non-Kramers ions . . . 110
6.2.3 Quantum spin ice theory . . . 111
6.2.4 Photon excitations . . . 114
6.3 Experimental research on QSI candidates . . . 115
6.3.1 $Tb_2Ti_2O_7$ experimental background . . . 115
6.3.2 $Pr_2Zr_2O_7$ experimental background . . . 117
6.3.3 Disorder and QSI . . . 120
6.3.4 Quadrupolar ordered phases . . . 121

7 $Pr_2Hf_2O_7$ experimental results **123**
7.1 Quantum spin ice candidate $Pr_2Hf_2O_7$ . . . 123
7.2 Thermal conductivity results . . . 125
7.2.1 Methods . . . 125
7.2.2 Results . . . 127
7.3 Discussion of PHO results . . . 132
7.3.1 Searching for photon excitations . . . 134
7.3.2 Models of phonon scattering . . . 137
7.3.3 In-field behaviour . . . 142
7.4 Interpretation of $Pr_2Hf_2O_7$ ground state . . . 143

Summary **146**

References **149**

Appendices **166**

A Thermal transport theory **167**
A.1 Kinetic theory . . . 167
A.2 Thermal conductivity of metals . . . 168
A.3 Phonon thermal conductivity . . . 169
A.3.1 Boundary-limited thermal conductivity . . . 169
A.3.2 Finite boundaries . . . 171
A.3.3 Phonon scattering with disorder . . . 171
A.3.4 Resonance scattering in paramagnetic crystals . . . 175
A.4 Callaway model fitting . . . 175
A.4.1 Callaway model . . . 175
A.4.2 Scattering with sample disorder . . . 176
A.4.3 Fitting . . . 177

B YbB_{12} thermal conductivity **178**

List of Tables

5.1 SmB_6 floating zone grown samples, dimensions, geometric factor g and inverse resistivity ratio (iRRR) at 0.5 K and at 0.1 K for comparison. Toews reports the iRRR values for FZ1 and FZ2 [1]. The sample FZ2p is the sample FZ2 after electropolishing to reduce its cross-sectional area. 55

5.2 Coefficients of fits below 0.5 K to $\kappa/T = A + BT^{\delta-1}$ for SmB_6 samples FZ1, FZ2 (FZ2p is after electropolishing to reduce sample dimensions), and FZ3. 68

5.3 Dilatometer capacitance, converted to a plate separation assuming parallel plates $D_{\parallel}$ and assuming aparallel plates D_{tilt} at (a) room temperature and 53 mK, and after readjustment at (b) room temperature and 117.2 K, responding to the thermal expansion of SmB_6 FZ1. 81

5.4 Parameters adapted from Fourier transform peaks in Figure 5.15c, using LK theory: the frequencies of the peaks F_i, the Fermi wavevectors k_F and the corresponding carrier density for an approximately spherical Fermi surface n_{3D}. 87

5.5 Parameters for a linear fit $\Delta\kappa = A + BT$ of the enhanced thermal conductivity $\Delta\kappa = \kappa(12\text{ T}) - \kappa(0\text{ T})$. 88

6.1 Anisotropy of saturated magnetizations under applied magnetic fields, with $\mu_{\text{eff}} = g_{\text{eff}} J_{\text{eff}} \mu_B$ [2]. 104

7.1 Dimensions of PHO samples S1, S2 and S3 reported as length × width × height, and the geometric factor, which is the average length between sample contacts divided by the cross-sectional area. 126

List of Figures

1.1 (a) Vapour pressure as a function of temperature on a log log scale for cryoliquids ^{3}He, ^{4}He, hydrogen and nitrogen. Black dots are practical minimum temperature limits reached by evaporative cooling with each cryoliquid [3]. (b) Schematic of a 1 K pot in a vacuum can, drawing liquid ^{4}He through an impedance into the helium container with a pump, and (c) sample drawing of a pumped ^{4}He cryostat [4]. *Reproduced with permission from Springer Nature.* 7

1.2 Phase-separation line for the phases of a ^{3}He-^{4}He mixture with respect to temperature and ^{3}He concentration x [5]. *Reproduced with permission from Springer Nature.* 9

1.3 (a) Schematic of the closed cycle of a ^{3}He-^{4}He mixture in a dilution refrigerator [5]. *Reproduced with permission from Springer Nature.* (b) Dilution refrigerator used for experiments at temperatures below 1 K. 10

2.1 (a) Schematic of a typical thermal conductivity setup. Heat $\dot{Q}$ is applied to one end of the sample and the opposite end of the sample is thermally anchored to a heat sink maintained at temperature T_0, driving a thermal gradient ΔT between the hot thermometer T_H and the cold thermometer T_C. (b) Schematic of the thermal current circuit in the above figure. 14

2.2 Thermal conductivity setup with a copper box used for radiation shielding [6]. 15

3.1 Coupled relations between thermodynamic effects, as adapted from Chandrasekhar and Fawcett [7]. Small changes in the elastic stress σ, strain ϵ, applied magnetic field H, temperature T, magnetization M, and entropy S are proportional to the product of small changes of the respective quantity at the arrow's tail and the physical property captioning the arrow connecting the two properties. 21

3.2 Landau levels for a Fermi gas under applied field H on a spherical Fermi surface (broken line) with circular cross-sectional areas [8]. At constant energy, the permitted occupied electronic states conform to the illustrated cylindrical tubes according to the Onsager relation of Equation (3.9). *Reproduced with permission from Cambridge University Press.* 23

3.3 Labelled schematic of the copper dilatometer used for magnetostriction measurements adapted from engineering drawings by Liu [9]. 25

3.4 Illustration of plate tilt in dilatometer plates at a distance D apart, with a plate tilt off-centering by distance a from the average plate separation. Image reproduced from Pott and Schefzyk [10]. 27

4.1 Comparison of interaction parameter strengths between the binding energy of a Kondo singlet, approximately of order T_K (blue curve), and the RKKY ordering energy, approximately of order T_{RKKY} (red curve). The illustration assumes $\rho = 1$. The RKKY interaction dominates below $J \sim 0.2$ in this figure, and the Kondo energy overtakes the RKKY interaction on the right hand side of this point [11, 12]. It is worth noting that Doniach's weak coupling formula for a Kondo singlet is not applicable in the large Kondo coupling limit. 34

4.2 Figure from Dzero *et al.* [12], visualizing the band gap for a trivial insulator compared to a topological insulator. (a) A band gap for a trivial insulating phase with $Z_2 = +1$. (b) A band crossing illustrated for a high symmetry point Γ, where a Dirac point connects the even parity (+) trivial insulating state and the odd parity (−) bulk state at the surface of the sample. The Dirac point has a chiral spin phase arising from the opposing parities. *Used with permission of Annual Reviews; permission conveyed through Copyright Clearance Center, Inc.* 37

4.3 Images from Takimoto [13]. (a) High-symmetry points Γ, X, M and R on a cubic reciprocal lattice with the first Brillouin zone quadrant of a [001] surface shown at the top of the image. Time reversal invariant points are marked with red dots. (b) Calculated energy bands E for SmB_6 scaled by the hopping parameter t_d for the $4f^6$ (blue), $4f^5 5d$ (red), and hybridized (black) states of the samarium ion. The X points have negative parity due to band inversion between the $4f^6$ and $4f^5 5d$ bands. ©2011 *The Physical Society of Japan.* 40

4.4 (a) A basic schematic of a four terminal inverted resistance measurement [14], with a current differential in region I between concentric terminals $1 \rightarrow 2$, and a voltage differential measured in an adjacent region II between terminals $3 \rightarrow 4$. Using this setup, Eo *et al.* report inverted resistance measurements of SmB_6 [15], with four concentric terminals on the top of the sample as shown in (b) and two concentric terminals on the bottom of the sample as shown in (c). Their converted bulk resistivity for stoichiometric flux-grown sample S1 and non-stoichiometric flux-grown samples S2, S3 and S4 is shown in (d). *Reprinted (a) with permission from* [14]. *Copyright 2018 by the American Physical Society.* 42

4.5 Specific heat normalized by temperature versus temperature for flux-grown SmB_6 single crystals (black and red) grown from the same batch, compared to a $38 - 53$ µm powder derived from a crushed single crystal (green). *Reprinted figure with permission from* [16]. *Copyright 2016 by the American Physical Society.* 43

4.6 Quantum oscillations in torque magnetization in floating zone grown samples of SmB_6, by Tan *et al.* [17]. (a) Oscillatory magnetization at 0.5 K and a field angle of $\theta = 41$ deg with the normal [001] direction. Inset: a schematic of the measurement setup for torque magnetometry. (b) Quantum oscillation frequencies as a function of angle θ. Lines guide the eye to the frequencies expected for Fermi surface orbits. 45

4.7 (a) 3D rendering and (b) 2D cross-section of the ellipsoidal α band with frequencies shown in Figure 4.6b, calculated using density functional theory by Tan *et al.* [17]. High-symmetry Brillouin zone points indicated by Γ, X, R and M. The ε and γ bands are also labelled in (b). 46

4.8 Comparison of *bulk* electrical resistivity and dislocations between aluminum flux grown and floating zone grown samples of SmB_6 [18]. Using chemical etching, Eo *et al.* reveal etch pit dislocations in (a) a floating zone grown sample and (b) a flux grown sample of SmB_6. (c) Bulk electrical conductivity measurements of flux grown and floating zone grown SmB_6 samples plotted as a function of inverse temperature on a log-log scale for different sample growths. *Reprinted figures with permission from* [18]. *Copyright 2021 by the American Physical Society.* 49

4.9 Oscillatory torque measurements of flux-grown SmB_6 before and after polishing to remove aluminum inclusions. (a) Amplitude of oscillatory torque $\tau_{\rm osc}$ normalized by the sample mass m_0/m versus inverse field, with images of the sample after progressive polishing. (b) Amplitude of fast Fourier transform for the above oscillations, scaled by mass, versus frequency in units of Tesla. Inset showing the spectra of oscillations for polycrystalline aluminum flux, that shows a broader spectrum than the oriented single crystal SmB_6 samples. *Reprinted figures with permission from* [19]. *Copyright 2019 by the American Physical Society.* 50

4.10 A comparison of magnetization among SmB_6 floating zone grown samples by Hartstein *et al.* [20]. The authors compare the samples previously reported to have bulk quantum oscillations [21] with the floating zone grown samples of Furhman *et al.* [22]. 53

5.1 Thermal conductivity results for one of the low disorder floating zone grown samples (FZ1, FZ2) that are remeasured in this thesis, as reported by Hartstein *et al.* [21]. *Reproduced with permission from Springer Nature.* (a) Thermal conductivity plotted as κ/T versus T^2, with the dotted line indicating the estimate of the maximal thermal conductivity of phonons ($\kappa_{\rm ph}/T$). Inset: the enhancement of thermal conductivity in an applied field by subtracting the estimate of the maximal phonon thermal conductivity. (b) The field-dependent thermal conductivity for an FZ sample, normalized by the zero-field thermal conductivity, at 235 mK. Inset: Additional field-dependent thermal conductivity for the other FZ sample at 243 mK and for a flux grown sample at 340 mK. 56

5.2 SmB_6 sample FZ2 thermal conductivity before and after electropolishing. The red line is the theoretical estimate of the phonon boundary scattering limit before electropolishing. Inset: ratio of FZ2 thermal conductivity before and after electropolishing, with error bars indicating the Gaussian mean of the uncertainty in the geometric factors for both sample geometries. The fuchsia line is the theoretical ratio of phonon mean free paths in the boundary scattering limit. 58

5.3 Thermal conductivity of SmB_6 samples FZ2 and Boulanger *et al.*'s sample Z1 [23] in zero magnetic field, plotted as κ/T^3 versus T. The theoretical Casimir limit, where $\kappa/T^3 \propto \ell_C$ is shown as the lines on the graph. By sample geometries, $\ell_C = 3.5 \times 10^{-2}$ cm for the original FZ2 sample (dashed red line) and 4.1×10^{-2}cm for the original Z1 sample (solid cyan line). Both polished samples have similar cross-sectional areas with $\ell_C = 2.15 \times 10^{-2}$ cm (black dot-dash line). 59

5.4 SmB_6 FZ3 thermal conductivity data plotted as κ/T versus T^2, (a) in zero field (solid diamonds) and 12 T field (open diamonds) with the electron contribution to the thermal conductivity κ_{el} estimated by the Wiedemann-Franz law (green line). (b) Low temperature resistivity of FZ3 in zero applied magnetic field. 61

5.5 Thermal conductivity of FZ3 in zero field and 12 T field plotted as κ/T versus $T^{1.4}$. Solid lines are fits to $\kappa/T = A + BT^{1.4}$. 62

5.6 (a) Peak thermal conductivity of SmB_6 samples FZ2 (as previously reported by Toews [24]) and FZ3. The blue dots are for the SmB_6 sample reported by Laliberté *et al.* [25] with data below 5 K adapted from Boulanger *et al.* [23] and the blue line a guide to the eye. (b) Zero field thermal conductivity of FZ2 and FZ3. The black solid line is a fit of the FZ3 conductivity to $\kappa/T = BT^{\alpha-1}$, obtaining $\alpha \sim 2.4$. Dashed lines are the Casimir estimates of the thermal conductivity from phonons scattering with sample boundaries. 63

5.7 Phonon thermal conductivity modelled for SmB_6 FZ1 and FZ2 in zero field, with two parameters: boundary scattering proportional to the sample cross-sectional area, and point defects from samarium vacancies. The point defect coefficients assume $N_d = 1.22 \times 10^{20}$ cm^3, resulting in $c_p = 0.9\%$. 65

5.8 (a) The difference $\Delta\kappa$ between the thermal conductivity in a 12 T field and a 0 T field with respect to temperature and field orientation for samples FZ1, FZ2 and FZ3. (b) This difference for the FZ2 sample before and after polishing. Inset: ratio of $\Delta\kappa$ in a transverse 12 T field before and after polishing. Red line is the ratio of the cross-sectional areas for FZ2. 67

5.9 Thermal conductivity of FZ1, FZ2, FZ2p and FZ3 in zero field plotted as κ/T versus T^2. Lines show respective fits of the thermal conductivity below 0.5 K to Equation (5.3), obtaining parameters as listed in Table 5.2. 68

5.10 Circuit adapted from Smith *et al.* [26]. The applied heat $\dot{Q}$ dissipates through the contacts with resistivity from electrons $W_{\mathrm{c,e}}$ and phonons $W_{\mathrm{c,ph}}$. Then the heat current $\boldsymbol{j}$ travels through the parallel resistances from charge-neutral fermions $W_{\mathrm{s,f}}$ and phonons $W_{\mathrm{s,ph}}$, or through the fermion-phonon coupling resistance $W_{\mathrm{s,f\text{-}ph}}$. (b) Smith *et al.* plot the electronic thermal conductivity as a function of contact resistance r and temperature T, where T_D is the temperature above which the contact resistance can be neglected. *Reproduced figures with permission from* [26]. *Copyright 2005 by the American Physical Society.* 71

5.11 a. Thermal conductivity of SmB_6 FZ1 for a single run. Black line is extrapolation of $T > 0.5$ K data to lower temperatures assuming a cubic temperature dependence.b. Experimental data at set temperature points from previous figure, calculating temperature difference between thermometers as a function of time. Black line: extrapolated y-intercept from the previous figure converted to temperature difference. Anticipating a hypothetical residual linear term in floating zone grown sample FZ1 assuming much longer settling times required to reach thermal equilibrium. 74

5.12 A circuit imagining thermal conduction with n number of electrically disconnected, metallic "puddles" with thermal resistance $W_{\mathrm{s,el(i)}}$, along with continuous thermal resistance from phonons, $W_{\mathrm{s,ph(i)}}$ throughout the sample. For simplicity, this circuit explicitly examines the thermal gradient between thermometers T_1 and T_2 while neglecting contact resistance as well as electron-phonon coupling. The boundary conditions are assumed to be an electrically conductive surface in parallel with phonon conduction. . . . 75

5.13 Comparisons of thermal conductivities for (a) FZ1 and (b) FZ2 SmB_6 samples, with solid symbols in zero field and empty symbols in a 12 T field, plotted as κ/T versus T^2. Insets are scaled to show the lowest temperature ranges. 78

5.14 (a) SmB_6 FZ1 dilatometer capacitance measurement at a set temperature $T = 150$ mK in zero field as a function of time. (b) Fast Fourier transform amplitudes for the above capacitance (blue) and temperature (red) measurements. 80

5.15 Oscillatory magnetostriction in SmB_6 FZ1 from 12 T to 9.5 T at 50 mK. (a) Plotted as the plate separation measurement with respect to inverse field (blue), and a background fit to a linear equation (black dashed). (b) Plotted as the background-subtracted plate separation normalized by the sample length of 1.27 mm. (c) Amplitudes and frequencies of the FFT transform. 83

5.16 Oscillatory magnetostrictions of metals (a) LaB_6 and (b) PrB_6 in a longitudinal [100] applied field, by Sera *et al.* [27]. The background-subtracted oscillatory amplitude of LaB_6 is of the order $\Delta L/L \sim 2 \times 10^{-7}$ whereas the amplitude of oscillations for PrB_6 is a fraction of this value in the field range of $4 - 8$ T. ©1988 *The Physical Society of Japan.* 86

5.17 Thermal conductivity enhancement above phonon contribution for samples FZ2 (red) and FZ2p (blue) in a transverse 12 T field, with lines representing linear fits to $\kappa = A + BT$ below 0.4 K. 88

6.1 Illustration of frustration on a triangular lattice with a nearest-neighbour antiferromagnetic exchange interaction. If the spins are confined to pointing up or down on this lattice, only two of the three spins can satisfy the antiferromagnetic condition, leaving the third arrow (gray) with two equally unsatisfactory potential configurations. 93

6.2 Bramwell and Harris [28] map Anderson's model onto a pyrochlore lattice of corner-sharing tetrahedra with $\langle 111 \rangle$ Ising anisotropy. (a) Anderson's model of a uniaxial Ising constraint orders at $T_C \sim J$ for magnetic moments with a nearest-neighbour ferromagnetic (FM) exchange interaction and (b) lack ordering with an antiferromagnetic (AFM) exchange interaction. In Bramwell and Harris' model, a local $\langle 111 \rangle$ constraint results in (c) a disordered two-in/two-out ground state with a FM interaction and (d) an ordered all-in/all-out state at $T_N \sim |J|$ with an AFM interaction. © *IOP Publishing. Reproduced with permission. All rights reserved.* 94

6.3 (a),(b): Illustration of the "ice rule" for H_2O and a tetrahetron respectively, adapted from Bramwell *et al.* [29]. Each oxygen atom is strongly bonded to two hydrogen atoms (solid lines) and weakly bonded to two hydrogen atoms (dotted lines), forming a tetrahedral structure. 95

6.4 Possible configurations of frustrated spins on a square lattice, to represent microstates of a tetrahedron. (a) Illustration of an all-in state and an all-out state (b) Four states with a "one-in three-out" spin configuration and four states with a "three-in/one-out" spin configuration (c) Six states with a "two-in/two-out" spin configuration. 96

6.5 Phase diagram of dipolar spin ice in zero applied field from Monte Carlo simulations by den Hertog and Gingras [30]. The temperature T and effective exchange coupling J_{nn} are both normalized by the nearest-neighbour dipolar interaction D_{nn} on the axes of this diagram. *Reprinted figure with permission from* [30]. *Copyright 2000 by the American Physical Society.* . . 98

6.6 An illustration of corner-sharing tetrahedra in a segment of a pyrochlore lattice, with the diamond lattice in black. The red spheres at the tetrahedron vertices represent the positions of the A^{3+} (B^{4+}) ions in the A (B) sublattice as discussed in the main text. 99

6.7 The "dumbbell" model of magnetic monopoles. (a) Treating spins on the corners of tetrahedra as dipoles with spacially separated opposing charges, a two-in/two out configuration is charge neutral, (b) a three-in/one-out configuration has a net positive magnetic charge, and (c) a neighbouring tetrahedron with a one-in three-out has a net negative magnetic charge, maintaining a magnetic dipole. Images from Castelnovo *et al.* [31]. (d) An image by Castelnovo *et al.* [32] showing magnetic charges residing on vertices of the diamond lattice. Opposing charges are separated by a series of dipole pairs hilighted in white. *Reproduced with permission from Springer Nature.* . . . 100

6.8 (a) Illustration of a two-in/two-out state and the alignment of global [001], [111] and [110] axes with respect to the tetrahedron. (b),(c),(d): Orientation of spins at the tetrahedron vertices, which are constrained to the local $\langle 111 \rangle$ axis, after polarization by a large external magnetic field aligned with the (b) [001], (c) [111] and (d) [110] global axes [2]. In Figure (d), two spins remain unaffected by the external field as explained in the main text. . . . 102

6.9 Monte Carlo simulation of magnetization for CSI candidate $Dy_2Ti_2O_7$ [2]. Lines indicate the expected intermediate magnetization of 3.33 μ_B/Dy ion for an applied [111] field and the expected saturated magnetizations for field orientations [110], [111] and [100] as motivated in the main text. *Reprinted with permission from* [2]. *Copyright 2002 by the American Physical Society.* 103

6.10 (a) Specific heat of DTO in zero field and 0.5 T field, from Ramirez *et al.* [33]. Inset: Inverse susceptibility of DTO in a 0.02 T field. (b) DTO entropy found by integrating $C(T)/T$ data. *Reproduced with permission from Springer Nature.* 105

6.11 Time-dependent (a) specific heat capacity and (b) entropy for DTO from [34]. The authors find an absence of residual Pauling's entropy when waiting longer equilibration times. *Reproduced with permission from Springer Nature.* 106

6.12 Experimental magnetization of DTO at 1.8 K in magnetic fields oriented along [100], [111] and [110]. *Reproduced with permission from* [2]. *Copyright 2002 by the American Physical Society.* 107

6.13 (a) A schematic of the reciprocal space lattice for the pyrochlore structure of CSI along the h, h, l plane. The filled circles are the $q = 0$ high symmetry points and the empty circles are the $q = X$ high symmetry points. *Reprinted figure (a) with permission from* [35]. *Copyright 1997 by the American Physical Society.* (b) Scattering intensity in the h, h, l plane for DTO at 0.05 K in zero field, showing diffuse scattering at the $q = X$ points and and (c) in $B = 1.5$ T $\parallel [1\bar{1}0]$ field, showing Bragg scattering at $q = 0$ points and diffuse scattering features at $q = X$ points. *Reprinted figure (b), (c) with permission from* [36]. *Copyright 2005 by the American Physical Society.* . . 108

6.14 Thermal conductivity of HTO with total conductivity modelled as the sum of phonon and magnetic monopole conductivity, $\kappa_{\text{total}} = \kappa_{\text{ph}} + \kappa_{\text{mag}}$. *Reprinted figure with permission from* [37]. *Copyright 2013 by the American Physical Society.* 109

6.15 (a) Local D_{3d} degrees of freedom on a rare earth ion site (orange spheres). The symmetry consists of a C_2 rotational symmetry along the local $\langle 111 \rangle$ axis (black line), and a perpendicular, local XY plane (purple disk) with three C_3 rotational axes (purple lines) [38]. (b) Pyrochlore lattice with hexagonal ring outlined in red. 112

6.16 The energy scales of excitations in the QSI model. Image from Gingras and McClarty [39]. © *IOP Publishing. Reproduced with permission. All rights reserved.* 114

6.17 Li *et al.* report the thermal conductivity of $Tb_2Ti_2O_7$ at temperatures up to 100 K on a log-log scale [40]. (a) Thermal conductivity of $Tb_2Ti_2O_7$ samples "A" and "B" with heat current $J_H \parallel [111]$. Inset: phonon mean free paths ℓ of $Tb_2Ti_2O_7$ sample A and $Y_2Ti_2O_7$ on a semi-log scale at temperatures up to 5 K. (b) Thermal conductivity of $Tb_2Ti_2O_7$ (sample "B"), $TbYTi_2O_7$ and $Y_2Ti_2O_7$. *Reprinted with permission from* [40]. *Copyright 2013 by the American Physical Society.* 116

6.18 Magnetization of PZO at 90 mK. Inset: magnetization with field parallel to [111] centered around 0 T, showing a slight hysteresis. *Reprinted with permission from* [41]. *Copyright 2016 by the American Physical Society.* . . . 118

6.19 PZO INS averaged for momentum transfer 0.5 $\text{Å}^{-1} \leq |\boldsymbol{q} \leq 2.2\ \text{Å}^{-1}$, at $T = 1.4$ K under an applied field parallel to [001]. Inset: Using an Ising exchange parameter $J^z_{\text{eff}} = 3.76$, the authors show that the INS spectrum in the main figure follows a Lorentzian-like distribution $\rho(\delta)$ as discussed in the main text. *Reprinted with permission from* [42]. *Copyright 2017 by the American Physical Society.* 119

6.20 Spinon condensation as a function of disorder average strength $\bar{h}$ and width δh. *Reprinted with permission from* [43]. *Copyright 2018 by the American Physical Society.* 122

7.1 (a) Susceptibility at 0.1 T and 1.0 T; and (b) magnetization of single-crystal PHO at 2 K. *Reproduced with permission from* [44]. *Copyright 2016 by the American Physical Society.* 124

7.2 Laue X-ray images of PHO samples used in this study. (a) PHO S1 showing the $[\bar{1}\bar{1}0]$ direction perpendicular to the heat current and transverse field directions. (b) PHO S2 showing the [001] direction that is oriented perpendicular to the heat current. 126

7.3 Thermal conductivity of PHO S2 at temperatures up to 50 K. 127

7.4 Thermal conductivity plotted as a function of temperature in zero field for S1, S2 and S3. Lines are the estimates of maximal phonon conductivity by using a mean free path equal to the geometric mean of the cross-sectional area as in Equation (A.13). 128

7.5 Thermal conductivity of PHO samples (a) S1, (b) S2 and (c) S3 at various magnetic fields plotted as κ/T versus T. The heat current is parallel to $[1\bar{1}0]$ for all three samples. 130

7.6 Field dependence of thermal conductivity for $Pr_2Hf_2O_7$. Solid points are obtained from the temperature sweeps in Figure 7.5 as a comparison. As discussed in the main text, the average temperature varies by 0.04 K for the sweeps with $B \parallel [001]$ and 0.02 K for the sweep with $B \parallel [1\bar{1}0]$. 131

7.7 Thermal conductivity ratio of S1 and S3, $\kappa(\text{S1})/\kappa(\text{S3})$ at temperatures below 1 K and in zero applied magnetic field, plotted on a semi-log plot. The line is the ratio of the Casimir values of the boundary-limited phonon mean free paths, $\ell_C(\text{S1})/\ell_C(\text{S3}) = 2.24$, as described in the main text. 133

7.8 Illustration of the estimated total expected phonon + photon thermal conductivity (gray shaded areas). Photon contributions are calculated using Equation (7.1) and Sibille *et al.*'s estimated photon speed, $v_{\text{pt}} \sim 3.6\ \text{m}\,\text{s}^{-1}$ [45], with photon mean free path ℓ_{pt} ranging from a minumum of $\lambda_C \approx 0.8\,a_0$ (solid black lines) to a maximum of ℓ_C (dashed lines). (a) Plotted as κ versus T on a log-log graph. The red circles are PHO S1 experimental data in zero field and the red line is the estimate of the maximal phonon thermal conductivity as in Figure 7.4. (b) Thermal conductivity ratio of S1 and S3, $\kappa(\text{S1})/\kappa(\text{S3})$ at temperatures below 1 K and in zero applied magnetic field plotted on a semi-log graph. 135

7.9 Comparisons of PHO 0 T thermal conductivity with QSI candidates $Tb_2Ti_2O_7$ [40], $Pr_2Zr_2O_7$ [46] and $Pr_2Ir_2O_7$ [47, 48]. (a) Low temperature thermal conductivity plotted on a log-log graph. (b) High temperature thermal conductivity. 138

7.10 Fitting thermal conductivity in zero field of S1 using the Callaway model with total scattering rates $\sum_i \tau_i^{-1} = v_s/\ell_C + \tau_{\text{exc}}^{-1}$ (solid blue line), $\sum_i \tau_i^{-1} = v_s/\ell + \tau_{\text{res1}}^{-1}$ (dashed black line), and $\sum_i \tau_i^{-1} = v_s/\ell_C + \tau_{\text{exc}}^{-1} + \tau_{\text{res2}}^{-1}$ where τ_{res2}^{-1} (dashed-dotted red line). The scattering rate components τ_{exc}^{-1}, τ_{res1}^{-1} and τ_{res2}^{-1} are given by Equations (7.4), (7.3) and (7.5) respectively. The fixed parameter v_s/ℓ_C is the expected phonon scattering by sample boundaries [Eq. (A.7)]. 140

A.1 Visualization of phonon transport using kinetic theory along the x direction. The thermal current at x_0 last scattered a distance ℓ from the point at an angle θ from the x-axis and travelled at speed v_s. 167

A.2 (a) Calculated ratios of the phonon mean free path in the boundary scattering limit ℓ normalized by the Casimir value ℓ_c for different proportions of diffuse scattering f and sample proportions R/L. The black dots are observed values of ℓ/ℓ_C for four different sample geometries, Image and data from Berman *et al.* [49]. (b) Calculated ratios of phonon thermal conductivity K to the Casmir expectation K_c for different values of f and R/L. □ rough sapphire crystal, ○ and △ smooth crystal at 5.9 and 4.5 K. Image from Berman *et al.* [50] 172

A.3 The thermal conductivity plotted as κ/T^3 versus T of Nd_2CuO_4 with as-grown (smooth) and roughened sample boundaries. The black line indicates the theoretical expectation for phonon conduction limited by sample boundaries with a mean free path proportional to the geometric mean of the sample cross-sectional area. *Reprinted with permission from* [51]. *Copyright 2008 by the American Physical Society.* 173

A.4 Typical thermal conductivity for a non-metallic crystal as a function of temperature [52, 53]. Qualitatively, the phonon-dominated thermal conductivity is limited by sample boundaries at the lowest temperatures, reaches a peak at intermediate temperatures ($\sim \Theta_D/30$ [53]) with a height suppressed by sample disorder, and Umklapp (phonon-phonon) scattering dominating at higher temperatures. 174

A.5 Reproduced from Berman [53]. (a) Energy gap of a splitting in zero field ΔE_0 and increase in the energy gap in applied field B. (b) A band of phonons scatter resonantly, removing the contributions of these phonons to thermal conductivity for a band of phonons that is centered around the energy gap. 175

B.1 (a) Thermal conductivity of YbB_{12} S1 in zero field and temperatures up to 50 K compared to the thermal conductivity in this range for SmB_6 samples FZ1 and FZ3. (b) Same but with the thermal conductivity normalized by the 50 K value to account for sample-dependent effects. 179

B.2 (a) Low temperature thermal conductivity of YbB_{12} sample in zero field and 12 T field on a log-log plot. Black line is a fit to $\kappa = AT^\alpha$ and blue line is the estimated maximum phonon thermal conductivity from the sample geometry and a Debye temperature $\Theta_D = 373$ K. (b) Ratio of thermal conductivity in applied field to zero field value as a function of applied field and at an average temperature of 560 mK. (c) Thermal conductivity in zero field plotted as κ/T versus $T^{1.32}$. Lines are fits to $\kappa/T = A + BT^{1.32}$. . . . 180

List of Symbols

β Lattice specific heat capacity 170

v_s Speed of sound 170

$N_{\mathbf{A}}$ Avogadro's constant 134

R Gas constant 170

V Unit cell volume. For lattice parameter a_0, unit cell volume $V = a_0^3$. 134, 170

Z Number of formula units per unit cell 134, 170

h Planck's constant 170

$k_{\mathbf{B}}$ Boltzmann constant 170

q Atoms per formula unit 170

Introduction

Advancements in materials research lead to the adaption of technology in our daily lives, from semiconducting transistors in household electronic devices to superconductors that are routinely used in diagnostic medical imaging. A plethora of novel "quantum materials", which manifest quantum mechanics effects at macroscopic scales, have the potential to further revolutionize our technology. Yet many of these materials still require fundamental research to fully understand how to efficiently reproduce these effects. This research is vital to continuing technological advancements including in quantum computing applications, such as improving information storage and transfer and reducing errors that corrupt information transmission. In particular, the quantum materials discussed in this thesis have unexplored potential due to the possibilities of new magnetic quasiparticle excitations, which we explore using thermal transport techniques.

Thermal conductivity gives information about the transport properties of novel excitations. This technique has the benefit of only having contributions from delocalized excitations. However, we must also carefully analyze this data to delineate the contributions of different heat-carriers. Our analysis is further informed by observing thermal conductivity behaviour with temperature and in an applied magnetic field along a known crystallographic direction in single crystals, which helps us to attribute unconventional field or temperature behaviour to novel magnetic excitations.

We use low temperature techniques to reach milliKelvin temperatures. Conducting experiments at these low temperatures allow us to approach the lowest energy excitations. In Chapter 1, first we introduce the low temperature techniques used to reach temperatures from 50 mK to 50 K. Next, we describe the two main measurement techniques used to investigate the novel magnetic excitations in these materials: thermal conductivity (Chapter 2) and oscillatory magnetostriction (Chapter 3). We use the thermal conductivity technique to probe delocalized quasiparticle excitations in the bulk of our single crystal samples. Furthermore, we use the oscillatory magnetostriction technique to learn about how a periodicity in the strain under applied magnetic field could be present in the bulk of a material.

We apply these methods to study two main classes of material, with novel phases that are yet to be unambiguously experimentally realized: topological Kondo insulator candidates and quantum spin ice candidates. Both classes of material have the potential for novel magnetic excitations at low temperatures that make them excellent materials for further study. In Chapter 4, we introduce topological Kondo insulators. Topological Kondo insulators are predicted to have an insulating ground state phase and conducting surface state that is topologically protected by transformations which conserve time reversal symmetry. Experimentally, the candidate materials characteristically have a transition from a bulk metallic state at room temperature to a bulk insulator as the temperature

decreases. Surprisingly, reports of exotic metallic-like bulk behaviour raises questions about the insulating nature of the bulk of this new class of materials. In Chapter 5, we show that our thermal conductivity results investigating the bulk of topological Kondo insulator SmB_6 imply the presence of charge-neutral, delocalized excitations in the bulk, and our preliminary oscillatory magnetostriction results call into question our usual understanding of quantum oscillations as a property emerging uniquely from an electrically conductive Fermi surface.

On the other hand, we test theoretical predictions of delocalized excitations in the quantum spin ice candidate $Pr_2Hf_2O_7$. In Chapter 6, we introduce quantum spin ice candidates, which show signs of strong spin fluctuations and a suppression of long range magnetism. A clear test of the three-dimensional quantum entangled U(1) quantum spin liquid state, that is predicted for such candidates, is the gapless photon excitation contributing to thermal conductivity. In Chapter 7, we show that our experimental results are not consistent with such excitations. Yet we explore the strong phonon scattering that we observe with a characteristic spin ice anisotropy, which we show is consistent with localized magnetic excitations and phonon resonant scattering.

An underlying theme in this thesis is the effect of disorder on interpretations of an underlying magnetic phase. Signs of novel magnetic excitations are most easily distinguished in high quality samples, particularly in thermal conductivity. In this transport measurement, phonon scattering by disorder suppresses thermal conductivity from conventional channels, requiring the need for a careful analysis of any contributions from novel delocalized magnetic excitations. With a sense of the transport mechanisms present in a sample, thermal conductivity analysis allows us to investigate the strength of phonon scattering by sample disorder to gain further information about intrinsic magnetic excitations in each material.

Quantum materials research allows us to harness collective quantum phenomena in technological applications. The results of this thesis contribute to the body of research on the quantum material classes of topological Kondo insulators and quantum spin ice candidates. To further advance research on these materials, we need corroboration of our findings. Experimental studies of exotic insulating properties in other growths of SmB_6, and generally other bulk insulating materials with a hybridized band gap, would help us understand the sample growth conditions needed to recreate these properties. Namely, thermal conductivity and bulk quantum oscillation studies of high quality SmB_6 samples that are free of metallic inclusions could uncover similar phenomena. Moreover, though we report a lack of gapless excitations in $Pr_2Hf_2O_7$, research into the lattice strain of non-Kramers quantum spin ice candidates could help us understand whether strain may drive real materials out of the anticipated U(1) quantum spin liquid ground state. As well,

it would be useful to conduct a similar thermal conductivity analysis of other emerging quantum spin ice candidates, such as the dipolar-octupolar quantum spin ice candidate $Ce_2Zr_2O_7$ [54, 55], to search for undeniable proof of the gapless photon excitation. Further research into collective phenomena in quantum materials helps us reliably recreate these effects prior to designing future technological applications.

Part I

Experimental techniques

Chapter 1

Cryogenic refrigeration

The quantum materials explored in this thesis are predominantly measured using thermal conductivity and magnetostriction techniques. Both techniques probe novel excitations in the bulk of samples. In Chapters 5 and 8 we analyze the experimental results using these techniques to reach conclusions about novel excitations in the bulk of SmB_6 and $Pr_2Hf_2O_7$. But first, we introduce these techniques and the low temperature refrigeration used to obtain our measurements.

We immerse our experiments in liquid helium using a pumped helium-4 cryostat or a dilution refrigerator to reach the low temperatures reported in our measurements. The pumped helium-4 cryostat uses evaporative cooling to control the thermal ground at temperatures below 2 K and can reach higher temperatures using a resistive heater mounted on the mixing chamber that regulates the temperature of the experimental apparatus. The dilution refrigerator uses a helium 3-helium 4 mix to reach temperatures below 1 K. We will next briefly describe the cooling mechanisms for each refrigerator. For a more comprehensive overview of low temperature techniques, the interested reader is referred to Pobell [56].

1.1 Pumped helium 4 cryostat

We use a pumped helium 4 (^{4}He) cryostat for measurements in the temperature range of $\sim 1-60$ K. This instrument uses evaporative cooling to reach temperatures below the boiling point of liquid helium. Evaporative cooling reduces the temperature of the cryoliquid by reducing the vapour pressure. Figure 1.1a shows the vapour pressures for cryoliquids,

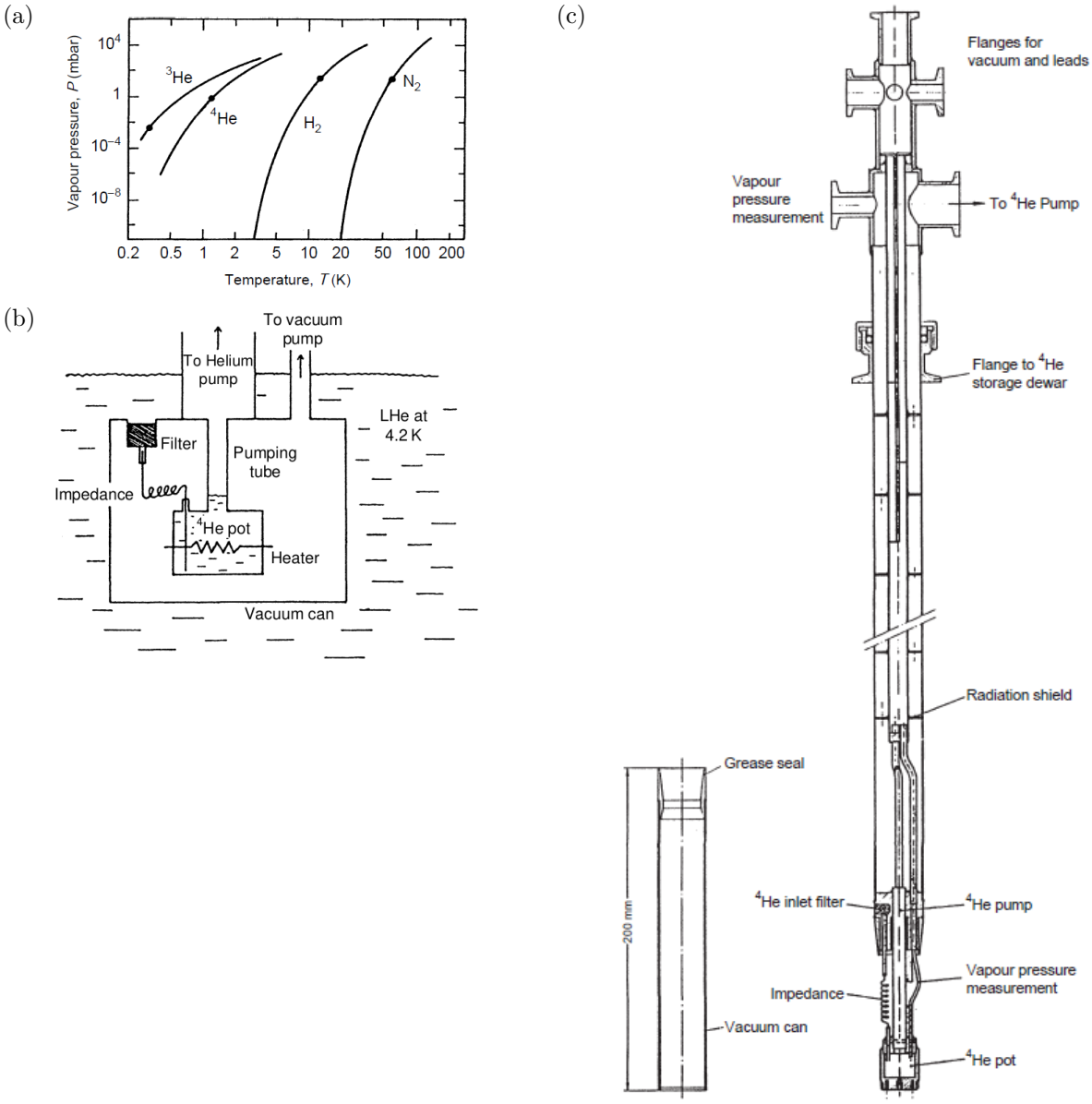


Figure 1.1: (a) Vapour pressure as a function of temperature on a log log scale for cryoliquids ^{3}He, ^{4}He, hydrogen and nitrogen. Black dots are practical minimum temperature limits reached by evaporative cooling with each cryoliquid [3]. (b) Schematic of a 1 K pot in a vacuum can, drawing liquid ^{4}He through an impedance into the helium container with a pump, and (c) sample drawing of a pumped ^{4}He cryostat [4]. *Reproduced with permission from Springer Nature.*

including ^{4}He, with practical temperature limits indicated by black dots. While pumping on the entire ^{4}He bath surrounding the cryostat would decrease the vapour pressure, it is more efficient and economical to only pump on a small volume of liquid helium that would cool the sample mount area. Pumping on the 1 K pot draws ^{4}He from the surrounding 4.2 K bath through an impedance into a vessel as illustrated in Figure 1.1b. A 1 K pot such as that shown in Figure 1.1b reduces the temperature of the apparatus by reducing the vapour pressure through pumping on the more kinetically energized particles at the surface of the liquid in the vessel. By reducing the vapour pressure in this way, the temperature of the helium remaining in this vessel decreases. This can operate in a continuous cooling manner to regulate the temperature so long as liquid remains in the 1 K pot. Nonetheless there exists a lower bound to the experimentally achievable temperatures, which depends on the heat load on the vessel. The balance of the heat load with the available cooling power leads to a practical temperature minimum of approximately 1.3 K using this cooling method, illustrated by the black dot on the ^{4}He curve in Figure 1.1b.

The pumped ^{4}He cryostat is a relatively easy way to achieve temperatures down to 1 K. A dipstick configuration close to the equipment we use is illustrated in Figure 1.1c. Its small profile and simple cooling mechanism allows for a quick turnaround time in experimental results. However a dilution refrigerator is more suited to measurements below 1 K. We will next describe how we reach temperatures below 1 K.

1.2 Helium 3-helium 4 dilution refrigerator

A helium 3-helium 4 (^{3}He-^{4}He) mix has fundamentally different properties than either ^{3}He or ^{4}He on its own, as described in Pobell [5]. While ^{4}He is bosonic due to its neutral spin, the more rare ^{3}He isotope is fermionic. In large enough concentrations, ^{3}He disrupts the Bose-Einstein condensate ground state of ^{4}He. A liquid mixture of these two isotopes follow a phase diagram with a phase-separation line as shown in Figure 1.2. When the ^{3}He concentration in the mixture, x, reaches a sufficient concentration of $x > 6.6\%$, the mixture separates into two phases below the phase-separation line with a ^{3}He-rich liquid sitting on the top of ^{4}He due to its lower density. The dilution refrigerator takes advantage of this phase separation to cool the mixing chamber to milliKelvin temperatures by evaporating then circulating the ^{3}He in the condensed mixture. Figure 1.3a shows a schematic of the phases of a ^{3}He-^{4}He mixture in different stages of the dilution refrigerator, which is kept in closed cycle to preserve the costly ^{3}He isotope and maintain a fixed volume of the mix that works with the equipment design. The mixture entering the fridge is first pre-cooled by the 1 K pot as well as by the mixture leaving the fridge through a series of heat exchangers

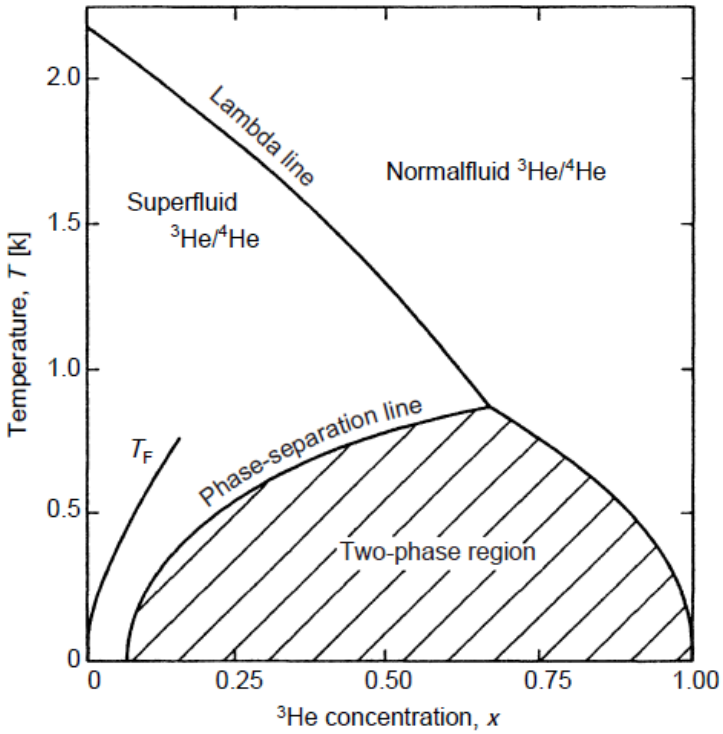


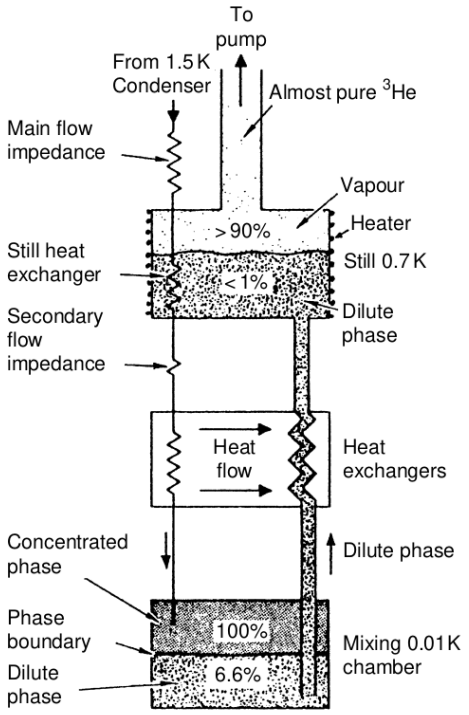
Figure 1.2: Phase-separation line for the phases of a ^{3}He-^{4}He mixture with respect to temperature and ^{3}He concentration x [5]. *Reproduced with permission from Springer Nature.*

and an impedance that regulates the flow of the mix. Then, at temperatures below the phase-separation line, this ^{3}He rich mix sits at the top of the phase boundary in the mixing chamber with a dilute phase sitting below. This dilute phase then exits the mixing chamber with the liquid filling the still. Owing to a larger vapour pressure, by heating the still to $\sim$ 0.7 K, the ^{3}He isotopes in the still evaporate while ^{4}He remains in its liquid state, allowing circulation of ^{3}He that's facilitated by a pump in order to maintain a consistent cooling power in the mixing chamber. This circuitry cools our experimental apparatus shown in Figure 1.3b.

1.3 Temperature stability

The minimum temperature attained by a fridge is colloquially referred to as the "base temperature". This is different for each cooling mechanism; the ^{3}He-^{4}He dilution refrigerator

(a)



(b)

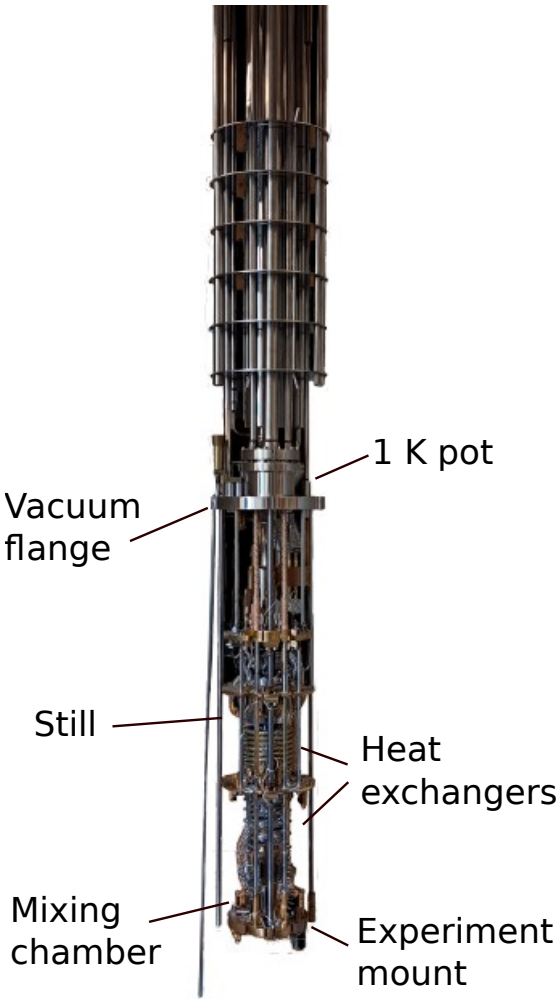


Figure 1.3: (a) Schematic of the closed cycle of a ^{3}He-^{4}He mixture in a dilution refrigerator [5]. *Reproduced with permission from Springer Nature.* (b) Dilution refrigerator used for experiments at temperatures below 1 K.

reaches sub-Kelvin temperatures, which is two orders of magnitude lower than the ~ 1 K base temperature reached using only ^{4}He evaporative cooling. A lower base temperature can also be quickly reached for short periods of time by moving the cooling environment out of equilibrium with tuning of the 1 K pot or removal of ^{3}He from the still. However we require temperature stability for longer periods of time while conducting our experiments. The base temperature depends on the heat load and cooling power of the instrument.

The heat load can change between different experimental setups due to the electronic heating and the effectiveness of the radiation shielding precautions. We try and make the most of our helium supply by mounting two or three experimental setups to the refrigerator at a time. Each experimental apparatus adds Joule heating to the system with its electronic sensors and therefore requires additional cooling power to cool the experimental box, even though space limitations of the magnetic bore limit the total available sample space in the refrigerators to a small volume of ~ 100 cm^3. We use twisted pairs of cryogenic wire for electrical leads and ensure experimental apparatuses are thermally anchored to reduce the heat load. Even so, adding these devices increases the base temperatures above the refrigerator specifications, which are fixed by the cooling power which is set by engineered variables including the pump power for evaporative cooling, the ratio of ^{3}He to ^{4}He in the mixture and the fridge design. We typically reach a stable base temperature of ~ 50 mK with the dilution refrigerator and ~ 1.5 K for the ^{4}He evaporative dipstick. The dilution refrigerator also loses temperature control above 1 K when the ^{3}He-^{4}He mix is condensed inside the refrigerator due to the high heat load of these temperatures on the mixing chamber. Typically this leaves a small gap in data collection between the temperature regime of each refrigerator.

1.4 Superconducting field

We conduct our measurements in an applied *dc* magnetic field using a superconducting magnet. The magnet is submersed within the helium bath with the experimental cold finger resting in its bore. By changing the current of the superconducting coil, we fine tune the magnetic field within the bore. We can also change the orientation of a field with respect to sample crystallographic directions by changing the orientation of the sample when mounting it to the cold finger prior to its measurement. With a helium bath at the boiling temperature of 4.2 K, the magnet can operate up to 14 T, though realistically operating at the upper boundary of this limit increases the risk of a magnet quench where the magnet temperature rises above the superconducting temperature and becomes normal, boiling off the liquid in the helium bath in a matter of minutes. In practice, we typically

operate the magnet within the range of ± 12 T.

Chapter 2

Thermal conductivity

2.1 Introduction to thermal transport

The ease with which thermal energy propagates along a sample is a material-dependent property. The Fourier law dictates that the thermal current $\boldsymbol{j}$ is

$$\boldsymbol{j} = -\kappa \boldsymbol{\nabla} T \tag{2.1}$$

where κ is the thermal conductivity tensor. When the temperature gradient is constrained to one dimension, the longitudinal thermal conductivity is given by

$$j_x = -\kappa_{xx} \frac{dT}{dx} \tag{2.2}$$

where κ_{xx} is the longitudinal thermal conductivity along the x axis. The negative sign of the thermal current j indicates that the current travels from the heat source to sink. Figure 2.1a shows a schematic for a steady-state longitudinal thermal conductivity measurement of a three dimensional sample. A heater with a controlled thermal energy $\dot{Q}$ drives the thermal current towards a heat sink that is maintained at a controlled temperature T_0. Then thermometers measuring temperatures T_H and T_C at a distance l apart sense a thermal gradient $\Delta T = T_H - T_C$. The thermal conductivity for a sample with cross-sectional area A and geometric factor $g = l/A$ is then

$$\kappa = -\frac{\dot{Q}}{\Delta T} \frac{l}{A}. \tag{2.3}$$

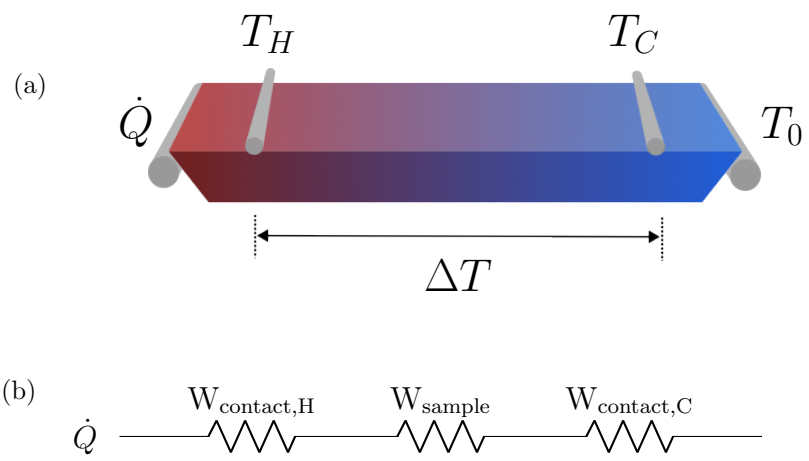


Figure 2.1: (a) Schematic of a typical thermal conductivity setup. Heat $\dot{Q}$ is applied to one end of the sample and the opposite end of the sample is thermally anchored to a heat sink maintained at temperature T_0, driving a thermal gradient ΔT between the hot thermometer T_H and the cold thermometer T_C. (b) Schematic of the thermal current circuit in the above figure.

2.2 Thermal conductivity measurement

The thermal conductivity results considered in this thesis are using a steady-state two-thermometer one-heater method on single crystal samples. The heater provides heat $\dot{Q}$ to the sample and the two thermometers measure the thermal gradient. The sample contacts are thermally conductive, typically silver wires with a conductive silver paste or epoxy to secure the wires to the sample. They are mounted in a shielded copper box shown in Figure 2.2a and described by Toews and Hill [6]. Ideally, all the heat applied to the sample would pass through the sample, but in reality, there are heat losses through radiation and contacts. The thermometers and heaters are kept thermally isolated from the copper box by suspending them on a thermally insulating material such as a thin strand of nylon or kapton. The electrical circuit for these components also uses highly resistive platinum tungsten coils to electrically connect these components to the circuit board while keeping heat losses to these components on the order of 1% or less.

The system can also lose heat through the resistance of the contacts that connect the sample with the heater, thermometers, and heat sink. Figure 2.1b illustrates a simple thermal circuit with thermal resistance $W = 1/(g\kappa)$. Ideally, we would like to limit thermal losses, including through sample contacts, to less than 1% of the sample thermal resistance as discussed by Toews and Hill [6]. Satisfying this limitation validates the assumption that the heater power $\dot{Q}$ is approximately equal to the heat input into the sample when

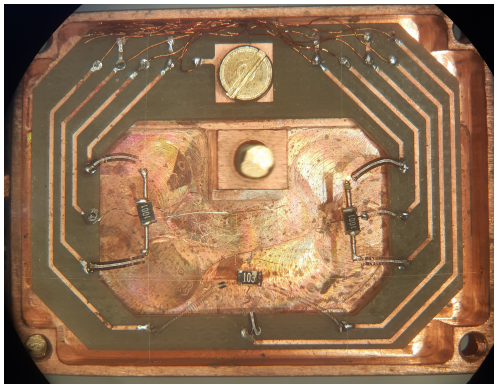


Figure 2.2: Thermal conductivity setup with a copper box used for radiation shielding [6].

calculating the thermal conductivity using Equation (2.3). In practice, in order to reach a non-negligible temperature gradient ($\Delta T/T_{\text{avg}} \approx 5 - 10\%$ where $T_{\text{avg}} = (T_H + T_C)/2$ is the average sample temperature), samples with high contact resistance can necessitate a larger heat input that increases the lowest achievable average temperature of a thermal conductivity dataset.

2.2.1 Thermometry

We use resistive thermometers in our thermal conductivity measurements. To maximize sensitivity, the thermometer choice depends on the temperature range. We use cernox thermometers in the pumped ^{4}He cryostat for temperatures above ~ 1 K and ruthenium oxide thermometers in the dilution refrigerator in the milliKelvin temperature range. Since resistance thermometry is a secondary thermometry technique, the resistance thermometers must be calibrated. We calibrate sample hot and cold thermometers in situ and use a calibrated reference thermometer to control the temperature of the heat sink, T_0. The in-situ calibration is as follows: first, we set the temperature T_0 for the thermal conductivity step, then we wait for the resistances of the hot and cold thermometers to settle. Keeping the sample heater off, we measure the hot and cold calibration points by averaging over a sufficient number of points. Then, we repeat this step at the same T_0 setting with the heat on. In order to generate a calibration curve, we use a polynomial fit of the logarithms of resistance, while removing outliers. We use these calibration curves to convert the averaged, heat on thermometer resistances to the temperatures of the hot and cold thermometers in order to obtain the temperature gradient ΔT and average temperature T_{avg} of the thermal conductivity measurement.

Resistive thermometers are also sensitive to an applied magnetic field. In the dilution refrigerator, the calibrated reference thermometer is situated in a field-compensated region to remove the effects of field, facilitating the usual approach to in-situ calibrations of the sample thermometers. When sweeping a magnetic field, we also compensate for the sample thermometer magnetoresistances obtained in situ in our calibration curves.

2.2.2 Error propagation and reduction

We use a scale micrometer with divisions as small as 0.01 mm and use ImageJ software to measure sample dimensions from pictures taken under an optical microscope. When capturing images, we ensure the camera sits level with the ocular lens and that imaged samples are in the plane of the reference scale[1]. This approach has the capability to measure sample dimensions with a precision of $\sim \pm 0.005$ mm. We can estimate the error propagation for random, independent errors. Using this approach, the fractional error in the cross-sectional area $A = w \times h$ is then the root sum of the squares of fractional errors in width w and height h,

$$\frac{\delta A}{A} = \sqrt{\left(\frac{\delta w}{w}\right)^2 + \left(\frac{\delta h}{h}\right)^2} \tag{2.4}$$

and the upper bound on the actual fractional error in area is equal to the absolute sum of the fractional errors in width and height [57]. Similarly, random errors in temperature control are kept below 0.1% using the in situ calibration procedure described by Toews and Hill [6].

However the largest error in these steady state thermal conductivity measurements is a systematic error in the sample contact lengths. These sample contacts are mounted by hand under a microscope using silver wires with diameters ranging from ~ 0.025 mm to 0.1 mm and using silver paint or silver epoxy to make a thermal contact with the sample. Since we do not know exactly where the thermal contact attaches on the sample, our error in the effective sample length — the distance between thermometer contacts — is much larger than our measurement resolution. We estimate the length between contacts $\bar{l}$ in the geometric factor g to be equal to the average length between the extremities of the silver

[1] This is most easily measured before mounting sample contacts, when the sample can be manipulated to measure all dimensions: its length, width and height. Sometimes we need to remeasure sample dimensions after mounting sample contacts. To preserve the integrity of sample contacts, we may use another sample dimension (ie. length) as a reference scale for one of the dimensions rather than the scale micrometer.

paint or epoxy. We also need these thermometer contacts to be sufficiently separated from the heater and heat sink contact locations, hence these contacts are often less than 1 mm apart. A typical error in contact length can be $\sim 10-20\%$. This systematic error appears as an error in the geometric factor $g = \bar{l}/A$, and any correction in this factor would simply systematically shift all thermal conductivity results of similar geometries by the same multiplicative constant. As well, sample inhomogeneity typically introduces a systematic error in the accuracy of the sample cross-sectional area measurements. While it is certainly desirable to keep systematic errors as small as possible by keeping the contacts well separated and by approximating inhomogenous dimensions by using geometric averages, we are limited by the sample geometry, the silver wire size and the skill of the contact mounter (these contacts are approximately the diameter of human hair, which makes them difficult to attach). Regardless, we proceed to propagate this error when we are concerned about the accuracy of the thermal conductivity measurement, such as when we wish to compare our results with theoretical expressions for the thermal conductivity.

If want to err on side of caution, we could combine random and systematic errors additively; $x = \bar{x} + \delta x_{\text{random}} + \delta x_{\text{systematic}}$. Such an approach would likely overestimate error; we can only give a maximal error for the systematic error and not a precise value because we do not have a way of knowing exactly where the heat conduction happens in the sample contacts. Another approach is to combine these errors in quadrature to get an estimate $\delta x = \sqrt{(\delta x_{\text{random}})^2 + (\delta x_{\text{systematic}})^2}$ [57]. While this approach is not rigorously justified, we can use this expression for the purposes of obtaining a more reasonable error estimate. This approach could be questioned if the data is far from the expected value, including its error bars. In practice, using the average contact length results in only a small deviation — if any — from theoretical estimates and such error bars dominated by a precautionary inclusion of systematic error are likely overestimating the true error in thermal conductivity measurements.

2.2.3 Sample error propagation calculations

Suppose that the error in sample geometry is as follows: a 10% systematic error in sample contact length $\delta l/l$, a 1% random error in sample width $\delta w/w$ and a1% random error in sample height $\delta h/h$. Then, combining these errors in quadrature, we obtain the error δg in the geometric factor $g = l/A$ as follows:

$$\begin{aligned}\frac{\delta g}{g} &= \sqrt{\left(\frac{\delta l}{l}\right)^2 + \left(\frac{\delta w}{w}\right)^2 + \left(\frac{\delta h}{h}\right)^2} \\ &= \sqrt{(10\%)^2 + (1\%)^2 + (1\%)^2} \\ &\approx 10\%.\end{aligned} \tag{2.5}$$

Propagating this error to the error in thermal conductivity, suppose that the error in heater power $\delta\dot{Q}/\dot{Q}$ and temperature gradient $\delta\Delta T/\Delta T$ is limited to 1%. Then the error in thermal conductivity $\delta\kappa/\kappa$ is estimated to be

$$\begin{aligned}\frac{\delta \kappa}{\kappa} &= \sqrt{\left(\frac{\delta g}{g}\right)^2 + \left(\frac{\delta \dot{Q}}{\dot{Q}}\right)^2 + \left(\frac{\delta \Delta T}{\Delta T}\right)^2} \\ &= \sqrt{(10\%)^2 + (1\%)^2 + (1\%)^2} \\ &\approx 10\%\end{aligned} \tag{2.6}$$

which is approximately equal to the relative systematic error in the sample contact length, $\delta l/l$. The relative error in thermal conductivity can be approximated as the relative systematic error in sample contact length if the error in w, h, $\dot{Q}$ and ΔT are kept below 1%.

Suppose we take the quotient of two thermal conductivities, κ_1 and κ_2, each with a 10% systematic error in sample contact length. Then the error in the ratio of the quotient, κ_1/κ_2, can be approximated as

$$\begin{aligned}\frac{\delta(\kappa_1/\kappa_2)}{(\kappa_1/\kappa_2)} &= \sqrt{\left(\frac{\delta \kappa_1}{\kappa_1}\right)^2 + \left(\frac{\delta \kappa_2}{\kappa_2}\right)^2} \\ &= \sqrt{(10\%)^2 + (10\%)^2} \\ &\approx 14\%.\end{aligned} \tag{2.7}$$

When comparing these estimates to experiments, an observed proximity to the expected value across multiple measurements could mean that the best estimate of the sample contact length is closer to the real value than the systematic error estimate might suggest.

Chapter 3

Magnetostriction

The change in length of a sample in response to a magnetic field is its magnetostriction, which measures the strain dependence of the lattice. This thermodynamic effect emerges indirectly from the specific heat capacity and magnetization through thermodynamic relations, as illustrated in Figure 3.1. Thermodynamic relations connect the nodes in this figure, with magnetostriction connecting the field dependence of the strain and the stress dependence of the magnetization. This is illustrated as follows. By taking the principal relations in the figure, as indicated by bold arrows, the magnetic susceptibility χ_{ab} relates incremental changes in the magnetization per unit volume M and the applied magnetic field $\boldsymbol{H}$ [7]

$$dM_a = \sum_b \chi_{ab}\, dH_b, \tag{3.1}$$

the specific heat capacity per unit volume C relates the entropy S per unit volume and the temperature T as

$$dS = \left(\frac{C}{T}\right) dT \tag{3.2}$$

and the strain ϵ_{ij} is related to the stress σ_{ij} by compliance tensor s_{ijkl} as

$$d\epsilon_{ij} = \sum_{k,l} s_{ijkl}\, d\sigma_{kl}. \tag{3.3}$$

The components of the strain and stress tensors use the indices such that $i = j$ are axial deformations and $i \neq j$ are shear deformations. In the case of magnetostriction, due to the symmetry of its tensor, the strain indices i and j commute [58]. The index pairs ij can be converted from Cartesian axes to Voigt notation in the usual way, $\{xx, yy, zz, yz, xz, xy\} = \{1, 2, 3, 4, 5, 6\}$, to simplify the full tensor representation.

Such thermodynamic equations demonstrate the connections between the responses of such properties. Here, we focus on the magnetostriction thermodynamic relation at constant temperature. The isothermal magnetostriction coefficients m_{aij} relate changes in the elastic strain ϵ_{ij} with respect to the strength and direction of an applied magnetic field as [7]

$$d\epsilon_{ij} = \sum_a m_{aij}\, dH_a, \tag{3.4}$$

resulting in a strain tensor

$$\epsilon_{ij} = \sum_{a,b} \frac{1}{2} m_{abij} H_a H_b = \sum_a \frac{1}{2} m_{aij} H_a, \tag{3.5}$$

where the right hand side of Equation (3.5) converts the fourth-rank tensor m_{abij} to the magnetostriction coefficients of Equation (3.4) using $m_{aij} = \sum_b m_{abij} H_b$.

Generally, the elastic strain tensor in a given direction depends on the crystal symmetry as well as the orientation of the applied magnetic field, reducing the magnetostriction coefficients to those allowed by the crystal symmetry. Using Equation (3.5) and the symmetries of a cubic crystal, the non-zero strain components in Voigt notation are the axial strain ϵ_1

$$\epsilon_1 = \frac{1}{2} m_{11} H_1^2 + \frac{1}{2} m_{12} \left(H_2^2 + H_3^2 \right), \tag{3.6}$$

and the shear strain ϵ_4

$$\epsilon_4 = m_{44} H_2 H_3 \tag{3.7}$$

using the convention $\boldsymbol{H} = H_1 \hat{x} + H_2 \hat{y} + H_3 \hat{z}$ [7]. The symmetries of the strain tensor dictate the relation between the magnetostriction and the applied magnetic field direction in a single crystal. As will be referred to in Section 5.3, the overall change in sample length

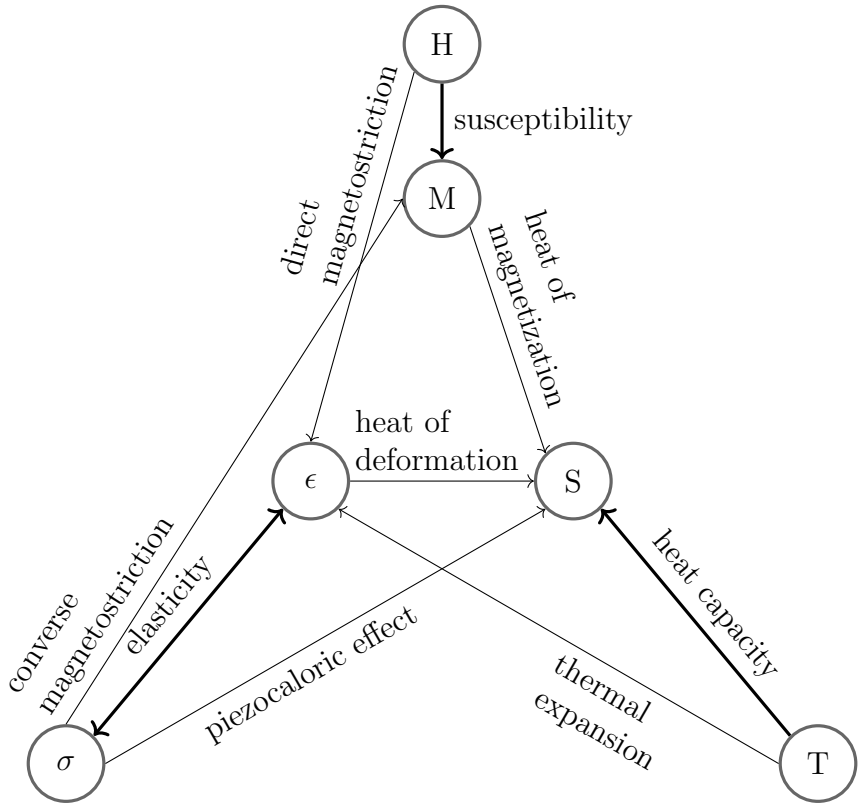


Figure 3.1: Coupled relations between thermodynamic effects, as adapted from Chandrasekhar and Fawcett [7]. Small changes in the elastic stress σ, strain ϵ, applied magnetic field H, temperature T, magnetization M, and entropy S are proportional to the product of small changes of the respective quantity at the arrow's tail and the physical property captioning the arrow connecting the two properties.

$\Delta L/L$ of a sample with cubic symmetry that is oriented in the [001] direction, in response to a longitudinal applied magnetic field $\boldsymbol{H}$, is simply

$$\left(\frac{\Delta L}{L}\right)_{[001]} = \frac{1}{2} m_{11} H_1^2. \tag{3.8}$$

In general, the volumetric strain ϵ_{ij}, which is the change in sample volume per unit volume, requires the full sum of Equation (3.5) while accounting for applied field directions and simplifications from crystal symmetries.

3.1 Quantum oscillations in magnetostriction

Quantum oscillations in metals originate from the quantization of cyclotron motion of the conduction electrons. In 1930, Landau theorized that this quantization could lead to an oscillatory magnetization with respect to an applied magnetic field, an effect now known as the "de Haas-van Alphen" (dHvA) effect after the observation of an oscillatory magnetic susceptibility in bismuth single crystals by de Haas and van Alphen that same year [8, 59, 60]. Measurements of this oscillatory magnetostriction probe the shape and size of the Fermi surfaces of conduction electrons. This is illustrated by Onsager's quantization relation that emerges from the quantization of magnetic flux [8, 61, 62],

$$a_k = (n + g_\gamma) 2\pi e H/\hbar, \tag{3.9}$$

with quantum number n and phase constant g_γ[1]. According to this relation, the allowed cross-sectional areas, a_k, of the Fermi surface are confined to tubes in momentum space, or "Landau levels" that transition discretely in a given applied magnetic field. Figure 3.2 illustrates the quantization of these levels on a spherical Fermi surface. As the field increases, the quantum number of the extremal allowed state decreases, and the allowed states successively occupy the extremal Fermi surface cross-sectional area A when $a_k = A$ is satisfied. Quantum oscillations in magnetic and metallic properties emerge from the changing conduction electron occupations as these Landau levels pass through the Fermi surface. Such oscillations are periodic in H^{-1} according to the difference in successive extremal areas [8],

[1]The phase constant $g_\gamma = \frac{1}{2}$ for a free electron.

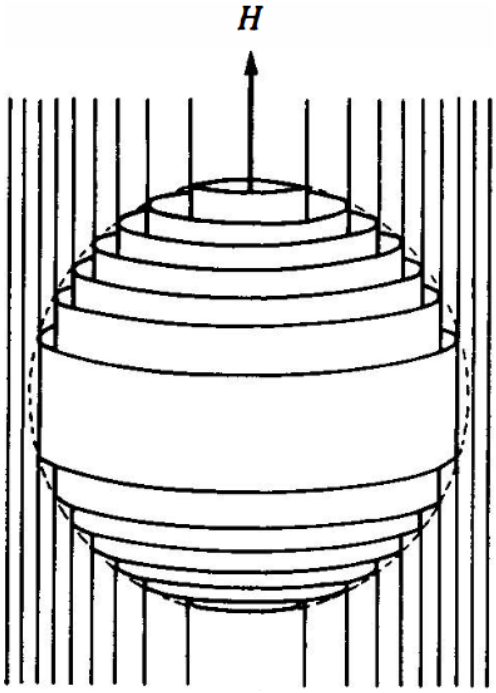


Figure 3.2: Landau levels for a Fermi gas under applied field H on a spherical Fermi surface (broken line) with circular cross-sectional areas [8]. At constant energy, the permitted occupied electronic states conform to the illustrated cylindrical tubes according to the Onsager relation of Equation (3.9). *Reproduced with permission from Cambridge University Press.*

$$\Delta(1/H) = \frac{2\pi e}{\hbar A}, \tag{3.10}$$

implying a frequency proportional to A as

$$F = \frac{\hbar A}{2\pi e}. \tag{3.11}$$

Therefore by probing quantum oscillation frequencies with respect to a changing magnetic field, one can determine the shapes and sizes of the cross-sectional extremal Fermi surface areas. Furthermore, changing the angle of the magnetic field in an oriented single crystal allows a three-dimensional probe of this Fermi surface, as is often conducted in torque magnetization measurements.

The Lifshitz-Kosevich (LK) formula describes periodic oscillations in the thermodynamic potential $\tilde{\Omega}$ arising from this electron quantization [8]. The oscillatory thermodynamic potential results in oscillatory magnetic properties through their thermodynamic relations, as visualized in Figure 3.1. Oscillations in the elastic strain $\tilde{\varepsilon}_{ij}$ are related to oscillations in the thermodynamic potential, given stress σ_{ij} as

$$\tilde{\varepsilon}_{ij} = -\partial\tilde{\Omega}/\partial\sigma_{ij} \tag{3.12}$$

with $\tilde{\Omega} = \sum_r \Omega_r \cos\left(\frac{2\pi F_r}{H} + \phi_r\right)$, summing over different dHvA frequencies F_r under applied field H [8]. This expression generalizes a phase factor ϕ_r and amplitude Ω_r for each frequency. Carrying out the differential in Equation (3.12) results in an expression for the oscillatory elastic strain

$$\tilde{\varepsilon}_{ij} = \sum_r \Omega_r \left(\frac{2\pi}{H}\right) \frac{\partial F_r}{\partial \sigma_{ij}} \sin\left(\frac{2\pi F_r}{H} + \phi_r\right). \tag{3.13}$$

This can also be related to the oscillatory magnetization $\tilde{M}$ with frequency-dependent amplitudes M_r. Given the thermodynamic relation for the magnetostriction $\boldsymbol{M}$ at a constant Fermi energy,

$$\boldsymbol{M} = -\boldsymbol{\nabla}_{\boldsymbol{H}}\Omega, \tag{3.14}$$

then the oscillatory portion of the magnetization can be expressed as

$$\tilde{M} = \sum_r M_r \sin\left(\frac{2\pi F_r}{H} + \phi_r\right) = -\sum_r \left(\frac{2\pi F_r}{H^2}\right) \Omega_r \sin\left(\frac{2\pi F_r}{H} + \phi_r\right). \tag{3.15}$$

with frequency-dependent amplitudes $Mr = -\frac{2\pi F_r}{H^2}\Omega_r$ [8]. The oscillatory strain, in terms of the amplitudes of oscillatory magnetization, is then

$$\tilde{\varepsilon}_{ij} = -\sum_r \left(\frac{\partial \ln F_r}{\partial \sigma_{ij}}\right) M_r H \sin\left(\frac{2\pi F_r}{H} + \phi_r\right). \tag{3.16}$$

The oscillatory magnetostriction $\Delta\tilde{L}/L$ is a directional physical property given by sum over the relevant strain components as explained in the previous section, though loosely

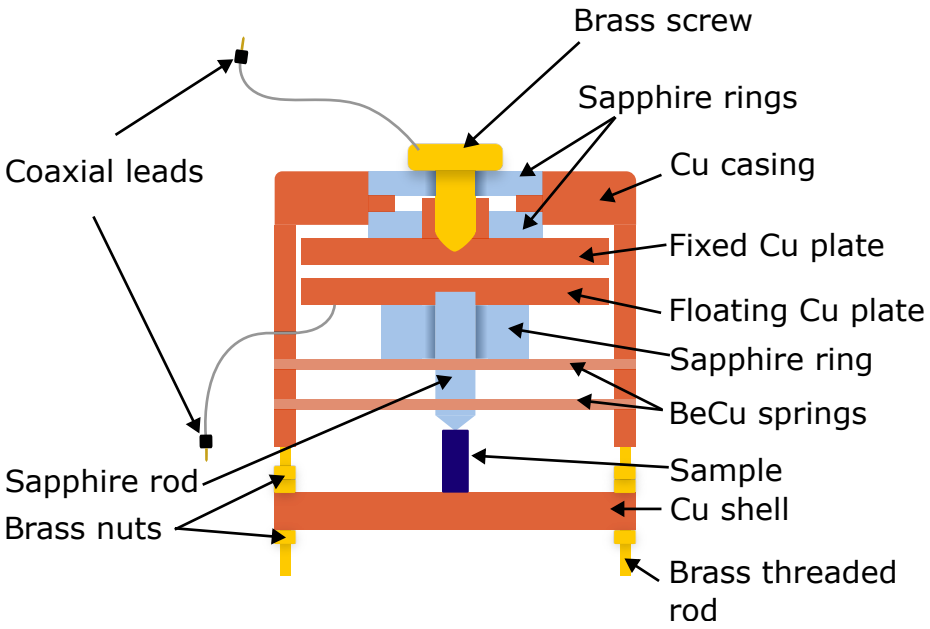


Figure 3.3: Labelled schematic of the copper dilatometer used for magnetostriction measurements adapted from engineering drawings by Liu [9].

speaking the largest component of the oscillatory strain of Equation (3.16) is often approximated as the oscillatory magnetostriction as it is on the same order of magnitude as $Delta\tilde{L}/L$ [8]. Its amplitude depends on derivative of the dHvA frequency with respect to strain, $\frac{\delta \ln F_r}{\delta \sigma_{ij}}$, which can be written as a derivative of the extremal Fermi surface area with respect to this strain using Equation (3.11) as $\frac{\delta \ln A_r}{\delta \sigma_{ij}}$. This is a measurement of the sensitivity of this extremal area to deformation upon the application of the external strain of an applied magnetic field. Smaller Fermi surface pockets such as those with a narrow "neck" are more sensitive to changes in strain and therefore may be more easily distinguished in magnetostriction due to a larger $\frac{\delta \ln F_r}{\delta \sigma_{ij}}$ factor, contributing to a higher oscillatory amplitude [27]. Therefore, when qualitatively comparing the oscillatory magnetostriction to dHvA results, while these two measurements share quantum oscillation frequencies, the amplitude of the oscillatory magnetostriction has an additional strain dependence compared to the oscillatory magnetization.

3.2 Capacitive dilatometer

We obtain our magnetostriction measurements using a capacitive dilatometer. As the sample expands or contracts in response to a change in magnetization, it pushes or contracts a sapphire rod constrained by a spring that changes the plate separation of a capacitor. A capacitance measurement of high precision detects the change in plate separation in the dilatometer.

Figure 3.3 shows the main components of our capacitive dilatometer. The sample is mounted on the copper shell that is held in place using brass nuts. For the dilatometer to measure a plate separation corresponding to a change in sample length, the sample pushes on the sapphire rod and beryllium-copper springs while still maintaining a plate separation between the floating and fixed copper plates. The plate separation is measured using the coaxial leads, which are electrically isolated from the dilatometer ground with sapphire rings. The starting plate separation is tuned by adjusting the brass nut spacers in order to fix a starting plate separation measured by the capacitance of the coaxial leads. In the limit where the plates are perfectly parallel to each other, the capacitance C is related to the plate separation d and plate surface area A as

$$C = \frac{\epsilon_0 A}{D}. \tag{3.17}$$

where A is the area of the plates. Our dilatometer has circular plates with a diameter of 12 mm, resulting in a plate area $A = 113 \times 10^{-6}$ m^2 [9]. Using Equation (3.17), we can calculate the change in plate separation in response to field, ΔD, which corresponds to the change in sample length ΔL. Often the magnetrostriction is reported as the change in sample length normalized by the sample length, $\Delta L/L$.

3.3 Error analysis in magnetostriction

When evaluating oscillatory magnetostriction, it's important to keep in mind the limits of the resolution based on the equipment. We use an Andeen-Hagerling 2550A bridge[2] which can resolve capacitance in the picoFarad (pF) range up to nine digits, depending on the signal loss. The bridge operates at a default frequency of 1 kHz, which could be prone to interference of electronic signals which operate at that frequency. To prevent interference,

[2]See documentation for model AH2550A for further information on the error resolution capacity of a similar bridge.

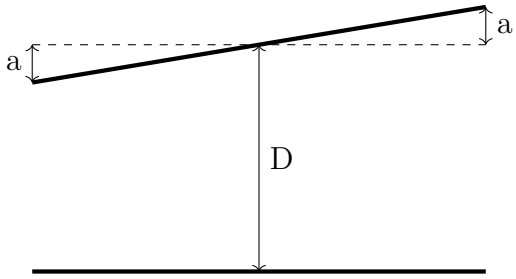


Figure 3.4: Illustration of plate tilt in dilatometer plates at a distance D apart, with a plate tilt off-centering by distance a from the average plate separation. Image reproduced from Pott and Schefzyk [10].

we ensure that other measurement equipment proximal to this bridge is operating at a frequency which will not interfere with the bridge. Moreover, regular power lines operating at 50 or 60 Hz can interfere with the signal at an elevated harmonic, and so are kept at a distance from the bridge to reduce such interference.

According to Equation (3.17), the change in plate separation ΔD is related to the change in capacitance ΔC as $\Delta C \sim -\frac{C^2}{\epsilon_0 A}\Delta D$. Equivalently, the magnitudes of the fractional changes in capacitance and plate separation are approximately equal, given by the relation $|\Delta C/C| \approx |\Delta D/D|$. We can therefore estimate the ability to resolve small changes in plate separation as follows. If the capacitance reading is 20 pF then the plate separation for parallel plates is 50 µm. Suppose that we would like to resolve a signal of $\Delta L/L \approx 1 \times 10^{-9}$ for a sample length $L \approx 1$ mm, in other words resolving an oscillatory displacement of $\Delta D \sim 0.01$ Å. We would need to observe a change in capacitance of $\Delta C \sim 4 \times 10^{-7}$ pF resolved over noise to be confident that such a change in capacitance is due to the oscillatory magnetostriction.

We can decrease the initial plate separation at room temperature to increase the fractional change in capacitance for an oscillatory change in plate separation. However we must consider plate tilt effects when we decrease this distance to ensure that plates are not shorting. Equation (3.17) assumes that the capacitor plates are parallel. In reality, the plates may be slightly tilted with respect to each other as illustrated in Figure 3.4, introducing an aparallel component to the conversion of capacitance to plate separation. In this scenario, the plate separation D then depends on the capacitance C as

$$D = \frac{\epsilon_0 A}{C}\left[1 + \left(\frac{C}{C_{\max}}\right)^2\right] \tag{3.18}$$

with maximum capacitance before the plates short, $C_{\max} = \frac{2\epsilon_0 A}{a}$ for a plate tilt distance a (as shown in Figure 3.4) [10]. When the capacitance is much smaller than the maximum value, Equation (3.17) is a sufficient approximation to convert the capacitance to a plate separation. However as we decrease the plate separation such that the plates nearly short in order to increase sensitivity to a change in capacitance, the average distance between plates now must account for aparallel effects. The change in plate separation is then estimated from a capacitance change by the expression

$$\Delta D \approx -\Delta C \frac{\varepsilon_0 A}{C^2}\left[1 - \left(\frac{C}{C_{\max}}\right)^2\right]. \tag{3.19}$$

For example, if $C = 20$ pF and $C_{\max} = 55$ pF, then $D = 57$ pF and an oscillatory capacitance of $\Delta C \sim 5 \times 10^{-7}$ pF converts to an oscillatory displacement of $\Delta D \sim 0.01$ Å. The absolute value of the plate separation is affected by this correction but the oscillatory amplitude can be approximately obtained using parallel plate equations. To summarize, we can adjust the plate separation to increase the sensitivity when measuring the oscillatory amplitude so long as the plates do not short.

When adjusting the plate separation, we are also limited due to the coarse adjustment method in our setup. As shown in Figure 3.3, we adjust the plate separation by changing the position of interlocking brass nuts along a threaded brass rod, which takes skill to make precise changes on the order of ~ 0.1 mm or less. The plate separation used in these dilatometer measurements is obtained by attempting to increase the sensitivity while avoiding shorting the capacitance plates given that the plates are slightly tilted.

3.3.1 Improving precision

Electrical noise can be reduced through shielding and removing sources of interference, but not completely removed. Some of the circuitry which can be a source for noise is also essential for the measurements. For example we are using a superconducting magnet which operates at 120 A, and its electronics are proximal to the AH bridge, which can cause electromagnetic interference in the measured signal due to the high power needed to create the magnetic fields. While the precision in capacitance bridge measurements is observed to be more reliable in zero magnetic field, a non-zero field is required for our measurements, and the short magnet power supply cable of 6 m as well as the location of the specialized plug receptacle in the laboratory limits the distance we can separate this power source from the bridge.

We require high precision to measure the changes in sample length in oscillatory magnetostriction, which can have oscillatory amplitudes smaller than an angstrom for a sample that is on the order of a millimeter in length. The sampling approach can improve precision in the presence of noise. There are two main sampling mechanisms that we adjust to improve the precision: sampling internal and external to the capacitance bridge. The AH bridge can internally average over a set number of points to improve the precision in its measured capacitance, and it only reports its capacitance to the least significant digit. The number of significant digits for a single sample can then be less than the bridge's full resolution ability (which is 10^{-8} pF) if the bridge cannot resolve this level of precision. Due to this feature, the level of precision can even change between points in a single run. A longer internal averaging time improves the precision by increasing the number of points sampled for each measurement. The bridge has the ability to take these measurements in rapid succession while the bridge is balanced to counteract deviations from random noise. On the other hand, if the bridge averaging time is above a certain threshold, the bridge must recalibrate itself at each measurement, which increases takes time and wears down the bridge relays. Given the high number of points we sample for the oscillatory magnetostriction measurements, we set the bridge to the largest averaging time that does not require frequent recalibration. This setting averages over 16 points and typically takes 2 seconds for each measurement. This approach results in a level of precision of 10^{-5} pF, or a relative precision of $\sim 5 \times 10^{-7}$ at 20 pF. This is quite a high precision for some applications, but would resolve only $\Delta L/L \sim 3 \times 10^{-8}$ for a 1 mm sample using the earlier arguments. Given that this order of magnitude is larger than the maximum oscillation amplitude for many magnetostriction measurements [7], we would prefer to improve the precision of the capacitance measurement. We can do so by averaging over many points externally from the bridge, which decreases the standard error δx by the square root of the number of points sampled N, $\delta x \sim \sigma_x/\sqrt{N}$ for standard deviation σ_x. Therefore, if the standard deviation in capacitance for each bridge measurement is $\sigma_x \sim 10^{-5}$ pF, we can reduce the standard error to $\Delta C \sim 10^{-6}$ pF by averaging over 100 points externally to the bridge. This level of precision equates to a sensitivity $\Delta L/L \sim 10^{-9}$ under equivalent conditions, which is more ideal for the small oscillations we are trying to measure. While the underlying sources of noise can still be reduced to improve precision, we have reduced the impact of this noise by sampling over dozens of points at each magnetic field and then averaging the values of these points. Practically speaking, this means setting up a run that does not record the capacitance while the field changes, and setting the field to persist at each sample point. Then, the program allows some settling buffer time where it measures the capacitance but does not record this in a running average, before averaging the points.

Given the high boiloff rate for the liquid helium in this type of measurement with the

frequent switches of the field to the normal state to change the superconducting current, we must be efficient with our measurement setup to make the best use of helium over a multi-day run. We used a short settling time to instead increase the point density with respect to inverse field and increase the number of points used in the sampling average. The bridge also can be inconsistent in the sampling time for a single measurement. It will perform a cold start if it detects that the bridge is off balance, even if the averaging setting is short enough to avoid needing this recalibration for each measurement. Therefore we set up Labview to wait for the bridge to communicate a response in order to record each measurement from the bridge regardless of the bridge measurement time rather than moving on from the bridge communication sequence too soon. Despite our best efforts, the capacitance bridge sometimes measured "excess noise" from real noise in the measurement in non-zero magnetic fields, which register as zeros in the recorded data. These points are removed and the data is re-averaged during data processing.

Part II

Topological Kondo insulators

Chapter 4

Topological Kondo Insulators: Literature Review

Topological Kondo insulator (TKI) candidates have a rich history with the possibility of topology combined with unusual magnetic properties from the Kondo effect. Before getting into experimental results for select TKI candidates SmB_6, YbB_{12} and $FeSb_2$ that were studied in this thesis work in Chapter 5, we will spend some time discussing theoretical models for topological Kondo insulators (TKIs) that emerged from this history. Specifically, we will first discuss Kondo physics, then introduce topology, and combine the two in the TKI model.

Then, we will delve into more recent experiments and theory examining a topological insulating state in more detail, unusual phenomena unconvered in the bulk, and current theories and open questions about the nature of this class of materials. While other TKI candidates have been identified, this thesis will focus on two of the most well-studied candidates, SmB_6 and YbB_{12} as well as an emerging candidate $FeSb_2$ to best align with the experimental results of this thesis work.

4.1 Early theories of TKI candidates

4.1.1 Kondo insulators

In Kondo insulating materials, a hybridization between the conduction electrons and the magnetic moments explains a transition from a metallic state at room temperature to an

insulating state upon decreasing the temperature. In the Kondo insulator model, conduction electrons screen localized moments to overcome Ruderman–Kittel–Kasuya–Yosida (RKKY) magnetic ordering [11, 12, 63]. Doniach's derivation of a one-dimensional Kondo lattice Hamiltonian combines a direct exchange hopping interaction with amplitude t and an antiferromagnetic exchange interaction J between f and d electrons [11]. As a result, instead of electrically inert f electrons, the Hamiltonian

$$H = -t \sum_{i,j} \sum_{\sigma} \left(c^{\dagger}_{i\sigma} c_{j\sigma} + c^{\dagger}_{j\sigma} c_{i\sigma} \right) + J \sum_{j} \sum_{\alpha,\beta} \left(c^{\dagger}_{j\beta} \vec{\sigma}_{\beta\alpha} c_{j\alpha} \right) \cdot \vec{S}_j \tag{4.1}$$

describes localized moments surrounded by mobile electrons. In this model, t is the hopping amplitude, $c^{\dagger}_{j\beta} \vec{\sigma}_{\beta\alpha} c_{j\alpha}$ is the spin density at site j, operators $c^{\dagger}_{i\sigma}$ and $c_{i\sigma}$ create and annihilate an electron at site i respectively, J is Kondo coupling parameter, and a local moment $\vec{S}_j$ is at each site j ($|\vec{S}_j| = 1/2$ for all j). In the Hamiltonian of Equation (4.1), the competition between interaction energies can be analysed in terms of their relative strengths, with a Kondo temperature $T_K \sim \sqrt{J\rho} \exp\left(-\frac{1}{2J\rho}\right)$ below which Kondo singlets form and an RKKY temperature $T_{\text{RKKY}} \sim J^2 \rho$ which leads to long range magnetic order at temperatures lower than T_{RKKY} [12]. Both temperatures depend on the conduction electron density ρ. This competition between interaction energies is illustrated in Figure 4.1. Doniach proposed that when the Kondo temperature exceeds that of the RKKY interaction, the formation of Kondo singlets overcomes the tendency for long range magnetic order, leading to a Kondo singlet ground state [11]. The eigenfunctions of the Hamiltonian are a mixture of spin singlets and triplets, with the Kondo singlet ground state favoured when the binding energy of the Kondo singlet exceeds the RKKY interaction.

Moving beyond Doniach's one-dimensional lattice of Kondo singlets, a mean field description using a periodic Anderson Lattice Model (ALM) at low energies provides the groundwork for the band gap of a Kondo insulator [12]. The ALM Hamiltonian,

$$H_{\text{ALM}} = H_f + H_c + H_{\text{hybrid}}. \tag{4.2}$$

has components H_f describing the interactions of f electrons, H_c describing that of conduction electrons and H_{hybrid} describing hybridized interactions between the two bands [12, 64]. Explicitly, the first term,

$$H_f = \sum_{i,j} \sum_{\alpha} t^{(1)}_{ij} \hat{f}^{\dagger}_{i\alpha} \hat{f}_{j\alpha} + \frac{U_f}{2} \sum_{i} \sum_{\alpha,\beta} \hat{f}^{\dagger}_{i\alpha} \hat{f}_{i\alpha} \hat{f}^{\dagger}_{i\beta} \hat{f}_{i\beta}, \tag{4.3}$$

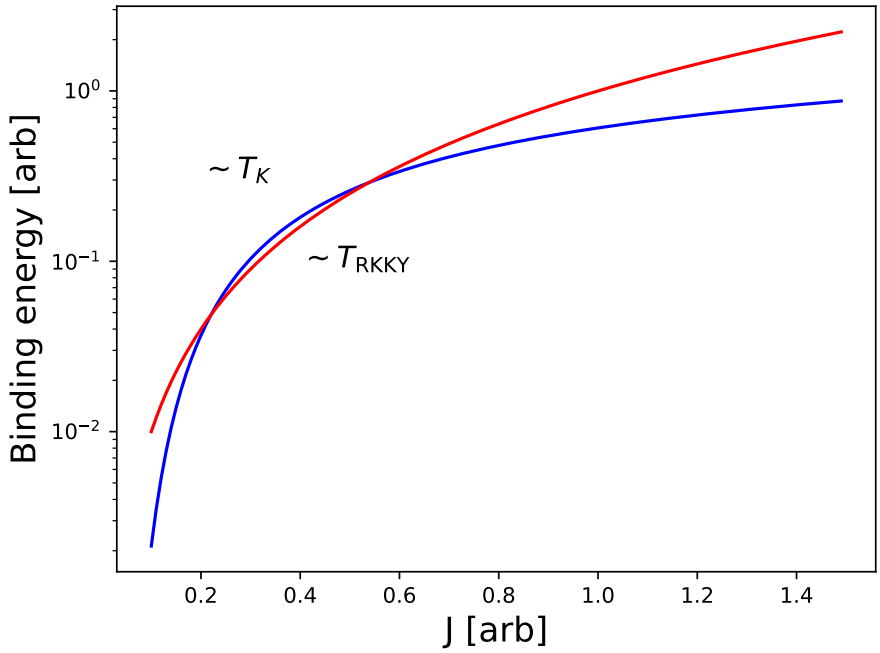


Figure 4.1: Comparison of interaction parameter strengths between the binding energy of a Kondo singlet, approximately of order T_K (blue curve), and the RKKY ordering energy, approximately of order T_{RKKY} (red curve). The illustration assumes $\rho = 1$. The RKKY interaction dominates below $J \sim 0.2$ in this figure, and the Kondo energy overtakes the RKKY interaction on the right hand side of this point [11, 12]. It is worth noting that Doniach's weak coupling formula for a Kondo singlet is not applicable in the large Kondo coupling limit.

describes hopping between f electrons as well as the Coulomb interaction between f electrons. Here, $t_{ij}^{(1)}$ is the hopping amplitude between neighbouring f electrons, $\hat{f}_{i\alpha}^{\dagger}$ and $\hat{f}_{i\alpha}$ are f electron creation and annihilation operators on site i, $U_f > 0$ is the Coulomb repulsion for f electrons on a same site. The second term,

$$H_c = \sum_{i,j} \sum_{\sigma} \sum_{d,e} t_{id,je}^{(2)} \hat{c}_{i,d\sigma}^{\dagger} \hat{c}_{j,e\sigma}, \tag{4.4}$$

describes hopping between conduction electrons with usual creation operator $\hat{c}_{i,d\sigma}^{\dagger}$, hopping amplitude between conduction electrons $t_{id,je}^{(2)}$, spin $\sigma = \frac{1}{2}, -\frac{1}{2}$ and orbital index d, e. The last term,

$$H_{\text{hybrid}} = \sum_{i,j} \sum_{d,\sigma,\alpha} \left(V_{id\sigma,j\alpha} \hat{c}_{id\sigma}^{\dagger} \hat{f}_{j\alpha} + V_{i\alpha,jd\sigma} \hat{f}_{i\alpha}^{\dagger} \hat{c}_{jd\sigma} \right), \tag{4.5}$$

where $V_{id\sigma,j\alpha} = \sum_{\boldsymbol{k}} V_{d\sigma,\alpha}(\boldsymbol{k}) \exp\left[-i\boldsymbol{k} \cdot (\boldsymbol{r}_i - \boldsymbol{r}_j)\right]$, is the hybridization matrix diagonal, with spin-orbit coupling and topology included in this matrix. This results in high symmetry points, which are central to TKI theory. This theory expands on the Anderson Lattice model introduced for Kondo insulators and assumes a narrow band gap as in the Kondo insulator case [12, 65]. The resulting effect is the hybridization of the f electron band to become two bands with a narrow gap below the Kondo temperature [64]. If the Fermi surface lies within this gap, the material is considered a "Kondo insulator" [66]. Valence fluctuations in this model can account for a lack of magnetic order. Riseborough and Mills proposed a slight temperature dependence in the f electron occupation number and chemical potential using this model, noting that a pinning of the two bands can occur when they cross which is reflected in the paramagnetic susceptibility [67].

4.2 Topological insulators

Subsequently, in 2005, Kane and Mele suggested a model of graphene with a novel insulating phase in its bulk that is topologically distinct from the vacuum [68, 69]. This "topological insulator" phase of matter extends the classification of topological phases of matter by Thouless, Kohmoto, Nightingale and den Nijs [70] which relates the integer quantum Hall effect to a topological character. The groundbreaking developments on this new phase of matter are recognized by the 2016 Nobel Prize in Physics [71]. These developments find that phases of matter, such as insulators and metals, can have a topology that classifies how it can transform to other phases within the confines of its band structure. Importantly, some phases of matter are topologically distinct, meaning that their Fermi surfaces cannot adiabatically transform from one topology to another.

Insulating phases can be topologically distinct, meaning that an insulator with one topology cannot smoothly transform to an insulator with another topology while maintaining the nature of the band gap in the Fermi surface. For clarity, a topologically trivial band insulator has a conduction band and valence band separated by a gap with the Fermi energy lying in the gap. This band insulating phase is topologically equivalent to a vacuum since the band insulator is insulating both in the bulk as well as at an interface with a vacuum. Then a "topological" (topologically non-trivial) insulator has an insulating Fermi surface that cannot be adiabatically transformed to the vacuum state without closing the energy gap of the insulator or breaking time reversal symmetry, giving rise to non-insulating surface states at the boundaries of the topological insulating phase [12]. In theory, for strong topological insulators, such a topological surface state is robust against disorder that preserves time-reversal symmetry, unlike with conventional metallic states where the presence of weak disorder localizes conduction electrons [68, 72]. However, a topological surface state is vulnerable to changes in time-reversal symmetry such as with the application of a magnetic field or the introduction of magnetic impurities [73].

The metallic surface state can be distinguished from a trivial metallic state by the chirality of the electrons, driven by strong spin-orbit coupling, which is characterized by a Z_2 index. Fu and Kane introduced this Z_2 index, which is a measure of the parity of high-symmetry points in the magnetic Brillouin zone [74]. In three dimensions, there are eight high-symmetry points Γ_i in the Brillouin zone that are insensitive to time-reversal symmetry,

$$\Gamma_{i=n_1n_2n_3} = \frac{1}{2}(n_1\boldsymbol{b}_1 + n_2\boldsymbol{b}_2 + n_3\boldsymbol{b}_3), \tag{4.6}$$

for primitive reciprocal lattice vectors $\boldsymbol{b}_{1,2,3}$ and integers $n_{1,2,3} = 0, 1$. On a cubic lattice, Equation (4.6) corresponds to the high-symmetry Γ and R points, as well as three X and M points[1] [12]. The Z_2 number is then the product of the parity $\delta(\Gamma_i)$ of each of the four unique high-symmetry points Γ_i [12, 74]

$$Z_2 = \prod_{\Gamma_i} \delta(\Gamma_i). \tag{4.7}$$

An insulator with trivial topology can maintain its band gap at its edges as shown in Figure 4.2a. In contrast, a topological insulator cannot adiabatically connect to a conventional

[1]Takimoto presents these vectors explicitly for a cubic lattice [13]. For the primitive reciprocal lattice vectors of the cubic lattice, the high-symmetry points are located at the following reciprocal space coordinates: $\Gamma = (0,0,0)$, $R = (\pi,\pi,\pi)$, $X = (\pi,0,0), (0,\pi,0), (0,0,\pi)$ and $M = (\pi,\pi,0), (\pi,0,\pi), (0,\pi,\pi)$.

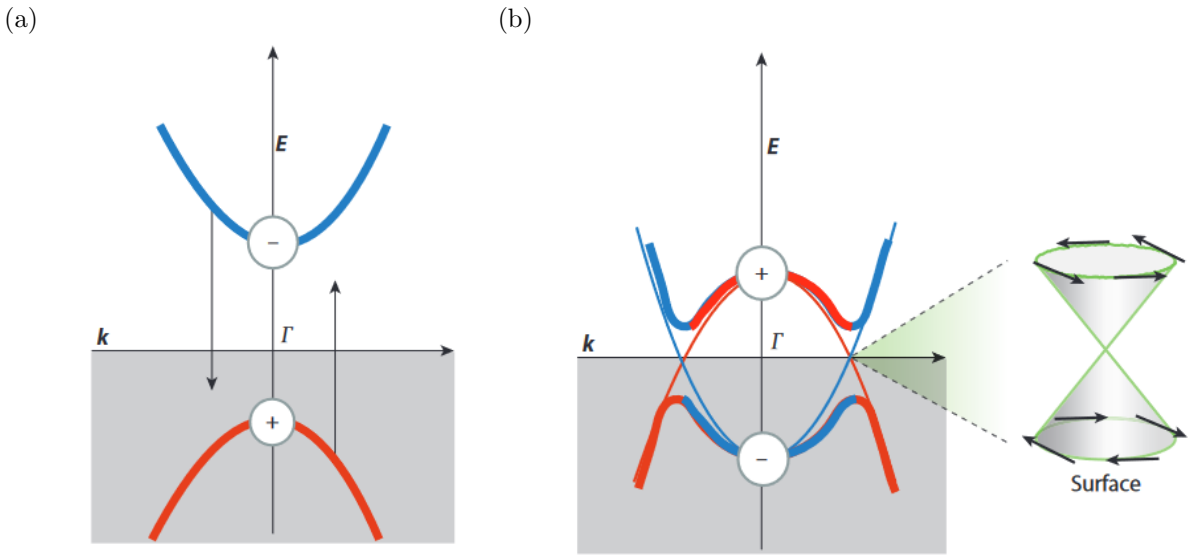


Figure 4.2: Figure from Dzero *et al.* [12], visualizing the band gap for a trivial insulator compared to a topological insulator. (a) A band gap for a trivial insulating phase with $Z_2 = +1$. (b) A band crossing illustrated for a high symmetry point Γ, where a Dirac point connects the even parity $(+)$ trivial insulating state and the odd parity $(-)$ bulk state at the surface of the sample. The Dirac point has a chiral spin phase arising from the opposing parities. *Used with permission of Annual Reviews; permission conveyed through Copyright Clearance Center, Inc.*

insulator state without closing the band gap, producing a "Dirac cone" of inverted spin chirality. Such band crossings are illustrated in Figure 4.2b [12, 75]. A "Dirac point" connects Kramers' degenerate points in the reciprocal lattice Γ_i, resulting in an odd time-reversal parity index $\delta(\Gamma_i) = -1$ associated with this band crossing [74]. An even number of such band crossings results in an insulating state that lacks topological protection with $Z_2 = +1$, whereas a strong topological insulator has an odd number of crossings and $Z_2 = -1$. The band crossing represents a transition to a metallic state with spin chirality at the edges of the sample, hence the prediction of "chiral edge states" as a sign of a topological insulator [72].

4.3 Topological Kondo insulators

Since the theoretical development of topological insulating phases, Dzero *et al.* demonstrate that the Kondo insulator model described by Equation (4.2) may also accommodate non-trivial topologies [65]. In particular, Kondo insulators with a Kramers' symmetry of the rare earth ion have an obvious potential to realize the degenerate surface states of topological insulators due to their degenerate ground states with opposing time-reversal parity [75]. Applying the ALM to Kondo insulators with Kramers' degenerate states, Dzero *et al.* [65] proposed a topological Kondo insulator (TKI) model by applying an odd parity to the f-electron form factor, facilitating the band inversion necessary for a non-trivial topology.

This led to a re-examination of Kondo insulators like SmB_6 in terms of a topological Kondo insulator picture. While both the Kondo insulator and TKI models require strong interaction between f and d electrons that places both bands in close proximity, rather than the hybridization predicted by the Kondo insulator model, the TKI model predicts a band crossing and topological phase transition when the two bands meet [12]. Depending on the strength of the interaction, the ALM applied to a Kondo lattice results in a topologically trivial Kondo insulator in the limit of localized f electrons [63], and a strong topological insulator with an odd number of band inversions in the mixed valence regime [12].

4.4 Experimental observations in SmB_6

4.4.1 Kondo insulator

Early experiments on heavy fermion materials such as SmB_6 and YbB_{12} revealed semiconducting-like properties such as a transition from a room temperature metallic state to a low temperature insulating state under atmospheric pressures. Measurements including photoemission spectroscopy confirmed the presence of a pseudogap consistent with the formation of a Kondo singlet state according to the Kondo insulator model in the periodic Anderson lattice [76]. Mössbauer-effect measurements of SmB_6 strongly support a mixed valence nature of the samarium ion, resulting from a hybridization of f and d electrons, perhaps even continuously alternating between valence states [77]. Rather than the valence electrons all residing on the outer $4f^6$ shell, in the non-magnetic ground state of Sm^{2+}, the ion hybridizes into $4f^5 5d^1$ with magnetic ion Sm^{3+} [78–80]. However the Kondo insulator model alone cannot explain the low temperature resistivity plateau. While Falicov and Kimball suggested a model to explain a metal-insulator transition in resistivity with a change in valence [81], this transition is not accompanied with a substantial change in

lattice constant or carrier density that would accompany a transition in the conduction electron hybridization[79]. The hybridization is reported as relatively robust ("homogenous"), with little variation in temperature and pressure [82–84]. Moreover, Cooley *et al.* report that the pressure dependence of the SmB_6 valence cannot be described completely by the hybridization model, notably observing that a change in hybridization with pressure is not accompanied by a transition to magnetic order [85]. The authors instead suggest that SmB_6 is a more exotic metal than that described by Kondo theory.

4.4.2 Topological surface states

The mixed valence band structure of SmB_6 could result in topologically protected metallic surface states. The TKI model provides an elegant explanation for the resistivity plateau at low temperatures: a topological insulating state in the bulk would limit the electrical charge carriers to the conduction electrons on the surface area of the sample, resulting in a charge conductivity that scales with the surface area rather than the bulk of the sample. Such a scenario is corroborated by charge transport measurements. By measuring the charge transport across the bulk of the sample separately from that along the surface, Wolgast *et al.* report a suppression of bulk conductivity below ~ 3.8 K with a robust surface conductivity dominating the low temperature regime [86]. Using a similar thickness-dependent measurement approach, Kim *et al.* report a low temperature crossover from a bulk Hall effect to a surface Hall effect in SmB_6 [87]. Such transport results that are dominated by surface conduction are consistent with a topologically insulating bulk that has a metallic band-crossing where the sample is exposed to the trivially insulating vacuum.

According to band structure calculations, SmB_6 has $Z_2 = -1$ due to the negative parity of the X points, making it a candidate for a strong topological insulating state with an odd number of Dirac cones at the high symmetry points marked in red in the cubic reciprocal space lattice for SmB_6 in Figure 4.3a [12, 13, 88]. Figure 4.3b also shows the calculated energies for the hybridized samarium ion with energy bands crossing the Fermi energy of $E_F/t_d \sim -4.05$ at the X points, suggesting a topologically protected metallic surface state.

Experiments probing the surface of SmB_6 report chiral edge states that are consistent with the surface state of a topological insulator. Xu *et al.* measured spin-resolved and angle-resolved photoemission spectroscopy (SARPES and ARPES respectively) to probe Berry curvature associated with time reversal symmetry [89]. They observe a spin-helical structure originating from surface states with a non-polarized bulk, suggesting that this material is a topological insulator with an insulating bulk. However, this conclusion of a topological Fermi surface at the metallic surface state of SmB_6 imaged by ARPES is

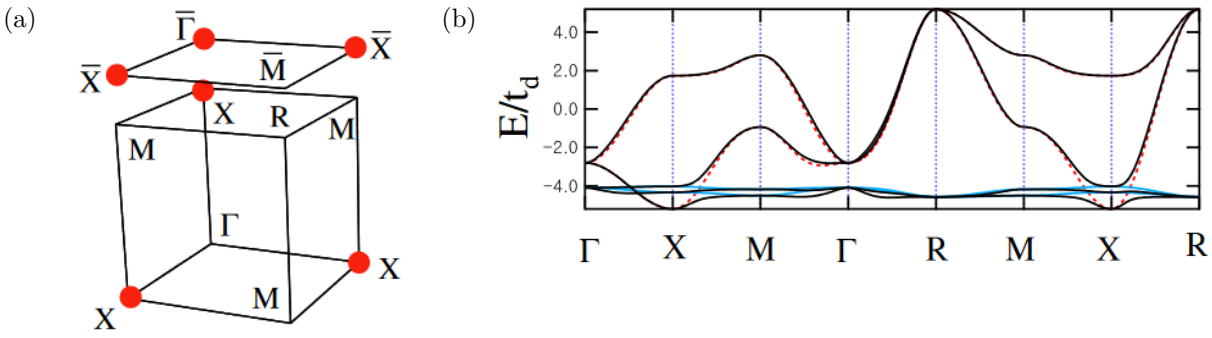


Figure 4.3: Images from Takimoto [13]. (a) High-symmetry points Γ, X, M and R on a cubic reciprocal lattice with the first Brillouin zone quadrant of a [001] surface shown at the top of the image. Time reversal invariant points are marked with red dots. (b) Calculated energy bands E for SmB_6 scaled by the hopping parameter t_d for the $4f^6$ (blue), $4f^55d$ (red), and hybridized (black) states of the samarium ion. The X points have negative parity due to band inversion between the $4f^6$ and $4f^55d$ bands. ©2011 *The Physical Society of Japan.*

by no means a universal conclusion. Hlawenka *et al.* reach a contradictory conclusion with ARPES measurements, arguing instead that SmB_6 is a trivial surface conductor [90]. While the SmB_6 surface state is still driving experimental and theoretical interest, it does have robust experimental support for the predictions of a topological surface state [91, 92]. The TKI theory also offers an elegant explanation for the experimental phenomena of an electrically conducting surface state and an insulating bulk state. Any competing explanations for the ground state of SmB_6 would also need to address why a surface conductor would have an insulating bulk. Moreover, more TKI candidates are proposed including YbB_{12}, FeSi and $FeSb_2$ [92]. Research on other TKI candidates helps to identify universal phenomena across different materials.

Meanwhile, the bulk state of TKI candidates remains more of an enigma, not only due to a lack of consensus of theoretical motivations for any mechanism beyond an insulating bulk, but also due to seemingly contradictory experimental measurements that report an electrically charge neutral bulk but not necessarily absent of a three-dimensional Fermi surface. we will next discuss experimental investigations into the insulating bulk state of TKI candidates.

4.4.3 Exotic insulating bulk

Recent research on topological Kondo insulators SmB_6 and YbB_{12} have discovered unusual bulk behaviours below the Kondo temperature. While it is expected that the bulk is insulating in TKI theory, and given electrical transport experiments showing a metallic surface and an insulating bulk [15, 86, 93], as well as thermal transport at low temperatures consistent with that of bulk insulators [21, 23, 94], one may expect the absence of a 3D Fermi surface originating from the bulk. Here we will discuss surprising and sometimes conflicting experimental results that attempt to characterize the Fermi surface of the insulating bulk in the low temperature regime. We will next discuss the groundbreaking anomalous bulk behaviour of SmB_6 and will introduce the findings for YbB_{12} in Appendix B.

Electrical transport measurements demonstrate the insulating nature of the SmB_6 bulk. Menth *et al.* reported a highly resistive SmB_6 at decreasing temperatures back in 1969 [78]. More robust measurements have since isolated the source of the electrical conduction to the surface of the material in the highly resistive regime [86]. Syers *et al.* investigate the residual resistivity ratio of different widths of SmB_6 [95]. Using a two-channel conductivity model, they report that the low-temperature limit of the bulk channel contribution is independent of sample thickness. In order to isolate the bulk conductivity from the surface conductivity in SmB_6, Eo *et al.* report developing an "inverted resistance measurement" technique which probes the inverse of the bulk resistivity [14]. This novel technique uses a closed loop geometry with current travelling from the inner disk to the outer disk and an additional two terminals for voltage measurement with a schematic of the experimental setup as shown in Figure 4.4a. Using the Corbino disk geometry on the top and bottom faces of a sample as in Figure 4.4b-c, Eo *et al.* report a highly resistive bulk at temperatures as low as 2 K, with the highest resistance observed in the stoichiometrically grown sample [15] (Fig. 4.4d). Furthermore, the zero field thermal conductivity of SmB_6 has a negligible contribution from mobile electrons that reflects the large residual resistivity [21, 23, 96, 97]. These transport signatures are consistent with conventional expectations of an insulating bulk.

Meanwhile, despite signatures of a charge-insulating bulk in electrical transport, other experimental results report behaviour that resembles fermionic carriers with a bulk origin. The specific heat of SmB_6 features an anomalous low temperature upturn that increases with modest applied fields, which has been previously explained as emerging from a growth in metallic-like in-gap states [98–100]. Wakeham *et al.*'s [16] work concludes that the linear specific heat likely originates from the bulk by comparing the low temperature specific heat of single crystal samples with higher surface area powdered samples of same growth. Figure 4.5 shows how the residual linear term in the specific heat reaches a similar value for

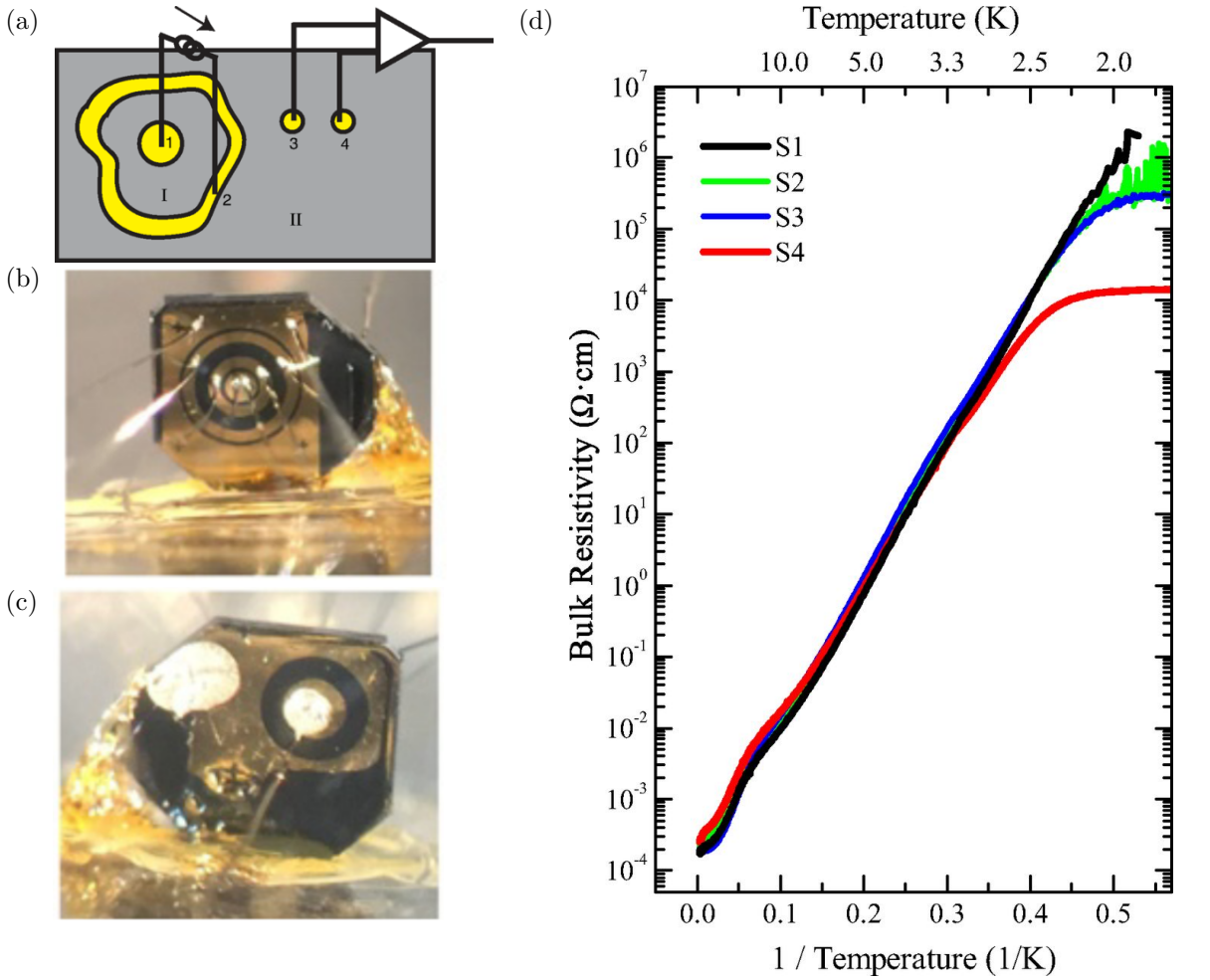


Figure 4.4: (a) A basic schematic of a four terminal inverted resistance measurement [14], with a current differential in region I between concentric terminals $1 \rightarrow 2$, and a voltage differential measured in an adjacent region II between terminals $3 \rightarrow 4$. Using this setup, Eo *et al.* report inverted resistance measurements of SmB_6 [15], with four concentric terminals on the top of the sample as shown in (b) and two concentric terminals on the bottom of the sample as shown in (c). Their converted bulk resistivity for stoichiometric flux-grown sample S1 and non-stoichiometric flux-grown samples S2, S3 and S4 is shown in (d). *Reprinted (a) with permission from* [14]. *Copyright 2018 by the American Physical Society.*

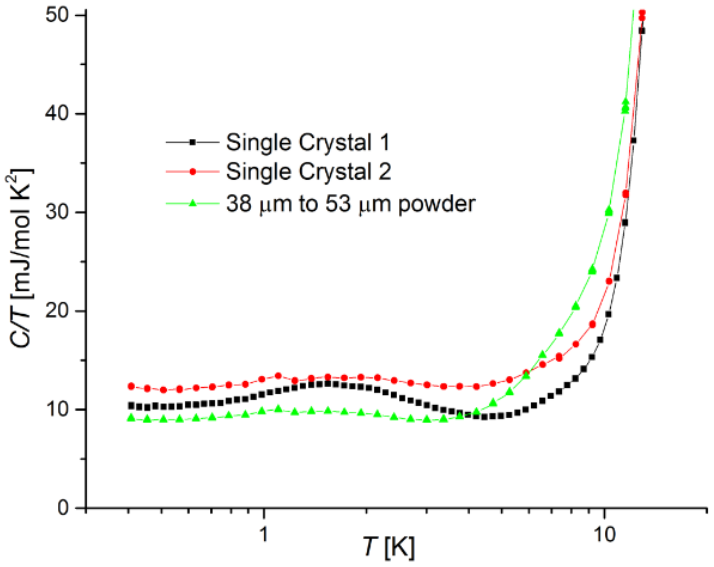


Figure 4.5: Specific heat normalized by temperature versus temperature for flux-grown SmB_6 single crystals (black and red) grown from the same batch, compared to a $38-53$ µm powder derived from a crushed single crystal (green). *Reprinted figure with permission from* [16]. *Copyright 2016 by the American Physical Society.*

single crystals as for powder, despite the large differences in surface area between the two measurements. The low temperature specific heat capacity of SmB_6 has been explained using conventional Fermi liquid theory with a term from phonons, $C_{\text{ph}} = \beta T^3$, a term from a Schottky anomaly, $C_{\text{Sh}} = BT^{-2}$, an electronic term linear in temperature from conventional electronic theory, $C_{\text{el}} = \gamma T$ where γ Sommerfeld coefficient, and a quasiparticle coupling term correcting the electronic coefficient (typically for electron-phonon coupling in conventional Fermi liquids), $C_{\text{el-ph}} = AT^3 \ln(T/T^*)$, with the latter effect assumed to be responsible for a low temperature growth in specific heat [98, 100, 101]. Normally, a specific heat enhancement due to fermionic carriers is also reflected in thermal conductivity by their kinetic theory relation [as given in Eq. (A.3) for the thermal conductivity contribution of electrons]. However, as mentioned previously, this is not the case in zero magnetic fields, and only Hartstein *et al.* report a fermionic term in the thermal conductivity under applied magnetic fields [21].

Furthermore, reports of de Haas van Alphen (dHvA) oscillations in SmB_6 are unexpected for a bulk insulating material, and suggest either that the material is a topological insulator with a metallic surface state and insulating bulk, or that the bulk hosts ex-

otic excitations [92]. In SmB_6, quantum oscillations are reported in torque magnetization and specific heat with differing conclusions about whether these originate from a two-dimensional Fermi surface at metallic sample boundaries or anomalously originate from the bulk of the material. The amplitude of dHvA oscillations in torque magnetostriction are analyzed using Landau theory to find light effective masses of $m^* \sim 0.12 - 0.14\ m_e$ and $m^* \sim 0.18 - 0.19\ m_e$ for the lowest frequency bands [17, 21, 97, 102] . On the other hand, the largest frequency reported [and conventionally, the extremal Fermi surface area as per Equation (3.11)] differs between groups as well as samples. High frequency oscillations — associated with a large extremal Fermi surface area for conduction electrons — are reported for high quality floating zone grown crystals but not flux grown samples. Such high frequency oscillation results for floating zone samples are reported by the Cambridge group, Tan *et al.* [17] and Hartstein *et al.* [21], and are shown in Figure 4.6. They relate these oscillations to metallic PrB_6 and LaB_6 which also have high frequency oscillations corresponding to a three-dimensional Fermi surface band and estimate contributions to a residual linear term in specific heat that is expected for fermionic carriers. This group reports an analysis consistent with low effective mass bands ρ', and ρ, but also high frequency oscillations particularly in the α band with effective mass $m^* \sim 0.70\ m_e$. Even though the dHvA oscillations are measured at high fields, they obtain quantitative agreement with the residual linear term of specific heat that they report in zero field, which may suggest that charge-neutral fermionic quasiparticles in the bulk could contribute to both quantities even in the absence of field. Moreover, an illustration of their calculated Fermi surface from density functional theory for the α band is in Figure 4.7a, with a two-dimensional projection in Figure 4.7b. This illustration has the ellipsoidal α bands centered at the X points and surrounding the Γ point that are predicted to be origins of the Dirac cones in TKI theory.

The differing interpretations have implications over the interpretation of the ground state. If the Fermi surface is two-dimensional, the implication is that the signal could originate from the metallic surface while the bulk is expected to be a conventional insulating phase, conforming with TKI theory. However, if the quantum oscillations cannot simply be attributed to a surface origin, the oscillations must have a contribution from the bulk of the sample, which is unexpected due to its charge insulating nature. This questions our fundamental understanding of quantum oscillations originating from the cyclotron motion of conduction electrons in metals.

The perplexing result of three-dimensional quantum oscillations has not been reproduced in SmB_6 torque magnetostriction [17, 21], but similar reports superficially corroborate the idea of charge-neutral fermions in the bulk in principle. Labarre *et al.* [103] report an oscillatory specific heat in flux grown samples of SmB_6 that they claim must

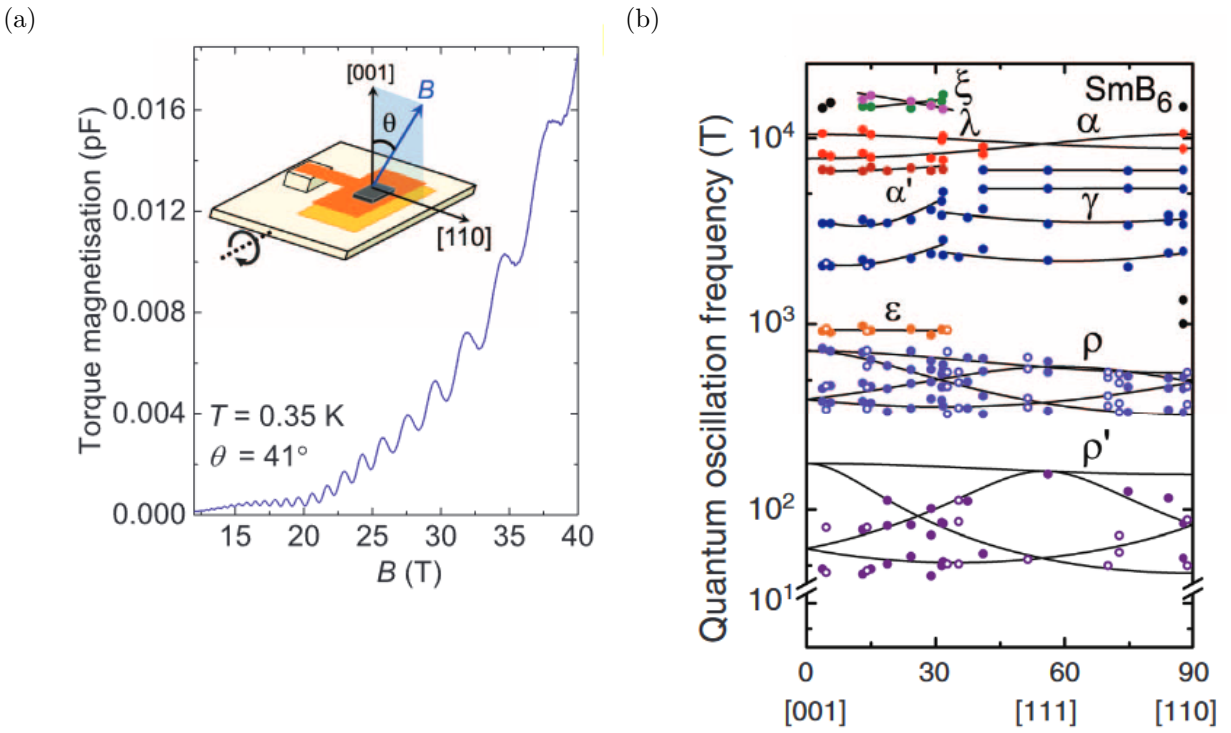


Figure 4.6: Quantum oscillations in torque magnetization in floating zone grown samples of SmB_6, by Tan *et al.* [17]. (a) Oscillatory magnetization at 0.5 K and a field angle of $\theta = 41$ deg with the normal [001] direction. Inset: a schematic of the measurement setup for torque magnetometry. (b) Quantum oscillation frequencies as a function of angle θ. Lines guide the eye to the frequencies expected for Fermi surface orbits.

originate from the bulk, though they fit their results to a significantly larger effective mass of $m^* \sim 6.6\, m_e$. Preliminary reports of Compton scattering measurements of floating zone grown samples also report an unconventional insulating bulk [104].

4.5 Theories of anomalous dHvA oscillations

Interest in reports of novel charge-neutral fermionic excitations drive theories of a new phase of matter, beyond the typical TKI scenario since both topological insulators and Kondo insulators are supposed to be in a gapped insulating state. On the other hand

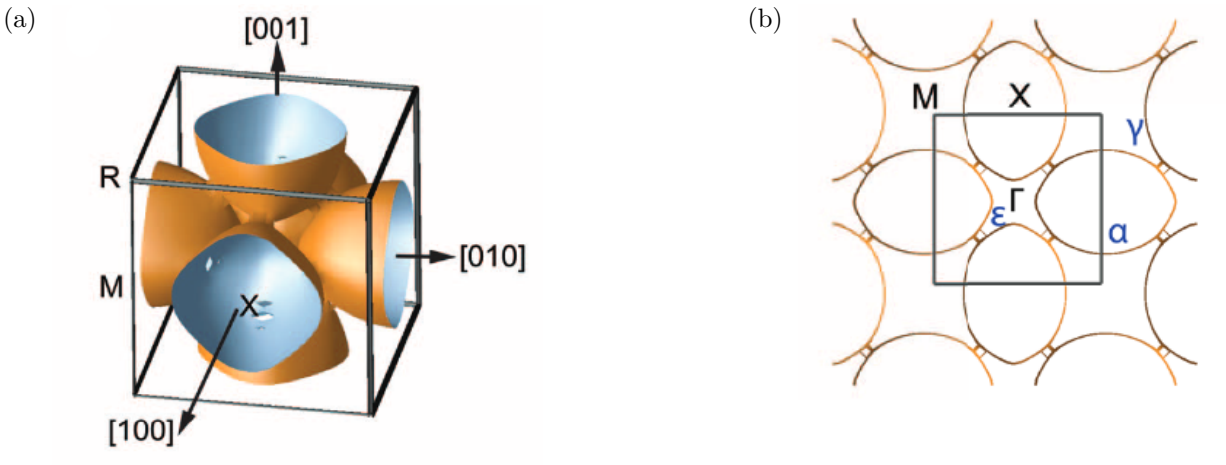


Figure 4.7: (a) 3D rendering and (b) 2D cross-section of the ellipsoidal α band with frequencies shown in Figure 4.6b, calculated using density functional theory by Tan *et al.* [17]. High-symmetry Brillouin zone points indicated by Γ, X, R and M. The ε and γ bands are also labelled in (b).

reports of a three-dimensional Fermi surface producing quantum oscillations in a bulk insulator is perplexing to reconcile with existing theories. Theories attempt to explain what kind of quasiparticles could exist in the bulk and how they can be electrically charge neutral but still have a Fermi surface and thermally conduct in a fermionic fashion. If such excitations couple to an external magnetic field despite their charge neutral character, then this nature of excitations could explain dHvA oscillations in the bulk. We will next briefly introduce some of these theories in order to compare predictions of these theories with experimental results.

Majorana fermions are a proposed charge-neutral quasiparticle in topological insulators. Baskaran proposes that such a quasiparticle exists as a fermionic sea in the bulk of SmB_6, motivating this using a tight-binding TKI model [105]. Not many predictions are listed in this preprint from 2015 however it is mused that the charge fluctuations predicted for these quasiparticles could explain a resistivity plateau at low temperatures as well as an anomalous increase in quantum oscillation amplitude. Erten *et al.* also propose an insulating state of Majorana fermions dubbed a "skyrme insulator" [106]. They argue that failed superfluidity in a superconducting state causes a liquid state of Majorana fermions in the bulk. An applied field larger than a critical field (estimated to be $\sim 10^{-4}$ T) would then result in a liquid of "skyrmion" excitations that behave analogously to a liquid of mobile vortices. Importantly, they offer testable predictions that differentiate their proposed phase

of matter from more conventional phases, including a longitudinal thermal conductivity that is linear in a transverse applied field $\kappa \propto H$ and vanishes in a longitudinal applied field due to the flux liquid property of the hypothetical quasiparticles.

The concept of a charge-neutral Fermi surface is not unique to the Majorana fermion proposal. Chowdhury *et al.* [107] propose a model of a "composite exciton Fermi liquid" that is electrically insulating in the bulk yet otherwise behaves as a Fermi liquid, motivating this theory by the mixed-valence property of samarium. They predict a fermionic contribution to specific heat $C = \gamma T$ with $\gamma = \ln(1/T)$ and longitudinal thermal conductivity that is linear in temperature as

$$\kappa_{xx} = \sum_{i=1,2} \frac{k_B^2 \tau_i}{9 m_i} \left(\frac{2 m_i \varepsilon_F}{\hbar^2} \right)^{3/2} T \tag{4.8}$$

which also depends on the masses m_i and relaxation times τ_i of the two pockets as well as the Fermi energy ε_F. Hence the disconnect in the reports of such terms in zero field poses as a challenge to this theory. Finally, Knolle and Cooper apply a model of magnetoexcitons to SmB_6 [108]. This model of charge-neutral bosons comprised of particles and holes that couple with an external magnetic field also is proposed to result in fermionic signatures in heat conduction and specific heat. Further theoretical developments still attempt to completely encompass key experimental phenomena, which is as of yet unresolved.

On the other hand, some proposed theoretical models do not rely fermionic quasiparticles to explain observations of Landau quantization in a bulk insulator. Knolle and Cooper [109] propose that quantum oscillations can in fact exist in a bulk insulator when the band gap is sufficiently small, smaller than the cyclotron energy $\hbar\omega_c$ of an anomalous de Haas van Alphen effect. Zhang *et al.* [110] and Peters *et al.* [111] have similar proposals that preserve the non-trivial topology of the TKI candidate. In the model of Knolle and Cooper, the oscillations arise from mobile electrons coupling to a flat band despite when these bands hybridize, such as in the Kondo insulators. This invites an alternative interpretation of quantum oscillations that could generalize LK theory to explain anomalous dHvA oscillations in a bulk insulator. The oscillations in this theory arise from an abrupt change in the diamagnetic moment due to a hybridized conduction band in the zero temperature limit [112].

The model of Knolle and Cooper [109] reconciles the possibility of dHvA oscillations in a bulk insulator yet still do not consolidate the anomalous thermal transport reported by Hartstein *et al.*, unlike the aforementioned theories of charge-neutral excitations. Conversely, other proposals suggest disorder could close an insulating band gap and give rise to

metallic phenomena in the bulk of SmB_6 [113–116] It has been suggested that even a small amount of Sm vacancies on the order of 1% can close a bulk hybridization gap, resulting in metallic behaviour as evidenced by complimentary Raman spectroscopy and specific heat measurements, possibly through a mechanism affecting the mixed valence nature of the hybridized electrons [117, 118]. However, the level of disorder needed to close an insulating gap is disputed [119]. Recent research attempts to explain whether these bulk phenomena originate from extrinsic effects from sample growth conditions or intrinsic effects that would be present in the most pristine samples. We will next discuss experimental progress in delineating the effects of sample growth and disorder.

4.6 Sample growth and disorder

Disorder effects are inevitable in real materials but can be characterized and controlled to tune material properties. A discussion of disorder in TKI candidates is necessary to distinguish exotic behaviour that is intrinsic to a material from those that arise due to the sample growth conditions. While the effect of disorder on conventional metals, semimetals and insulators is well-studied, the effect of disorder on the insulating bulk and metallic surface measurements of TKI candidates are less obvious. Studies characterizing disorder effects on experimental results help disentangle these extrinsic effects from inherent behaviour for TKI candidates.

There is an ongoing debate on whether unusual metallic properties in SmB_6 are due to intrinsic or extrinsic origins [92, 120] . A centre of this debate is how the growth technique influences the experimental observations. Two main sample growth methods are in the literature for such materials: using a flux to start polycrystal formation into single crystals then removing excess by taking advantage of its lower melting point [121], and using a high powered lamp to melt the starting polycrystals into a large single crystal structure [122]. The choice of growth method influences the types of disorder typically observed in the sample. Flux grown samples are scrutinized for the possibility of metallic inclusions obscuring quantum oscillation interpretations [20]. For example, in Figure 4.9, Thomas *et al.* show how polishing flux grown samples to remove embedded aluminum reduces the amplitude of oscillatory dHvA signal, which provides compelling evidence that the two-dimensional dHvA oscillations reported in flux grown samples could have an extrinsic origin. However this explanation does not apply to floating zone grown samples, which do not require a metallic flux and yet have reports of quantum oscillations. We will next consider signatures of disorder in floating zone grown SmB_6 samples.

While flux grown samples use an aluminum flux that can produce a residue in the bulk,

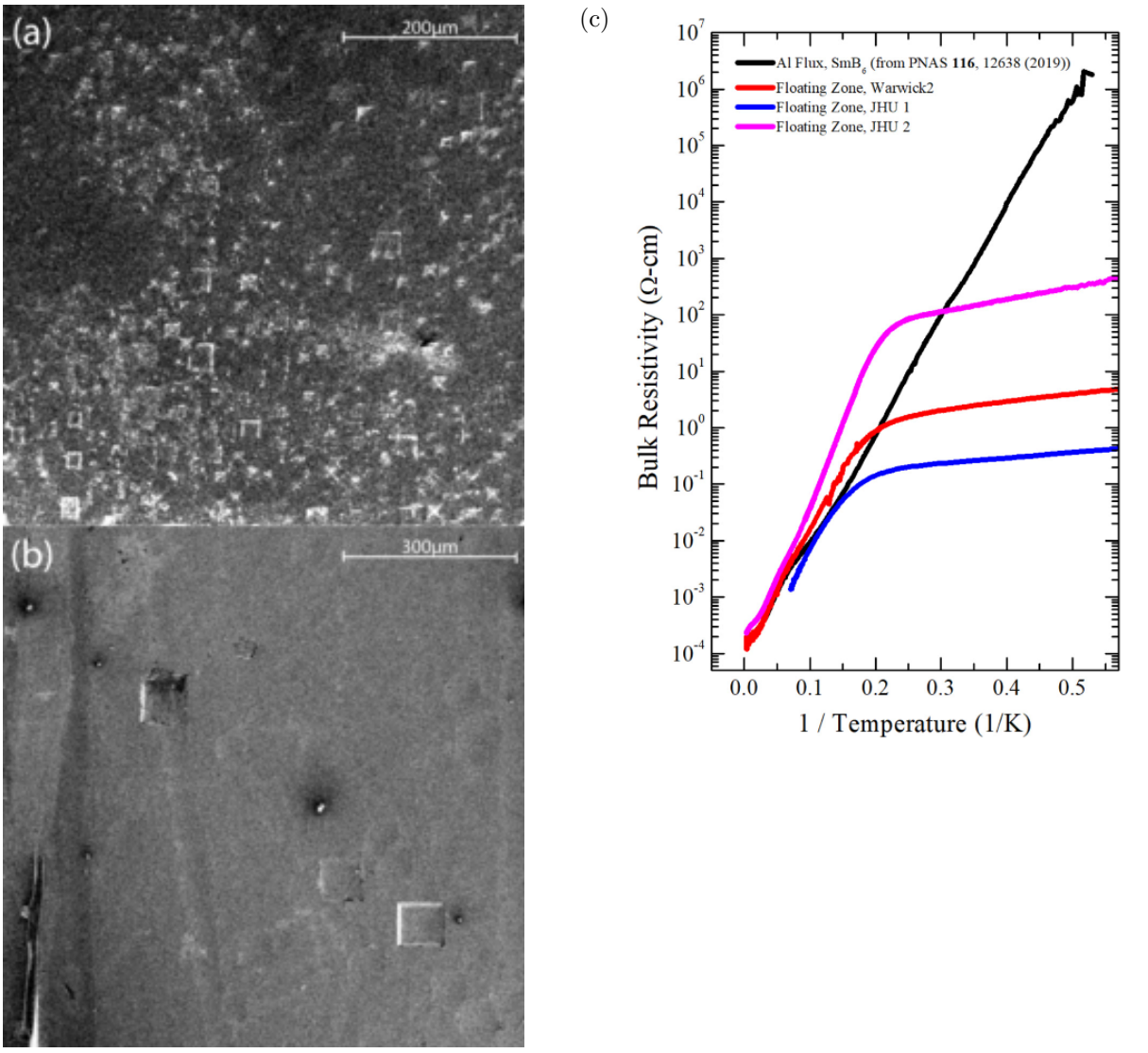


Figure 4.8: Comparison of *bulk* electrical resistivity and dislocations between aluminum flux grown and floating zone grown samples of SmB_6 [18]. Using chemical etching, Eo *et al.* reveal etch pit dislocations in (a) a floating zone grown sample and (b) a flux grown sample of SmB_6. (c) Bulk electrical conductivity measurements of flux grown and floating zone grown SmB_6 samples plotted as a function of inverse temperature on a log-log scale for different sample growths. *Reprinted figures with permission from* [18]. *Copyright 2021 by the American Physical Society.*

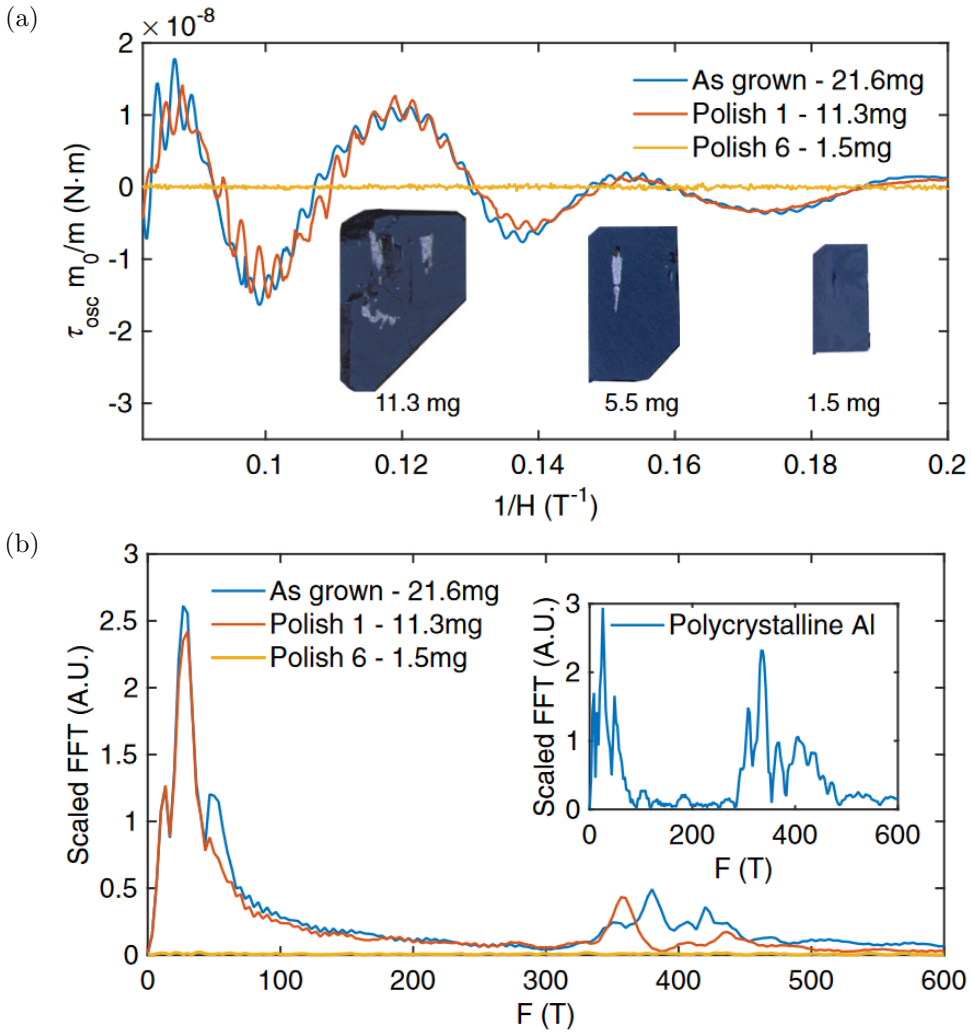


Figure 4.9: Oscillatory torque measurements of flux-grown SmB_6 before and after polishing to remove aluminum inclusions. (a) Amplitude of oscillatory torque τ_{osc} normalized by the sample mass m_0/m versus inverse field, with images of the sample after progressive polishing. (b) Amplitude of fast Fourier transform for the above oscillations, scaled by mass, versus frequency in units of Tesla. Inset showing the spectra of oscillations for polycrystalline aluminum flux, that shows a broader spectrum than the oriented single crystal SmB_6 samples. *Reprinted figures with permission from* [19]. *Copyright 2019 by the American Physical Society.*

floating zone grown materials could also be prone to other types of disorder. In particular, very small amounts of unwanted residue in the source of the rare earth starting materials could result in enhanced metallic-like behaviour [22] and the furnace lamp growth technique could also introduce vacancies on the samarium site [113]. Electron spin resonance measurements of samples with different concentrations of magnetic impurities suggest that metallic islands can cause apparent metallic effects such as quantum oscillations while remaining unnoticed in other measurements [116]. Magnetic impurities could account for exotic metallic phenomena in SmB_6 such as an upturn in specific heat at low temperature [123]. Despite the notable differences in bulk measurements between samples of different growths, the Cambridge group reporting dHvA oscillations originating from the SmB_6 bulk also reported a negligibly low concentration of magnetic impurities in these floating zone grown samples [20]. To summarize, the role of disorder in the reportings of novel quantum oscillations originating from a bulk Fermi surface is highly contested. In the next section, we will introduce new experimental findings on high quality floating zone grown samples.

Sample quality can affect interpretations of thermal conductivity results, especially when trying to discern whether phonons scatter predominantly from sample boundaries at the lowest temperatures. Toews *et al.* [21, 24] discuss sample growth observations — in flux grown samples of SmB_6, even those of high quality, the thermal conductivity does not have a large field response. This is consistent with an observed lack of field response in flux grown samples by Xu *et al.* [94]. But Boulanger *et al.* also look at the thermal conductivity of floating zone grown SmB_6, seeing an increase with field and concluding that a reduction in phonon scattering is responsible, rather than additional excitations [23]. Interestingly, Eo *et al.* show evidence of a higher concentration of dislocations in a floating zone grown sample (Fig. 4.8a) than in a flux grown sample (Fig. 4.8b) [18].

The sample polishing method can influence the low temperature electrical conductivity. Eo *et al.* find that roughly polishing samples results in subsurface cracks that reduce the low temperature resistance plateau, emphasizing the importance of using a fine polishing technique [124]. Naively, the aluminum flux insertions observed in flux-grown samples raise questions about whether novel metallic phenomena could be attributed instead to this source of disorder. However Eo *et al.* report that flux grown samples still have a reportedly high bulk electrical resistivity indicating bulk insulating behaviour, in contrast even to a lower bulk resistivity in floating zone grown samples that is attributed to magnetic impurities or dislocations (Fig. 4.8c) [18].

Even in samples grown without purposeful doping, trace amounts of magnetic disorder may originate from natural impurities present in the samarium seed material [78]. Recently, such disorder is hypothesized as an extrinsic source of metal-like properties reported in the bulk of floating zone grown SmB_6, including quantum oscillations [22, 125]. Doping studies

investigate the effects of such impurities, allowing comparisons of disorder between samples of different growths. Fuhrman *et al.* demonstrate that while SmB_6 is thought to be paramagnetic, magnetic impurities can add a diamagnetic-like feature in the magnetization [22, 126]. This model of paramagnetic background magnetization associated with stoichiometric samples and an additional contribution from weak interactions amongst impurities in off-stoichiometric samples allows for a comparison of magnetic impurity concentrations among different sample growths by examining the sample magnetization. Hartstein *et al.* [20] show how the non-oscillatory magnetization of floating zone grown samples displaying bulk quantum oscillations in the group's earlier study [21] are paramagnetic, consistent with the undoped samples instead of showing extrinsic magnetic impurities (Fig. 4.10). Their analysis, indicating only trace amounts of magnetic impurities in the samples showing bulk dHvA oscillations, calls into question leading theories that the oscillations are extrinsically caused by to disorder-induced in-gap states. However, the lack of reproduction of such high frequency oscillations is yet to be reproduced in other samples, and the strong sample variation of bulk metal-like features is yet to be fully understood.

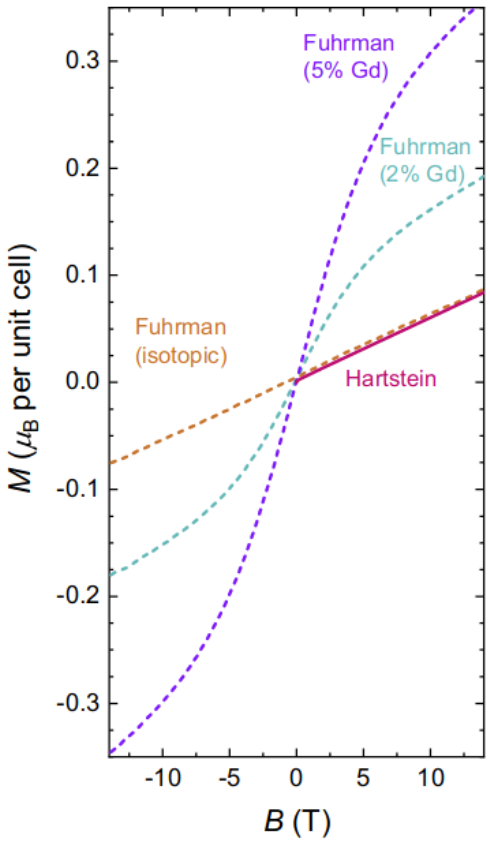


Figure 4.10: A comparison of magnetization among SmB_6 floating zone grown samples by Hartstein *et al.* [20]. The authors compare the samples previously reported to have bulk quantum oscillations [21] with the floating zone grown samples of Furhman *et al.* [22].

Chapter 5

SmB_6 experimental results

Samarium hexaboride was the first TKI candidate to be discovered. As discussed in Chapter 4, its bulk fermionic properties along with signs of an electrically insulating bulk present an enigma to researchers. These discoveries of exotic signatures typically associated with bulk metallic behaviour have attracted much attention and debate [92]. Certainly this material cannot be classified as a conventional metal or insulator, and metallic signatures in an insulating bulk challenge conventional theories of insulators. In this chapter, we will extend what is known about the novel charge-neutral fermionic excitations in the insulating bulk by reporting new thermal conductivity and oscillatory magnetostriction results.

5.1 Sample information

The SmB_6 single crystal samples considered in this study are grown by our collaborators using the image furnace technique with a high powered xenon arc lamp image furnace [127]. During sample processing, mechanical polishing is avoided on these samples due to the extreme hardness of rare-earth hexaboride materials [128]. Instead, our collaborators use an electropolishing process to reduce sample dimensions, which results in smooth reflective surfaces. Sample characteristics are listed in Table 5.1. Toews *et al.* [21, 24] report thermal conductivity results for samples FZ1 and FZ2, which are included in Figure 5.1 for reference. Figure 5.1 shows that the zero field thermal conductivity is consistent with the estimate of the maximum thermal conductivity of phonons (which is indicated by the red line in Fig. 5.1a). Under an applied field, the thermal conductivity increases above this maximal limit for phonons, leading to a conclusion of delocalized quasiparticle excitations conducting heat in the presence of an applied magnetic field. As shown in the

Sample	dimensions (mm^3)	g (cm^{-1})	ρ(0.5 K)/ρ(300 K)	ρ(0.1 K)/ρ(300 K)
FZ1	$1.3 \times 0.275 \times 0.360$	86.1	4.38×10^4	4.37×10^4
FZ2	$2.0 \times 0.22 \times 0.36$	190.8	4.71×10^4	4.80×10^4
FZ2p	$2.0 \times 0.125 \times 0.290$	326.8		
FZ3	$2.6 \times 0.712 \times 0.296$	77.3	2.19×10^4	8.09×10^4

Table 5.1: SmB_6 floating zone grown samples, dimensions, geometric factor g and inverse resistivity ratio (iRRR) at 0.5 K and at 0.1 K for comparison. Toews reports the iRRR values for FZ1 and FZ2 [1]. The sample FZ2p is the sample FZ2 after electropolishing to reduce its cross-sectional area.

inset to Figure 5.1a, this enhanced conductivity potentially has a residual linear term that is not reflected in charge conductivity according to the Wiedemann-Franz law, hence the enhancement from quasiparticles is considered fermionic but electrically charge-neutral. Hartstein *et al.* [21] also report a sample growth dependence in the thermal conductivity enhancement. The thermal conductivity of the floating zone ("FZ") grown samples are enhanced up to twice their zero field value in a 12 T field, but the flux grown sample in the inset to Figure 5.1b lacks such a discernible enhancement. Samples from this study also show quantum oscillations in the bulk of the material. Regarding the nature of the charge-neutral quasiparticles in transport measurements, even though the thermal conductivity dependence on specific heat capacity is conventionally expected to result in a *zero-field* residual linear thermal conductivity, no groups report observing a linear term in the absence of a field, resulting in a contradiction that is difficult to reconcile with theoretical models of charge-neutral fermionic quasiparticles[1].

As part of our work, we remeasure the thermal conductivity results in a transverse zero field and 12 T field on the sample FZ1 and on the smaller, polished geometry of sample FZ2 to verify earlier reports from our group. The samples were left in room temperature and pressure conditions over time, and the sample contacts changed from the original contact length due to a need to reapply contacts in the sample mounting process, however we carefully measured these geometries using a scale micrometer. Then we measured the thermal conductivity with respect to an applied transverse field to test the prediction that the $\kappa \propto H$ only for a field orientation perpendicular to the heat current, as proposed for theoretical "skyrmion" quasiparticles [106].

[1]The lack of low temperature and high field also complicates interpretations of a linear term in specific heat capacity. In one of the few such studies, Flachbert *et al.* [100] note a considerable increase in the specific heat capacity at fields $B > 1\,\mathrm{T}$ and temperatures $T < 0.3\,\mathrm{K}$ due to nuclear effects in their highest quality sample.

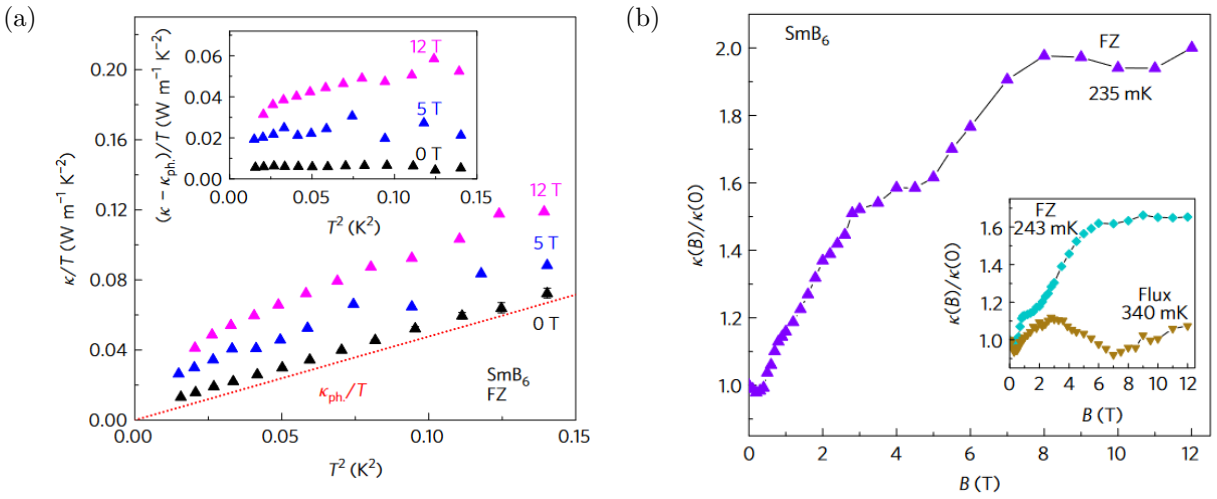


Figure 5.1: Thermal conductivity results for one of the low disorder floating zone grown samples (FZ1, FZ2) that are remeasured in this thesis, as reported by Hartstein *et al.* [21]. *Reproduced with permission from Springer Nature.* (a) Thermal conductivity plotted as κ/T versus T^2, with the dotted line indicating the estimate of the maximal thermal conductivity of phonons ($\kappa_{\rm ph}/T$). Inset: the enhancement of thermal conductivity in an applied field by subtracting the estimate of the maximal phonon thermal conductivity. (b) The field-dependent thermal conductivity for an FZ sample, normalized by the zero-field thermal conductivity, at 235 mK. Inset: Additional field-dependent thermal conductivity for the other FZ sample at 243 mK and for a flux grown sample at 340 mK.

5.2 Thermal conductivity results

5.2.1 Phonon conductivity in high quality samples

This work builds on the results of charge-neutral fermionic excitations in high-quality floating zone grown samples as reported previously by our group and our collaborators [1, 20, 21]. Toews *et al.* [21, 24] find that the thermal conductivity results of two floating zone grown samples, labelled FZ1 and FZ2, reach the phonon boundary scattering limit at the lowest temperatures in zero field and report an enhancement in conductivity in applied field. This argument depends on the theoretical maximum of the phonon boundary scattering as elaborated in Appendix A.3.1, given a lattice specific heat capacity coefficient equal to $\beta = 8.83 \times 10^{-4}$ mJ cm^{-3} K^{-4}, a speed of sound $v_s = 5.18 \times 10^5$ cm s^{-1}, and a phonon mean free path equal to the geometric mean of the cross-sectional area. This estimate is illustrated as a red line in Figure 5.1a for one of the high quality floating zone grown samples. To summarize this argument, the zero field conductivity for FZ1 and FZ2 agrees well with the estimated boundary-limited phonon conductivity as expected for high quality insulating samples. Therefore the increase in conductivity observed in applied field in Fig. 5.1a and b must originate from another delocalized excitation.

On the other hand, not all thermal conductivity analyses agree with this interpretation of phonon conduction. Boulanger *et al.* [23] report a lack of enhancement of thermal conductivity above that expected for phonons in a variety of samples of SmB_6, interpreting an increase in thermal conductivity with applied field as a reduction in phonon scattering due to the lack of increase above the maximum phonon conductivity limit for fields as high as 15 T. To address the alternative scenario proposed by Boulanger *et al.*, we perform measurements to empirically establish the phonon boundary scattering scenario. Furthermore, to test whether sample disorder could contribute to these differing interpretations, we also study a more disordered floating zone grown sample that was specifically chosen for comparison with these samples.

A precise test of boundary scattering in high quality insulating samples is to check the ratio of thermal conductivities κ_1/κ_2 for a sample before and after polishing, since this allows an analysis of phonon scattering for differing sample geometries according to Appendix A.3 while keeping the level of disorder consistent between samples. Figure 5.2 shows sample FZ2 before and after reduction of its cross-sectional area with electropolishing. Before polishing, using the dimensions in Table 5.1, we calculate that the phonon mean free path theoretical estimate in the boundary scattering limit is $\ell_{\mathrm{F2}} = 3.17 \times 10^{-2}$ cm, and after polishing it becomes $\ell_{\mathrm{F2p}} = 2.15 \times 10^{-2}$ cm. In other words the ratio between the two theoretical mean free paths is $\ell_{\mathrm{F2}}/\ell_{\mathrm{F2p}} = 1.47$. The inset to Fig. 5.2 shows the

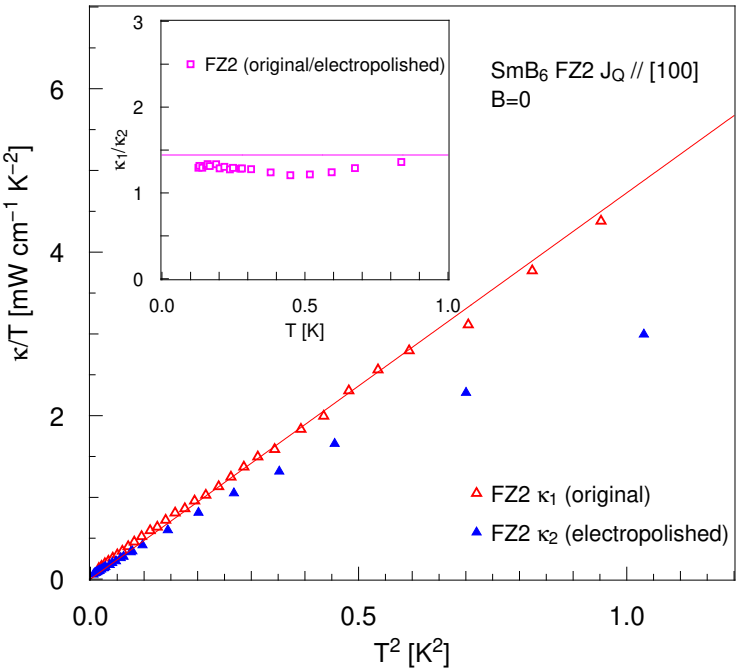


Figure 5.2: SmB_6 sample FZ2 thermal conductivity before and after electropolishing. The red line is the theoretical estimate of the phonon boundary scattering limit before electropolishing. Inset: ratio of FZ2 thermal conductivity before and after electropolishing, with error bars indicating the Gaussian mean of the uncertainty in the geometric factors for both sample geometries. The fuchsia line is the theoretical ratio of phonon mean free paths in the boundary scattering limit.

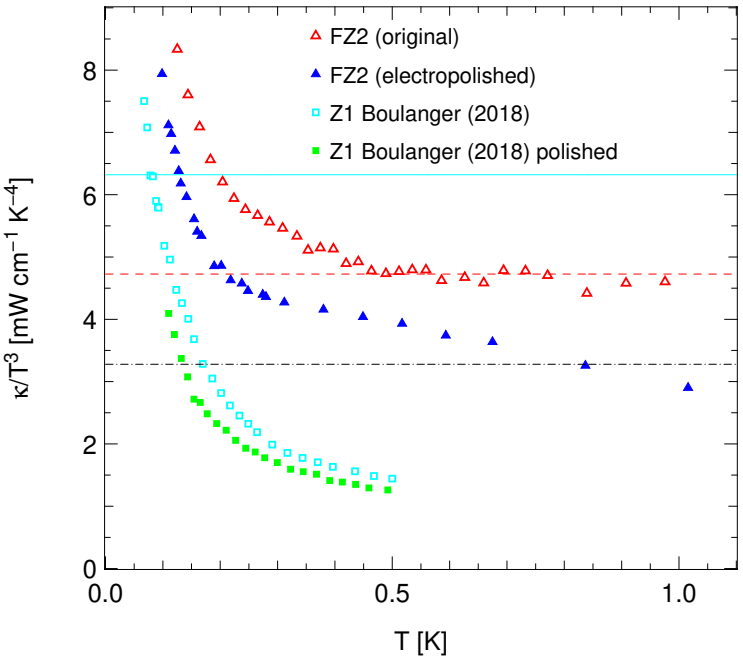


Figure 5.3: Thermal conductivity of SmB_6 samples FZ2 and Boulanger *et al.*'s sample Z1 [23] in zero magnetic field, plotted as κ/T^3 versus T. The theoretical Casimir limit, where $\kappa/T^3 \propto \ell_C$ is shown as the lines on the graph. By sample geometries, $\ell_C = 3.5 \times 10^{-2}$ cm for the original FZ2 sample (dashed red line) and 4.1×10^{-2}cm for the original Z1 sample (solid cyan line). Both polished samples have similar cross-sectional areas with $\ell_C = 2.15 \times 10^{-2}$ cm (black dot-dash line).

ratio of thermal conductivity, with the data reaching this expected scaling for the different sample geometries within the error bounds of the Gaussian mean of the systematic error in contact length using the approach in Equation (2.7). The SmB_6 floating zone grown sample FZ2 scales as expected for phonons only scattering with sample boundaries in zero magnetic field. This result reinforces the conclusion that the zero field thermal conductivity is dominated by phonon conduction and that the in-field enhancement is not due to a reduction in phonon scattering. Since we establish that the zero field heat conduction is in the theoretical maximum limit for phonons, that is having a mean free path that scales with sample boundaries, the phonon mean free path cannot exceed this limit with an applied field.

The phonon mean free path for boundary-dominated conduction may have slight corrections from the geometric mean of the cross-sectional area due to finite length and specular

reflection effects (as discussed in Appendix A.3.2). Li *et al.* [51] find that the power law of the thermal conductivity for samples with reflective surfaces may be closer to $\kappa \sim T^2$ due to specular reflection, though the absolute value of the phonon mean free path can still exceed the value calculated from the geometric mean. In contrast, samples with roughened surfaces can still demonstrate these specular reflection effects at the lowest temperatures, but show more agreement with the Casimir estimate of the phonon mean free path in the higher temperature range, as also briefly reviewed in Appendix A.3.2. This effect also likely applies to our electropolished samples of SmB_6 with their mirror-like surfaces. After electropolishing to reduce the cross-sectional area, the surface of FZ2 is visibly more reflective than in its original state. In Figure 5.3, we show the temperature-dependence of the agreement with the Casimir expectation for thermal conductivity [Eq. (A.13)] for sample FZ2 before and after polishing. We also compare this to the findings of Boulanger *et al.* [23] for the "Z1" sample. We find that though both samples show characteristics of specular reflection in their departure from the theoretical cubic temperature dependence and increase above the expected boundary-limited thermal conductivity at the lowest temperatures[2], the FZ2 sample approaches the Casimir limit at higher temperatures for both geometries, which indicates that the phonon conduction in FZ2 still demonstrates boundary-limited scattering in spite of the boundary specularly reflecting these phonons. In contrast, the Z1 sample remains well below the expected limit at all temperatures which indicates additional phonon scattering in zero field that is not present in FZ2 and is therefore not intrinsic to the material. A boundary-limited mean free path, even with specularly reflected phonons, is still not affected by an applied magnetic field and cannot explain our observed thermal conductivity enhancement in applied fields. However SmB_6 samples that do not approach boundary-limited behaviour in zero field may instead have additional disorder that obscures the material's intrinsic physical properties.

Disorder increases phonon scattering, decreasing the phonon mean free path and thermal conductivity as described in Appendix A3. To investigate the effect of disorder on SmB_6, we also measured the thermal conductivity of FZ3, a floating zone grown sample that has higher disorder compared to FZ1 and FZ2 according to metrics that will be discussed in Section 5.2.2. In Figure 5.4a we show the low temperature thermal conductivity of FZ3 in zero field and in an applied 12 T field. We see an enhancement of the thermal conductivity in applied field. We also measured the electrical resistivity of FZ3 in zero field, shown in Figure 5.4b. This shows two plateaus in the electrical resistivity: the resis-

[2]This departure is similar to that reported for the as-grown sample of Nd_2CuO_4 [51], which reaches a value that is three times that of the Casimir limit as shown in Figure A.3. After roughening the sample surfaces, the authors report closer agreement to the Casimir limit, indicating that such an enhancement is likely due to specular reflection of phonons by mirror-like surfaces.

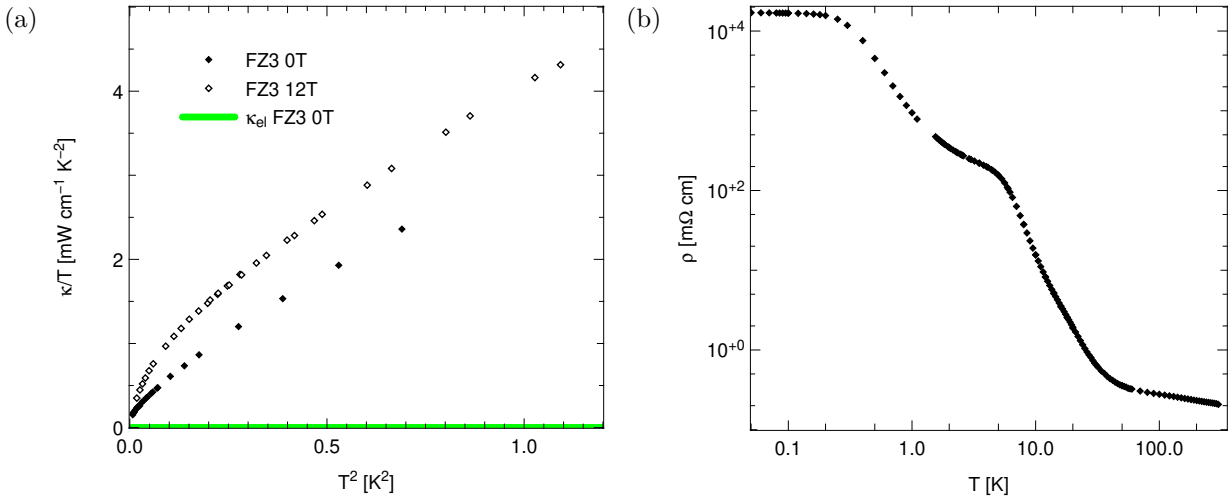


Figure 5.4: SmB_6 FZ3 thermal conductivity data plotted as κ/T versus T^2, (a) in zero field (solid diamonds) and 12 T field (open diamonds) with the electron contribution to the thermal conductivity κ_{el} estimated by the Wiedemann-Franz law (green line). (b) Low temperature resistivity of FZ3 in zero applied magnetic field.

tivity reaches a maximum of $\sim 10^4$ mΩ cm at the lowest temperatures and steps down to $\sim 10^2$ mΩ cm at ~ 7 K. The electron contribution estimated by the Wiedemann-Franz law (discussed in Appendix A.2), illustrated in Figure 5.4a, is about five orders of magnitude below the observed conductivity which is consistent with the electrically insulating nature of the bulk at these low temperatures. We next compare our results with the expectations for bulk insulators with sample disorder.

While we suspect that FZ3 is higher disorder, we still need to quantify the level of disorder in this sample in relation to FZ1 and FZ2. Naively, we could use the sample iRRR as a measure of disorder, which is reportedly lower in doped samples [129, 130]. However, given the two-step nature of the electrical conductivity for FZ3 in comparison to the singular plateaus for FZ1 and FZ2 (discussed by Toews [1]), the conclusions drawn from this comparison depend on the temperature attained to measure the residual resistivity. As reported in Table 5.1, the iRRR for FZ3 rises above that for FZ1 and FZ2 when using the residual resistivity at 0.1 K in this ratio. When comparing this to the observations of a lower iRRR for samples with magnetic impurities, we may incorrectly conclude that FZ1 and FZ2 have stronger disorder. In reality, multiple measurements show that these samples and samples from the same batch have low disorder, particularly in comparison with other literature. Using inductively coupled plasma optical emission spectrometry, Hartstein *et*

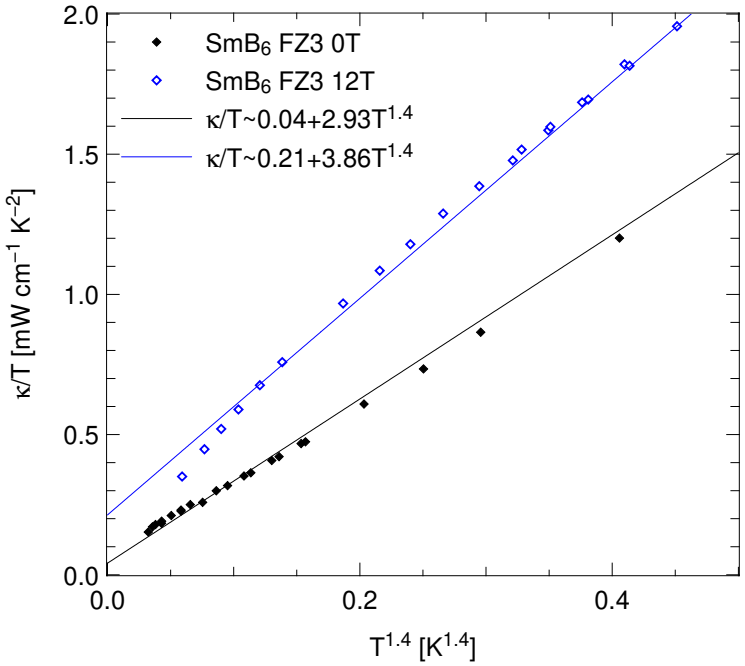


Figure 5.5: Thermal conductivity of FZ3 in zero field and 12 T field plotted as κ/T versus $T^{1.4}$. Solid lines are fits to $\kappa/T = A + BT^{1.4}$.

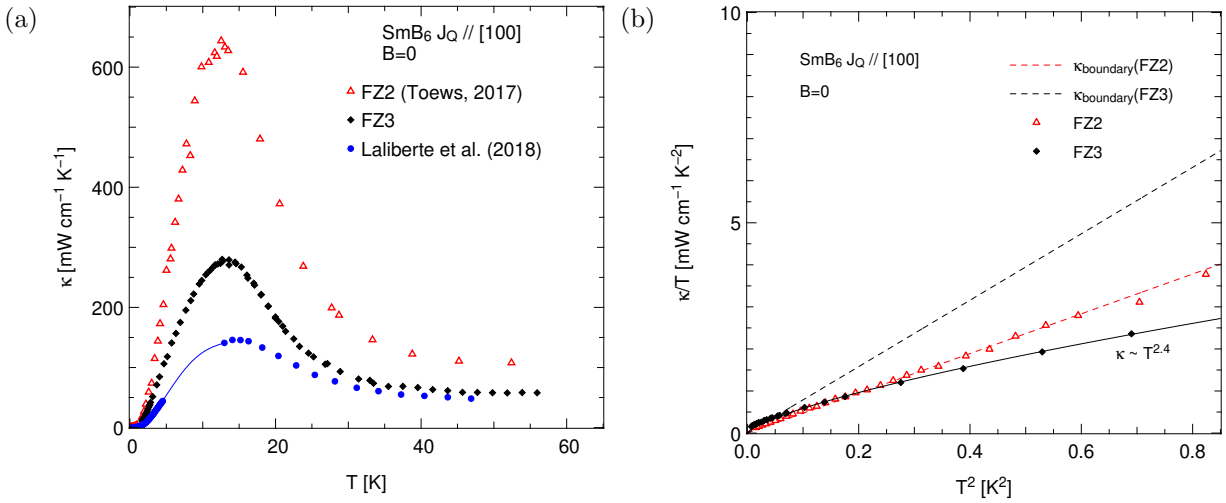


Figure 5.6: (a) Peak thermal conductivity of SmB_6 samples FZ2 (as previously reported by Toews [24]) and FZ3. The blue dots are for the SmB_6 sample reported by Laliberté *et al.* [25] with data below 5 K adapted from Boulanger *et al.* [23] and the blue line a guide to the eye. (b) Zero field thermal conductivity of FZ2 and FZ3. The black solid line is a fit of the FZ3 conductivity to $\kappa/T = BT^{\alpha-1}$, obtaining $\alpha \sim 2.4$. Dashed lines are the Casimir estimates of the thermal conductivity from phonons scattering with sample boundaries.

al. [20] report that samples from a similar floating zone grown batch as FZ1 and FZ2 contain extrinsic disorder of at most $\approx 100 - 1000$ parts per million (ppm) for tellurium and yttrium, and a concentration below the limits of detection (≈ 100 ppm in most cases) for all other possible extrinsic impurities. They also report a low residual value of specific heat that is most consistent with a lack of magnetic disorder. Such an analysis of material composition and specific heat has not been reported for FZ3, however as discussed earlier, we do not observe boundary-limited thermal conductivity in the FZ3 sample, which can indicate additional phonon scattering with disorder.

5.2.2 Signatures of bulk sample disorder

In the absence of sample characterization information on sample disorder, we need a less ambiguous signature of disorder in transport than the iRRR. Most measurements of iRRR only reach $\sim 2 - 4$ K but, as discussed in the last section, we observe a second plateau in resistivity below 1 K in FZ3. Moreover, this method does not distinguish between bulk and surface effects and therefore could qualitatively obtain different results between differ-

ent measurements of the same sample depending on the location of the contacts. When analysing our thermal transport results between samples of different qualities, we need to compare the influence of impurities in the bulk of the material rather than the impurity influence on the electrically conductive surface. The peak thermal conductivity of high quality, insulating crystals can qualitatively characterize the level of phonon scattering between different samples of the same material as discussed in Appendix A.3.3. Toews *et al.* report measurements of peak thermal conductivity for FZ1 and FZ2 [21, 24]. We also measured the thermal conductivity of a third flux grown sample FZ3, with lower quality according to its iRRR and a larger residual specific heat value for comparison. Figure 5.6a shows peak conductivity of FZ2 compared with FZ3. Qualitatively, the bulk of FZ3 is more disordered than FZ2, as evidenced by a lower peak thermal conductivity, which indicates increased scattering of phonons with sample disorder which appears at temperatures where the wavelength of thermally excited phonons is comparable in magnitude to the aperiodicity of the lattice (as further explained in Appendix A.3.3). Figure 5.6b shows the low temperature thermal conductivity of FZ3 in comparison with other samples. Qualitatively larger phonon scattering at the peak is reflected in lower temperature results as a temperature dependence further below cubic of $\kappa \sim T^{2.4}$, leading to a strong deviation from boundary scattering limit expectations. We did see an increase in thermal conductivity with field for FZ3 as well as shown in Figure 5.6b, but it would be more difficult to claim unambiguously that this increase is due to the presence of excitations rather than a reduction in phonon scattering. It is possible that the same excitations observed in FZ1 and FZ2 are in this sample as well. However, magnetic field-induced excitations are most easily distinguished from phonons in highest quality flux grown samples.

We can numerically model the thermal conductivity to gain information about the relative concentrations of crystal imperfections in floating zone grown samples. While previous analysis has been done on samples FZ1 and FZ2 at intermediate temperatures [24], such analysis approximates the Debye phonon spectrum as cubic rather than using the Callaway model discussed in Appendix A.4. Using the Callaway model, we will next investigate scattering behaviour at temperatures near the peak conductivity and compare the analysis to that of other floating zone growths with the benefit of educated assumptions about disorder based on other literature. It is noted that floating zone grown samples of SmB_6 can be subject to vacancy defects even if they are less prone to other inclusions [113, 117]. Given theories that charge neutral quasiparticles could be driven by mixed valence [131], changes in such vacancies could in theory change the mixed valence character of SmB_6, affecting novel bulk excitations. Defects such as vacancies typically also leave fingerprints in other thermodynamic properties, allowing a quantitative analysis to compare defect strength to make a statement on whether observations are intrinsic or extrinsic. We

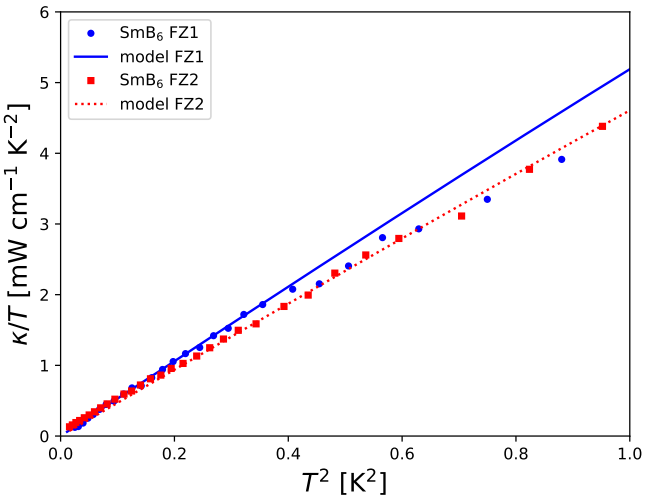


Figure 5.7: Phonon thermal conductivity modelled for SmB_6 FZ1 and FZ2 in zero field, with two parameters: boundary scattering proportional to the sample cross-sectional area, and point defects from samarium vacancies. The point defect coefficients assume $N_d = 1.22 \times 10^{20}$ cm^3, resulting in $c_p = 0.9\%$.

can model the scattering rate for point defects in thermal conductivity due to the difference in mass using Equation (A.16). Moreover, we can estimate the concentration of defects based on the value of the linear coefficient of specific heat capacity. Skinner estimates that in SmB_6, the linear coefficient of specific heat capacity C_V/T is related to number of defects as

$$C_V/T \sim 100 c_p^{2/3} \text{ mJ mol}^{-1} \text{ K}^{-2} \tag{5.1}$$

for doping fraction $c_p = N_d a^3$ that depends on the number of defects per unit volume N_d [119]. Using the residual value for samples of the batch of high quality sample growths of $C_V \sim 4.2$ mJ mol^{-1} K^{-2} [21], estimate $c_p \sim 0.01$ for high quality floating zone grown samples discussed here, which is at most 1% as also reported for these samples [20]. For a vacancy, assume the mass is off by a factor $\Delta M/M \sim 1$. Modeling the scattering rate in Equation (A.16), and assuming that the scattering from sample boundaries is well approximated by the geometric mean of the cross-sectional area as per the ratio of the Casimir estimates of the mean free path in Equation (A.7), the lines plotted in Figure 5.7 are the theoretical thermal conductivity estimates in the Debye model according to the

Callaway model [Eq. (A.15)]. This models the effect of vacancies in form of point defects in order to compare them to thermal conductivity results. Figure 5.7 shows that the zero field low temperature thermal conductivity of FZ1 and FZ2 are well modelled by a simple model of boundary scattering with $\sim 1\%$ point defects, reinforcing that these are high quality samples with a small and expected amount of phonon scattering from disorder. In contrast, Skinner estimates that the critical doping fraction needed to transition from a bulk insulator to a bulk metal is much larger than this, on the order of one defect per lattice site [119]. Nonetheless the thermal conductivity approaching the boundary scattering limit is consistent with expectations of low levels of disorder given the residual value of specific heat on the lower end of reported values.

5.2.3 Field-induced excitations

The field-dependent resistivity is well described by the Zeeman effect given the ground state hybridization of Sm ions, and Boulanger *et al.* [23] also argue that a Zeemen effect is responsible for the enhancement of a field-dependent thermal conductivity, originating from scattering with magnetic impurities. The low temperature magnetoresistance of SmB_6 FZ1 and FZ2 can be reasonably described by a two-band model $\rho(T) = (\rho_s^{-1} + \rho_B^{-1} \exp(-\Delta/k_B T))^{-1}$ where ρ_s is the resistivity of the surface and ρ_B is the coefficient of the activated bulk resistivity, and T_0 is the energy gap in the bulk [24, 95]. In this model, the gap Δ takes the form of a Kondo gap, whose energy decreases with field according to the Zeeman energy expression $\Delta(B) = \Delta(B = 0) - g\mu_B B$ [132]. Here, g is the Lande factor which depends on the hybridization of Sm ions. However the in-field resistivity is too small for electrons to substantially contribute to the enhanced thermal conductivity according to the Wiedemann-Franz law. We will next explore scenarios for the the enhanced thermal conductivity in an applied magnetic field.

If the zero field thermal conductivity is consistent with phonons scattering only with sample boundaries, then an increase in thermal conductivity with field is most simply explained as contributions by additional heat-carrying excitations rather than as a reduction in phonon scattering. To characterize the nature of such excitations and inspire theoretical models, it is useful to check if there is an anisotropic response with field direction. In particular, Erten *et al.*'s model of a Skyrme insulator predicts anomalous excitations that have a field-dependent thermal conductivity $\kappa \propto H$ and travel perpendicular to the field direction [106]. We can test the validity of this prediction by measuring the thermal conductivity in a longitudinal applied field. Figure 5.8a compares the enhanced thermal conductivity in a 12 T field for longitudinal and transverse fields. For samples FZ1 and

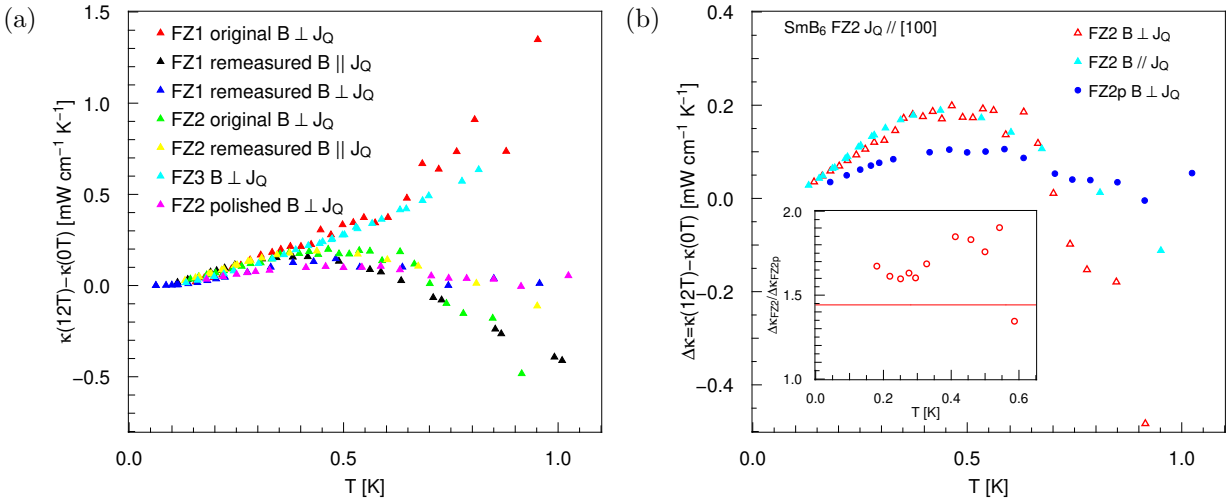


Figure 5.8: (a) The difference $\Delta\kappa$ between the thermal conductivity in a 12 T field and a 0 T field with respect to temperature and field orientation for samples FZ1, FZ2 and FZ3. (b) This difference for the FZ2 sample before and after polishing. Inset: ratio of $\Delta\kappa$ in a transverse 12 T field before and after polishing. Red line is the ratio of the cross-sectional areas for FZ2.

FZ2, the enhancement of conductivity with field is independent of the heat current direction, unlike the prediction for "skyrmion" excitations. The skyrmion model outlines a clear test of the prediction by thermal conductivity. We could not find evidence to support this model when executing this test. We will explore other possible explanations that depend on a residual linear term in both the thermal conductivity and specific heat.

Figure 5.8b compares the enhancement in FZ2. The inset shows the ratio of the enhancement between the unpolished and polished sample in the transverse field orientation. At temperatures below $\sim$ 0.5 K, the enhancement is roughly linear in temperature and also roughly scales with the sample cross-sectional area. This is consistent with a scenario of fermionic heat carriers in the bulk of the sample. Moreover, the enhancement is comparable in this region even for the more disordered FZ3 sample, suggesting a disorder independence of this contribution. The decrease in the enhancement and the qualitatively differing behaviour between measurements at temperatures above $\sim$ 0.5 K could indicate the onset of an additional scattering mechanism.

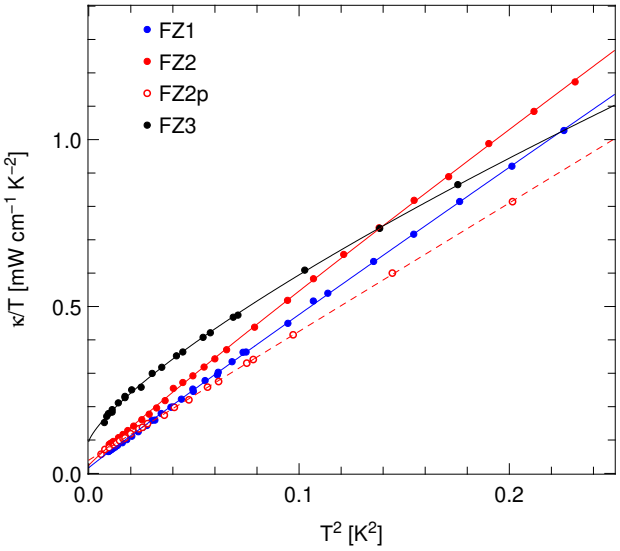


Figure 5.9: Thermal conductivity of FZ1, FZ2, FZ2p and FZ3 in zero field plotted as κ/T versus T^2. Lines show respective fits of the thermal conductivity below 0.5 K to Equation (5.3), obtaining parameters as listed in Table 5.2.

Sample	A (mW cm^{-1} K^{-2})	B (mW cm^{-1} K$^{\delta-1}$)	δ
FZ1	0.017	4.30	2.94
FZ2	0.024	4.62	2.89
FZ2p	0.040	3.84	3.00
FZ3	0.095	2.91	2.53

Table 5.2: Coefficients of fits below 0.5 K to $\kappa/T = A + BT^{\delta-1}$ for SmB_6 samples FZ1, FZ2 (FZ2p is after electropolishing to reduce sample dimensions), and FZ3.

5.2.4 Fermionic contributions to thermal conductivity

Reconciling the lack of a residual linear term in the zero field thermal conductivity with interpretations of a delocalized charge-neutral fermionic excitation requires some discussion on the limitations of the residual linear term contribution. If such quasiparticles exist, then it's puzzling why they would be most apparent in high fields, and no theoretical justification so far could explain the absence of a similar contribution to thermal conductivity in zero fields. A few possibilities exist that could provide an explanation for this conundrum experimentally. Specular reflection effects could mask a real linear term, a poor phonon-quasiparticle coupling could result in a phonon bottleneck effect, or perhaps some of the quasiparticles contributing to the linear term in specific heat capacity are localized in zero field and do not contribute to thermal conductivity.

Bulk metals have contributions to the thermal conductivity from phonons and electrons. Most simply, an electronic contribution to the thermal conductivity κ_{el} is given by the Wiedemann-Franz law, where κ_{el} linearly depends on temperature with a slope inversely related to the resistivity ρ [133]. The magnitude of this slope arises from the linear specific heat $C_{\mathrm{el}} = \gamma T$, the dependence of the Sommerfeld coefficient γ on carrier density and Fermi energy [see Equation (A.5)], as well as the dependence of electrical resistivity on these same physical quantities. The Wiedemann-Franz law can be summarized as

$$\kappa_{\mathrm{el}} = \frac{1}{\rho}\frac{\pi^2}{3}\left(\frac{k_{\mathrm{B}}}{e}\right)^2 T. \tag{5.2}$$

The larger the value of the resistivity, the smaller this contribution will be at the lowest temperatures. In fact, given the large residual resistivity observed in SmB_6, the electronic contribution expected by the Wiedemann Franz law is negligibly small [21, 23, 94] and the charge carriers contributing to electrical conductivity at the lowest temperatures are predominantly at the surface of the samples [14]. The thermal conductivity of high quality floating zone grown samples is well modeled by

$$\kappa/T = A + BT^{\delta-1} \tag{5.3}$$

with $\delta \sim 3$ and $A \sim 0$, consistent with phonons in boundary scattering regime [24]. We are limited in any interpretation of contributions from electrons to thermal conductivity at the lowest temperatures using the Wiedemann-Franz law due to the lack of a residual linear term and a large electrical resistivity. Moreover, the agreement to Equation (5.3) is demonstrated by the fittings plotted in Figure 5.9 with fitting coefficients listed in Table 5.2.

On the other hand, a simple picture of phonon conduction with an electronically insulating bulk is difficult to reconcile with observations that the large residual linear specific heat originates from the bulk. If the Sommerfeld coefficient is quite large, why is this not reflected in the thermal conductivity? It's conceivable that a weak coupling between surface electrons and a novel fermionic charge carrier in the bulk results in behaviour consistent with bulk metallicity in some measurements but particularly affects thermal conductivity measurements. Coleman suggests perhaps longer equilibrium times are needed to see a linear term in the thermal conductivity due to such an effect [134]. While typical measurements wait for thermometer equilibrium, SmB_6 settling times were quite long compared to typical metals, taking hours to reach a thermal equilibrium at the lowest temperatures. We will next address the feasibility of this idea and whether such long time periods can be practically observed.

A major factor in transport measurements, and unknown in these materials is exactly how the electrons and phonons on the metallic surface of the material couple to the delocalized quasiparticles in the bulk. A poor coupling between these heat carriers could introduce a thermal resistivity contribution from a bottleneck process, resulting in poor heat transfer. In the electron-phonon decoupling process described by Smith *et al.* [26], normally this reduction in coupling strength is observed as a violation of the Wiedemann-Franz law due to the electrical conductivity remaining metallic over a given temperature range and the thermal conductivity showing a downturn at a rate that is unexpected for a metal. Figure 5.10a shows a rough schematic of a thermal resistance circuit for heat transfer from the heater, through the contact resistances of phonons and electrons on the surface, then through the phonons and charge-neutral fermions in the bulk. Smith *et al.* describe the thermal conductance within the sample for such a circuit as

$$\frac{\dot{Q}}{T_4 - T_2} = \frac{1}{W_{\text{s,f}} + W_{\text{s,f-ph}}} + \frac{1}{W_{\text{s,ph}}} \tag{5.4}$$

such that the fermionic contribution to the conductance depends on the relative magnitudes of $W_{\text{s,f}}$ and $W_{\text{s,f-ph}}$ [26]. If we use the same schematic for charge-neutral fermions in the bulk with heat transport behaviour analogous to the electrons in Smith *et al.*'s model, then the heat current $\boldsymbol{j}$ travels mediated by phonons and fermions in the bulk when the coupling resistance $W_{\text{s,f-ph}}$ is small — typically at higher temperatures[3], equilibrating temperatures T_2 and T_3. On the other hand, if this coupling resistance is large, then the

[3]Smith *et al.* report an electron-phonon coupling resistance with the temperature dependence $W^{-1}_{\text{s,e-ph}} = \Omega K T^n$ for a sample with volume Ω and K a constant related to the resistance of electron-phonon coupling [26]. They note that n is typically on the order $4 - 5$.

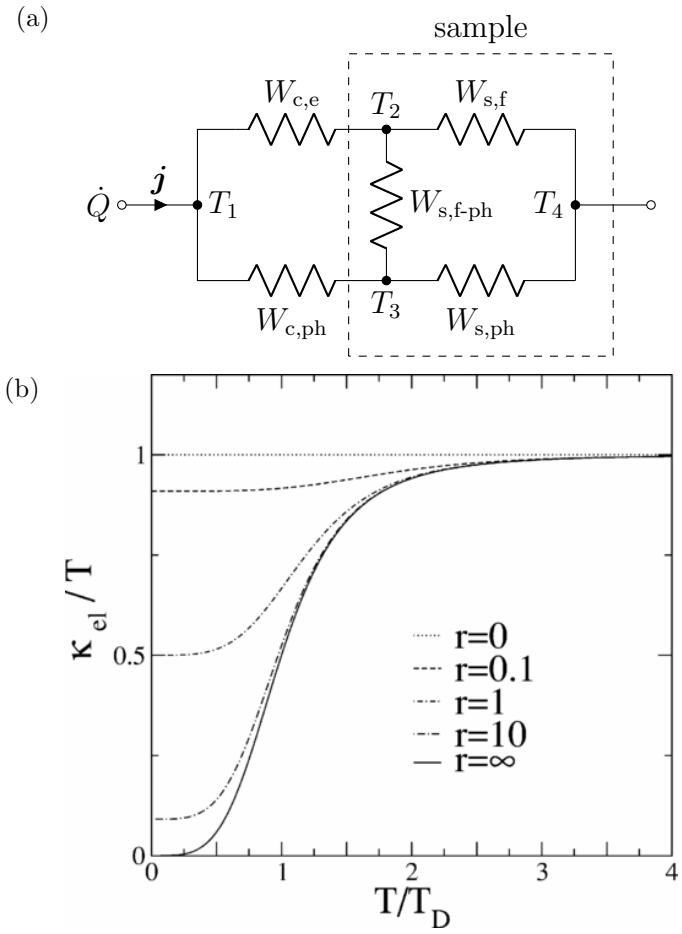


Figure 5.10: Circuit adapted from Smith *et al.* [26]. The applied heat $\dot{Q}$ dissipates through the contacts with resistivity from electrons $W_{c,e}$ and phonons $W_{c,ph}$. Then the heat current $\boldsymbol{j}$ travels through the parallel resistances from charge-neutral fermions $W_{s,f}$ and phonons $W_{s,ph}$, or through the fermion-phonon coupling resistance $W_{s,f\text{-}ph}$. (b) Smith *et al.* plot the electronic thermal conductivity as a function of contact resistance r and temperature T, where T_D is the temperature above which the contact resistance can be neglected. *Reproduced figures with permission from* [26]. *Copyright 2005 by the American Physical Society.*

current travels through the coupling resistance and the phonons rather than through the fermionic quasiparticles, and the temperatures T_2 and T_3 are no longer equilibrated. Then, instead of Equation (5.3), a main result of the aforementioned paper suggests a thermal conductivity (for electronic quasiparticles)

$$\kappa/T = A\frac{1}{1+\frac{r}{1+r(T/T_D)^{n-1}}} + BT^2 \tag{5.5}$$

where r is the ratio of the electron resistance at the contacts and in the sample (assumed to be constant), $T_D = (\gamma/Kl_s^2)^{1/(n-1)}$ is the temperature below which the electron-phonon coupling resistance becomes non-negligible, and l_s is the length of the sample along the heat current direction. The dependence of the first term on r and temperature normalized by T_D is illustrated in Figure 5.10b, showing that the linear-in-temperature portion of Equation (5.5) is expected to become negligible at temperatures below T_D when the electron thermal resistance at the contacts is large.

Now that we have motivated how decoupling of electrons and phonons can reduce a residual linear term in the thermal conductivity, we will discuss how this effect may hypothetically apply to SmB_6 in the case of charge-neutral fermions in the bulk instead of electrons. The phonon bottleneck effect results in poor heat transfer from decoupling, such that the applied heat $\dot{Q}$ is greater than the heat transferred to the bulk of the sample, and the material does not reach a thermal equilibrium. In the case of SmB_6, we know electrical conductivity is insulating and the contribution from the negligible linear contribution according to the WF law is satisfied. What if instead, the quasiparticles poorly couple to other heat carriers in SmB_6, resulting in a similar bottleneck effect and downturn in this channel of thermal conductivity? Suppose that the temperature of a bottleneck onset, T_D, is $\sim$ 0.5 K due the signs of quicker thermometer equilibration above that temperature. Taking experimental data for floating zone grown samples, the longest relaxation times occurred at the lowest temperatures. Assuming $\kappa/T = A + BT^{\delta-1}$, an extrapolation of data above 0.5 K for a single run to lower temperatures on a plot of κ/T versus T^2 can estimate what linear term is consistent with this data set.

We can assume a scenario of poor phonon-quasiparticle coupling leading to out of equilibrium dynamics in an attempt to determine whether a residual linear contribution from fermionic quasiparticles could be obscured in the thermal conductivity. In Figure 5.11a we use the extrapolated linear relationship and the applied heat to find expected δT consistent with such a hypothetical residual linear term. With an estimated hypothetical κ_0 value, plot ΔT versus time for a lower temperature point of 0.24 K and compare this with the settling time scales at higher temperatures 0.35 K, 0.52 K in Figure 5.11b. If

thermometer equilibration occurs linearly in time, and if a residual linear term is suppressed by this effect, it would take at least $\sim 7-8$ hours to reach the substantially lower ΔT expected by the extrapolation. If instead thermometer equilibration is the exponential decay function plotted in Figure 5.11b, more than twice as long of a settling time is required to get within 2 mK of the desired temperature gradient. Regardless, the expected ΔT at 0.24 K is only ~ 5.2 mK, approximately 2% of the average temperature. Though we may be able to resolve such a change in temperature given that thermometer fluctuations for heat on steps result in a standard deviation of ~ 50 µK in this temperature range, any error in the temperature gradient proportionally has a larger effect on the thermal conductivity thus we aim for a larger temperature gradient as a percentage of the average sample temperature in our measurements. We would typically increase the heater power, increasing the average temperature to $\sim 5-10\%$ in the attempt to increase confidence in the thermal conductivity results. Though unlikely, such a scenario of out of equilibrium effects is difficult to test experimentally using this conventional one-heater two-thermometer technique on single crystal samples, which relies on the assumption that the thermometers are approximately in thermal equilibrium. Another heat transmission method, such as heat by radiation from a light source, may help improve confidence in the thermal conductivity measurement should a phonon-quasiparticle decoupling effect be suspected.

The order of magnitude of the estimate of any residual linear term can be compared with a few assumptions using previous experimental results. If $\gamma \sim 4$ mJ mol^{-1} K^{-2}, unit cell $a = 0.413$ nm, [21], molar mass 215.3 g mol^{-1}, $Z = 1$ formula units per unit cell then translates to 0.1 mJ cm^{-3} K^{-2}. From kinetic theory $\kappa = \frac{1}{3}Cv\ell$, where v is the speed of the carriers (typically electrons in metal for residual linear term) and ℓ is the mean free path. Assuming a Fermi surface with Fermi velocity $v_F = \hbar k_F/m^*$, taking the high frequency (11 kT) α band presumed to originate from bulk in quantum oscillation measurements of samples of these growths, $m^* \sim 0.7\ m_e$ and $k_F = 5.6 \times 10^9$ m^{-1} [21], get $v_F \sim 9\times 10^7$ cm s^{-1}. If $\ell \sim 10^{-6}$ cm as in high frequency oscillations at high fields [21], then we expect to see $\kappa/T \sim 3$ mW cm^{-1} K^{-2}, which is only an order of magnitude larger than $A \sim 5 \times 10^{-1}$ mW cm^{-1} K^{-2} obtained from the extrapolation (see Figure 5.11a). These estimates should be viewed with skepticism; it's difficult to get a sense of the mean free path for such excitations when accounting for phonon scattering or the Fermi velocity of a band contributing to the thermal conductivity considering no such residual linear term has been observed. Moreover, the scenario of poor phonon-quasiparticle coupling in SmB_6 is also challenged by the absence of a significant drop in thermal conductivity with temperature below a hypothetical T_D like that shown in Figure 5.10b in order to cause a vanishing fermionic contribution to the thermal conductivity. As well, there isn't a precedent for such a drop in these systems. The phonon-electron decoupling effect is observed in d-wave

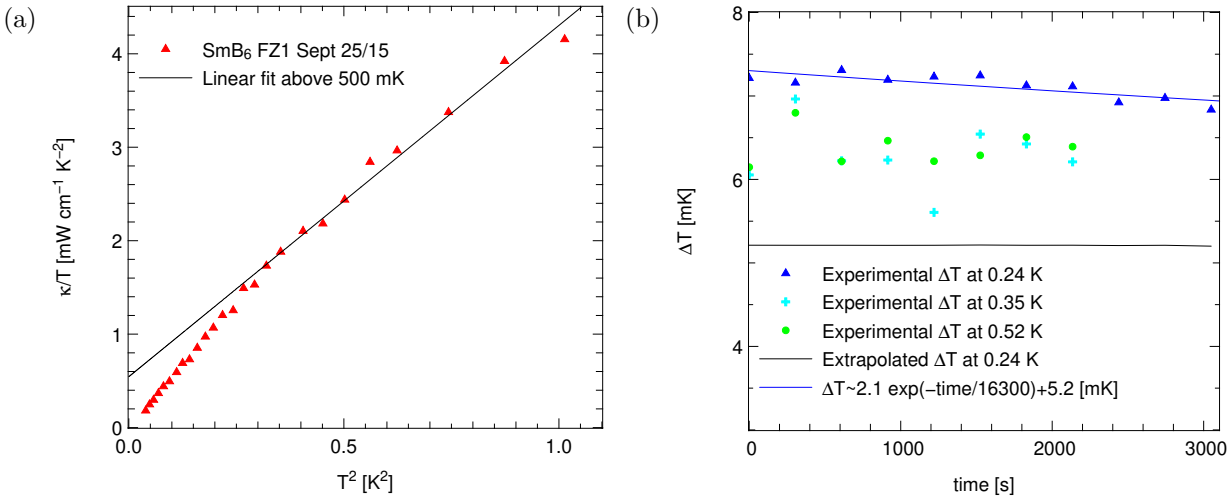


Figure 5.11: a. Thermal conductivity of SmB_6 FZ1 for a single run. Black line is extrapolation of $T > 0.5\,\mathrm{K}$ data to lower temperatures assuming a cubic temperature dependence.b. Experimental data at set temperature points from previous figure, calculating temperature difference between thermometers as a function of time. Black line: extrapolated y-intercept from the previous figure converted to temperature difference. Anticipating a hypothetical residual linear term in floating zone grown sample FZ1 assuming much longer settling times required to reach thermal equilibrium.

superconductors with two-dimensional Fermi surfaces but it may be naive to apply such a model to a TKI candidate with fermionic quasiparticles with a three-dimensional Fermi surface. More theoretical development is required to understand if and how such a model of phonon-quasiparticle decoupling may apply to SmB_6.

Nonetheless, the finite specific heat coefficient characteristic of bulk metals along with thermal conduction consistent with a bulk insulator is difficult to reconcile. Conventionally, Fermi liquid theories describe provide insight into how conduction electrons contribute to metallic-like properties. We will next discuss how such models can shed light on the nature of quasiparticles in the SmB_6 bulk, in particular by examining the scenario of metallic inclusions in an insulating bulk.

A scenario of n conduction electrons "puddles" in an insulating bulk can be modelled as a thermal circuit, such as that illustrated in Figure 5.12. In this scenario, the thermal resistances add in parallel and series,

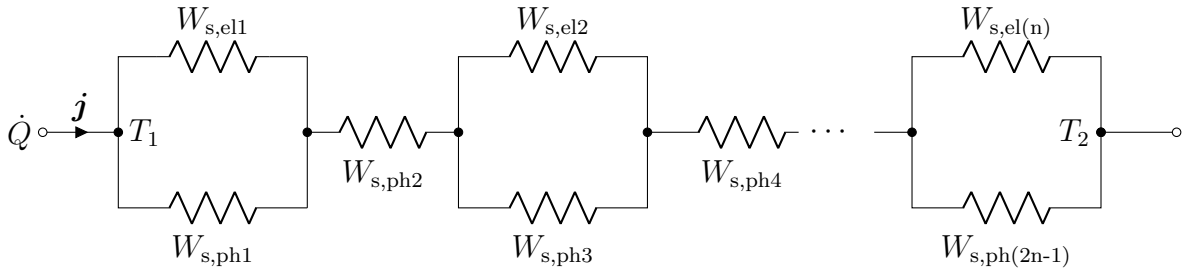


Figure 5.12: A circuit imagining thermal conduction with n number of electrically disconnected, metallic "puddles" with thermal resistance $W_{\text{s,el(i)}}$, along with continuous thermal resistance from phonons, $W_{\text{s,ph(i)}}$ throughout the sample. For simplicity, this circuit explicitly examines the thermal gradient between thermometers T_1 and T_2 while neglecting contact resistance as well as electron-phonon coupling. The boundary conditions are assumed to be an electrically conductive surface in parallel with phonon conduction.

$$\begin{aligned} W_{\text{tot}} &= \sum_{i}^{n-1}\left[\left(\frac{1}{W_{\text{s,el(i)}}}+\frac{1}{W_{\text{s,ph(2i-1)}}}\right)^{-1}+W_{\text{s,ph(2i)}}\right]+\left(\frac{1}{W_{\text{s,el(n)}}}+\frac{1}{W_{\text{s,ph(2n-1)}}}\right)^{-1} \\ &= \sum_{i}^{n-1}\left[\frac{W_{\text{s,el(i)}}W_{\text{s,ph(2i-1)}}}{W_{\text{s,el(i)}}+W_{\text{s,ph(2i-1)}}}+W_{\text{s,ph(2i)}}\right]+\frac{W_{\text{s,el(n)}}W_{\text{s,ph(2n-1)}}}{W_{\text{s,el(n)}}+W_{\text{s,ph(2n-1)}}} \end{aligned} \tag{5.6}$$

to sum to a total thermal resistance W_{tot}. In the limit that the disconnected "puddles" have identical thermal resistance, $W_{\text{s,el(1)}} = W_{\text{s,el(2)}} = ... = W_{\text{s,el(n)}} \equiv W_{\text{s,el}}$ as well as $W_{\text{s,ph(1)}} = W_{\text{s,ph(3)}} = ... = W_{\text{s,ph(2n-1)}} \equiv W_{\text{s,ph(puddle)}}$ and the insulating regions also have a constant thermal resistance, $W_{\text{s,ph(2)}} = W_{\text{s,ph(4)}} = ... = W_{\text{s,ph(2n-2)}} \equiv W_{\text{s,ph(insulating)}}$, Equation (5.6) simplifies to

$$W_{\text{tot}} = n\frac{W_{\text{s,el}}W_{\text{s,ph(puddle)}}}{W_{\text{s,el}}+W_{\text{s,ph(puddle)}}}+(n-1)W_{\text{s,ph(insulating)}}. \tag{5.7}$$

Such a scenario could be plausible if the density of conductive regions remains constant such that they are equally spaced out. This expression assumes that $n \geq 1$, given the electrically conductive outer surfaces that must be at the thermometer boundaries, given that such a surface state is well established in SmB_6. Simplifying Equation (5.7) in the low temperature limit using the Wiedemann-Franz law relation $W_{\text{s,el}}^{-1} \propto \gamma T$ and assuming a thermal

conduction of phonons in parallel, $W^{-1}_{\text{s,ph(puddle)}} \propto \beta T^3$, and in series, $W^{-1}_{\text{s,ph(insulating)}} \propto \beta' T^3$, then the total thermal conductance in the limit of $n = 1$ becomes

$$\begin{aligned} W^{-1}_{\text{tot,n=1}} &= \frac{W_{\text{s,el}} + W_{\text{s,ph(puddle)}}}{W_{\text{s,el}} W_{\text{s,ph(puddle)}}} \\ &\propto \frac{\gamma^{-1}T^{-1} + \beta^{-1}T^{-3}}{\gamma^{-1}\beta^{-1}T^{-4}} \\ &= \gamma T + \beta T^3. \end{aligned} \tag{5.8}$$

This scenario of $n = 1$ recovers the usual kinetic theory expression. The result of Equation (5.8) shows that the total thermal conductance, which is proportional to the thermal conductivity times a sample-dependent geometric factor, is equal to a sum of the individual thermal conductivity channels from phonons and electrons. In other words. $W^{-1}_{\text{tot,n=1}} \propto \kappa_{\text{tot}} = \kappa_{\text{el}} + \kappa_{\text{ph}}$ with $\kappa_{\text{el}} \propto T$ and $\kappa_{\text{ph}} \propto T^3$ as expected for a metallic material (the usual kinetic theory expression is discussed in Appendix A.2). Therefore, the case with a single region of electronic and lattice conductivity recovers the usual result for a material that is metallic in its bulk, though in the case of SmB_6, the coefficient of the linear term γ must be negligibly small due to the lack of observed residual linear term and the prohibitively large electrical resistance in the low temperature regime.

While this check verifies that Equation (5.7) is valid in the $n = 1$ limit, we are interested the $n > 1$ case where electrically conductive puddles are separated by electrically insulating regions, such as in Figure 5.12. For example, if $n = 2$, then using the same approach,

$$\begin{aligned} W^{-1}_{\text{tot,n=2}} &= \left[\frac{2W_{\text{s,el}}W_{\text{s,ph(puddle)}} + W_{\text{s,ph(insulating)}}(W_{\text{s,el}} + W_{\text{s,ph(puddle)}})}{W_{\text{s,el}} + W_{\text{s,ph(puddle)}}}\right]^{-1} \\ &\propto \frac{\gamma^{-1}T^{-1} + \beta^{-1}T^{-3}}{\gamma^{-1}(2\beta^{-1} + \beta'^{-1})T^{-4} + \beta^{-1}\beta'^{-1}T^{-6}} \\ &= \left(\beta' T^3 + \frac{\beta\beta'}{\gamma}T^5\right)\left(\frac{1}{1 + \frac{2\beta' + \beta}{\gamma}T^2}\right). \end{aligned} \tag{5.9}$$

In the low temperature limit, T is small, so the expression on the right simplifies to $(1 + \frac{2\beta' + \beta}{\gamma}T^2)^{-1} \approx 1 - \frac{2\beta' + \beta}{\gamma}T^2$. Using this result, to leading order in T, Equation (5.9) becomes

$$
\begin{aligned}
W_{\mathrm{tot,n=2}}^{-1} &\approx \beta' T^3 - 2\frac{2\beta'^2}{\gamma} T^5 + \mathcal{O}(T^7) \\
&\approx \beta' T^3
\end{aligned}
\tag{5.10}
$$

This result implies that when one region of phonon-only conduction disconnects two electrically conductive puddles, then phonon conduction dominates in the low temperature limit. Likewise, for general $n > 1$,

$$
\begin{aligned}
W_{\mathrm{tot,n}}^{-1} &= \left(\frac{n W_{\mathrm{s,el}} W_{\mathrm{s,ph(puddle)}} + (n-1) W_{\mathrm{s,ph(insulating)}} (W_{\mathrm{s,el}} + W_{\mathrm{s,ph(puddle)}})}{W_{\mathrm{s,el}} + W_{\mathrm{s,ph(puddle)}}} \right)^{-1} \\
&\propto \frac{\gamma^{-1} T^{-1} + \beta^{-1} T^{-3}}{\gamma^{-1} \left[n\beta^{-1} + (n-1)\beta'^{-1} \right] T^{-4} + (n-1)\beta^{-1}\beta'^{-1} T^{-6}} \\
&= \left[\frac{\beta'}{n-1} T^3 + \frac{\beta\beta'}{(n-1)\gamma} T^5 \right] \left[1 + \gamma^{-1} \left(\beta + \frac{n\beta'}{n-1} \right) T^2 \right]^{-1} \\
&\approx \left[\frac{\beta'}{n-1} T^3 + \frac{\beta\beta'}{(n-1)\gamma} T^5 \right] \left[1 - \gamma^{-1} \left(\beta + \frac{n\beta'}{n-1} \right) T^2 \right] \\
&\approx \frac{\beta' T^3}{n-1} \left[1 - \frac{n\beta'}{(n-1)\gamma} T^2 \right] + \mathcal{O}(T^7),
\end{aligned}
\tag{5.11}
$$

which is approximately equal to the thermal conductance of the insulating regions normalized by the number of conductive "puddles", $\beta' T^3/(n-1)$. Therefore such a scenario actually reduces the thermal conductance compared to the maximal phonon thermal conductivity in the boundary scattering limit. However, this is not consistent with the observations reported by Hartstein *et al.* [21] or those reported in Section 5.2, where the phonon conduction in zero field reaches the magnitude and scaling expected for this maximal limit. The analysis of this section reinforces that the simplest explanation of thermal conductivity observations in FZ1 and FZ2 must be phonons scattering by sample boundaries, as well as an intrinsic source of novel heat-conducting excitations that are enhanced by an applied magnetic field. These novel excitations may also be present in the disordered FZ3, but the presence of additional phonon scattering with extrinsic disorder could complicate interpretations of intrinsic heat-conducting excitations.

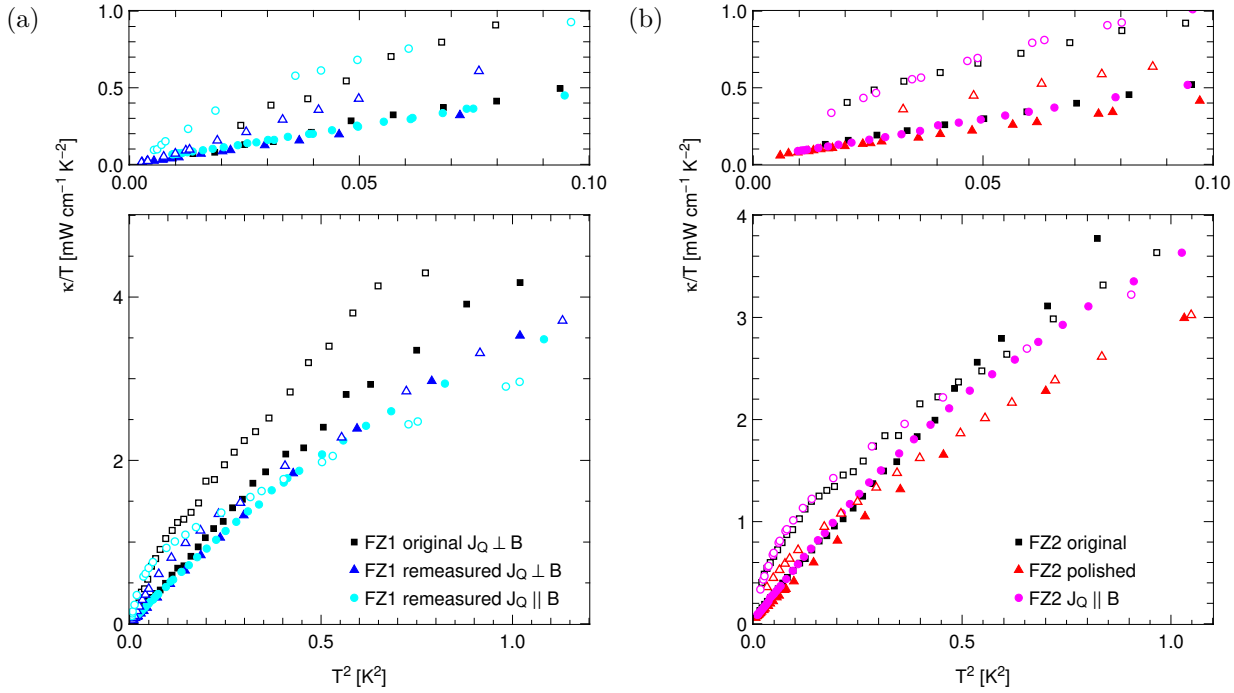


Figure 5.13: Comparisons of thermal conductivities for (a) FZ1 and (b) FZ2 SmB_6 samples, with solid symbols in zero field and empty symbols in a 12 T field, plotted as κ/T versus T^2. Insets are scaled to show the lowest temperature ranges.

5.2.5 Comparison of results among identical samples

The thermal conductivity is expected to give identical results amongst identical samples in the same environmental conditions, noting that the change in sample geometric factor from remounting sample contacts for samples FZ1 and FZ2 introduces a systematic error that can scale the results by a common factor. In this section, we will compare the remeasured thermal conductivity to the original published data for each sample.

Figure 5.13 shows the thermal conductivity for the different field orientations for each sample. The FZ1 low temperature results are consistent within the systematic error of the uncertainty in the geometric factor, but the original results at times show a higher thermal conductivity at the higher temperatures. Moreover, the FZ2 zero field results for identical geometries is comparable without the need for scaling geometric factors. The polished geometry for FZ2 also has a real lower thermal conductivity contribution from phonons alone due to its smaller geometry hence does not match up with the original geometry measurements in zero field.

5.3 Magnetostriction

5.3.1 Dilatometer setup

We use the capacitive dilatometer described in Section 3.2 to measure the magnetostriction of SmB_6 floating zone grown sample 1 (FZ1). The sample is mounted in the dilatometer by securing one end to the copper mount by silver epoxy, and the opposing end pushes on the sapphire rod shown in Figure 3.3. The length of the sample, which is oriented to the [100] crystallographic axis, is parallel to an applied magnetic field. The edge connecting with the sapphire rod is slightly slanted, which could result in some slight misalignment of the magnetostriction measurement from the [100] axis.

We took care to reduce error in measurement results. Decreasing the plate separation increases the sensitivity of the capacitance to changes in sample length. An initial cooldown allows us to estimate the thermal contraction or expansion of the sample from room temperature to the temperatures of interest for magnetostriction measurements, to attempt to achieve a high sensitivity without shorting the capacitance plates of the dilatometer upon cooldown. Assuming parallel plates, we were able to achieve a plate separation at room temperature of 72.5 µm, which decreased by 22.1 µm upon cooling to 53 mK. The corresponding capacitances are listed in Table 5.3, using Equation (3.17) to convert capacitances to parallel plate separations. We attempted to decrease the plate separation in order to increase the sensitivity to an oscillatory magnetostriction, reading a higher capacitance of $\sim$ 35.95 pF at room temperature but the plates shorted below 117 K at a maximum capacitance of 54.21 pF, suggesting aparallel plates. Using Equation (3.18), a maximum capacitance of 54.21 pF equates to an off-center tilt $a = 36.9$ µm and an effective plate separation of 40.1 µm at room temperature. The "aparallel" plate separations in Table 5.3 are calculated assuming a maximum capacitance of 54.21 pF. It's possible that the sample mounting process between cooldowns may have introduced a tilt, and the quantitative behaviour of oscillations in magnetostriction would be independent of the background plate separation calculation approach. Hence for consistency, the calculation of plate separation in the magnetostriction results assumes parallel plates.

Any real signal should be resolved regardless of averaging approach or sampling frequency over time. In Figure 5.14a, the capacitance and temperature log over a period of over an hour in zero applied field is shown. The deviation in capacitance in this data is larger than the least significant digit detectable by the bridge. To increase the precision in capacitance measurement, we sample points by sitting at each field step, letting the points settle for a short amount of time before measuring and averaging the capacitance over a larger number of points, resulting in a standard deviation in plate separation of

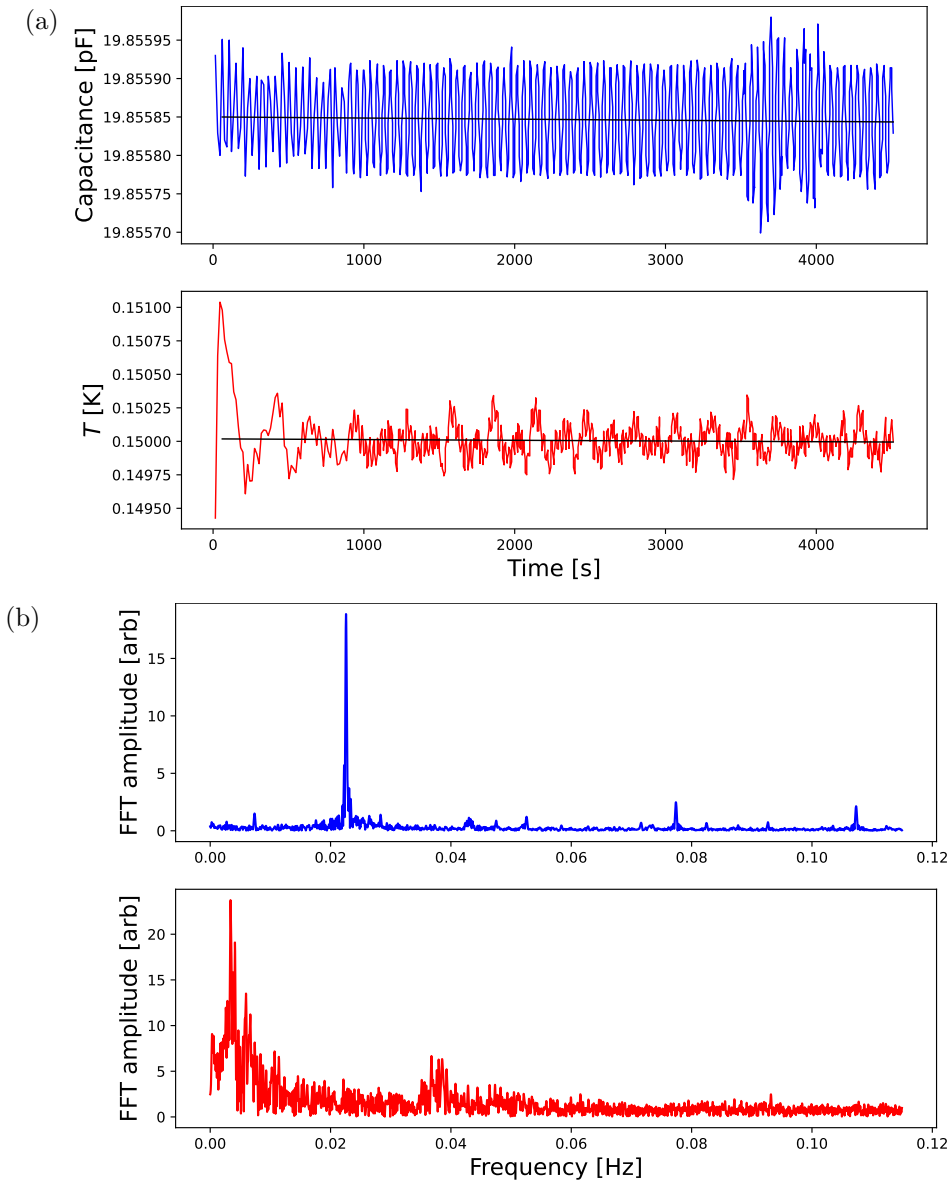


Figure 5.14: (a) SmB_6 FZ1 dilatometer capacitance measurement at a set temperature $T = 150$ mK in zero field as a function of time. (b) Fast Fourier transform amplitudes for the above capacitance (blue) and temperature (red) measurements.

Temperature	Capacitance (pF)	$D_{\parallel}$ (µm)	D_{tilt} (µm)
(a) Room temperature	13.80	72.5	77.2
53 mK	19.85	50.4	57.2
(b) Room temperature	35.95	27.8	40.1
117.2 K	54.21	18.5	36.9

Table 5.3: Dilatometer capacitance, converted to a plate separation assuming parallel plates $D_{\parallel}$ and assuming aparallel plates D_{tilt} at (a) room temperature and 53 mK, and after readjustment at (b) room temperature and 117.2 K, responding to the thermal expansion of SmB_6 FZ1.

$\sim 0.04 - 0.09$ Å. Any noisy points registering zero capacitance are also removed and the data point is then reaveraged before analysing the Fast Fourier Transform (FFT) of the data. We also separate field steps so they are evenly spaced in inverse field to ensure an evenly spaced sample for the FFT, though we also apply a padding factor prior to the transform to increase the number of points by interpolation to ensure we are not biasing the transform frequencies based on the spacing of the points.

We also want to make sure that any oscillations resolved are not due to any background electromagnetic signal that has periodicity with respect to time. Figure 5.14a shows a sampling of oscillatory capacitance over time, as well as the periodicity in the temperature control at 150 mK, keeping the magnetic field off. Figure 5.14b shows the FFT frequencies of these samplings. The capacitance data shows a peak at frequency 0.0225 Hz and the temperature control shows a peak at 0.0034 Hz. If any oscillations in temperature control exist, they do not seem to appear as oscillations in the capacitance, which is understandable given the relatively small change in thermal expansion for a temperature change of less than 1 mK. Moreover, by sitting at each field point for $\sim 5 - 10$ minutes, the periods in capacitance that are on the order of ~ 45 s would be averaged in the magnetostriction data. Hence we have taken precautions to ensure that any capacitance changes measured correspond to a change in sample length. We will next discuss the oscillatory magnetostriction results.

5.3.2 Quantum oscillations in magnetostriction

To further investigate the nature of the SmB_6 bulk, we use the bulk measurement of magnetostriction. Quantum oscillations in torque magnetization are related to those in magnetostriction in Landau theory by [135].

$$\frac{\partial \ln A}{\partial \sigma_i} = \frac{\partial \ln F}{\partial \sigma_i} = -\frac{\epsilon_i}{\tau}\frac{\partial \ln F}{\partial \theta} \tag{5.12}$$

where A is the extremal cross-sectional area of the Fermi surface normal to the field direction, $F = \hbar A/2\pi e$ is the dHvA frequency and $\frac{\partial \ln A}{\partial \sigma_i}$ is the derivative of the stress in the direction of the measurement ϵ_i, τ is the oscillatory torque magnetization. Equation (5.12) removes the amplitude dependence, such that the oscillatory magnetostriction and the oscillatory torque are most simply related by a constant. Measurements of oscillatory magnetostriction complement those in torque magnetization to reach a conclusion on the origin of the oscillatory signal, hopefully settling the debate on whether the signal originates from the surface of the material or the bulk. In order to compare results to expectations, we can use the oscillatory magnetostriction results in metallic LaB_6 and PrB_6 to make some assumptions about an expected signal, given that their Fermi surfaces are comparable to the quantum oscillation frequencies found in SmB_6 by Hartstein *et al.* [21].

Figure 5.15a shows the oscillations plotted as the plate separation versus inverse magnetic field. The plate separation — and sample length — decreases by about 3 Å as the field increases from 9.5 T to 12 T. This is only an order of magnitude larger than the standard deviation in each averaged plate separation point. Neglecting the data extremities, the black line in the figure shows a linear fit to model the non-oscillatory magnetostriction. After subtracting the background in this field range, the oscillatory amplitude is plotted as $\Delta L/L$ for sample length $L \sim 1.27$ mm at room temperature, as reported in Table 5.1. With a background-subtracted oscillatory change in length of ~ 0.3 Å, we are unable to resolve an amplitude larger than the standard deviation in each data point of ~ 0.1Å, implying a signal to noise ratio of ~ 10, lower than ideal. Nonetheless, we can still analyse the oscillatory magnetostriction to compare the frequencies of oscillation with previous findings. Figure 5.15c shows the oscillation frequencies and amplitudes after applying a FFT to the background-subtracted oscillatory magnetostriction. The oscillation with the largest amplitude appears at the lowest frequency, 0.94 kT. Then, two high frequency peaks are resolved at 9.3 and 12.3 kT. We will next discuss the analysis of these results.

The oscillatory longitudinal magnetostriction in the [100] direction $\tilde{\varepsilon}$ is related to the oscillatory magnetization $\tilde{M}$ as

$$\tilde{\varepsilon}_{[100]} = -\left(\frac{\partial \ln F}{\partial \sigma_{[100]}}\right)\tilde{M}H \tag{5.13}$$

where the first term is related to the change in Fermi surface volume with respect to stress [8]. Most simply, for our observations to be consistent with LK theory, quantum

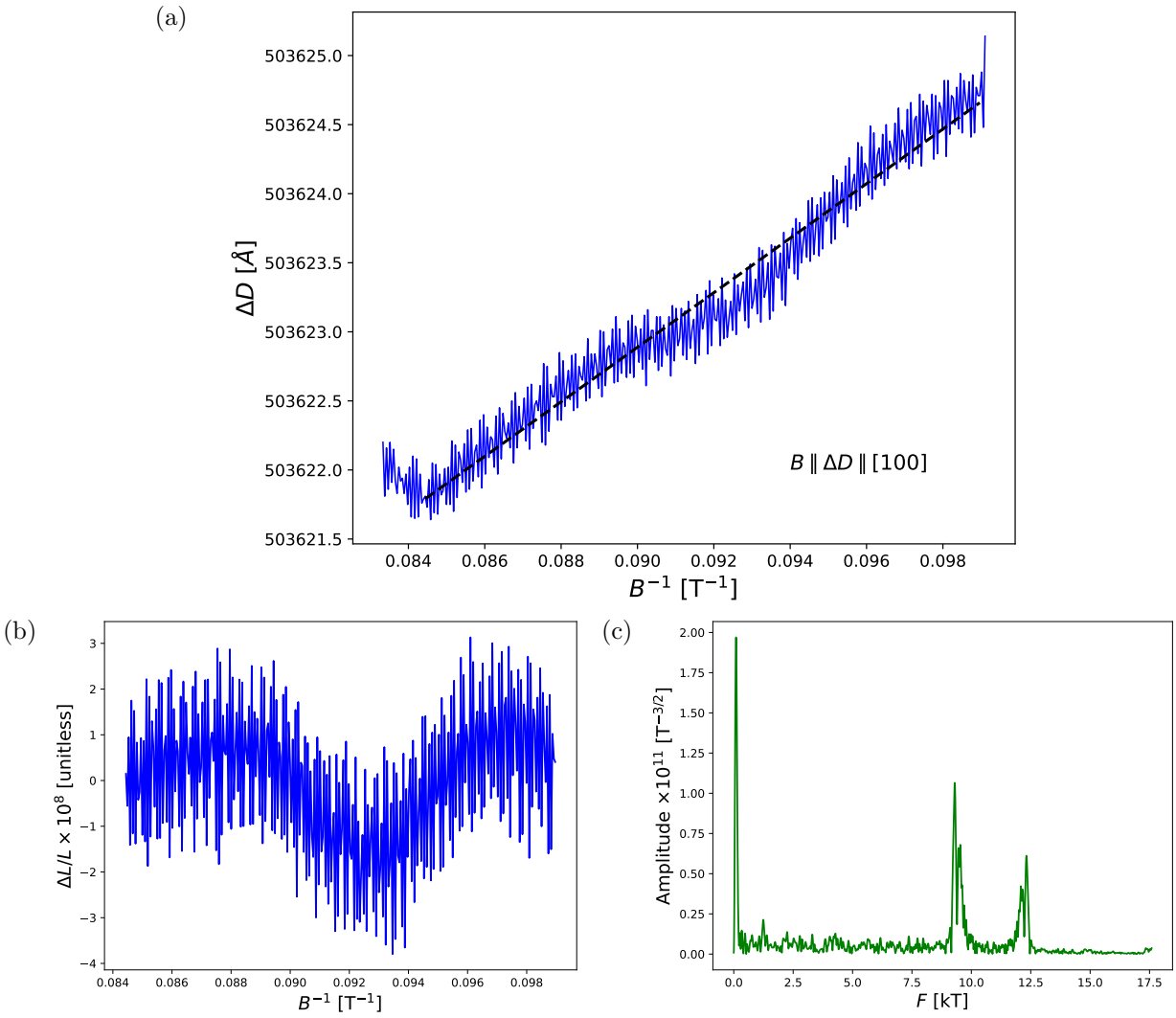


Figure 5.15: Oscillatory magnetostriction in SmB_6 FZ1 from 12 T to 9.5 T at 50 mK. (a) Plotted as the plate separation measurement with respect to inverse field (blue), and a background fit to a linear equation (black dashed). (b) Plotted as the background-subtracted plate separation normalized by the sample length of 1.27 mm. (c) Amplitudes and frequencies of the FFT transform.

oscillation frequencies should be directly comparable between these two measurements. The 94 T frequency could be consistent with the lowest frequency ρ' band reported for SmB_6, with a minimum frequency of 31 T and a maximum of $\sim 10^2$ T. The highest two frequencies we report, 9.3 and 12.3 kT, are within the range of the high frequency α band oscillations reported by our collaborators with a minimum frequency ~ 8 kT and a maximum frequency ~ 11 kT for a field orientation along [100] [17, 21]. Slight deviations in frequencies from dHvA reports for the [100] orientation are expected due to the possibility that the SmB_6 FZ1 sample is marginally tilted with respect to the applied field direction in the dilatometer mount. Despite this possibility, we can gain information by comparing the frequencies of oscillatory magnetostriction to those reported in dHvA measurements. First, assuming LK theory applies, the lowest frequency ρ' band is equivalent to a small Fermi surface area, which means that strain effects can influence its relative change in area more obviously than higher frequency (lower area) bands. This would show up as a larger term $\partial \ln F/\partial\sigma_{[100]}$, increasing the amplitude of the oscillations originating from this band in magnetostriction results. This is comparable to the reports of magnetostriction of LaB_6 in Figure 5.16a, where the small neck orbits of the ρ' band in LaB_6 contribute the largest to the oscillatory magnetostriction, and the large amplitude and low frequency compared to PrB_6 indicates a smaller Fermi surface area of this band that is more sensitive to strain effects [27]. Even though both materials have higher frequency orbits in the magnetization, these aren't necessarily resolved in the magnetostriction. It is perhaps not surprising then to resolve the lowest frequency band reported for SmB_6 in magnetostriction but not intermediate frequency bands, particularly in the limited field range of observation. In addition, a two-dimensional version of this low frequency band is observed by Li *et al.* in torque magnetization of flux-grown samples, corroborating the existence of quantum oscillations in this band across different samples [102].

We can estimate any extremal cross-sectional area of a Fermi surface perpendicular to the field for each band using the oscillation frequencies by $F = (\hbar/2\pi e)A_F$ then, assuming a circular area, we can approximate the Fermi wavevector as $k_F = \sqrt{A_F/\pi}$. The wavevectors for the three main oscillations in Fig. 5.15c are listed in Table 5.4. They are within the expected values reported by Hartstein *et al.* [21] after accounting for eccentricity of the Fermi surface area that can deviate from a circle. Hence we have identified frequencies that are consistent with the ρ' and α bands through a comparison to the three-dimensional torque magnetization results reported by our collaborators.

The order of magnitude of the extremal oscillatory magnetostriction amplitude in this field range is within the realm of typical magnetostriction results. It is smaller than for LaB_6, which has a reported $\Delta L/L \sim 2 \times 10^{-7}$ at 4 T (Fig. 5.16a). However the order of magnitude of oscillatory magnetostriction for SmB_6 is still on par with other oscillatory

magnetostriction measurements such as for PrB_6 (Fig. 5.16b). The amplitude of oscillations is related to the lower amplitude of the magnetization oscillations in this field range, which is approximately $\tilde{M} \sim 10^{-5}$ μ_B/Sm [21]. Converting this to different units using the volume of the unit cell, which contains one Sm ion per unit cell, this is equivalent to $\tilde{M} \sim 1.31$ A m^{-1}. We can estimate the order of magnitude of the deformation parameter $\partial \ln F/\partial \sigma_{[100]}$ with Equation (5.13), using an oscillatory amplitude $\Delta\tilde{L}/L \sim 2 \times 10^{-8}$. Then, at an applied field of 12 T, we estimate an order of magnitude of deformation 1×10^{-9} m^2 N^{-1} for the largest amplitude oscillations associated with the ρ' orbits. This is on par with the deformation of bismuth and is larger than the deformation parameter for these "neck" orbits of metals including copper, silver and gold [7, 8]. This parameter is also related to the Young's modulus Y and Poisson's ratio α for the material. If we assume a spherical Fermi surface, then this deformation parameter in the limit of uniaxial tension σ per unit area is

$$\frac{\partial \ln F}{\partial \sigma} = -\frac{2}{3}(1-\alpha)Y \tag{5.14}$$

where the above expression especially agrees with the order of magnitude of this parameter for the bellies of noble metals but is empirically smaller for the neck orbits [7]. Though the elastic parameters are anisotropic for SmB_6 we can compare the estimate of this deformation parameter from elastic constant expectations to the above estimate. Using elastic parameters in the low temperature limit for SmB_6 [136], Equation (5.14) gives $\partial \ln F/\partial \sigma \sim -2 \times 10^{-12}$ m^2 N^{-1}, which is slightly smaller than the estimate from the oscillatory magnetostriction, a typical discrepancy for the neck orbits. Conversely, we do not see evidence for a unusually large amplitude ~ 330 T frequency oscillation as was reported for the torque magnetization. The dependence of oscillatory magnetostriction on the stress dependence of the Fermi surface, $\left(\frac{\partial \ln F}{\partial \sigma_{[100]}}\right)$, could partly explain this difference in measurement techniques. Oscillations in magnetostriction shows up best in smallest Fermi surfaces due to the larger change in the Fermi surface area in response to stress, with the lowest frequency (and smallest area) oscillations more readily appearing in magnetostriction [8]. The lowest frequency ρ' does appear to have the largest amplitude oscillations in our results, consistent with this observation. However, this lowest frequency must be interpreted with extreme caution as the field range of Figure 5.15a spans less than two periods for this FFT result. Measurements of the oscillatory mangetostriction across a broader field range could help gain confidence in the lowest frequency FFT peak. Moreover, we expect the oscillatory amplitude to be larger in fields above 12 T based on the field-dependence of the oscillatory amplitude. Experiments at higher fields could more readily resolve amplitude effects. Nonetheless an oscillatory magnetostriction observed using the capacitive dilatom-

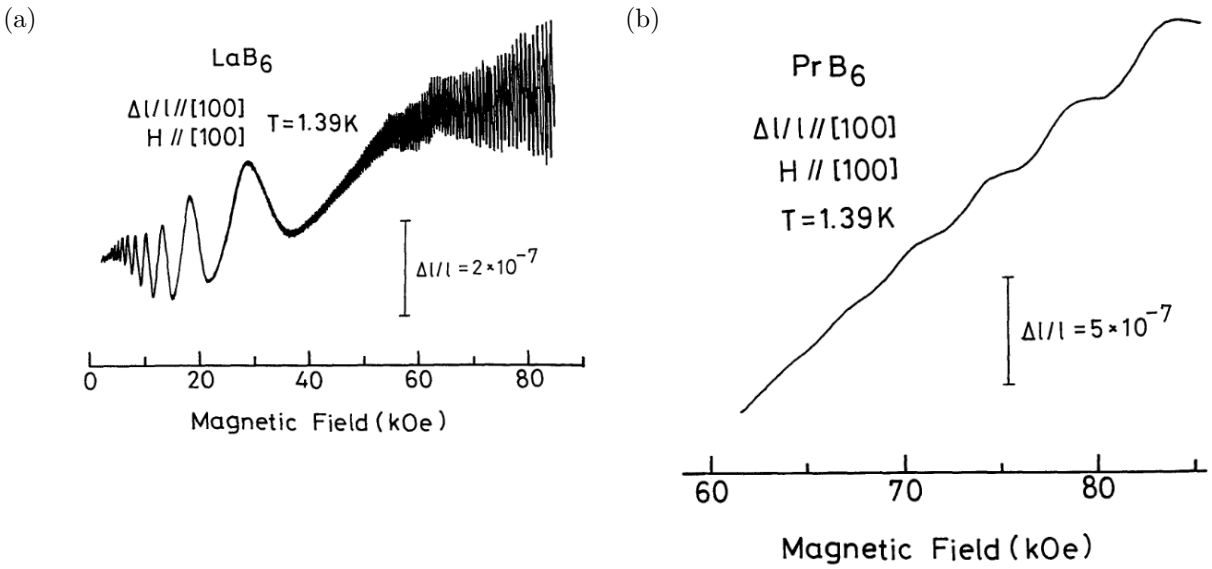


Figure 5.16: Oscillatory magnetostrictions of metals (a) LaB_6 and (b) PrB_6 in a longitudinal [100] applied field, by Sera *et al.* [27]. The background-subtracted oscillatory amplitude of LaB_6 is of the order $\Delta L/L \sim 2 \times 10^{-7}$ whereas the amplitude of oscillations for PrB_6 is a fraction of this value in the field range of $4 - 8$ T. ©1988 *The Physical Society of Japan.*

etry technique implies a bulk origin for the quantum oscillations. Next we will discuss implications of this preliminary confirmation of bulk quantum oscillations in SmB_6.

5.3.3 Characterizing quasiparticles in SmB_6

Given this preliminary finding of quantum oscillations in the magnetostriction of bulk insulating SmB_6, the interpretation of such a result defies conventional LK theory, which assumes the presence of a Fermi surface that is not usually associated with insulators. Yet, many leading theories invoke a charge-neutral Fermi surface to explain emerging reports of quantum oscillations in the bulk of TKI candidates. The following section assumes a charge-neutral Fermi surface and applies LK theory to attempt to reconcile properties across different measurements.

Reported carrier densities of SmB_6 frustratingly differ between different experimental reports, which has complicated a consensus on this quasiparticle characteristic [124]. In particular, a plurality of reports assume a two-dimensional carrier density arising from the metallic surface states of this TKI candidate. On the other hand, our observations of an

Band	F (kT)	k_F (nm^{-1})	n_{3D} (cm^{-3})
ρ'	0.094	0.54	5×10^{18}
α	9.3	5.3	5×10^{21}
α	12.3	6.1	8×10^{21}

Table 5.4: Parameters adapted from Fourier transform peaks in Figure 5.15c, using LK theory: the frequencies of the peaks F_i, the Fermi wavevectors k_F and the corresponding carrier density for an approximately spherical Fermi surface n_{3D}.

oscillatory magnetostriction cannot be reconciled with charge carriers only located at the sample surface. We can convert the oscillation frequencies to carrier densities, assuming a 3D carrier density due to earlier arguments about carriers being present in the bulk for magnetostriction oscillations. Then naively, relation is $n_{3D} = k_F^3/(3\pi^2)$ [8]. The resulting carrier densities are in Table 5.4. Suppose these quasiparticle excitations with this carrier density are responsible for the enhanced thermal conductivity in field.

While the carrier density is simply an estimate that assumes isotropic Fermi surfaces, if (charge-neutral) Fermi surfaces are the source of the bulk quantum oscillations, then the quasiparticles responsible for the dHvA effect should also appear across different measurements. We can directly compare the quasiparticle transport to the quantum oscillations using an estimate of the carrier density. The enhanced thermal conductivity (above the phonon contribution in zero field) for FZ2 in Figure 5.8b fits to $\Delta\kappa_{\mathrm{FZ2}} \sim A + BT$ below 0.4 K, with the fits in Figure 5.17 and parameters listed in Table 5.5. In Chowdhury *et al.*'s composite exciton theory, the coefficient of the linear enhancement of thermal conductivity corresponds with a constant akin to the Wiedemann-Franz law, with the total summation over the two pockets that contribute to composite excitons in this theory [see Eq. (4.8)]. The mean free paths are unknowns in this model, but would be expected to scale with sample diameters if the carriers originate from the bulk, which appears to be approximately the case for FZ2 and FZ2p as shown in the inset to Figure 5.8b and is reflected in the ratio of the B parameters in the linear fit. If this constant slope corresponds to the prediction of Chowdhury *et al.*, it could be that not all of the orbits contributing to dHvA oscillations would contribute to the enhancement of thermal conductivity despite them seemingly all contributing to the linear coefficient of the specific heat capacity (see Hartstein *et al.* for analysis of torque magnetization, thermal transport and specific heat [21]). Despite the scaling of the enhanced thermal conductivity with sample size, the corresponding mean free paths derived using dHvA parameters for the Fermi surfaces are much smaller than the sample boundaries, instead being of comparable size to the mean free path derived from the Dingle damping factor, which is independent of sample size. Perhaps then the

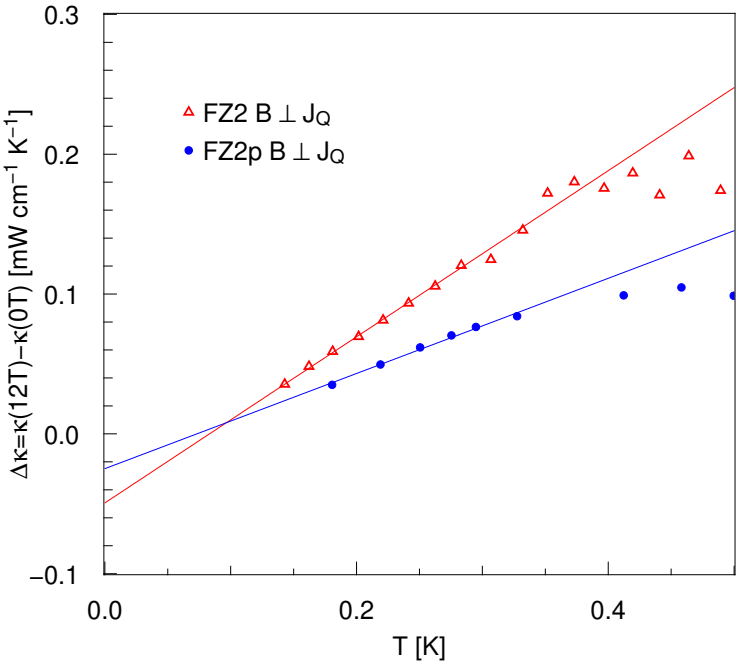


Figure 5.17: Thermal conductivity enhancement above phonon contribution for samples FZ2 (red) and FZ2p (blue) in a transverse 12 T field, with lines representing linear fits to $\kappa = A + BT$ below 0.4 K.

mean free path of quasiparticles that contribute to thermal conductivity may have a sample dependence that obscures interpretations, or the exotic bulk phenomena reported in this chapter isn't captured by the usual understanding of Fermi liquid theory.

Sample	A (mW cm^{-1}K^{-1})	B (mW cm^{-1}K^{-2})
FZ2	−0.05	0.59
FZ2p	0.02	0.34

Table 5.5: Parameters for a linear fit $\Delta\kappa = A + BT$ of the enhanced thermal conductivity $\Delta\kappa = \kappa(12\text{ T}) - \kappa(0\text{ T})$.

5.4 Summary of SmB_6 results

Topological Kondo insulator candidates, including SmB_6, have emerging reports of exotic bulk insulating behaviour as introduced in Chapter 4. In Chapter 5, we report measurements that are consistent with such exotic behaviour in the insulating bulk of single crystal SmB_6 samples. Namely, we report additional evidence of a thermal conductivity enhancement above phonon conduction in an applied magnetic field and we report preliminary evidence of bulk quantum oscillations in magnetostriction. Adding to the literature on this exotic behaviour, we attempt to settle a debate over whether such phenomena are intrinsic properties of the material or are extrinsic artifacts from sample disorder that's introduced in the sample preparation process.

Our results and subsequent analysis strongly suggest that the exotic bulk phenomena of charge-neutral, delocalized excitations and quantum oscillations — as observed in our studies under the application of a magnetic field — are inherent properties of high quality SmB_6 samples. We use thermal conductivity analysis to show that this enhancement is most obvious in samples that have minimal metallic inclusions or point defects, such that the thermal conductivity in zero field reaches the magnitude and scaling associated with phonon scattering by sample boundaries. In such samples, the enhanced thermal conductivity that is observed in an applied field cannot be attributed to a reduction in phonon scattering. Conversely, we show how a floating zone grown sample with stronger disorder in the bulk, as evidenced by a lower peak thermal conductivity, has a low-temperature thermal conductivity that remains below this maximal limit of phonon scattering by sample boundaries. The thermal conductivity remains below this limit even in an applied magnetic field, obscuring whether such an enhancement is due to a reduction in phonon scattering, additional contributions from novel delocalized excitations, or a combination thereof. The results of this thesis highlight the need to consider sample quality when interpreting thermal conduction by novel delocalized quasiparticles.

Given the large electrical resistivity of topological Kondo insulator candidates, the delocalized excitations contributing to the enhanced thermal conductivity in SmB_6 must be charge-neutral, as previously proposed in Hartstein *et al.* [21]. However, alternative interpretations of experimental results from similar studies by other groups call into question the complementary proposal by this group that dHvA oscillations in SmB_6 originate from the electrically insulating bulk of similarly grown high quality samples [92]. We address this question by measuring the oscillatory magnetostriction of floating zone grown sample FZ1, which has a thermal conductivity consistent with expectations of a high-quality insulator [20, 21, 24]. Considering of the expected magnitude of signals of the capacitive dilatometer technique, an observable oscillatory magnetostriction signal must originate from the bulk

of the sample. We report preliminary measurements of an observable oscillatory magnetostriction amplitude in SmB_6 using this technique, including high frequency oscillations within the range of those reported in the oscillatory magnetization by our collaborators [17, 20, 21]. In contrast, an oscillatory amplitude would be too small to detect using our measurement approach if the signal originates exclusively from a metallic surface state, implying that our findings are inconsistent with the surface origin of dHvA oscillations proposed by the Michigan group [92, 97, 102]. Instead, our magnetostriction results corroborate evidence of exotic metal-like behaviour in the bulk of SmB_6 and highlight the need for continued work on theories of bulk quantum oscillations in correlated insulating materials.

Part III

Quantum spin ice

Chapter 6

Quantum spin ice literature

Spin ice materials can evade long range magnetic ordering. This is a realization of Ising anisotropy in a geometrically frustrated system, meaning each magnetic moment chooses one of two possible directions. To illustrate this concept, imagine an equilateral triangular lattice in two dimensions with the spins confined to point up or down as in Figure 6.1, with a nearest-neighbour antiferromagnetic exchange interaction such that neighbouring spins are predisposed to anti-align. However, on a triangular lattice, only two spins can satisfy this condition, leaving the third frustrated. Such a frustration can lead to exotic magnetic phases. This concept can be applied in three dimensions to a tetrahedral structure.

Originally, Anderson proposes a geometrically frustrated model of corner-sharing tetrahetra on a diamond lattice with spins constrained to a local Ising anisotropy and a nearest-neighbour ferromagnetic exchange interaction [137]. In Anderson's model, magnetic moments on this lattice with a ferromagnetic exchange interaction order below a critical temperature, as illustrated in Figure 6.2a. In contrast, magnetic moments with an antiferromagnetic exchange interaction — meaning the spins are predisposed to anti-align with nearest-neighbours — lack magnetic ordering in the ground state (Fig. 6.2b). However Bramwell and Harris [28] note that the Ising constraint is only satisfied on this lattice if the spins are constrained to the local $\langle 111 \rangle$ Ising direction such that they point either into or out of a corner-sharing tetrahedron, and the disordered ground state counterintuitively occurs with a local ferromagnetic exchange interaction, as shown in Figure 6.2c, whereas a local antiferromagnetic exchange leads to antiferromagnetic order (Fig. 6.2d). They use this "spin ice" model to explain the lack of ordering in the pyrochlore $Ho_2Ti_2O_7$ which does not show characteristic signs of ordering despite having a ferromagnetic exchange coupling.

The ground state ordering possibilities in such a model depends on the crystal field

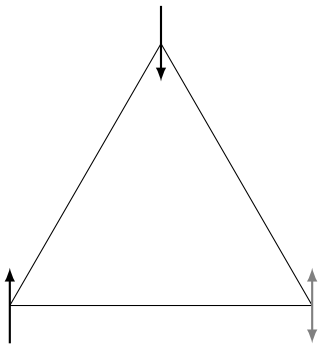


Figure 6.1: Illustration of frustration on a triangular lattice with a nearest-neighbour antiferromagnetic exchange interaction. If the spins are confined to pointing up or down on this lattice, only two of the three spins can satisfy the antiferromagnetic condition, leaving the third arrow (gray) with two equally unsatisfactory potential configurations.

symmetries and strengths of the magnetic moment. First, we will introduce the classical spin ice ("CSI") model which is realized in pyrochlore lattices with a large magnetic moment along the local $\hat{z}$ axis. Then, we will extend the CSI model to the case where the transverse components of the magnetic ion are of non-negligible strength in relation to the local $\hat{z}$ component to introduce the theoretical quantum spin ice ("QSI") ground state. The interested reader is referred to the book "Spin Ice" (2021) for an in-depth overview [138]. Finally, we will briefly discuss experimental studies in quantum spin ice candidates to motivate the following chapter on experimental results in $Pr_2Hf_2O_7$.

6.1 Classical spin ice

6.1.1 Ice rules

The frustrated tetrahedral structure in Figure 6.2c demonstrates a configuration with two spins oriented towards the center of the tetrahedron and two spins oriented away from the center, minimizes the local energetic constraints. This is an example of a minimal energy configuration imposed by the crystal electric field. On a macroscopic scale, the frustrated lattice described by Bramwell and Harris [29] is minimized by orienting the spins such that two point into each tetrahedron and two point out, following a constraint known as the "ice rule". This spin ice structure is a realization of a frustrated tetrahedral structure analogous to that anticipated for its namesake, water ice. In its ground state, this configuration of

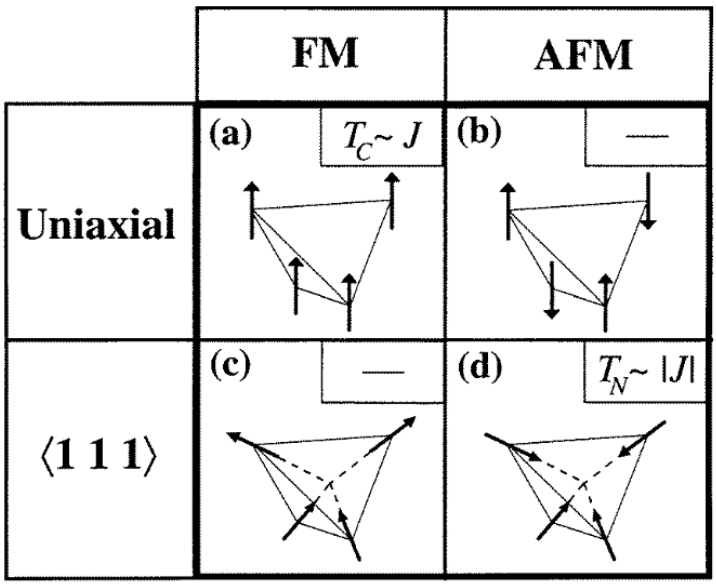


Figure 6.2: Bramwell and Harris [28] map Anderson's model onto a pyrochlore lattice of corner-sharing tetrahedra with ⟨111⟩ Ising anisotropy. (a) Anderson's model of a uniaxial Ising constraint orders at $T_C \sim J$ for magnetic moments with a nearest-neighbour ferromagnetic (FM) exchange interaction and (b) lack ordering with an antiferromagnetic (AFM) exchange interaction. In Bramwell and Harris' model, a local ⟨111⟩ constraint results in (c) a disordered two-in/two-out ground state with a FM interaction and (d) an ordered all-in/all-out state at $T_N \sim |J|$ with an AFM interaction. © *IOP Publishing. Reproduced with permission. All rights reserved.*

(a) (b)



Figure 6.3: (a),(b): Illustration of the "ice rule" for H_2O and a tetrahetron respectively, adapted from Bramwell *et al.* [29]. Each oxygen atom is strongly bonded to two hydrogen atoms (solid lines) and weakly bonded to two hydrogen atoms (dotted lines), forming a tetrahedral structure.

water ice can be described on a tetrahedral lattice as shown in Figure 6.3a, where each oxygen atom forms strong covalent bonds with two adjacent hydrogen atoms and weak hydrogen bonds with two next-nearest-neighbour hydrogen atoms, such that the electric dipolar moments of H_2O follow the ice rule identified by Bernal and Fowler [29, 139–141]. The relative strength of the chemical bonds in the ice crystal, where the molecules are frozen in a tightly packed structure, also has a tetrahedral structure with electric dipolar moments at the tetrahedron corners in a two-in/two-out structure as illustrated in Figure 6.3b. Macroscopically, due to these ice rules, the degeneracy of the spin ice ground state results in a residual "Pauling" entropy [137]. This ground state is degenerate with six out of the sixteen possible configurations of a tetrahedron satisfying the two-in/two-out spin orientation. Hence the total number of macrostates for N tetrahedra has an upper bound of $\Omega \leq 2^{2N}\,(6/16)^N = (3/2)^N$ giving a residual entropy of $S_0 = k_{\mathrm{B}} \ln(\Omega) = N k_{\mathrm{B}} \ln(3/2)$ or Pauling's entropy [140]. The unique microstates are illustrated in a square lattice analogue in Figure 6.4. The spins cannot uniquely satisfy the nearest-neighbour effective interactions due to their geometry, leading to the prediction of a residual entropy on a macroscopic scale. The dipolar spin ice Hamiltonian encompasses a more fulsome picture of the competing dynamics of such spins for multiple tetrahedra with the Ising anisotropy constraint, while including not just local exchange interactions but also the effect of the dipole moment on neighbouring spins.

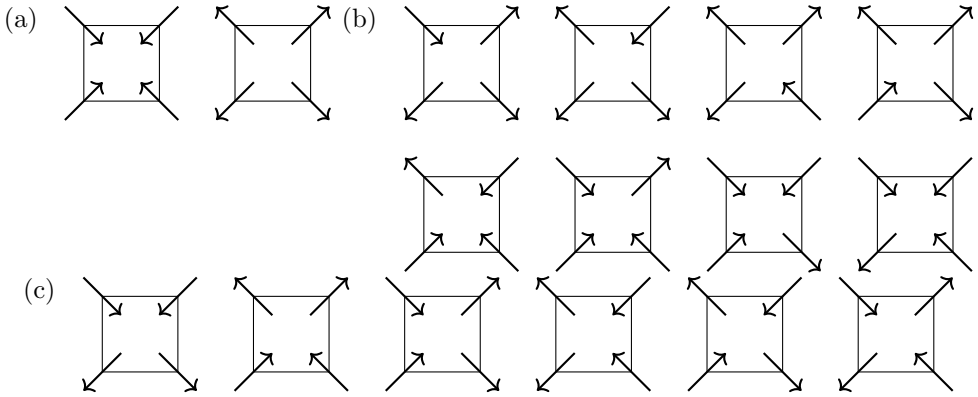


Figure 6.4: Possible configurations of frustrated spins on a square lattice, to represent microstates of a tetrahedron. (a) Illustration of an all-in state and an all-out state (b) Four states with a "one-in three-out" spin configuration and four states with a "three-in/one-out" spin configuration (c) Six states with a "two-in/two-out" spin configuration.

6.1.2 Dipolar spin ice model

Geometrical frustration in magnetism can result in spin ordering in the ground state. Simply in the case of a classical dipole moment, each spin can point in one of two directions (ie. up or down), and depending on the geometry, the energy is minimized in the ground state for certain microstates in each lattice unit giving rise to long range magnetic phases. For example the Ising Hamiltonian for Ising spins $\boldsymbol{\sigma}_i$, $\boldsymbol{\sigma}_j$ on nearest-neighbour sites i, j

$$\mathcal{H}_{\text{Ising}} = J \sum_{\langle ij \rangle} \boldsymbol{\sigma}_i \cdot \boldsymbol{\sigma}_j \tag{6.1}$$

is minimized when nearest-neighbour spins are (anti)aligned for a (anti)ferromagnetic exchange interaction $J < 0$ ($J > 0$). While a form of this Ising Hamiltonian can simply apply to spin ice, the microscopic interactions are more complex leading to a range of ground states depending on dipolar and pseudospin exchange interactions. Spin ice can evade magnetic ordering in its ground state despite nearest-neighbour ferromagnetic interactions due to the relative positions of the spins. This frustration gives rise to novel magnetic excitations that are described by the dipolar spin ice model.

In the dipolar spin ice model, magnetic moments are confined to either point into or out of each tetrahedron along the local Ising $\langle 111 \rangle$ axis due to the symmetry imposed by the crystal field at the rare earth lattice sites [142]. The dynamics of interactions with

this single ion anisotropy restriction are described in the dipolar spin ice model by the Hamiltonian [140]

$$H_{\text{dip}} = -J \sum_{\langle i,j \rangle} \boldsymbol{S}_i^z \cdot \boldsymbol{S}_j^z + D r_{\text{nn}}^3 \sum_{i>j} \frac{\boldsymbol{S}_i^z \cdot \boldsymbol{S}_j^z}{|\boldsymbol{r}_{ij}|^3} - \frac{3(\boldsymbol{S}_i^z \cdot \boldsymbol{r}_{ij})(\boldsymbol{S}_j^z \cdot \boldsymbol{r}_{ij})}{|\boldsymbol{r}_{ij}|^5} \tag{6.2}$$

for nearest-neighbour Ising spins $\boldsymbol{S}_i^z$, $\boldsymbol{S}_j^z$ with exchange energy J, dipole-dipole coupling strength D and nearest-neighbour separation $|\boldsymbol{r}_{ij}| = r_{\text{nn}} = (a/4)\sqrt{2}$ where a is the lattice constant [29, 140, 143] . In this model, the dipole-dipole coupling strength $D = \frac{\mu_0}{4\pi} \frac{\mu^2}{r_{\text{nn}}^3} > 0$ can lead to a ferromagnetic Ising exchange interaction even with nearest-neighbour antiferromagnetic ($J < 0$) spin-spin interactions. The predicted ground state in this model depends on the relative size of these competing interactions. In particular, considering the angle of nearest-neighbour spins with respect to one another, the effective exchange interaction is $J_{\text{nn}} = J/3$ and the nearest-neighbour dipole interaction is $D_{\text{nn}} = 5D/3$ [30]. This dipolar spin ice model predicts a spin ice phase near the ground state[1] for rare earth pyrochlores with nearest-neighbour exchange interactions $J < 0$ so long as the competition between these two effects yields $J_{\text{nn}}/D_{\text{nn}} > -0.905$ with a phase diagram shown in Figure 6.5 [30, 145].

The pyrochlore lattice is an example of the geometric configuration needed to realize the dipolar spin ice Hamiltonian. This lattice consists of corner-sharing tetrahedra with magnetic moments from the rare earth ion situated on these vertices, as illustrated in Figure 6.6. Alternatively, it can be described in terms of the diamond lattice, with tetrahedron centers lying on a diamond lattice skeleton as illustrated by the black lines in Figure 6.6. In particular, the insulating rare-earth pyrochlores discussed in this thesis have chemical formulae $A_2B_2O_7$ where A is a rare earth ion and B is a transition metal. There are two inter-penetrating tetrahedral sublattices for such materials, one consisting of the A^{3+} ion sitting on the tetrahetral vertices ("A sublattice") and a complementary sublattice with the B^{4+} ion on these corners ("B sublattice") [146]. While other magnetic configurations are possible, the materials discussed here have the magnetic moments on the A sublattice. The spin dynamics discussed in this thesis therefore originate from the magnetic moment of the A site ion. Pyrochlore materials can have an ordered ground state with all spins pointing either into or out of a tetrahedron (Fig. 6.2d shows the all-in state) due to the aforementioned competition between interaction strengths, but of particular interest is

[1] Though this spin ice phase lacking long range magnetic order is experimentally observed at the lowest temperatures achieved, the theoretically predicted ground state of the dipolar spin ice model is in fact a long range ordered phase [144]. Longer thermal equilibrium times may recover experimental signatures of a magnetically ordered ground state [34].

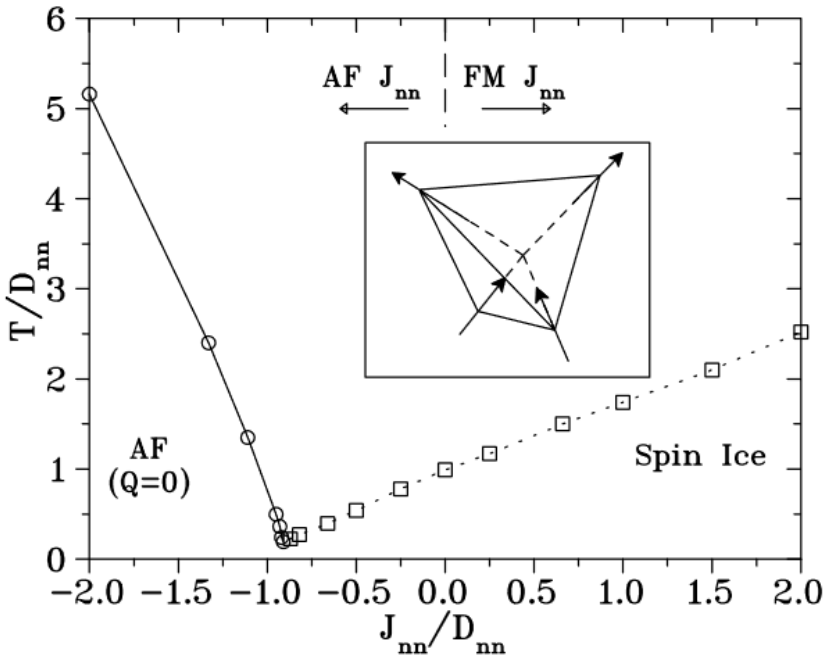


Figure 6.5: Phase diagram of dipolar spin ice in zero applied field from Monte Carlo simulations by den Hertog and Gingras [30]. The temperature T and effective exchange coupling $J_{\rm nn}$ are both normalized by the nearest-neighbour dipolar interaction $D_{\rm nn}$ on the axes of this diagram. *Reprinted figure with permission from* [30]. *Copyright 2000 by the American Physical Society.*

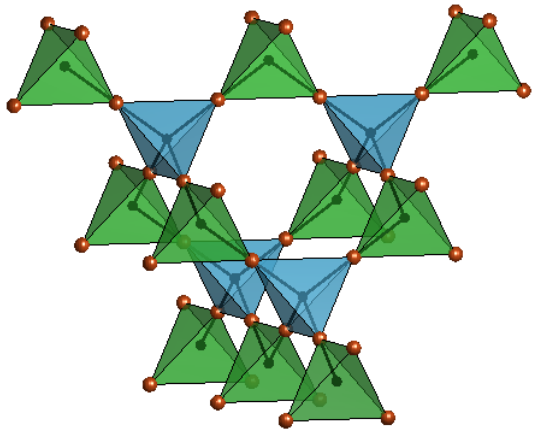


Figure 6.6: An illustration of corner-sharing tetrahedra in a segment of a pyrochlore lattice, with the diamond lattice in black. The red spheres at the tetrahedron vertices represent the positions of the A^{3+} (B^{4+}) ions in the A (B) sublattice as discussed in the main text.

realizing the spin ice state that evades long-range magnetic ordering, which is often referred to as the "classical spin ice" (CSI) state. We will next discuss phenomena realized in CSI candidates before introducing the quantum spin ice model.

The frustrated magnetism in the CSI state gives rise to fractionalized magnetic excitations at finite energy scales. The result is a prediction of magnetic excitations that could be described as isolated magnetic charges, or "magnetic monopoles" and their "antimonopole" counterpart of opposite magnetic charge, interacting with an emergent magnetic charge that can be locally modelled by an analogous Gauss' law and Coulombic interaction akin to that described by Maxwell's equations for electrons. While the "ice rules" dictate that the sum of spins in a tetrahedron is zero in the two-in/two-out state as shown in Figure 6.7a, a spin in this state could overcome an energy barrier to flip, resulting in neighbouring tetrahedra with a three-in/one-out (Fig. 6.7b) and one-in three-out configuration. These neighbouring tetrahedra would each have a net magnetic moment of opposing charges, producing a dipole initially between neighbouring tetrahedra (Fig. 6.7c). Castelnovo *et al.* [32] describe such a phenomena using a "dumbbell" model, where the pseudospin charge is visualized as residing on the diamond lattice of the pyrochlore structure spin as shown in Figure 6.7d. The magnitude of these charges is a fraction of the magnetic moment, $2\mu/(\sqrt{3/2}\, r_{\mathrm{nn}})$. Nearest-neighbouring charges could then be separated with a series of flips of spins in neighbouring tetrahedra with no additional energy cost due to the tetrahe-

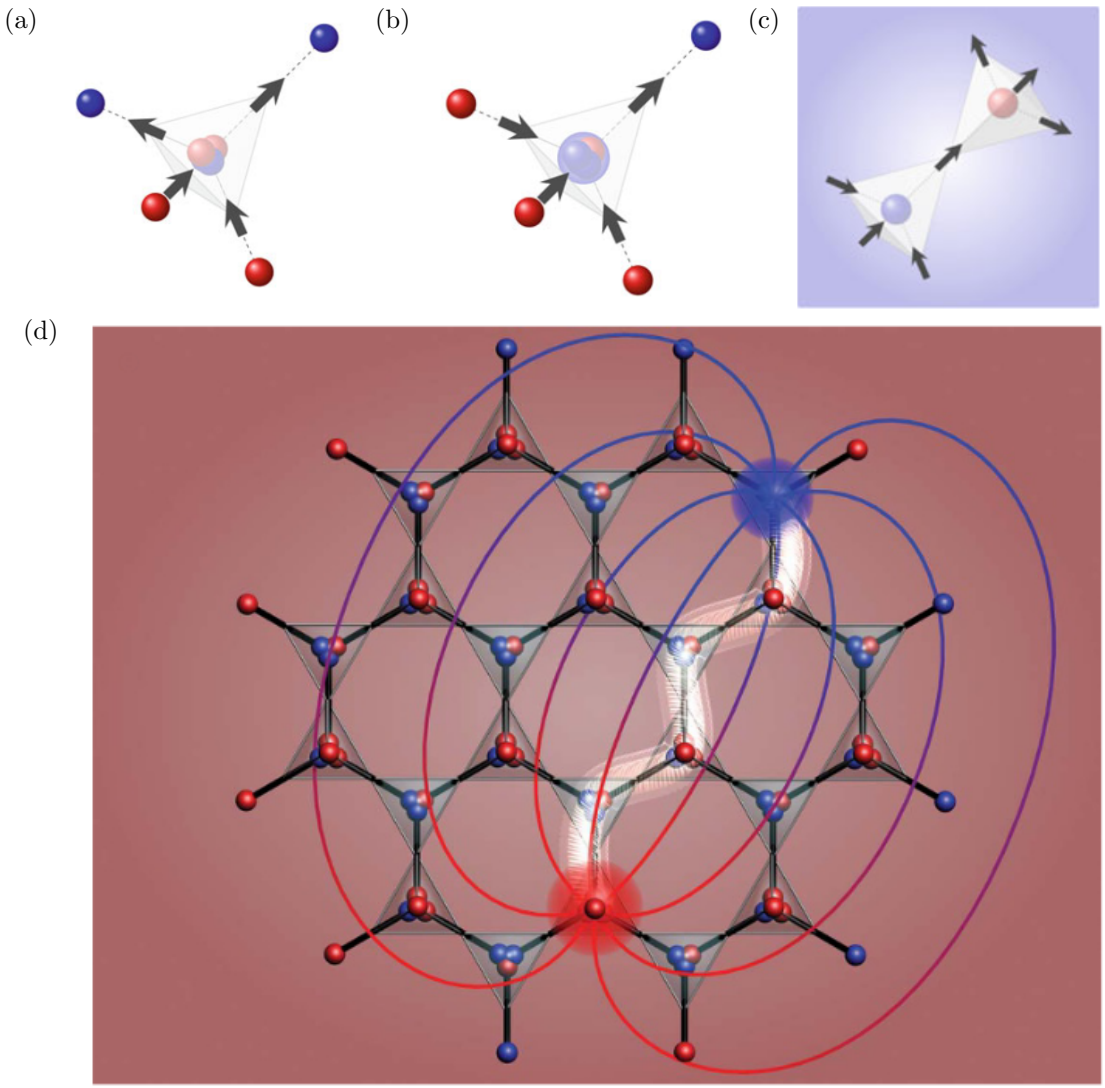


Figure 6.7: The "dumbbell" model of magnetic monopoles. (a) Treating spins on the corners of tetrahedra as dipoles with spacially separated opposing charges, a two-in/two out configuration is charge neutral, (b) a three-in/one-out configuration has a net positive magnetic charge, and (c) a neighbouring tetrahedron with a one-in three-out has a net negative magnetic charge, maintaining a magnetic dipole. Images from Castelnovo *et al.* [31]. (d) An image by Castelnovo *et al.* [32] showing magnetic charges residing on vertices of the diamond lattice. Opposing charges are separated by a series of dipole pairs hilighted in white. *Reproduced with permission from Springer Nature.*

dron in an excited state returning to the ground state configuration (and exciting a spin in a next-nearest-neighbour tetrahedron). This chain of subsequent spin flips is colloquially referred to as a "Dirac string" in this literature, which is illustrated as the white lines in Figure 6.7d. According to the theory behind these magnetic monopoles, they proliferate at a rate depending on the energy cost of flipping a spin to create a monopole-antimonopole pair [147].

6.1.3 Signatures of spin ice physics

The magnetic frustration resulting from this Ising anisotropy can be confirmed with signs of characteristic internal and external magnetic field transitions associated with changes in the effective magnetic moment in the tetrahedra on a macroscopic scale. The internal magnetic field of the two-in/two-out state can be motivated by rewriting the Hamiltonian in terms of the effective magnetic moment in the tetrahedra.

The two-in/two-out condition of the ice rule can be rewritten in terms of the effective magnetic charge at the centre of each tetrahedron being equal to zero. If the effective magnetic moment is zero, then the divergence of the magnetic field generated by this moment is also zero, $\boldsymbol{\nabla} \cdot \boldsymbol{B} = 0$. Given that the internal magnetization of this state is characteristically zero, this forms a predictable pattern to search for with this probe of magnetic correlations [148]. The divergence-free condition results in pinch points in neutron scattering [149]. The local magnetization is also dynamic in this phase rather than static, but an application of a magnetic field can change the local magnetization as well as pin the magnetic moments into a static configuration.

This finite energy required to flip a spin and create a monopole excitation implies testable signatures of the CSI model. This model predicts characteristic in-field behaviour related to transitions between a spin ice state and a macroscopically ordered state. A magnetic field can excite pseudospins out of the ground state, or pin them to align with the field direction. Theoretically, the effect of a magnetic field can be derived assuming local Ising anisotropy for each pseudospin and calculating the Zeeman energy along the spin direction to determine the magnetization on each site. We will next outline this anisotropy in the presence of an applied magnetic field.

The effect of a magnetic field on each magnetic moment can be calculated explicitly. Figure 6.8a shows three high-symmetry axes relevant to CSI theory: [001], [110] and [111], with the spins in one of the ground state two-in/two-out configurations. Fukazawa *et al.* [2] derive the Zeeman energies in each of these high-symmetry field directions given the constraints of the CSI model. As the field magnitude increases, the Zeeman energy for a

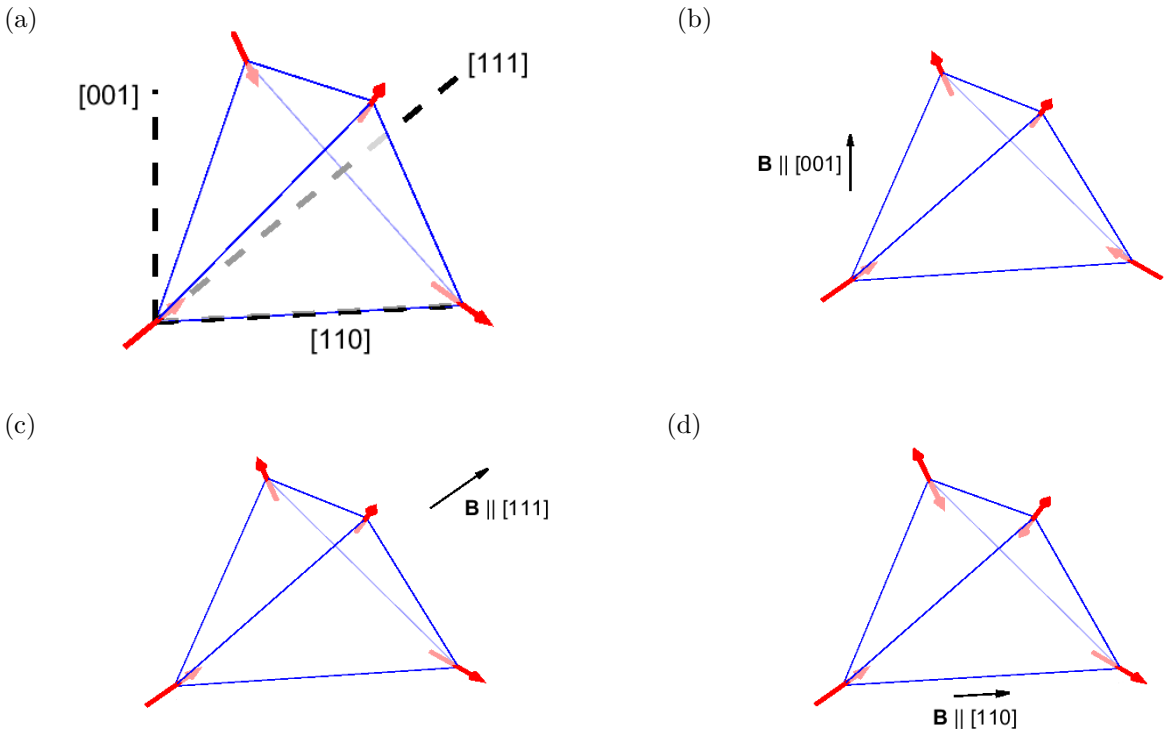


Figure 6.8: (a) Illustration of a two-in/two-out state and the alignment of global [001], [111] and [110] axes with respect to the tetrahedron. (b),(c),(d): Orientation of spins at the tetrahedron vertices, which are constrained to the local ⟨111⟩ axis, after polarization by a large external magnetic field aligned with the (b) [001], (c) [111] and (d) [110] global axes [2]. In Figure (d), two spins remain unaffected by the external field as explained in the main text.

spin can overcome the exchange interaction J_{eff} to align the spin with the magnetic field. The magnitude of this spin flip energy depends on the projection of the effective magnetic moment along the field direction. Applying a [111] field can further test the Ising anisotropy of the spin character. At the intermediate field magnitude $(1/3)\mu_{\text{eff}}B$, the Zeeman energy overcomes the local effective exchange interaction for exactly one spin per tetrahedron in this model while the other three spins that are not oriented along the field axis still obey the ice rule constraints of the local effective exchange interactions, reaching a magnetization of $\{[1+(1/3)]/4\}\mu_{\text{eff}}$. Then, at large enough fields, the magnetization saturates due to the optimized spin alignment with field. Such orientations are shown in Figure 6.8b, c and d

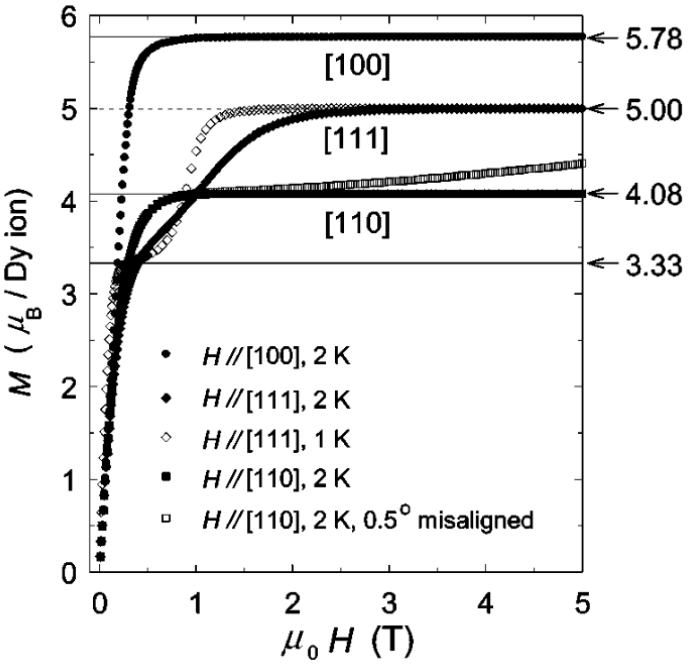


Figure 6.9: Monte Carlo simulation of magnetization for CSI candidate $Dy_2Ti_2O_7$ [2]. Lines indicate the expected intermediate magnetization of 3.33 μ_B/Dy ion for an applied [111] field and the expected saturated magnetizations for field orientations [110], [111] and [100] as motivated in the main text. *Reprinted with permission from* [2]. *Copyright 2002 by the American Physical Society.*

for an applied field oriented in the [001], [111] and [110] axes respectively. The different configurations result in an anisotropic magnetization with values of saturated moments listed in Table 6.1. The expected magnetization curves for this competition are shown in Figure 6.9, with an anisotropic magnetization resulting from these geometric arguments.

As mentioned above, a field applied exactly parallel to [110] that is strong enough to pin two of the four spins is still exactly perpendicular to the remaining two moments due to the geometry of the lattice. It is expected that these two remaining spins remain decoupled from the magnetic field, but nonetheless attempt to satisfy the ice rules [144]. In neutron scattering of CSI candidates $Dy_2Ti_2O_7$ (DTO) and $Hy_2Ti_2O_7$ (HTO), Fennel *et al.* corroborate this theory with a report of a coexistence of long range magnetic order and short-range anti-ferromagnetic interactions which they attribute to decoupled, perpendicular chains of spins [150]. It's therefore useful to differentiate these chains of spins. Hiroi

Field orientation	Spin orientations	Saturated magnetization
[100]	two-in/two-out	$\mu_{\text{eff}}/\sqrt{3}$
[111]	three-in/one-out	$\mu_{\text{eff}}/2$
[110]	one-in/one-out, two free	$\sqrt{3}\mu_{\text{eff}}/\sqrt{2}$

Table 6.1: Anisotropy of saturated magnetizations under applied magnetic fields, with $\mu_{\text{eff}} = g_{\text{eff}} J_{\text{eff}} \mu_B$ [2].

et al. name the chains parallel to the field, which order ferromagnetically with the applied magnetic field, "α" chains and name those that are perpendicular to the field, lacking long range magnetic order as "β" chains [151].

6.1.4 CSI experimental results

The CSI candidates DTO and HTO have extensive experimental evidence corroborating predictions of the CSI model. Both have an effective ferromagnetic interaction with a positive Curie-Weiss temperature[2] and have similar dipolar interaction strengths with a magnetic moment $\mu \sim 10\mu_B$. We will next briefly discuss some of the characteristic spin ice features observed in these materials.

The residual finite entropy observed in spin ice candidates drew early interest and comparisons to water ice. Figure 6.10a shows the specific heat capacity for DTO that is integrated as $C(T)/T$ to get the total entropy in Figure 6.10b. The entropy has a residual magnetic component in zero field that is reduced with an applied 0.5 T field. The dashed lines compare the experimental results to Pauling's prediction of $R(\ln(2) - 1/2\ln(3/2))$, assuming a full spin entropy of $R\ln(2)$. The observed residual magnetic entropy in DTO is consistent with spin ice predictions [152, 153]. There are hints that the low temperature dynamics of CSI state could recover the residual entropy over time. Theoretically, Melko *et al.* [144] report the possibility for long range order in a two-in/two-out ground state that recovers the residual entropy. While they note that spin freezing is observed to occur experimentally and prevent this ground state order, Pomaranski *et al.* report a time dependence of specific heat measurements of DTO below $T < 0.5$ K that deviates from the Pauling prediction in the limit of longer time scales [34] (see Figure 6.11). Though spin

[2]The Curie-Weiss temperature θ_W is derived using a fit of the inverse susceptibility to $\chi^{-1} \propto (T - \delta_W)^{-1}$. For example, the DTO data in the inset of Figure 6.10 has a small, positive intercept, leading to a Curie-Weiss temperature $\theta_W \approx 0.5$ K [33]. A positive(negative) sign of this constant is interpreted as a ferromagnetic(antiferromagnetic) interaction.

freezing and a residual entropy is an oft-cited characteristic of these CSI candidates (see ie. [154]), the long range dynamics of the ground state could have more complex time-dependent behaviour reminiscent of spin glasses that is still a topic of current research [155].

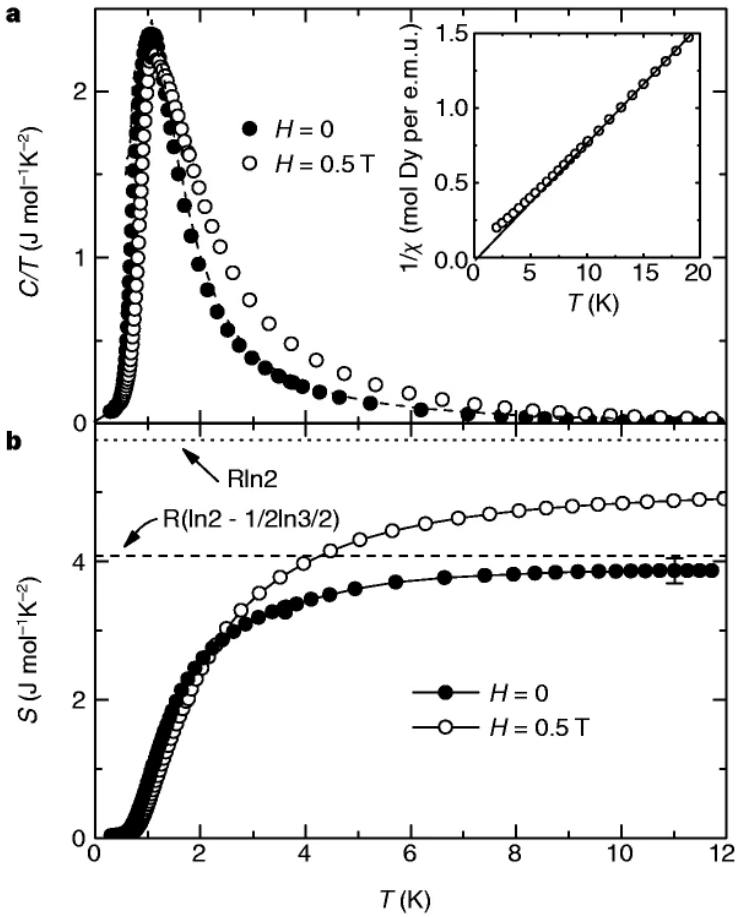


Figure 6.10: (a) Specific heat of DTO in zero field and 0.5 T field, from Ramirez *et al.* [33]. Inset: Inverse susceptibility of DTO in a 0.02 T field. (b) DTO entropy found by integrating $C(T)/T$ data. *Reproduced with permission from Springer Nature.*

The magnetization of CSI candidates demonstrates spin ice anisotropy. DTO has saturated magnetic moments and field transition in magnetization consistent with those expected in the dipolar spin ice model, as shown in Figure 6.12 [2]. The experimental magnetization approaches the magnetization expected (Fig. 6.9) for spin ice anisotropy in each field direction.

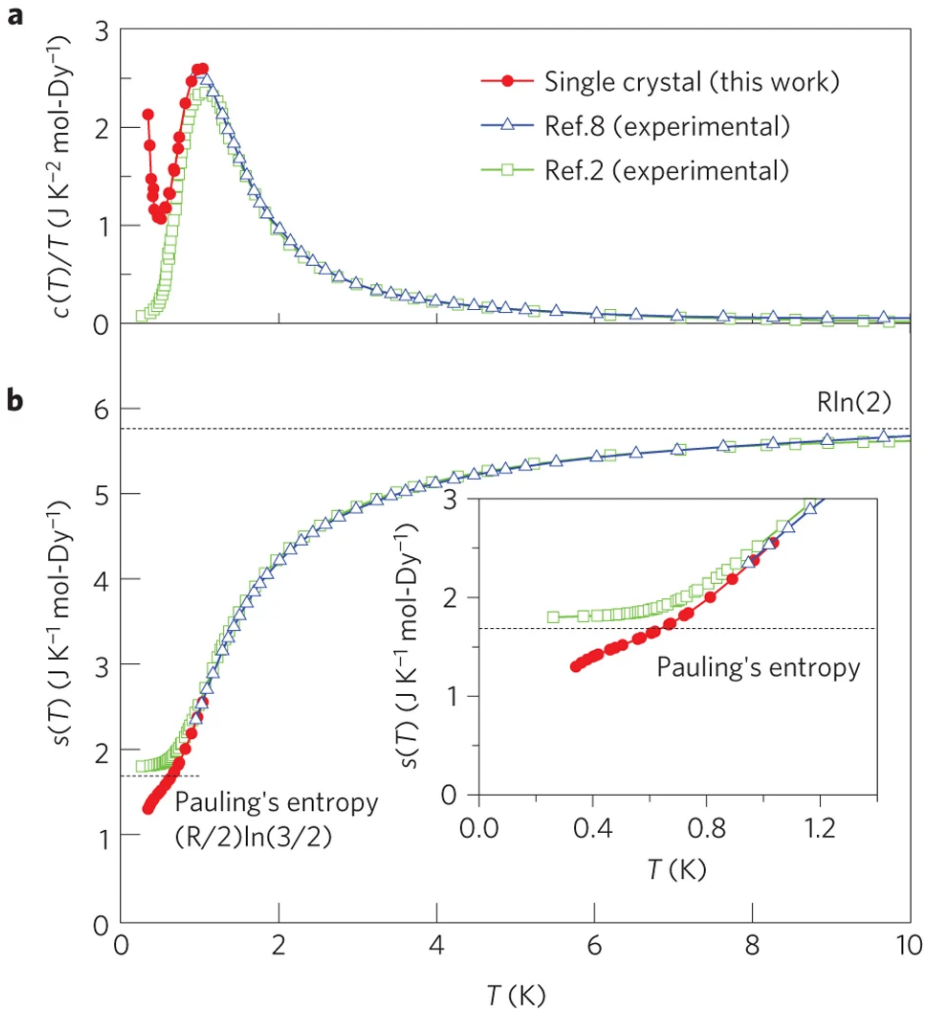


Figure 6.11: Time-dependent (a) specific heat capacity and (b) entropy for DTO from [34]. The authors find an absence of residual Pauling's entropy when waiting longer equilibration times. *Reproduced with permission from Springer Nature.*

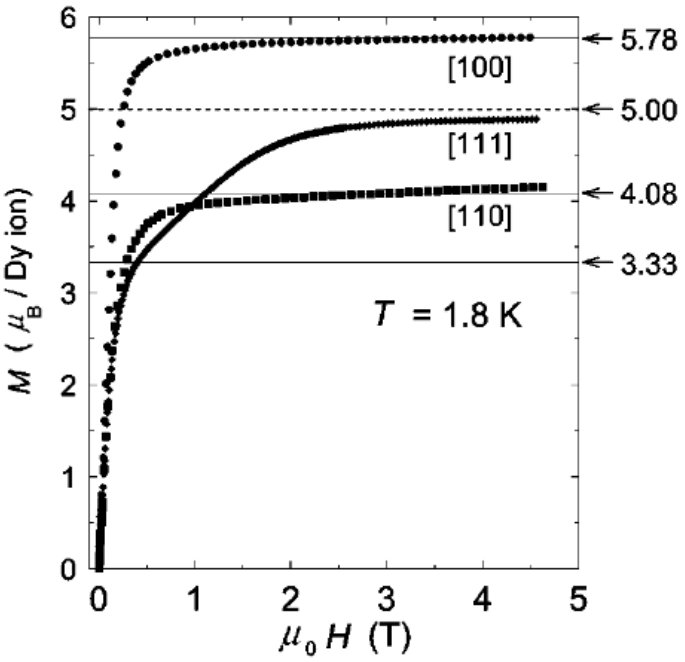


Figure 6.12: Experimental magnetization of DTO at 1.8 K in magnetic fields oriented along [100], [111] and [110]. *Reproduced with permission from* [2]. *Copyright 2002 by the American Physical Society.*

Neutron scattering detects CSI correlations and magnetic crossover behaviour consistent with predictions of the dipolar spin ice model. HTO and DTO show diffuse scattering that is consistent with short range ordering, and Bragg scattering with the application of a magnetic field consistent with predicted magnetic ordering [29, 35, 36, 156, 157]. Analysis of neutron scattering behaviour at characteristic points in momentum-space, such as at the $q = 0$ and $q = X$ points illustrated in Figure 6.13a, corroborates spin ice crossovers in applied field. For example, in Figure 6.13b, the diffuse scattering of DTO in zero field at points such as (003) indicates short range order, but the figure lacks sharp magnetic Bragg peaks, as expected for the CSI state [36]. In contrast, in the presence of a 1.5 T field applied parallel to $[1\bar{1}0]$, magnetic Bragg peaks develop at the $q = 0$ points, but diffuse scattering features persist at the $q = X$ points (Fig. 6.13c). This is interpreted as 1.5 T field parallel to $[1\bar{1}0]$ being sufficient to align the spins on the α chains (at $q = 0$ points) with the field direction while the spins on the perpendicular β chains (at $q = X$ points) anti-align with the field, while still satisfying the ice rules. This is consistent with the spin orientations illustrated in Figure 6.8d.

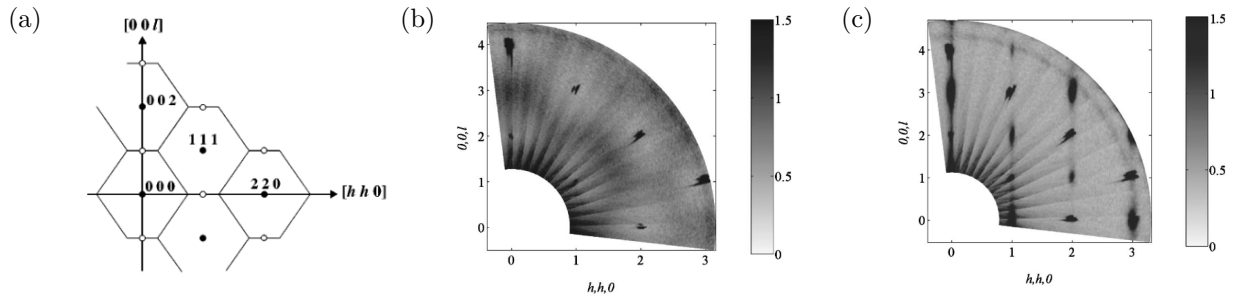


Figure 6.13: (a) A schematic of the reciprocal space lattice for the pyrochlore structure of CSI along the h, h, l plane. The filled circles are the $q = 0$ high symmetry points and the empty circles are the $q = X$ high symmetry points. *Reprinted figure (a) with permission from* [35]. *Copyright 1997 by the American Physical Society.* (b) Scattering intensity in the h, h, l plane for DTO at 0.05 K in zero field, showing diffuse scattering at the $q = X$ points and and (c) in $B = 1.5$ T $\parallel [1\bar{1}0]$ field, showing Bragg scattering at $q = 0$ points and diffuse scattering features at $q = X$ points. *Reprinted figure (b), (c) with permission from* [36]. *Copyright 2005 by the American Physical Society.*

While direct evidence of emergent magnetic monopoles may be difficult to unambiguously obtain, experiments do corroborate the emergent local magnetic charge predicted by this theory. Some of the more compelling evidence involves observations of magnetic correlations consistent with the length scales for monopole interactions. Using polarized neutron scattering, Fennel *et al.* observe diffuse scattering in HTO that can be modelled as a separation of monopoles by a Dirac string [157]. This interpretation of diffuse scattering behaviour is also consistent with observed zero field specific heat of DTO [158]. Bramwell and Fennell provide an in-depth summary of experimental results on DTO and HTO that corroborate a monopole description [148]. Of particular relevance for this thesis is the detection of such quasiparticles in thermal transport measurements. These measurements can also describe the mobility of quasiparticles: delocalized excitations contribute to thermal conductivity by transporting heat, whereas both localized and delocalized excitations may reduce the phonon thermal conductivity through scattering behaviour. In fact, low temperature studies on HTO and DTO report evidence of magnetic monopoles in zero field thermal transport with a reduced density in applied magnetic fields, though the interpretation of mobility and scattering differs between reports [1, 159–163] Toews *et al.* report a monopole contribution to thermal conductivity in HTO with a monopole-phonon scattering rate proportional to the predicted monopole density (Fig. 6.14) [37]. This magnetic contribution could be enhanced by the presence of disorder, even after accounting for a suppressed lattice conductivity from phonon scattering with disorder. Comparing

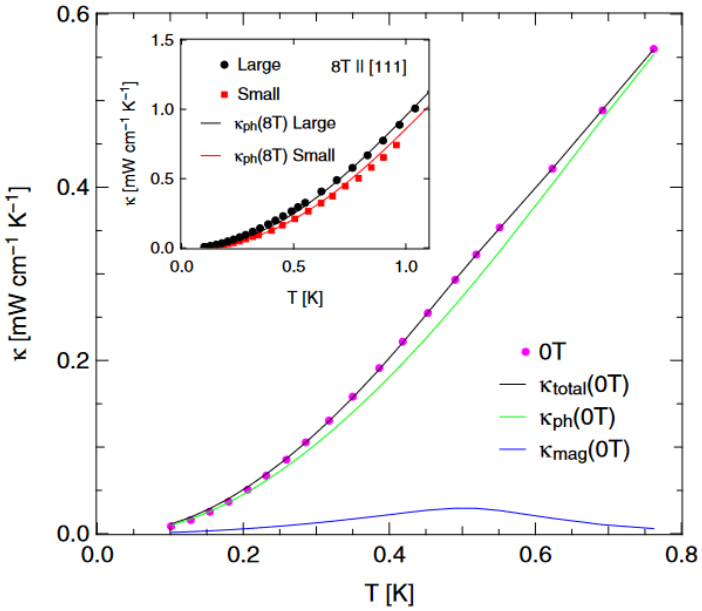


Figure 6.14: Thermal conductivity of HTO with total conductivity modelled as the sum of phonon and magnetic monopole conductivity, $\kappa_{\text{total}} = \kappa_{\text{ph}} + \kappa_{\text{mag}}$. *Reprinted figure with permission from* [37]. *Copyright 2013 by the American Physical Society.*

samples with differing magnitudes of disorder, Toews *et al.* report an enhanced magnetic contribution to thermal conduction in the DTO sample that shows evidence of higher levels of off-stoichiometry [1]. The enhancement is attributed to an increased monopole density that may originate from a lowered spin flip energy.

CSI candidates provide a useful reference point when discussing pyrochlore materials with spins that are not as strictly confined to the local easy Ising axis. Nonetheless, the CSI model serves as a base point for more exotic phases. We will next discuss another phase of the spin ice model that behaves more as a liquid than as a frozen spin state.

6.2 Quantum spin ice

6.2.1 U(1) quantum spin liquid

Quantum spin liquids (QSLs) are such named because degenerate ground states are entangled over long ranges, quantum mechanically tunnelling from one ground state to another and hence evading order. They are often classified according to gauge symmetries. For example, a Z_2 QSL has two-dimensional Ising anisotropy and is arguably realized in select frustrated materials such as $\alpha-RuCl_3$ and two-dimensional organic salts [164]. However, an unambiguous report of signatures of such a phase is still lacking. Key signatures for this phase are fractionalized excitations, an emergent gauge field and a lack of ordering, but distinguishing these signatures from other physical effects is not straightforward in practice [165].

A gapless QSL with three-dimensional U(1) gauge symmetry and linearly dispersive excitations in the ground state is theoretically predicted to apply to a pyrochlore lattice with transverse fluctuations lifting a global Z_2 gauge symmetry [166]. Molavian *et al.* coin the term "quantum spin ice" (QSI) to describe a pyrochlore spin ice model with local transverse fluctuations and identify the pyrochlore $Tb_2Ti_2O_7$ as a potential candidate for the QSI phase [167]. Later proposals suggest a nearest-neighbour model for a U(1) QSL state that could be realised in rare-earth pyrochlores, giving rise to gapped excitations as well as a gapless collective mode [168, 169]. The gapless excitations predicted for QSI are unambiguously a signature of this U(1) QSL phase. Moreover, these excitations are predicted to be detectable in thermal transport measurements [166, 170]. Experimentally testing predictions of gapless excitations in a rare earth pyrochlore is a main focus of this portion of the thesis. We will next introduce QSI theory and motivate the search for a QSI candidate using thermal conductivity measurements.

6.2.2 Kramers versus non-Kramers ions

When selecting materials for spin ice dynamics, the time reversal symmetry of the rare earth ion affects behaviour in magnetic field and susceptibility to structural disorder effects. According to Kramer's theorem, rare earth ions with an odd number of electrons ("Kramers") are protected by time reversal symmetry and have energy levels that are at least doubly degenerate [171]. The Zeeman energy for a magnetic moment is given by the Hamiltonian

$$\mathcal{H}_{\text{Zeeman}} = -g_J \mu_B \boldsymbol{J} \cdot \boldsymbol{H} \tag{6.3}$$

for Landé factor g_J, total angular momentum $\boldsymbol{J}$ and applied field $\boldsymbol{H} = \frac{1}{\mu_0}\boldsymbol{B}$ [172, 173]. When $\boldsymbol{J}$ is half-integral, the crystal field of the "Kramers" magnetic moment produces a series of degenerate states in the easy axis which are odd under time-reversal symmetry and have a Zeeman energy that linearly increases with applied magnetic field [171, 173]. These materials are sensitive to the Zeeman effect from an applied magnetic field along the local $\hat{z}$ axis, but are relatively insensitive to a field along the local transverse plane. In contrast, non-Kramers ions with integer values of $\boldsymbol{J}$ allow the existence of singlet, non-degenerate states that have no projection along the local $\hat{z}$ axis, but can have quite large quadrupolar or multipolar degrees of freedom in the transverse plane (and further allow doublets which split according to the above Zeeman energy expression) [171, 172].

The dipolar spin ice model of Equation (6.2) assumes a dominant dipolar interaction compared to multipolar effects. It has successfully modelled both non-Kramers and Kramers pyrochlores where this assumption holds true. In contrast, QSI models investigate the effective spin-1/2 Hamiltonians of pyrochlores with Kramers and non-Kramers magnetic ions where higher order interactions are non-negligible, by expanding the dipolar spin ice model to include multipolar interactions [174, 175]. These higher order interactions introduce quantum fluctuations [167].

When comparing Kramers and non-Kramers rare earth ions, effects due to the superexchange interactions differ between these two types of moments due to their respective crystal field symmetries. The full expression of the magnetic moment of Kramers ions has both a component parallel to and perpendicular to the local Ising direction due to the sensitivity of the transverse multipolar moments to magnetic field, whereas the non-Kramers ions only have a parallel component since the perpendicular component is insensitive to field, decoupling the two directions. The general QSI Hamiltonian for Kramers and non-Kramers pyrochlores is discussed in the following section.

6.2.3 Quantum spin ice theory

As discussed in Section 6.1.2, the CSI model describes pyrochlore materials with a strong Ising anisotropy, such that the pseudospins are confined to point into or out of the tetrahedra along the local $\hat{z}$ axis. The QSI Hamiltonian has a similar structure as CSI owing to the Ising anisotropy of the ground state doublet, along with additional terms from locally transverse interaction strengths at these vertices. Simply, this can be illustrated as an

(a) (b)



Figure 6.15: (a) Local D_{3d} degrees of freedom on a rare earth ion site (orange spheres). The symmetry consists of a C_2 rotational symmetry along the local $\langle 111 \rangle$ axis (black line), and a perpendicular, local XY plane (purple disk) with three C_3 rotational axes (purple lines) [38]. (b) Pyrochlore lattice with hexagonal ring outlined in red.

exchange interaction component along the local XY axis as shown in Figure 6.15a. To motivate the QSL model, a general Hamiltonian for pseudospin-1/2 on a pyrochlore lattice is [176]

$$\begin{aligned}\mathcal{H} = \sum_{\langle i,j \rangle} [&J_{zz} S_i^z S_j^z - J_{\pm} \left(S_i^+ S_j^- + S_i^- S_j^+ \right) + J_{\pm\pm} \left(\gamma_{ij} S_i^+ S_j^+ + \gamma_{ij}^* S_i^- S_j^- \right) \\ &- J_{z\pm} \left(\gamma_{ij}^* S_i^z S_j^+ + \gamma_{ij} S_i^z S_j^- + \gamma_{ji}^* S_j^z S_i^+ + \gamma_{ji} S_j^z S_i^- \right)]\end{aligned} \tag{6.4}$$

where γ_{ij} is a complex unimodular matrix, J_{zz}, $J_{\pm}$, $J_{\pm\pm}$, and $J_{z\pm}$ are effective exchange constants, and S_i^+, S_i^- are pseudospin components along the local XY plane [168, 169]. The Ising anisotropy of the dipolar spin ice model is recovered in this Hamiltonian for the limit that all exchange interactions are negligible except for the J_{zz} component. The second term is the coupling of quadratic pseudospin $J_{\pm}$ to the normal component of the moment $S_i^{\pm}$. The third and fourth terms are more difficult to interpret physically as they depend on the unimodular matrices derived from a rotational transformation of the exchange couplings for neighbouring tetrahedral vertices to a Hamiltonian of up to four symmetries as allowed by the ground-state doublet [38, 168, 169]. The exchange interaction $J_{z\pm}$ is non-negligible for materials with magnetic ions possessing Kramers symmetry, but materials with non-Kramers symmetry have an Ising component that is odd under time-reversal symmetry and a quadrupolar moment that is even, decoupling the local Ising and XY components. In Kramers materials, the magnetic moment has a dipolar moment perpendicular to the Ising axis, but this transverse component is exactly zero in non-Kramers materials due to the

lack of coupling between the multipoles and a magnetic field due to the symmetries of the crystal fields, as introduced in Section 7.1.4. Hence while pyrochlores with Kramers ions may use all four effective exchange interactions in Equation (6.4), those with non-Kramers ions have $J_{z\pm} = 0$ [38]. Regardless of the mechanism behind the transverse coupling, the excitations predicted in a QSI ground state remain consistent across these candidates.

Like other QSL models, the QSI model predicts excitations that can be probed with experiments to test the theory in real materials. The gapped excitations in the QSI model also include a "magnetic" monopole that is a source of magnetic field analogously to in the CSI state. Unlike the CSI state, the QSI model predicts emergent electrodynamics from the movement of monopole excitations. In particular, the monopole-antimonopole pairs can rotate in a "ring exchange" on the hexagonal neighbouring sites depicted in Figure 6.15b. The ring exchange is due to the quantum mechanical tunnelling of spins from one configuration, such as neighbouring spins pointing clockwise around the hexagonal structure, to its conterpart, or a counterclockwise configuration in the previous example. This is described by a tunnelling term in the Hamiltonian that is a leading order non-zero term in the perturbative regime,

$$\mathcal{H}_{\text{ring}} \sim g \sum_{i,j,k,l,m,n \in hex} \left[S_i^+ S_j^- S_k^+ S_l^- S_m^+ S_n^- + \text{h.c.} \right] \tag{6.5}$$

where the indices i, j, k, l, m, n denote nearest-neighbour sites in a single hexagonal plaquette, the sum is over all plaquettes in the pyrochlore lattice, and "h.c." denotes the Hermition conjugate [39, 166, 168, 177, 178]. This ring exchange term motivates a gapped vison excitation, which is an emergent fictitious electric field created by the separation (then annihilation) of a monopole-antimonopole pair [166].

In QSI theory, photon excitations are most easily distinguished from other excitations below the energy scales of the gap of visons and monopoles. The interaction strength for magnetic monopoles is J_{zz} in Equation (6.4). The nuances of this theory also predict vison excitations from higher order exchange interactions in the Hamiltonian. Emerging from exchange interactions is a coupling strength $J_{\pm}^3/J_{zz}^2$, the magnitude of the vison gap, and since the model assumes that the Ising strength J_{zz} is larger than transverse couplings $J_{\pm}$, the vison gap is smaller than the monopole gap [39]. So when looking for these excitations, only photons would appear at the lowest energy scales since they are gapless, while visons appear at small energies, and monopoles at the largest energies, as illustrated in Figure 6.16 [39]. Notably, while many features derived from Ising anisotropy are similar between classical and quantum Hamiltonians, a clear difference between the CSI and QSI theories is this prediction of excitations that behave as photons with a linear dispersion relation

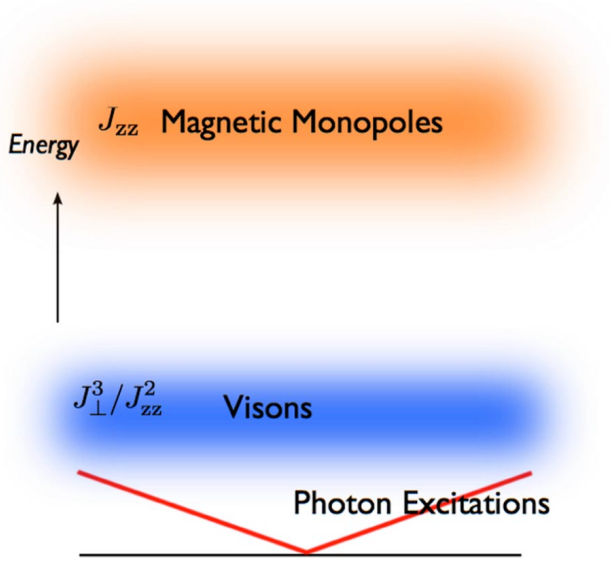


Figure 6.16: The energy scales of excitations in the QSI model. Image from Gingras and McClarty [39]. © *IOP Publishing. Reproduced with permission. All rights reserved.*

in the low temperature limit. We are particularly interested in the prediction of gapless photon excitations due to their distinguishing features that could unambiguously identify a U(1) QSL. We will next discuss predicted properties for these excitations.

6.2.4 Photon excitations

In the low temperature limit, linearly dispersive photons are expected to have a contribution to specific heat capacity and thermal conductivity that is cubic in temperature, analogously to linearly dispersive phonons as described in Appendix A.3.1 [166]. Theoretical developments on the magnitude of the specific heat capacity and speed of sound allow us to compare experimental results with expectations for the QSI phase. Even though the predicted temperature dependence of the specific heat is comparable to phonons, due to the large entropy available in the degenerate spin ice ground state and due to a small speed of "light" $v_{\text{pt}} \sim g a_0$[3], the photon specific heat capacity is expected to be significantly larger

[3] v_{pt} is proportional to the exchange parameter $g \sim 12 J_\pm^3/J_{zz}^2 \ll J_{zz}$ that is crudely estimated as being on the order of 1 K or less, and the lattice constant $a_0 \approx 10$ Å [176, 177]. Therefore v_{pt} is predicted to be $\sim 10 - 100\ \text{m}\,\text{s}^{-1}$, which is typically $\sim 1 - 2$ orders of magnitude smaller than a typical phonon speed of sound in pyrochlores.

than that of phonons [176]. Benton *et al.* estimate the photon contribution to specific heat as

$$C_{\mathrm{pt}} = \left(\frac{\pi^2}{30}\right) R \left(\frac{k_{\mathrm{B}} a_0}{\hbar v_{\mathrm{pt}}}\right)^3 T^3 \tag{6.6}$$

where R is the molar gas constant and a_0 is the lattice constant [177], which is reminiscent of the expression for phonons in Equation (A.9).

6.3 Experimental research on QSI candidates

Many of the theoretical signatures of QSI resemble those of CSI. Like CSI, this state is characterized by a lack of ordering and cooperative spin dynamics. While conclusive evidence of photon excitations remains to be verified in QSI candidates, signs of spin ice anisotropy are reported in some non-Kramers QSI candidates. We will discuss the experimental observations of QSI candidates $Tb_2Ti_2O_7$ and $Pr_2Zr_2O_7$.

6.3.1 $Tb_2Ti_2O_7$ experimental background

The pyrochlore $Tb_2Ti_2O_7$ (TbTO) is one of the first pyrochlores investigated as a quantum spin liquid. This cooperative paramagnet has a Tb^{3+} rare earth ion with a (J=6) non-Kramers ground state doublet [38, 179]. However the terbium ion has a smaller Ising component of its magnetic moment, leading to a deviation from the Ising anisotropy that is observed in the non-Kramers CSI candidate $Ho_2Ti_2O_7$ [180]. The terbium pyrochlore also has a low lying CEF first excited state at $\sim$ 16 K leading to complex dynamics, for example a proposed "magnetoelastic mode" from this state hybridizing with an acoustic phonon [181].

Figure 6.17 shows the thermal conductivity of $Tb_2Ti_2O_7$ as reported by Li *et al.* [40]. The authors note a short phonon mean free path that is well below the mean free path of non-magnetic reference material $Y_2Ti_2O_7$ as demonstrated in the inset to Figure 6.17a, resulting in a thermal conductivity lower than expected for both of their reported samples (Fig. 6.17a main figure). Due to the recovery of the phonon mean free path and thermal conductivity in non-magnetic reference material $Y_2Ti_2O_7$, the authors attribute the strong phonon scattering to a magnetic origin. The thermal conductivity of this material does not show obvious signs of a photon contribution, but does have a rich magnetic field behaviour

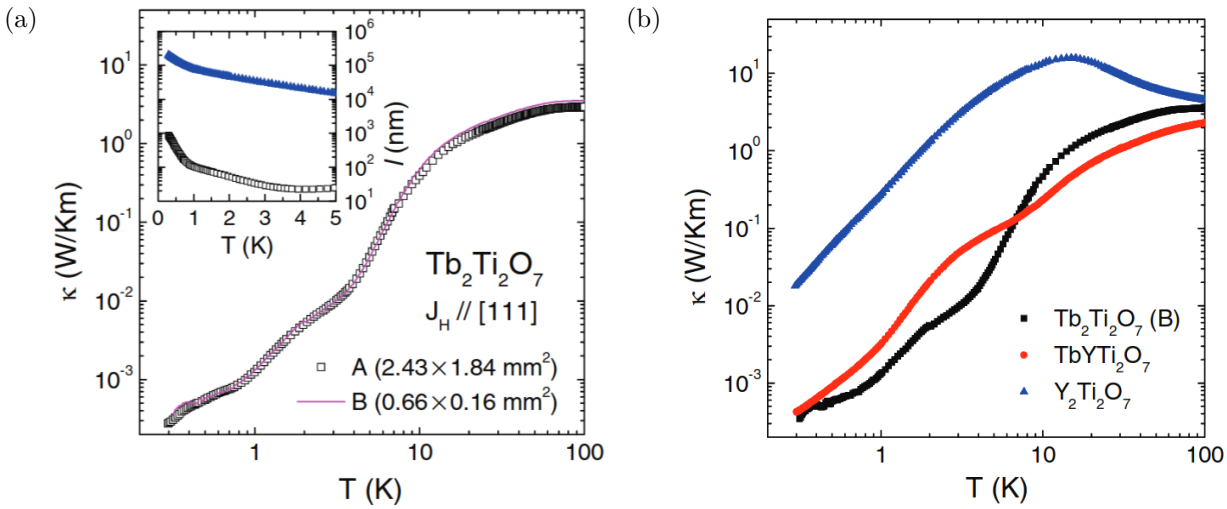


Figure 6.17: Li *et al.* report the thermal conductivity of $Tb_2Ti_2O_7$ at temperatures up to 100 K on a log-log scale [40]. (a) Thermal conductivity of $Tb_2Ti_2O_7$ samples "A" and "B" with heat current $J_H \parallel [111]$. Inset: phonon mean free paths ℓ of $Tb_2Ti_2O_7$ sample A and $Y_2Ti_2O_7$ on a semi-log scale at temperatures up to 5 K. (b) Thermal conductivity of $Tb_2Ti_2O_7$ (sample "B"), $TbYTi_2O_7$ and $Y_2Ti_2O_7$. *Reprinted with permission from* [40]. *Copyright 2013 by the American Physical Society.*

with a short phonon mean free path as small as 20 nm, even shorter than the mean free path for amorphous (glassy) materials that lack long range periodicity [40]. Puzzlingly, it demonstrates an anomalously large thermal Hall conductivity [182] that is attributed to phonons rather than magnetic excitations [183].

Despite decades of research, the ground state of $Tb_2Ti_2O_7$ is still being rigorously investigated. There are reports that the magnetic Tb^{3+} ion may drive real samples towards ordering. Minimally doped polycrystalline samples $Tb_{2+x}Ti_{2-x}O_7$ with $x = 0.005$ show signs of antiferromagnetic ordering as evidenced by a sharp discontinuity in the specific heat and Bragg peaks in the INS spectrum, though those that are underdoped at $x = -0.005$ only show signs of short range order [184]. When considering the ordering behaviour, the nature of quadrupolar ordering is still an intriguing area of research that may shed light on the ground state magnetic behaviour. Recently, ultrasonic and magnetostriction measurements identify transitions in elastic moduli at ~ 0.5 K despite the lack of an obvious anomaly in the magnetic susceptibility, which could indicate a transition to quadrupolar order [185, 186]. The reported coupling between quadrupolar degrees of freedom and magnetic moments are possibly also relevant to understanding the physics of other non-Kramers QSI candidates.

6.3.2 $Pr_2Zr_2O_7$ experimental background

The dipolar spin ice candidates with praseodymium rare earth have attracted attention as QSI candidates, particularly due to the greater separation between the ground state and first excited state simplifying the magnetic dynamics in comparison to $Tb_2Ti_2O_7$. The ground state for Pr^{3+}-based pyrochlores is found to be a non-Kramers doublet that is well separated from the first excited state by an energy gap ~ 110 K [187], an order of magnitude of separation larger than for the Tb^{3+} ion. In the insulating pyrochlore $Pr_2Zr_2O_7$ (PZO), the praseodymium rare earth ion has a smaller effective magnetic moment of $\mu_{\text{eff}} \sim 2.5\,\mu_B$ [188] than for the typical CSI candidates ($\mu \approx 10\ \mu_B$ for HTO and DTO [189, 190]). The small dipolar exchange interaction arising from the magnitude of the magnetic moment suggests that the superexchange interaction dominates in the dipolar spin ice model. However, magnetic order is not realized in this material down to milliKelvin temperatures despite a negative Curie-Weiss temperature of -0.4 K that is naively associated with an antiferromagnetic effective exchange interaction and the tendency towards "all-in-all-out" order [188, 191]. Moreover, a broad peak in specific heat centered at ~ 2 K could indicate an excess entropy associated with a spin ice crossover [187, 192, 193]. The lack of ordering along with features associated with strong spin fluctuations makes PZO a candidate for a spin ice ground state with quantum fluctuations. PZO demonstrates pinch point pattern

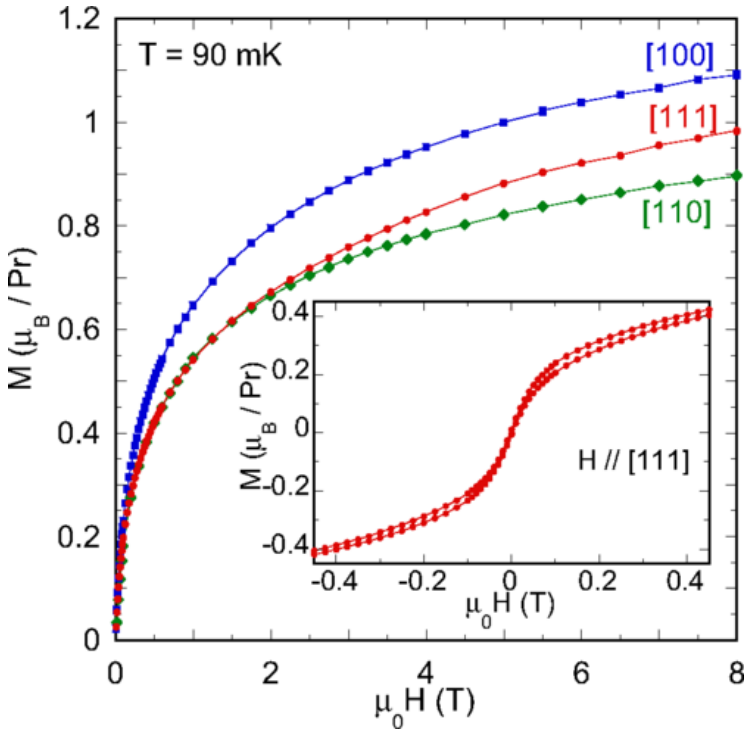


Figure 6.18: Magnetization of PZO at 90 mK. Inset: magnetization with field parallel to [111] centered around 0 T, showing a slight hysteresis. *Reprinted with permission from* [41]. *Copyright 2016 by the American Physical Society.*

in elastic neutron scattering measurements as well as a lack of ordering, but unlike the classical spin ices, Kimura *et al.* also identify signatures a broad diffuse peak in the inelastic neutron scattering that may originate from magnetic correlations of fluctuating spins [187]. Promisingly, Tokiwa *et al.* report an enhancement of thermal conductivity above that expected for phonons that they attribute to photon excitations in a QSI ground state [46]. While these reports of direct evidence of photon excitations in the thermal conductivity of a QSI candidate have not been corroborated by other groups, they certainly add anticipation that the QSI state and a U(1) QSL can be realised in real materials.

Conversely, other reports consider that PZO may be in a paramagnetic phase that is proximal to a QSI due to random strains in the lattice displacing the Pr^{3+} ions. Compared to the CSI candidates, the magnetization does not saturate above the expected spin ice transition, as shown in Figure 6.18, which may be due to a degeneracy lifting of the non-Kramers doublet [194]. Wen *et al.* report that the diffuse spectrum in inelastic neutron

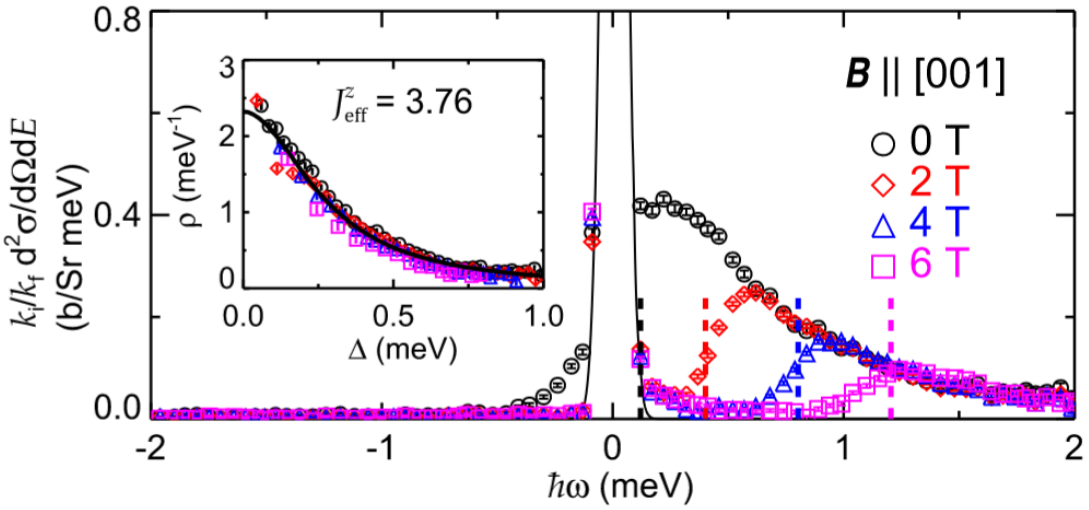


Figure 6.19: PZO INS averaged for momentum transfer 0.5 $\text{Å}^{-1} \leq |\boldsymbol{q} \leq 2.2$ Å^{-1}, at $T = 1.4$ K under an applied field parallel to [001]. Inset: Using an Ising exchange parameter $J^z_{\text{eff}} = 3.76$, the authors show that the INS spectrum in the main figure follows a Lorentzian-like distribution $\rho(\delta)$ as discussed in the main text. *Reprinted with permission from* [42]. *Copyright 2017 by the American Physical Society.*

scattering under a [001] field, shown in Figure 6.19 is consistent with a half-Lorentzian distribution $\rho(\Delta) \propto \frac{2\Gamma}{\pi(\Delta^2+\Gamma^2)}$ of spectrum of split non-Kramers ground state doublets with width $\Gamma = 0.27(1)$ meV [42]. The authors show that the distribution of splittings Δ_i in zero applied field is consistent with a physical scenario where split ground state doublets from disorder act as a random transverse field along the local $\hat{x}$ direction. Though the authors suggest that such disorder is not necessarily inconsistent with a QSI ground state, other reports place the ground state phase of PZO away from a QSI due to such detectable disorder. Petit *et al.* instead motivate that the aforementioned inelastic spectrum is instead consistent with an antiferromagnetic interaction between quadrupolar moments, proximal to an antiferroquadrupolar ordered phase [41]. The authors explain that the apparent contradiction of a pinch point pattern in neutron scattering as well as a negative Curie-Weiss temperature (associated with nearest-neighbour antiferromagnetic interactions) is justified for such a phase, though they note that the lack of specific heat anomaly may place PZO in an antiferroquadrupolar liquid phase rather than a phase with quadrupolar ordering.

6.3.3 Disorder and QSI

Non-Kramers rare earth ions are susceptible to symmetry-breaking from structural disorder. In the presence of such elastic strain or magnetic imperfections that break the D_{3d} symmetry, a ground state non-Kramers doublet which is normally protected under time-reversal symmetry instead becomes two singlets that are no longer protected under this symmetry [38]. As discussed in the previous section, Wen *et al.* report that structural disorder acts as a random transverse field on the Pr^{3+} ion in this QSI candidate, splitting the ground state doublet into singlet states in spite of an absence of signatures of off-stoichiometry [42]. Yet even stoichiometric samples can have disorder that distorts the crystal field. Using local structure probes, Trump *et al.* show how samples without detectable off-stoichiometry, site-mixing and cation defects do have a symmetry-breaking off-centering of the Pr ion, proposing that this structural deformation is driven by a mismatch in size between the A and B sites of the pyrochlore [195]. Regardless of the source of disorder that breaks the crystal field symmetry, the effect of a splitting of the non-Kramers doublet in PZO is successfully modelled using a random transverse field Ising model (RTFIM)

$$\mathcal{H} = J \sum_{\langle i,j \rangle} \sigma_i^z \sigma_j^z - \sum_i h_i \sigma_i^x \tag{6.7}$$

where the first term is the spin ice component that has minimal energy state with the spins on each tetrahedron in the 2-in-2-out pattern for $J > 0$. The second term represents a field of random strength h_i that couple to lattice imperfections, acting as a transverse field with pseudospin operators σ_i^x [42, 43, 178, 196]. Using this model, Wen *et al.* report a "half" Lorentzian distribution of transverse field splittings, $\rho(\Delta) \propto (\Delta^2 + \Gamma^2)^{-1}$ with half-width $\Gamma = 0.27(1)$ meV and propose that PZO is a candidate for disorder-induced QSI given the theoretical stability of the QSI state to perturbations from disorder [42].

The impact of a split ground state doublet on the realization of a QSI state is disputed. The effect of crystal fields generated by the breaking of this symmetry are modelled as a random transverse field that may still stabilize into a QSI ground state in the small disorder limit where the perturbations could introduce quantum fluctuations to enhance monopole movement [42, 43, 178, 196, 197]. While such a splitting is accounted for in theoretical models for PZO that predict a QSI ground state with a random transverse field component, the exact disorder strengths needed for a QSI ground state and whether these conditions are satisfied in PZO are still a subject of debate. In particular, Benton suggests that the strong disorder indirectly apparent in previous reports of PZO place it in a more trivial paramagnetic ground state rather than the QSI state, despite the aforementioned evidence of spin ice characteristics [43]. Using this model, it has been suggested that small amounts of disorder can stabilize a quantum spin ice state in PZO [42, 178]. On the other hand, as shown in Figure 6.20, Benton argues that if the disorder in the RTFIM model reaches the threshold

$$2J - 3\bar{h} + \frac{7}{8J}\delta h^2 - \frac{5\bar{h}^2}{8J} > 0 \tag{6.8}$$

where the width $\delta h = \sqrt{\bar{h^2} - \bar{h}^2}$ and average random transverse field strength $\bar{h}$, then the QSL state is possible, otherwise spinons condense into a trivial paramagnetic ground state as demonstrated in Figure 6.20 [198]. According to Benton, existing data for PZO has it in the trivial paramagnetic phase.

6.3.4 Quadrupolar ordered phases

Despite a lack of signs of ordering in PZO and the interest in it as a QSI candidate, the ground state could be different than QSI phase. The quadrupolar moments in PZO could also order while the dipolar moments remain disordered. For rare earth ions with non-Kramers symmetry, the magnetic moment is strictly along the local Ising axis $\boldsymbol{m} =$

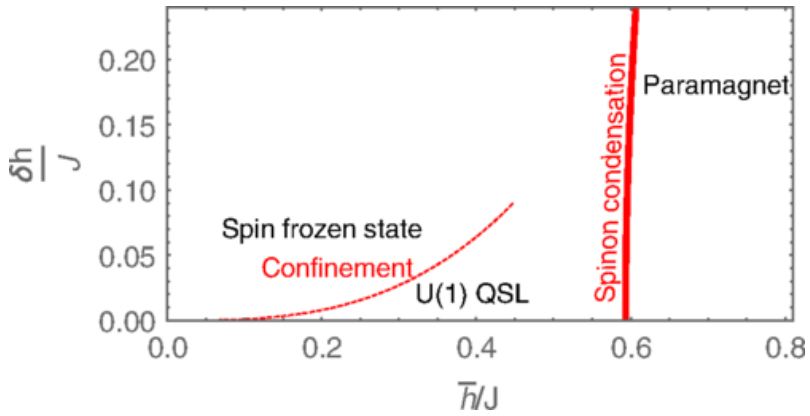


Figure 6.20: Spinon condensation as a function of disorder average strength $\bar{h}$ and width δh. *Reprinted with permission from* [43]. *Copyright 2018 by the American Physical Society.*

$g_{\|}\mu_B \langle S_i^z \rangle \hat{\boldsymbol{z}}_i$, while the pseudospin components normal to this axis are related to the multipolar moment (which is a quadrupolar moment in the case of Pr^{3+}) [169]. Therefore the transverse couplings are mediated by the quadrupolar moment for these praseodymium-based pyrochlores. On the other hand, the sensitivity of the non-Kramers doublet to time-reversal symmetry also makes it sensitive to disorder that breaks its D_{3d} symmetry.

The experimental results of these non-Kramers QSI candidates thus far appear to lack ordering yet still are not conclusively in a QSI ground state. Even if the ground state is not a QSI, it can still be a novel frustrated magnetic phase. Even without ordering of the magnetic dipole moment, the quadrupolar moments may order depending on the magnitude of their coupling strengths relative to the Ising coupling strength. Using PZO as an example, Martin *et al.* motivate two phases with a lack of dipole ordering and an ordered quadrupolar phase: a quadrupolar spin ice (Q-SI) phase and a quadrupolar all-in/all-out (Q-AIAO) phase [196]. In this model, the pseudospin lies along the local XY plane in the quadrupolar ordered phases, and this pseudospin has the same sign in the Q-AIAO phase but a staggered sign in the Q-SI phase. According to the parameters for PZO, Martin *et al.* propose that its phase lies in the Q-AIAO quadrupolar ordered phase, however a clear consensus on the strength of coupling parameters would help to determine where PZO lies in this phase diagram.

Chapter 7

$Pr_2Hf_2O_7$ experimental results

7.1 Quantum spin ice candidate $Pr_2Hf_2O_7$

The pyrochlore $Pr_2Hf_2O_7$ (PHO) is a new material that shares physical characteristics with the QSI candidate $Pr_2Zr_2O_7$ (PZO), which is discussed in Section 7.2.4. It has a non-Kramers doublet ground state with a distant first excited crystal electric field state (singlet) at 8.82 meV $\sim$ 100 K [44]. Lacking signs of magnetic ordering down to temperatures as low as 0.07 K, it has a small ferromagnetic Curie-Weiss temperature and an effective magnetic moment of $\mu_{\text{eff}} \approx 2.51\ \mu_B$/Pr inferred from the inverse susceptibility shown in Figure 7.1a [44, 199]. As shown in Figure 7.1b, the magnetization data demonstrates an Ising anisotropy, yet it doesn't quite saturate as expected for the CSI model, even at fields as high as 14 T and 2 K [44]. The observed magnetizations in field orientations [100] and [111] at 14 T are close to the estimated saturated values of $M_{[100]} = 1.45\ \mu_B$/Pr, $M_{[111]} = 1.26\ \mu_B$/Pr however the magnetization in an applied [110] field rises above the expected value of 1.02 μ_B/Pr. Anand *et al.* hypothesize that the deviations from the spin ice model could be a symptom of non-Ising dynamics in the Hamiltonian, and the lack of saturated magnetization could also be due to mixing of the ground state multiplet. Similar characteristics are also reported in PZO and can be attributed to the symmetries of the Pr^{3+} ion [194]. Petit *et al.* also observe a lower magnetic moment than expected and a lack of saturation of the moment in PZO, attributing the gradual increase in magnetization to a competition between Ising and quadrupolar components of the magnetic moment [41]. Such an explanation is consistent with the non-negligible transverse exchange coupling parameters motivated for a QSI model. Both materials have signs of cooperative magnetism that are characteristic of the degeneracy of a spin ice ground state. The *ac*-susceptibility

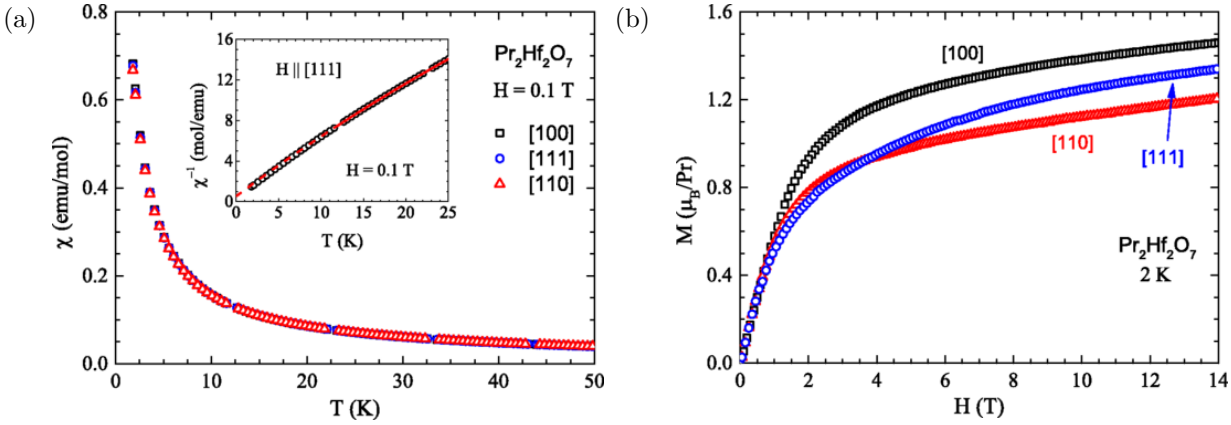


Figure 7.1: (a) Susceptibility at 0.1 T and 1.0 T; and (b) magnetization of single-crystal PHO at 2 K. *Reproduced with permission from* [44]. *Copyright 2016 by the American Physical Society.*

measurements show a broad peak that is consistent with the slow spin dynamics of a spin ice state [44, 199]. PZO [41, 187, 191] and PHO [199] also show a broad peak at ~ 2 K in the zero field specific heat capacity that is associated with the onset of magnetic correlations and can be explained as a crossover to a spin ice state [193]. Therefore, like PZO, the physical characteristics of PHO are consistent with a spin ice state that lacks long range magnetic order.

Even though PZO and PHO share these magnetization properties, the signatures of spin ice physics in inelastic neutron scattering (INS) qualitatively differ between the two materials. While both materials have reports of the pinch points in elastic neutron scattering that are characteristic of a tetrahedral structure following ice rules, PZO has a strong inelastic signal that suggests that pseudospins lie in the the local XY plane rather than in the local $\hat{z}$ axis [41, 42, 187]. In contrast, the inelastic neutron scattering of PHO produces a quasi-elastic pattern that resembles expectations of a QSI ground state [45, 200]. The inelastic spectrum in PZO has often been suggested to be caused by a broad spectrum of Pr^{3+} splittings that can be modelled with adapting a random transverse field Ising model (RTFIM) in the spin ice Hamiltonian [42, 43, 178]. Due to its non-Kramers symmetry, the Pr^{3+} ground state doublet is susceptible to distortion from disorder that breaks the D_{3d} crystal field symmetry of this rare earth ion. While such disorder is typically measured using stoichiometric characterization, Trump *et al.* show that even in stoichiometrically ideal samples, the Pr^{3+} ion is displaced ~ 0.01 nm from its ideal position in the $Fd\bar{3}m$ structure of PZO and propose that this displacement in pyrochlores with chemical formulae $A_2B_2O_7$

is due to strain from a mismatch in ionic radii between the A site and B site cations [195]. Strain from the Pr^{3+} ion has been hypothesized as a source of the continuum of splittings in the non-Kramers doublet ion reported in the INS spectra of PZO [42]. If such a structural distortion is due to mismatch in cation radii, we may consider how replacing the transition metal in PZO affects this distortion by comparing it to PHO. The radius of the Hf^{4+} ion of 0.72 Å is slightly smaller than the radius of the Zr^{4+} ion of 0.73 Å [201–203]but the ratio of cations still stabilizes a pyrochloric structure [204, 205]. Despite the slightly larger mismatch in cation radii in comparison with PZO, PHO lacks similar evidence of disorder in the INS spectrum. Therefore, PHO has the potential to actualize a QSI ground state in the absence of the structural distortion that is reported in the QSI candidate PZO.

Reports to date place PHO in a possible spin ice ground state due to pinch points in the elastic neutron scattering, Ising anisotropy in the magnetization, slow spin dynamics and a lack of signatures of magnetic order. Moreover, PHO displays a low temperature anomaly in the field dependence of the magnetization that can be used to estimate the strength of interaction of a spin ice Hamiltonian. Measuring the magnetization at a temperature of 0.08 K, Sibille *et al.* report an anomaly at $\mu_0 H_c \sim 2.4$ T when the field is parallel to [111] which is equivalent to an effective coupling strength of $J_{zz} \approx 1.2$ K based on the expected transition from a "two-in/two-out" to a "three-in/one-out" in the spin ice model [199]. Even so, like PZO, the signatures of transverse exchange interactions in PHO result in softened signatures of Ising anisotropy which differentiate these pyrochlores from CSI candidates. Furthermore, Sibille *et al.* report neutron scattering that is more consistent with a QSI model (as opposed to a CSI model), predicting a speed of photon excitations $v_{pt} \approx 3.6\ \mathrm{m\,s^{-1}}$ at $T = 0.05$ K [45]. However, as of yet, direct unambiguous evidence of the photons, monopoles and visons predicted in the QSI model is lacking for the material. Evidence of a non-phononic linearly dispersive contribution to thermal conductivity at temperatures below the magnetic monopole and vison activation energies would provide a clear signature of the photon excitations that are unique to QSI theories. By measuring the thermal conductivity of PHO, we can examine delocalized excitations in the material and compare our observations with predictions for a QSI ground state.

7.2 Thermal conductivity results

7.2.1 Methods

Anand *et al.* synthesize single crystals of PHO using the floating zone technique, obtaining a lattice parameter of $a_0 = 10.6727(1)$ Å [206]. The transparent and fluorescent green

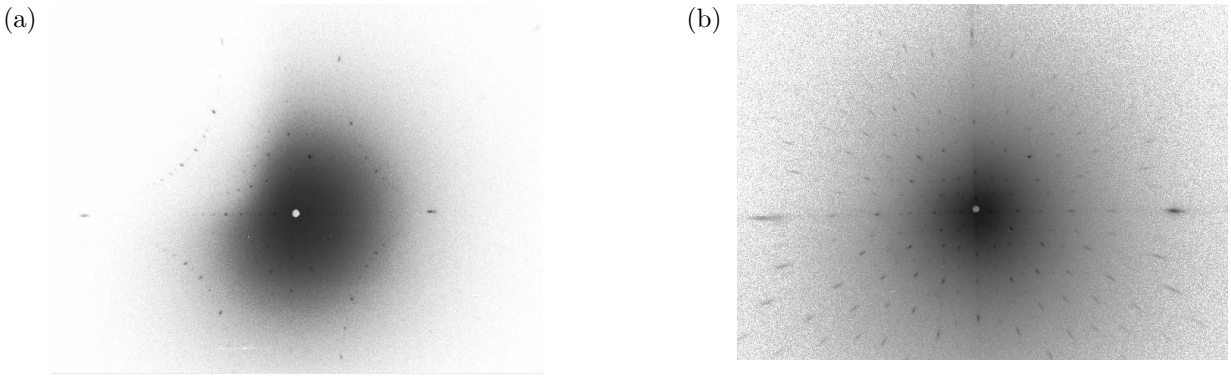


Figure 7.2: Laue X-ray images of PHO samples used in this study. (a) PHO S1 showing the $[\bar{1}\bar{1}0]$ direction perpendicular to the heat current and transverse field directions. (b) PHO S2 showing the [001] direction that is oriented perpendicular to the heat current.

Sample	Dimensions (mm^3)	Geometric factor (cm^{-1})
S1	$1.59 \times 0.592 \times 0.395$	46.6
S2	$0.92 \times 0.394 \times 0.385$	36.9
S3	$1.08 \times 0.234 \times 0.200$	157

Table 7.1: Dimensions of PHO samples S1, S2 and S3 reported as length $\times$ width $\times$ height, and the geometric factor, which is the average length between sample contacts divided by the cross-sectional area.

samples are high quality as indicated by a lack of off-stoichiometry or oxygen deficiency in high-resolution X-ray diffraction refinement, limiting such disorder effects to below 0.5% if present in the samples [44, 206]. We measure the thermal conductivity of three different single crystal samples of PHO. We confirm the orientations of samples using X-ray diffraction, as shown in Figure 7.2. The sample orientation is such that the heat current J_Q is parallel to $[1\bar{1}0]$ and a transverse magnetic field is oriented parallel to [001] for all three samples. After characterizing sample orientations, we cut S2 and S3 from the same starting material by embedding them in crystal bond and using a diamond saw to obtain geometries with smaller cross-sectional areas. Then, we polish the samples to remove any rough surfaces and refine their geometries to the dimensions given in Table 7.1. We use the pumped helium-4 cryostat described in Section 1.1 to obtain thermal conductivity measurements above 1 K and the dilution refrigerator described in Section 1.2 at lower temperatures. We use the steady-state thermal conductivity technique described in Chapter 2 to obtain our results.

7.2.2 Results

We investigate delocalized excitations in PHO using thermal transport. In this section, we present thermal conductivity results of PHO samples S1, S2 and S3 with respect to temperature and magnetic field. We first examine the thermal conductivity of S2 at temperatures up to 50 K. Figure 7.3 shows the resulting thermal conductivity of S2, which increases with temperature most rapidly at temperatures below $\sim$ 15 K. The thermal conductivity has a reduction in slope at $\sim$ 15 K and continues to gradually increase with temperature up to 50 K.

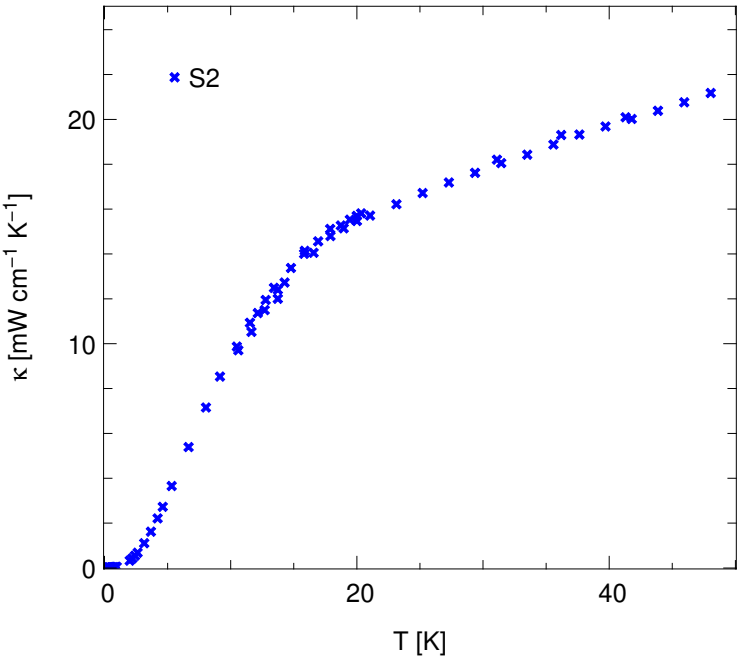


Figure 7.3: Thermal conductivity of PHO S2 at temperatures up to 50 K.

Figure 7.4 reports thermal conductivity results for all samples at temperatures below 1 K on a *log-log* scale. We note two qualitatively different regimes with a transition in behaviour at $\sim 0.1 - 0.2$ K. Below 0.1 K, the thermal conductivity of all three samples reaches a magnitude that depends on the sample cross-sectional area, indicated by the lines that are calculated using Equation (A.13). The exponent of the temperature dependence increases in this regime and approaches the $\kappa \propto T^3$ limit of these lines. In contrast, above 0.1 K, the thermal conductivity of all samples have a decreasing exponent of temperature dependence and start to deviate from a magnitude that depends on sample geometry. By

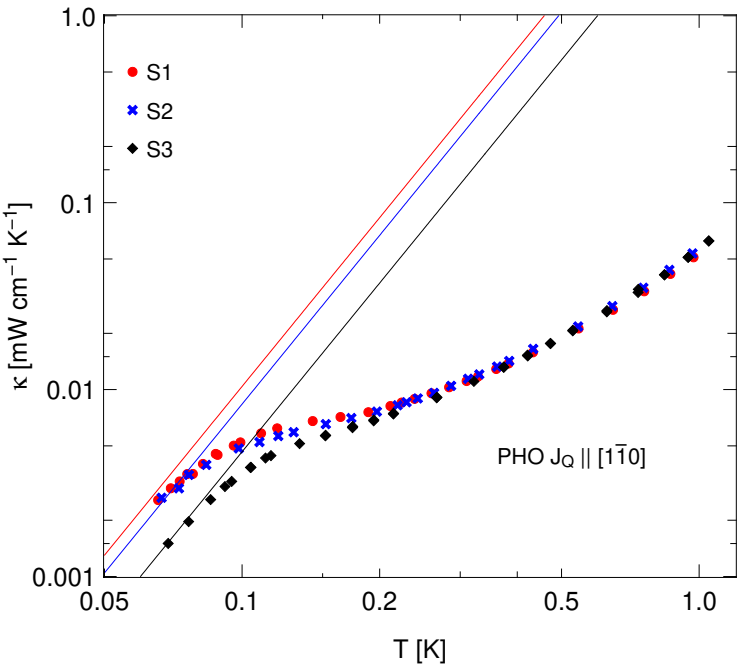


Figure 7.4: Thermal conductivity plotted as a function of temperature in zero field for S1, S2 and S3. Lines are the estimates of maximal phonon conductivity by using a mean free path equal to the geometric mean of the cross-sectional area as in Equation (A.13).

0.2 K, the curves for all three samples overlap, indicating a lack of dependence on sample geometry[1]. The magnitude of the temperature dependence in Figure 7.4 is closer to linear above 0.2 K, however, the lack of conformity to a straight line in this log-log plot indicates that a single power law does not capture the nuances of the temperature dependence of the experimental results.

We next contrast the zero field results with the thermal conductivity in applied magnetic field. Figure 7.5 shows low temperature sweeps for S1, S2 and S2 in applied magnetic fields with heat current parallel to $[1\bar{1}0]$. In Figure 7.5a, above 0.1 K, the thermal conductivity of S1 dramatically increases with the application of even a small magnetic field of 750 mT when orienting the magnetic field perpendicular to the heat current. However, increasing the magnitude of the applied field in this orientation up to 12 T does not significantly increase the thermal conductivity, indicating a relative insensitivity of the phonon scattering to applied field strength. We observe similar behaviour in a transverse applied field for S2 in Figure 7.5b. On the other hand, when orienting a 12 T field parallel to the heat current, the resulting conductivity is significantly lower than that observed in the transverse field orientation. Examining the lowest temperatures, the thermal conductivity for all fields meets at ~ 0.1 K. This field independence at temperatures below 0.1 K is also true for the sample S3 with a smaller cross-sectional area, as shown in Figure 7.5c.

We further explore the field dependence and anisotropy by keeping the temperature constant and changing the magnetic field. In Figure 7.6 we plot the thermal conductivity in applied field, normalized by the zero field value. The unusually dramatic increase in thermal conductivity with an applied field transverse to the heat current direction was not factored in the heating power estimate. While we tried to maintain a constant average sample temperature in the field-dependent results, in actuality this varies by up to 0.04 K for the transverse field configurations from the lack of accounting for a field dependence in thermal conductivity when setting this heater power. However, we obtain qualitative agreement between our field sweeps and temperature sweeps since the solid points in Figure 7.6 are in agreement with the qualitative features of the curve. The largest discrepancy is at the maximum value with field, with both data sets agreeing on a maximal thermal conductivity at ~ 2 T applied transverse to the heat current and at the observed average temperature of ~ 0.55 K. Given the qualitative agreement with the temperature sweep results at a fixed field, the observed anisotropy is clearly due to the application of field rather than any changes in average temperature.

[1]Normally, the thermal conductivity of high quality, non-magnetic or magnetically ordered insulators depends on the sample geometry in the low temperature regime as described in Appendix A.3.1.

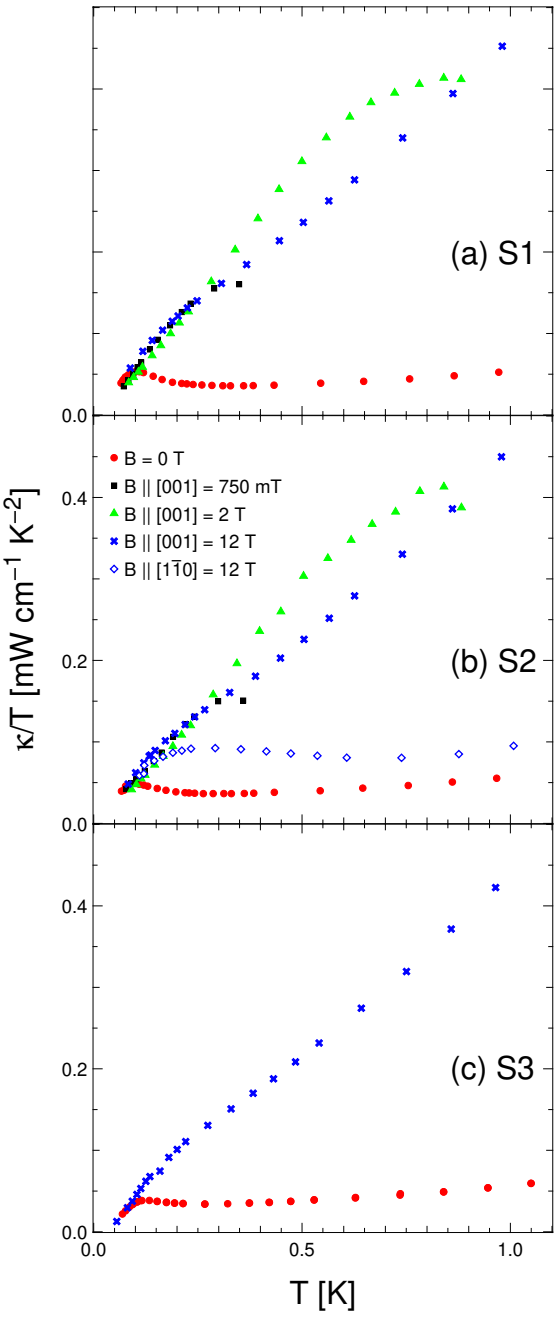


Figure 7.5: Thermal conductivity of PHO samples (a) S1, (b) S2 and (c) S3 at various magnetic fields plotted as κ/T versus T. The heat current is parallel to $[1\bar{1}0]$ for all three samples.

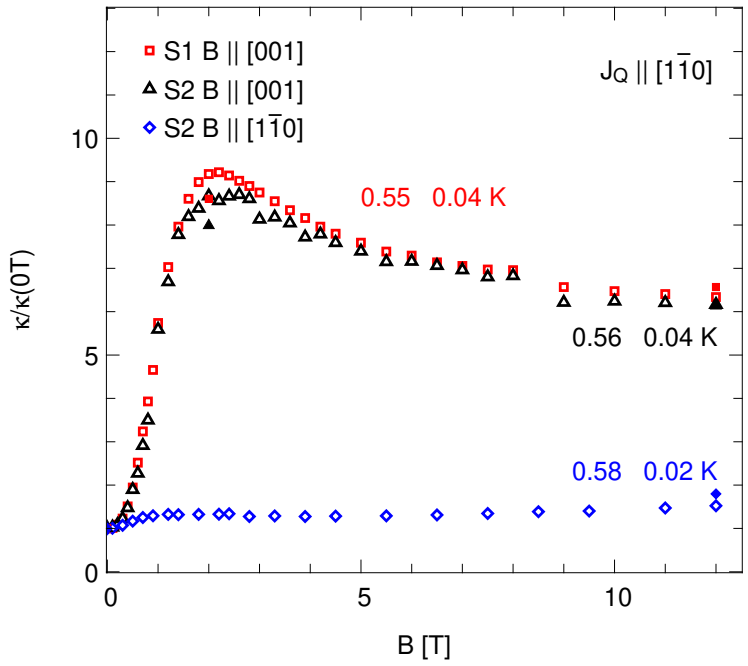


Figure 7.6: Field dependence of thermal conductivity for $Pr_2Hf_2O_7$. Solid points are obtained from the temperature sweeps in Figure 7.5 as a comparison. As discussed in the main text, the average temperature varies by 0.04 K for the sweeps with $B \parallel [001]$ and 0.02 K for the sweep with $B \parallel [1\bar{1}0]$.

7.3 Discussion of PHO results

We discuss our results in comparison to conventional expectations for insulating crystals with phonons as the dominant heat carriers. A brief overview of phonon contributions to thermal conductivity is in Appendix A.3. In insulating crystals, the temperature regime where the phonon wavelength is comparable to the length of crystal imperfections is typically where the phonon scattering with sample disorder becomes most apparent. Phonon scattering in samples with a larger concentration of defects will decrease the maximal conductivity, or the "peak conductivity". However, we observe a striking qualitative suppression of phonon conduction at temperatures above 1 K. Instead of measuring a peak conductivity, we observe a gradual increase across this temperature range. This differs from observations of CSI candidates such as $Dy_2Ti_2O_7$, which reaches a peak conductivity at $T \sim 13$ K for all reported samples including those with detectable concentrations of stoichiometric disorder [1]. The roughly linear in temperature thermal conductivity and the suppression of peak conductivity observed for these high quality samples of PHO bears a superficial resemblance to amorphous materials such as fused silica, which lack a long-range periodic lattice structure [52], despite this material being a single crystal with no disorder detected in X-ray diffraction. When comparing this qualitative behaviour to other single crystals, a peak conductivity is also suppressed in QSL candidates $EtMe_3Sb[Pd(dmit)_2]_2$ [207], $Tb_2Ti_2O_7$ [40] and $YbMgGaO_4$ [208]. In these latter materials, the phonon scattering is thought to be by strong spin fluctuations. The lack of a peak thermal conductivity could then also indicate a spin glass-like state in PHO.

However this strong phonon scattering is reduced at temperatures below 0.1 K. In this regime, the thermal conductivity of high quality insulating crystals is typically is limited by the sample geometry, with a maximal thermal conductivity from phonons estimated using the Casimir limit of Equation (A.13) as discussed in Appendix A.3. The lines in Figure 7.4 show the estimated phonon thermal conductivity in the Casimir limit given by Equation (A.13) and using the sample geometries reported in Table 7.1. At the lowest temperatures, we observe that the thermal conductivity approaches the magnitudes and temperature dependences expected for boundary-limited phonon scattering. This is consistent with our interpretation that the samples are high quality since the predominant term in the phonon scattering rate in Equation (A.14) is a temperature-independent constant that is consistent with the interpretation that sample boundaries limit the phonon mean free path. We can visualize this by plotting the ratio of thermal conductivities of S1 and S3 as plotted in Figure 7.7. Above 0.5 K, this ratio approaches 1 as expected for a material with a strong phonon scattering mechanism. Below 0.1 K, this ratio approaches the ratio of ℓ_C as determined by sample geometries, which indicates a mean free path that is limited by

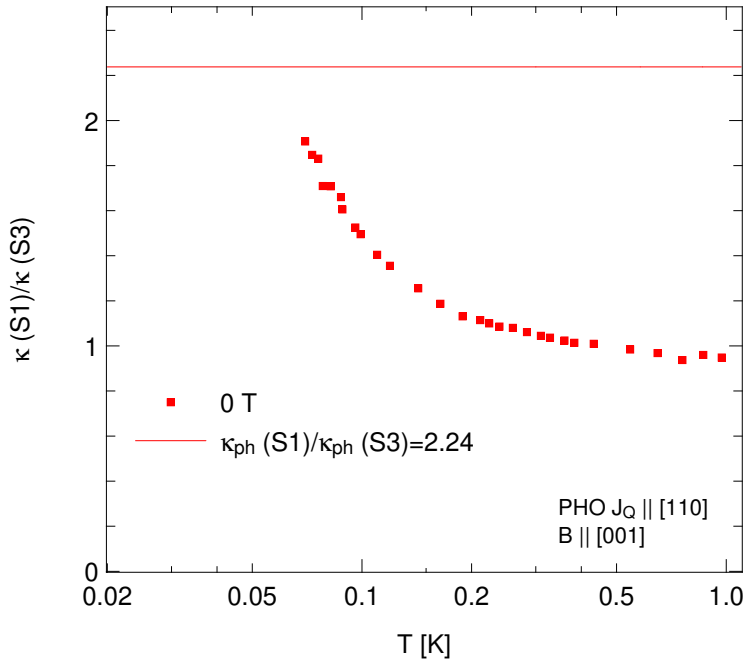


Figure 7.7: Thermal conductivity ratio of S1 and S3, $\kappa(\mathrm{S1})/\kappa(\mathrm{S3})$ at temperatures below 1 K and in zero applied magnetic field, plotted on a semi-log plot. The line is the ratio of the Casimir values of the boundary-limited phonon mean free paths, $\ell_C(\mathrm{S1})/\ell_C(\mathrm{S3}) = 2.24$, as described in the main text.

sample boundaries[2].

An additional phonon scattering mechanism activates at approximately 0.1 K, leading to the aforementioned sample-independent conductivity that is well below the maximal conductivity from phonons. The thermal conductivity magnitude above 0.2 K is notably small and is intrinsic to the material rather than being dependent on sample geometry. The low magnitude of thermal conductivity and lack of scaling of the phonon mean free path with sample size are also indications that PHO displays poor heat conduction in this regime; the thermal conductivity magnitude at 0.3 K is comparable to that of carbon fiber and fibreglass rods, which are composite materials used for thermal insulation in cryogenic applications [209]. These characteristics help to place limits on a phonon scattering model as will be discussed in Section 7.3.2. Next, we will examine the low temperature regime to compare the boundary-limited thermal conductivity with expectations of the QSI model.

[2]The red line in Figure 7.7 is the ratio of $\ell_C(\mathrm{S1})/\ell_C(\mathrm{S3})$, which have $\ell_C(\mathrm{S1}) = 5.46 \times 10^{-2}$ cm and $\ell_C(\mathrm{S3}) = 2.44 \times 10^{-2}$ cm respectively.

7.3.1 Searching for photon excitations

We analyze the low temperature thermal conductivity of QSI candidate PHO to investigate whether magnetic monopoles, visons and particularly photons are detectable as delocalized, heat conducting excitations. Given predictions of gapless, linearly dispersive photons, we expect to see an enhancement of thermal conductivity at the lowest temperatures, above the magnitude expected for phonon conductivity if this material is in fact a QSI. We also expect a change in behaviour of excitations when applying a magnetic field due to the impact of this field on the spins that generate such excitations. While the exact behaviour of photons with field is yet to be experimentally realized, Lee and Moon [170] predict that an external magnetic field reduces the photon scattering rate due to decreased scattering with visons, increasing the thermal conductivity in temperature regions where visons could be energetically activated. Conversely, as discussed in Section 6.1.5, an applied magnetic field reduces the magnetic monopole density in CSI candidates including $Dy_2Ti_2O_7$ and $Ho_2Ti_2O_7$. In either case, by polarizing spins, the excitations generated by frustrated spins depend on the strength of the applied magnetic field. However, as discussed in the previous section, the thermal conductivity in the lowest temperature regime does not exceed the maximal thermal conductivity from phonons. In this section, we will compare the magnitude and scaling with sample size of the zero field thermal conductivity below 0.1 K to that expected for photon excitations.

For us to rule out photons, we need to take into account the size of the photon contribution that we are expecting to see. The contribution from photons can be estimated using the usual kinetic theory expression described in Appendix A.1 and the specific heat of photon excitations C_{pt} in Equation (6.6). Using these expressions, and converting specific heat the usual way from moles to volume by multiplying by number density Z/V and Avogadro's constant N_{A}, and by knowing the speed of light in the material v_{pt}, we can estimate the thermal conductivity contribution from photons, κ_{pt}, as

$$\kappa_{\text{pt}} = \left(\frac{\pi^2}{90}\right) \frac{RZ}{N_{\text{A}}} \left(\frac{k_{\text{B}}}{\hbar}\right)^3 \frac{\ell_{\text{pt}}}{v_{\text{pt}}^2} T^3 \tag{7.1}$$

for photon mean free path $\ell_{pt}(T)$. The unknowns are the speed of light and the mean free path, given that we do not have any confirmed realizations of photon excitations. Lee and Moon [170] predict that similarly to phonons, the mean free path will scale with sample boundaries at the lowest temperatures. They show that in this limit, the ratio of the photon conductivity κ_{pt} to the total conductivity κ_{tot} is approximately related to the ratio of the speeds $\alpha \equiv v_s/v_{\text{pt}} \gg 1$ due to the dependence on specific heat and velocity as

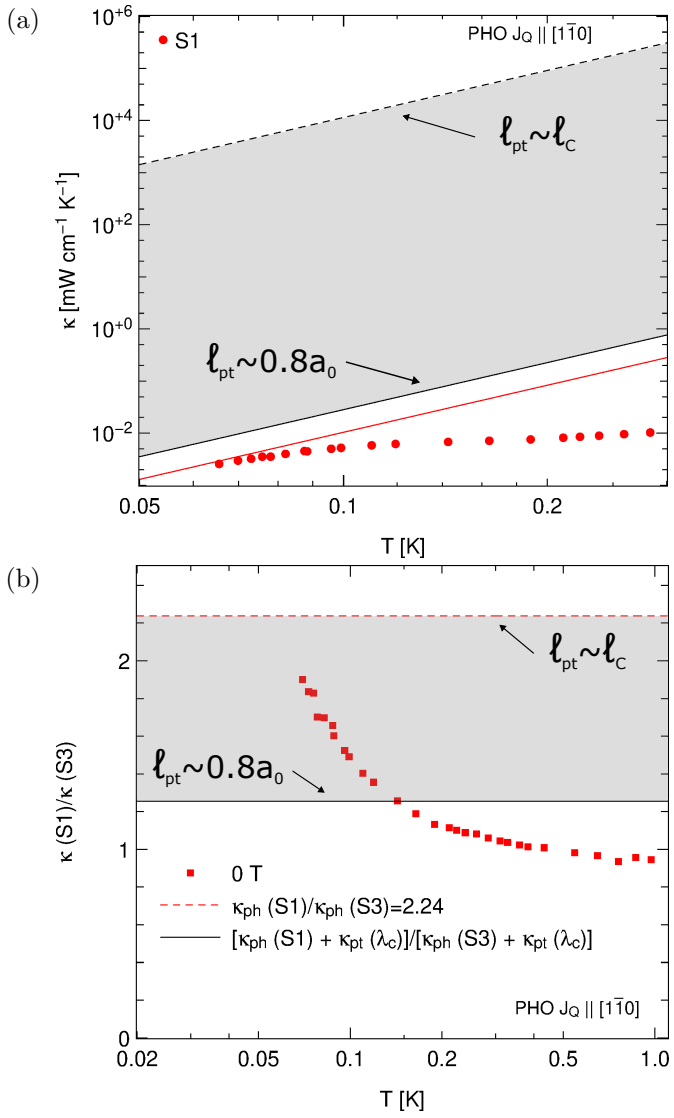


Figure 7.8: Illustration of the estimated total expected phonon + photon thermal conductivity (gray shaded areas). Photon contributions are calculated using Equation (7.1) and Sibille *et al.*'s estimated photon speed, $v_{\rm pt} \sim 3.6\ {\rm m\,s^{-1}}$ [45], with photon mean free path $\ell_{\rm pt}$ ranging from a minumum of $\lambda_C \approx 0.8\,a_0$ (solid black lines) to a maximum of ℓ_C (dashed lines). (a) Plotted as κ versus T on a log-log graph. The red circles are PHO S1 experimental data in zero field and the red line is the estimate of the maximal phonon thermal conductivity as in Figure 7.4. (b) Thermal conductivity ratio of S1 and S3, κ(S1)/κ(S3) at temperatures below 1 K and in zero applied magnetic field plotted on a semi-log graph.

$$\frac{\kappa_{\mathrm{pt}}}{\kappa_{\mathrm{tot}}} = \frac{C_{\mathrm{pt}} v_{\mathrm{pt}}}{C v_s + C_{\mathrm{pt}} v_{\mathrm{pt}}} \approx \frac{v_s^2}{v_s^2 + v_{\mathrm{pt}}^2} = \frac{\alpha^2}{\alpha^2 + 1} \tag{7.2}$$

noting that aside from the differing quasiparticle speeds, the photon specific heat capacity $C_{\mathrm{pt}} \propto T^3$ [Eq. (6.6)] only differs from the phonon specific heat capacity C in Appendix A.3.1 by a scaling factor, facilitating the above approximation. Since speeds of sound are typically on the order of $10^3\ \mathrm{m\,s^{-1}}$ compared to hypothetical speeds of light of magnitude $v_{\mathrm{pt}} \sim 10\ \mathrm{m\,s^{-1}}$, the boundary limited thermal conductivity in QSI materials is expected to be dominated by photon conduction ($\kappa_{\mathrm{pt}}/\kappa_{\mathrm{tot}} \approx 1$) [170]. Specifically for PHO, we can estimate the speed of sound using the Debye temperature $\Theta_{\mathrm{D}} = 574\ \mathrm{K} \pm 4\ \mathrm{K}$ of non-magnetic reference material $La_2Hf_2O_7$ [3] with Equation (A.10) getting $v_s = 4.63 \times 10^3\ \mathrm{m\,s^{-1}}$ which is three orders of magnitude larger than Sibille *et al.*'s estimate of $v_{\mathrm{pt}} \sim 3.6\ \mathrm{m\,s^{-1}}$ at $T = 0.05\ \mathrm{K}$ [45]. In comparison, Tokiwa *et al.* report a best fit to the specific heat capacity of PZO using speed of light $v_{\mathrm{pt}} \approx 90\ \mathrm{m\,s^{-1}}$ [46], which is still nearly two orders of magnitude smaller than their reported speed of sound of $v_s \approx 3.7 \times 10^3\ \mathrm{m\,s^{-1}}$. Therefore, the assumption $\alpha \gg 1$ is satisfied for these materials should they conform to the QSI model. Hence, if the photon mean free path is comparable to sample boundaries in high quality QSI materials at the lowest temperatures, then we expect to observe a photon thermal conductivity that is overwhelmingly larger than the phonon contribution. We plot this estimate with the zero field conductivity in Figure 7.8a. The estimated photon thermal conductivity according to Equation (7.1) and a mean free path $\ell_C = \sqrt{4A/\pi}$ [using Eq. (A.7)] is six orders of magnitude larger than our observed thermal conductivity at the lowest temperatures, and this estimate further deviates from our observations as temperatures increase. At $< 0.0001\%$ of the estimated total thermal conductivity of photons and phonons, our observed thermal conductivity is simply to small to justify that photons with such behaviour are present in our samples.

To reconcile our observations with predicted photon excitations in this QSI candidate, suppose instead that photons could be present in the material but are strongly scattered. Our data can place limits on the expectations of such a scenario. Benton *et al.* [177] find a photon coherence length λ_C that tunes the curvature of the photon dispersion relation. In the QSI region of their model, the authors numerically estimate $\lambda_C \approx 0.8\ a_0$, with longer wavelengths promoting linearly dispersive photons and shorter wavelengths instead approaching the classical dipolar correlations. If we suppose that the photon mean free path is limited by its shorter wavelength instead of sample boundaries and take the minimal limit

[3] Debye temperature of $La_2Hf_2O_7$ obtained by correspondence with collaborators, fitting low temperature data from [210] to $C_p = \gamma T + \beta T^3 + \delta T^5$ and using the relation $\Theta_{\mathrm{D}} = \left(\frac{12\pi^4 nR}{5\beta}\right)^{1/3}$.

of the mean free path equal to this coherence length, we would expect a photon contribution that is cubic in temperature and slightly larger in magnitude than the phonon contribution (Figure 7.8a black line). Our measured thermal conductivity is approximately one third of the estimate with the shortest reasonable photon mean free path. However, due to the large photon specific heat capacity, even if a photon mean free path is significantly smaller than sample boundaries, the total thermal conductivity is still dominated by this contribution and would therefore approach a sample-independent scaling even at the lowest temperatures. Figure 7.8b compares the expected scaling in each mean free path extreme with our results. We see a scaling with sample geometries that is consistent with linearly dispersive, delocalised quasiparticles scattering with sample boundaries. This scaling is consistent with expectations of phonons in the boundary scattering limit as discussed in Section 7.2.2, or, using identical arguments, with an additional photon contribution so long as the photon mean free path also approaches this sample-dependent limit ℓ_C. Since we rule out a contribution of photons that reaches this limit, we cannot reconcile both the sample scaling observations and the magnitude of thermal conductivity with an additional photon contribution. Rather, our observations are most simply explained as phonons with a mean free path approaching ℓ_C below 0.1 K and additional, gapped phonon scattering mechanism(s) reducing the phonon mean free path at higher temperatures.

7.3.2 Models of phonon scattering

If we rule out photon excitations, we can assume that the main heat-carrying excitations are phonons. Above 0.1 K, a scattering mechanism reduces the phonon mean free path from the expected scaling with sample boundaries, resulting in an approximately linear thermal conductivity. We will next explore how we interpret and model the phonon scattering behaviour. Such a strong temperature dependence and the large phonon scattering sustained up to temperatures as high as 20 K is unusual even among other frustrated pyrochlores as discussed in Section 7.3. Instead, the results more closely resemble glassy behaviour which can suppress a peak thermal conductivity. The slow growth of the zero field conductivity with temperature and suppression of peak conductivity is also observed in the thermal conductivity of non-Kramers QSI candidates $Tb_2Ti_2O_7$ [40], $Pr_2Zr_2O_7$ [46], and metallic spin liquid candidate $Pr_2Ir_2O_7$ [47, 48]. In Figure 7.9a, the slopes of these materials run nearly parellel above 0.5 K, indicating that these materials share a similar exponent α for the power law $\kappa \propto T^{\alpha}$. Moreover, in Figure 7.9b, we observe that a high temperature peak thermal conductivity is suppressed for $Tb_2Ti_2O_7$ and $Pr_2Ir_2O_7$[4]. The

[4] An interpretation of peak conductivity behaviour is inconclusive for $Pr_2Zr_2O_7$, since Tokiwa *et al.*'s thermal conductivity reports only extend up to ~ 10 K [46].

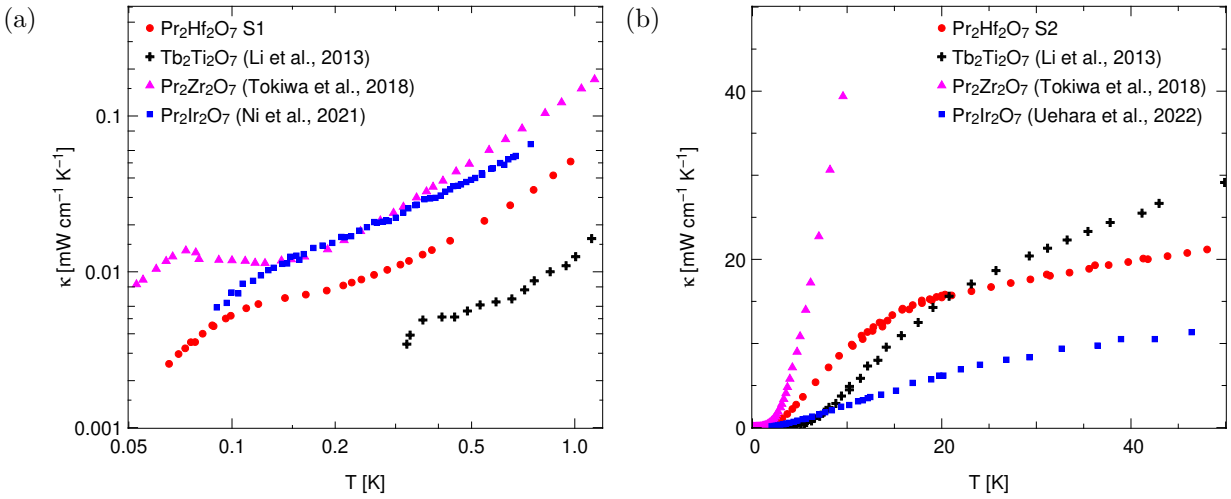


Figure 7.9: Comparisons of PHO 0 T thermal conductivity with QSI candidates $Tb_2Ti_2O_7$ [40], $Pr_2Zr_2O_7$ [46] and $Pr_2Ir_2O_7$ [47, 48]. (a) Low temperature thermal conductivity plotted on a log-log graph. (b) High temperature thermal conductivity.

authors attribute the thermal conductivity in these materials to phonon scattering from spin fluctuations. Such an explanation can also apply to PHO, whose *ac*-susceptibility has a frequency-dependent peak associated with spin freezing at temperatures below 0.2 K [44, 199]. Indeed, our results can be qualitatively understood as phonons scattering with spin fluctuations, and a freezing of these fluctuations at $\sim 0.1 - 0.2$ K resulting in a recovery of a boundary-limited phonon mean free path. Unfortunately, a quantitative analysis of phonon scattering rate of the thermal conductivity is unreported to date for the aforementioned pyrochlores, which is unsatisfactory when attempting to fully characterize quasiparticle excitations in the material[5].

Both the praseodymium and terbium pyrochlores with reports of strong spin fluctuations have a non-Kramers magnetic ion, which is sensitive to disorder that causes lattice strain, altering the symmetry of the crystal electric field (CEF) to split a ground state doublet into two singlets. Even though lattice disorder from non-magnetic impurities (such as point defects, vacancies, stacking faults and grain boundaries) typically does not result in a field-dependent thermal conductivity, the energy separation of two singlets in close

[5]Recently, Uehara *et al.* [48] report a successful Monte Carlo simulation for $Pr_2Ir_2O_7$ using a RTFIM Hamiltonian to describe how a continuum of splittings can reduce the thermal conductivity, with an expression resembling Orbach's expression of a specific heat contribution from a low-lying optical mode [211]. Though this expression requires multiple fitting parameters, such a numerical approach may also be possible when reproducing the thermal conductivity of PHO.

proximity does have a field dependence as observed in paramagnetic resonance scattering in the thermal conductivity. A Zeeman effect increases the separation of a split ground-state doublet, shifting the energy of the phonons required to interact with the splitting as described in Appendix A.3.4. Phonon resonant scattering from such a scenario could be consistent with the strong field dependence that is discussed in Section 7.2.2. Applying this concept to PHO, paramagnetic resonance scattering could result from phonons interacting with praseodymium ions with a ground state non-Kramers doublet split by the presence of lattice strain that breaks the local $\langle 111 \rangle$ symmetry of the magnetic dipole moment. As discussed in Section 6.3.2 on PZO, even a small displacement ~ 0.01 nm of the magnetic Pr^{3+} ion, a structural disorder which can go undetected by conventional characterization studies, could explain observations of a continuum of splittings in the INS spectra [42, 195]. Compared to PZO, the quasi-elastic spectra observed in PHO places a smaller limit on the potential strength of these splittings but does not necessarily rule them out. Given that our thermal conductivity measurements access lower energies than are typically available by neutron scattering, we consider a model that includes the effects of such splitting in our thermal conductivity results despite the lack of evidence of a quasi-elastic neutron scattering spectra in PHO. A split Pr^{3+} ground state doublet could induce phonon resonant scattering, similarly to observations of the thermal conductivity of praseodymium ethyl sulphate and $PrCl_3$ [212–214]. Inspired by the relaxation time for a simple mechanical oscillator, Pohl models phonon resonant scattering for a single resonance frequency with the scattering rate

$$\tau_{\text{res1}}^{-1} = \frac{AH\omega^2}{(\omega^2 - \omega_0^2)^2 + (\Lambda/\pi)^2\omega_0^2\omega^2} \tag{7.3}$$

with resonance frequency ω_0, half width $H = \frac{\Lambda\omega_0}{2\pi^2}$, and logarithmic decrement Λ[6] [215]. This model of phonon scattering successfully fits the thermal conductivity of praseodymium ethyl sulphate [213]. The black line in Figure 7.10 shows a fit of our 0 T thermal conductivity of PHO S1 to Equation (A.15) with $\sum_i \tau_i^{-1} = v_s/\ell_c + \tau_{\text{res1}}^{-1}$ where the first term is the expected phonon scattering from the sample cross-sectional area given by Equation (A.7). The fit to this simple expression is not successful in reproducing the reduction in phonon scattering with decreasing temperature.

Another possibility is that gapped magnetic monopole excitations scatter phonons. In classical spin ice, the contribution to thermal conductivity is related to the monopole density $\rho(T)$ which is activated due to a monopole gap Δ, $\rho(T) \sim \exp(-\Delta/T)$ [1, 37, 216]. It has been reported that monopoles are expected to be localized, scattering phonons in the

[6]The logarithmic decrement is related to the strength of dampening in a mechanical oscillator [215].

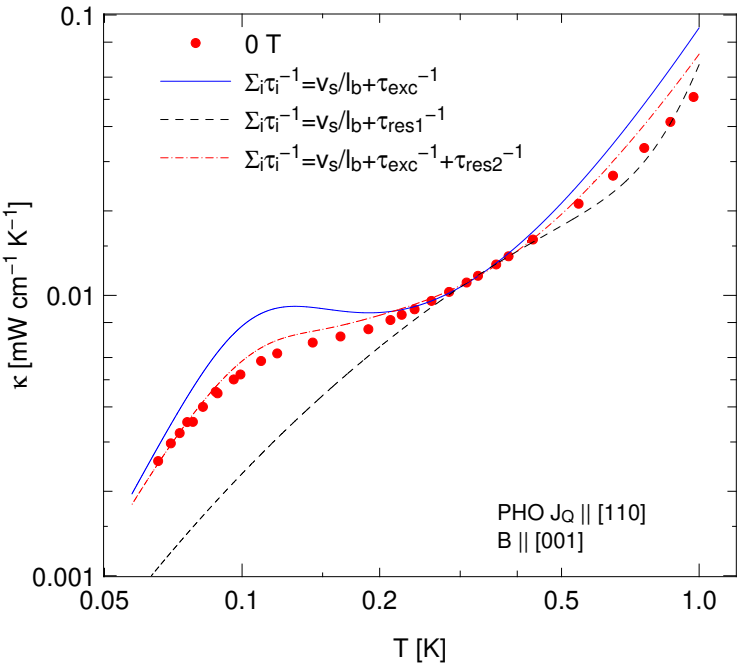


Figure 7.10: Fitting thermal conductivity in zero field of S1 using the Callaway model with total scattering rates $\sum_i \tau_i^{-1} = v_s/\ell_C + \tau_{\rm exc}^{-1}$ (solid blue line), $\sum_i \tau_i^{-1} = v_s/\ell + \tau_{\rm res1}^{-1}$ (dashed black line), and $\sum_i \tau_i^{-1} = v_s/\ell_C + \tau_{\rm exc}^{-1} + \tau_{\rm res2}^{-1}$ where $\tau_{\rm res2}^{-1}$ (dashed-dotted red line). The scattering rate components $\tau_{\rm exc}^{-1}$, $\tau_{\rm res1}^{-1}$ and $\tau_{\rm res2}^{-1}$ are given by Equations (7.4), (7.3) and (7.5) respectively. The fixed parameter v_s/ℓ_C is the expected phonon scattering by sample boundaries [Eq. (A.7)].

spin-fluctuating QSI rather than contributing to heat transport [40], similar to the role of spin fluctuations scattering phonons in electron-doped superconductor $Ba(Fe_{1-x}Co_x)_2As_2$ [217], Kitaev spin liquid candidate α-$RuCl_3$ [218] and Z_2 QSL candidate herbertsmithite [219]. Most simply, we can fit a monopole excitation as an activated phonon scattering term

$$\tau_{\text{exc}}^{-1} = B \exp(-\Delta/T). \tag{7.4}$$

In comparison, Sibille *et al.* report a relaxation time energy scale of 0.86 K for this form of relaxation rate in the susceptibility of PHO [199]. The best fit to a total scattering rate of $\sum_i \tau_i^{-1} = v_s/\ell_C + \tau_{\text{exc}}^{-1}$ is illustrated by the blue line in Figure 7.10. This fit does not resemble our observations either. Qualitatively, the fit to scattering by a gapped excitation has a similar shape to our results but does not reproduce the quantitative values, and the resonant scattering model deviates more from observations at lowest temperatures, possibly due to expectation of ground state gap ω_0. A combination of both scattering terms, $\sum_i \tau_i^{-1} = v_s/\ell_C + \tau_{\text{res1}}^{-1} + \tau_{\text{exc}}^{-1}$ also is not successful in reproducing our results.

Another possibility is that the paramagnetic scattering term takes a different form than that of Equation (7.3) due to a different underlying process dominating the scattering. Scattering of the form $\tau_{\text{res1}}^{-1} \propto \omega^2$, like Equation (7.3), arises from single phonon absorption and emission, but Toombs and Sheard [220] propose an alternate scattering behaviour arising from the coupling of spins and phonons that is proportional to ω^4 in analogy to the elastic Rayleigh scattering of photons by smaller particles. Their expression for spin-phonon scattering by paramagnetic ions is

$$\tau_{\text{res2}}^{-1} = \frac{3\pi c \epsilon^4 \omega_0^4 \omega^4}{2\omega_D^3(\omega^2 - \omega_0^2)^2} \tag{7.5}$$

where $c = N_s/N$ is the ratio of the number of spins contributing to this process N_s and the number of magnetic ions N. Typically, the unitless spin-lattice coupling parameter ϵ^4 is $\sim 10^4$ for strong coupling, and c is a concentration that is less than unity by definition, while the Debye frequency ω_D is a known quantity [220–223]. Though this form of scattering alone still does not explain our results, by using $\tau_{\text{tot}}^{-1} = v_s/\ell_C + \tau_{\text{res2}}^{-1} + \tau_{\text{exc}}^{-1}$ to fit S1 data to four unknowns, we obtain excellent agreement with the zero field results. The red line in Figure 7.10 shows a fit of S1 to this total scattering rate, obtaining $c\epsilon^4 = 6.8 \times 10^3$, $\omega_0 = 0.69$ K, $B = 2.7 \times 10^9$ s^{-1} and $\Delta = 0.79$ K. Physically, Mori *et al.* also relate scattering behaviour in the form of Equation (7.5) to the quadrupolar moments in the terbium gallium garnet $Tb_3Ga_5O_{12}$, justifying the scattering rate proportional to ω^4 as originating from the

quadrupole Coulomb interaction of excess (superstoichiometric) Tb^{3+} ions [224], which is also a plausible physical scenario for PHO. This scenario will be discussed in more detail when analysing the in-field results in Section 7.3.3.

7.3.3 In-field behaviour

The in-field behaviour offers more clues to the origin of the strong phonon scattering in zero field. The observed anisotropy could be consistent with the gapped excitations expected in a QSI ground state. As shown in Figure 7.5, the thermal conductivity at temperatures below ~ 0.1 K is effectively field independent in the absence of magnetic scattering, ruling out photon excitations as a source of strong scattering. So we instead look for gapped magnetic excitations causing phonon scattering to explain the field dependent thermal conductivity at higher temperatures. Since we do not see evidence of the predicted QSL ground state, we look to other excitations in spin ice models. In particular, we can compare our observations with monopole excitations. Due to the geometry of the pyrochlore, a field applied parallel to [001] interacts with spins on all corners of the tetrahedron, whereas a field parallel to $[1\bar{1}0]$ polarizes spins on the α chain, leaving spins on the β chain free to move. When applying field parallel to [001] and transverse to heat current, we observe a larger reduction in scattering than when applying field parallel to $[1\bar{1}0]$ as well as heat current. The observed decreased phonon scattering (and higher thermal conductivity) in a [001] field compared to a $[1\bar{1}0]$ field, as shown in Figures 7.5 and 7.6, is consistent with reduced spin fluctuations in spin ice anisotropy. A similar anisotropy is reported in neutron scattering [200] and magnetization [199] of PHO, with a transition appearing at fields $H \sim 2.5$ T. So the peak in the 0.5 K, $B \parallel [001]$ field sweep data at ~ 2 T could indicate a transition from a two-in/two-out state to a three-in/one-out, one-in/three-out state using the spin ice model. Slight deviations in the transition field could be due to a small misalignment of the magnetic field or a variation in average sample temperature in the $B \parallel [001]$ field sweep runs due to the drastic changes in thermal conductivity, which increases up to a factor of 9 from the zero-field data, an anomalously large variation. Naively in classical spin ice picture, we would expect a large [001] field to polarize all spins, decreasing spin fluctuations, whereas a $[1\bar{1}0]$ field polarizes two spins per tetrahedron along α chains, still allowing fluctuations along β chains. Notably though, the thermal conductivity does not reach the maximal limit expected for phonons, even in fields as high as 12 T as shown in Figure 7.5. A similar deviation from the CSI anisotropy is observed in the magnetization of PHO and is explained as a possible mixing of the ground state multiplet or non-Ising contributions [44]. Perhaps the spin ice picture alone cannot explain the magnetic field dependence of thermal conductivity.

Alternatively, we can qualitatively explain our observed field dependence by examining the strong spin-phonon scattering. This form of scattering is also invoked in QSI candidate $Tb_2Ti_2O_7$, which has a large phonon Hall effect whose origin is still a matter of debate, but may be attributed to the spin-phonon interactions without invoking an explanation of novel excitations [182, 183]. The magnetoelastic interaction strengths from spin-phonon coupling have a non-trivial relation to the elastic constants, and this relation could hypothetically be applied to the analysis of PHO in order to anticipate magnetic field effects. However, we would need to invoke a more involved fitting to apply these concepts to PHO in the presence of a magnetic field. An anisotropic spin-phonon coupling also does not rule out the possibility of other gapped excitations, but it does complicate an attempt to model the field-dependence of the thermal conductivity. For example, it's plausible that a large applied [001] field eliminates τ_{exc}^{-1} in the fitting shown by the red line in Figure 7.10 while an applied $[1\bar{1}0]$ field still promotes such phonon-scattering excitations through the two unpinned spins, but this scenario is unprecedented within the pyrochlores and hence difficult to fit with confidence. We have also attempted modelling the in-field conductivity using the field-dependent spin-phonon scattering expression of Mori *et al.* [224], which successfully reproduces coupling parameters and phonon Hall conductivity in $Tb_3Ga_5O_{12}$, but have yet to reproduce our PHO results using the physical parameters of the model. Nonetheless, the exotic field dependence in PHO is unique among the pyrochlores, even in comparison with praseodymium-based rare-earth pyrochlores PZO [46] and $Pr_2Ir_2O_7$ [47]. Therefore, PHO is an intriguing material for examining the interplay of quadrupolar degrees of freedom with spin fluctuations on a pyrochlore lattice.

7.4 Interpretation of $Pr_2Hf_2O_7$ ground state

If we assume that the three-parameter fit to total phonon scattering rate $v_s/\ell_C + \tau_{\text{exc}}^{-1} + \tau_{\text{res2}}^{-1}$ in Figure 7.10 quantitatively explains our results, we can compare the magnitudes of our fit parameters to the energy scales of other reports for PHO. Here, we will assume that the physical interpretation of ω_0 is the average separation of the ground state singlets of Pr^{3+} ions with split ground state doublets from strain in the lattice disrupting the D_{3d} symmetry. Even though the size of the splitting reported here is of a small scale, smaller that the typical energy levels accessible by neutron scattering, theoretically, PHO could still be driven out of a QSI phase by disorder as discussed in Section 7.2.5. According to Equation (6.7), the critical value of the average random transverse field strength $\bar{h}$ that drives a QSI candidate with similar disorder out of a QSI ground state is $\approx 0.6\,J$ [43, 197]. We can look to classical spin ice to interpret the excitation gap found from the fit shown

by the red line in Figure 7.10 in terms of an estimate for J. According to Castelnovo *et al.*, at $T \to 0$, the monopole density for CSI is $\rho \sim \exp(-\Delta/T)$ where Δ is the dressed monopole density that also appears in the magnetic relaxation time in the susceptibility as $\tau \sim \tau_0 \exp(\Delta/T)$ for time scale τ [147]. While the exact relation between the dressed monopole and the bare monopole density is not trivial due to accounting for interactions with other monopoles, at low temperatures the energies should be of comparable strengths. Approximating $J_{\text{eff}} \sim \Delta \approx 0.79$ K from the best fit parameter for Equation (7.4), then the maximum theoretical average random transverse field in the limit of zero distribution width that keeps the phase a QSL is $\bar{h} \approx 0.6J \sim 0.5$ K [Eq. (6.8)], which is of comparable magnitude to the splitting magnitude derived from the fit of $\omega_0 \sim 0.69$ K. Incorporating a distribution width of up to $\delta h = \omega_0/2 \sim 0.35$ K increases this maximal average slightly to 0.5 K to satisfy the relation $2J - 3\bar{h} + \frac{7}{8J}\delta h^2 - \frac{5\bar{h}^2}{8J} > 0$, which is also comparable to ω_0. Using these rough estimates places PHO on the verge of the energy scales predicted for a QSI state. But absent observations of the photon excitations predicted to contribute to thermal conductivity in this phase, it is possible that PHO is in a paramagnetic ground state phase that is proximal to the predicted QSI phase. Such a phase may have gapped magnetic excitations (ie. monopoles or visons) that scatter phonons, given the agreement of our fitting that includes a relaxation rate of the form in Equation (7.4).

Our thermal conductivity results at low temperatures are most consistent with phonons as the sole heat-conducting contribution, approaching the maximal contribution expected given sample geometries at the lowest temperatures. We observe strong phonon scattering at temperatures above ~ 0.2 K that results in stronger phonon scattering than that of amorphous materials. While we have no direct evidence of disorder in our PHO samples, perhaps a splitting of the Pr^{3+} ground state doublet similar to reports for PZO could cause this anomalous scattering. Moreover, given the reports consistent with spin ice physics for this material and the Ising anisotropy observed in the thermal conductivity, gapped magnetic excitations such as magnetic monopoles could also explain the observed phonon scattering.

The lack of observation of heat-conducting photon excitations in the PHO thermal conductivity casts serious doubt on the material having a QSI ground state. We instead interpret the thermal conductivity in this material as having some features consistent with spin ice physics as well as single ion physics. Nonetheless, experimental observations in the material have striking differences from reported CSI materials namely strong phonon scattering that isn't fully reduced in fields as high as 12 T. In terms of potential ground states in the spin ice theory, we cannot rule out novel states with quadrupolar correlations [174, 196, 225].

Our results may in fact be most consistent with pseudospins favouring an orientation

along quadrupolar degrees of freedom. Given the reports of a gapless, linearly dispersive mode in neutron scattering [45], such a state may instead be proximal to an antiferro-quadrupolar (Q-AIAO) phase with pseudospins aligned along the local $\langle 100 \rangle$ axis, as suggested for PZO [41, 196]. The ψ_3 phase has a linearly dispersive excitation with a small gap [38, 41]. It is of interest to further characterize the excitations using this model to compare the energy scales of excitations with experimental results in PHO.

Summary

Quantum materials with strong magnetic interactions are prime candidates for research when attempting to discover new phases of matter. In particular, the topological Kondo insulator candidates as well as the quantum spin ice candidate studied in this thesis have rich magnetic behaviour accompanying a suppression of magnetic ordering. However in real materials, the introduction of disorder in the lattice can leave open questions about intrinsic magnetic ordering behaviour and whether disorder drives the ground state away from theoretical predictions.

Our studies of thermal transport probe delocalized quasiparticles to answer such questions about the ground state magnetic phases. In the materials studied, despite a lack of magnetic ordering, the ground states are not obviously a trivial paramagnet and deserve more studies to characterize their phases. Distinguishing observations from those expected for conventional insulators is key to test ground state predictions.

We place the SmB_6 FZ1 and FZ2 samples in the high quality limit by reporting a mean free path that scales with sample boundaries at the lowest temperatures. To explain seemingly contradictory interpretations of thermal conductivity results, such as the magnetic scattering scenario proposed by Boulanger *et al.* [23], we measure a disordered sample FZ3. By measuring FZ3, we show how the presence of additional disorder can complicate interpretations of a thermal conductivity enhancement with applied field, such that the enhancement could be obscured by a lower phonon conduction. Therefore sample disorder must be considered when interpreting an anomalous thermal conductivity enhancement.

Additionally, we test the oscillatory magnetostriction of SmB_6 FZ1 and report preliminary data that requires further investigation. This preliminary data corroborates a previous report by our collaborators of exotic metallic-like behaviour in the bulk of these samples that challenges our understanding of quantum oscillations as an exclusive metallic property [21]. Since the reproducibility of such a finding currently poses a challenge [92], to reconcile the variation in interpretations of quantum oscillations in these TKI candidates, it is of future interest to investigate the role of disorder by measuring bulk quantum oscillations of different SmB_6 sample growths. Nonetheless, the independent reports of quantum oscillations in the specific heat of flux grown SmB_6 [103], as well as quantum oscillations and an anomalous thermal conductivity enhancement in floating zone grown TKI YbB_{12} [226–228] suggest that exotic metallic-like behaviour may not be exclusive to floating zone grown samples of SmB_6. A thorough examination of other Kondo insulators for metallic-like bulk properties could help characterize the conditions required to observe such exotic bulk phenomena.

We also report the thermal conductivity of QSI candidate $Pr_2Hf_2O_7$ to unequivocally detect the "photon" excitations predicted for this U(1) QSL state. However, we do not de-

tect such excitations. The lack of an obvious photon contribution to thermal conductivity means we cannot claim that this material settles into a predicted QSI ground state. Instead, we observe signs of strong spin-phonon scattering in the QSI candidate $Pr_2Hf_2O_7$. This scattering could stem from quadrupolar effects, which could potentially be enhanced by distortions of the crystal lattice that split the non-Kramers doublet ground state. Agreement between our zero-field results and the trial model of spin-phonon scattering with localized, phonon-scattering magnetic monopole excitations suggest the possibility of a ground state that is proximal to quadrupolar antiferromagnetic order. A quantitative analysis of the strong magnetic anisotropy that we report could help us understand whether localized magnetic monopoles are indeed ground state excitations in the material.

References

[1] W. H. Toews, J. A. Reid, R. B. Nadas, A. Rahemtulla, S. Kycia, T. J. S. Munsie, H. A. Dabkowska, B. D. Gaulin, and R. W. Hill, Physical Review B **98**, 134446 (2018).

[2] H. Fukazawa, R. G. Melko, R. Higashinaka, Y. Maeno, and M. J. P. Gingras, Physical Review B **65**, 054410 (2002).

[3] F. Pobell, in *Matter and Methods at Low Temperatures* (Springer, 2007) 3rd ed., Chap. 2, pp. 7–32.

[4] F. Pobell, in *Matter and Methods at Low Temperatures* (Springer, 2007) 3rd ed., Chap. 5, pp. 115–138.

[5] F. Pobell, in *Matter and Methods at Low Temperatures* (Springer, 2007) 3rd ed., Chap. 7, pp. 149–189.

[6] W. H. Toews and R. W. Hill, Review of Scientific Instruments **85**, 043905 (2014).

[7] B. Chandrasekhar and E. Fawcett, Advances in Physics **20**, 775 (1971).

[8] D. Shoenberg, *Magnetic Oscillations in Metals*, Cambridge Monographs on Physics (Cambridge University Press, Cambridge, 1984).

[9] Liu, Kevin, *A Thermal Expansion Coefficient Study of Several Magnetic Spin Materials via Capacitive Dilatometry*, Master's thesis, UWSpace (2013).

[10] R. Pott and R. Schefzyk, Journal of Physics E: Scientific Instruments **16**, 444 (1983).

[11] S. Doniach, Physica B+C **91**, 231 (1977).

[12] M. Dzero, J. Xia, V. Galitski, and P. Coleman, Annual Review of Condensed Matter Physics **7**, 249 (2016).

[13] T. Takimoto, Journal of the Physical Society of Japan **80**, 123710 (2011).

[14] Y. S. Eo, K. Sun, c. Kurdak, D.-J. Kim, and Z. Fisk, Physical Review Applied **9**, 044006 (2018).

[15] Y. S. Eo, A. Rakoski, J. Lucien, D. Mihaliov, c. Kurdak, P. F. S. Rosa, and Z. Fisk, Proceedings of the National Academy of Sciences **116**, 12638 (2019).

[16] N. Wakeham, P. F. S. Rosa, Y. Q. Wang, M. Kang, Z. Fisk, F. Ronning, and J. D. Thompson, Physical Review B **94**, 035127 (2016).

[17] B. S. Tan, Y.-T. Hsu, B. Zeng, M. C. Hatnean, N. Harrison, Z. Zhu, M. Hartstein, M. Kiourlappou, A. Srivastava, M. D. Johannes, T. P. Murphy, J.-H. Park, L. Balicas, G. G. Lonzarich, G. Balakrishnan, and S. E. Sebastian, Science **349**, 287 (2015).

[18] Y. S. Eo, A. Rakoski, S. Sinha, D. Mihaliov, W. T. Fuhrman, S. R. Saha, P. F. S. Rosa, Z. Fisk, M. C. Hatnean, G. Balakrishnan, J. R. Chamorro, W. A. Phelan, S. M. Koohpayeh, T. M. McQueen, B. Kang, M.-s. Song, B. Cho, M. S. Fuhrer, J. Paglione, and c. Kurdak, Physical Review Materials **5**, 055001 (2021).

[19] S. M. Thomas, X. Ding, F. Ronning, V. Zapf, J. D. Thompson, Z. Fisk, J. Xia, and P. F. S. Rosa, Physical Review Letters **122**, 166401 (2019).

[20] M. Hartstein, H. Liu, Y.-T. Hsu, B. S. Tan, M. Ciomaga Hatnean, G. Balakrishnan, and S. E. Sebastian, iScience **23**, 101632 (2020).

[21] M. Hartstein, W. H. Toews, Y.-T. Hsu, B. Zeng, X. Chen, M. C. Hatnean, Q. R. Zhang, S. Nakamura, A. S. Padgett, G. Rodway-Gant, J. Berk, M. K. Kingston, G. H. Zhang, M. K. Chan, S. Yamashita, T. Sakakibara, Y. Takano, J.-H. Park, L. Balicas, N. Harrison, N. Shitsevalova, G. Balakrishnan, G. G. Lonzarich, R. W. Hill, M. Sutherland, and S. E. Sebastian, Nature Physics **14**, 166 (2018).

[22] W. T. Fuhrman, J. R. Chamorro, P. A. Alekseev, J.-M. Mignot, T. Keller, J. A. Rodriguez-Rivera, Y. Qiu, P. Nikolić, T. M. McQueen, and C. L. Broholm, Nature Communications **9**, 1539 (2018).

[23] M.-E. Boulanger, F. Laliberté, M. Dion, S. Badoux, N. Doiron-Leyraud, W. A. Phelan, S. M. Koohpayeh, W. T. Fuhrman, J. R. Chamorro, T. M. Mcqueen, X. F. Wang, Y. Nakajima, T. Metz, J. Paglione, and L. Taillefer, Physical Review B **97** (2018).

[24] Toews, William Henry, *An investigation of low energy quasiparticle excitations via thermal transport measurements* (UWSpace, 2017).

[25] F. Laliberté, M. E. Boulanger, M. Dion, S. Badoux, N. Doiron-Leyraud, L. Taillefer, W. A. Phelan, S. M. Koohpayeh, T. M. McQueen, X. Wang, Y. Nakajima, T. Metz, and J. Paglione, "Heat transport in the Kondo insulator SmB_6," (2018), presented at the American Physical Society March Meeting in Los Angeles, California.

[26] M. F. Smith, J. Paglione, M. B. Walker, and L. Taillefer, Physical Review B **71**, 014506 (2005).

[27] M. Sera, S. Kunii, and T. Kasuya, Journal of the Physical Society of Japan **57**, 13 (1988).

[28] S. T. Bramwell and M. J. Harris, Journal of Physics: Condensed Matter **10**, L215 (1998).

[29] S. T. Bramwell and M. J. P. Gingras, Science **294**, 1495 (2001).

[30] B. C. den Hertog and M. J. P. Gingras, Physical Review Letters **84**, 3430 (2000).

[31] C. Castelnovo and P. C. W. Holdsworth, in *Spin Ice*, Springer Series in Solid-State Sciences, edited by M. Udagawa and L. Jaubert (Springer International Publishing, 2021) Chap. 7, pp. 143–188.

[32] C. Castelnovo, R. Moessner, and S. L. Sondhi, Nature **451**, 42 (2008).

[33] A. P. Ramirez, A. Hayashi, R. J. Cava, R. Siddharthan, and B. S. Shastry, Nature **399**, 333 (1999).

[34] D. Pomaranski, L. R. Yaraskavitch, S. Meng, K. A. Ross, H. M. L. Noad, H. A. Dabkowska, B. D. Gaulin, and J. B. Kycia, Nature Physics **9**, 353 (2013).

[35] M. J. Harris, S. T. Bramwell, D. F. McMorrow, T. Zeiske, and K. W. Godfrey, Physical Review Letters **79**, 2554 (1997).

[36] T. Fennell, O. A. Petrenko, B. Fåk, J. S. Gardner, S. T. Bramwell, and B. Ouladdiaf, Physical Review B **72**, 224411 (2005).

[37] W. H. Toews, S. S. Zhang, K. A. Ross, H. A. Dabkowska, B. D. Gaulin, and R. W. Hill, Physical Review Letters **110**, 217209 (2013).

[38] J. G. Rau and M. J. Gingras, Annual Review of Condensed Matter Physics **10**, 357 (2019).

[39] M. J. P. Gingras and P. A. McClarty, Reports on Progress in Physics **77**, 056501 (2014).

[40] Q. J. Li, Z. Y. Zhao, C. Fan, F. B. Zhang, H. D. Zhou, X. Zhao, and X. F. Sun, Physical Review B **87**, 214408 (2013).

[41] S. Petit, E. Lhotel, S. Guitteny, O. Florea, J. Robert, P. Bonville, I. Mirebeau, J. Ollivier, H. Mutka, E. Ressouche, C. Decorse, M. Ciomaga Hatnean, and G. Balakrishnan, Physical Review B **94**, 165153 (2016).

[42] J.-J. Wen, S. M. Koohpayeh, K. A. Ross, B. A. Trump, T. M. McQueen, K. Kimura, S. Nakatsuji, Y. Qiu, D. M. Pajerowski, J. R. D. Copley, and C. L. Broholm, Physical Review Letters **118**, 107206 (2017).

[43] O. Benton, Physical Review Letters **121**, 037203 (2018).

[44] V. K. Anand, L. Opherden, J. Xu, D. T. Adroja, A. T. M. N. Islam, T. Herrmannsdörfer, J. Hornung, R. Schönemann, M. Uhlarz, H. C. Walker, N. Casati, and B. Lake, Physical Review B **94**, 144415 (2016).

[45] R. Sibille, N. Gauthier, H. Yan, M. Ciomaga Hatnean, J. Ollivier, B. Winn, U. Filges, G. Balakrishnan, M. Kenzelmann, N. Shannon, and T. Fennell, Nature Physics **14**, 711 (2018).

[46] Y. Tokiwa, T. Yamashita, D. Terazawa, K. Kimura, Y. Kasahara, T. Onishi, Y. Kato, M. Halim, P. Gegenwart, T. Shibauchi, S. Nakatsuji, E.-G. Moon, and Y. Matsuda, Journal of the Physical Society of Japan **87**, 064702 (2018).

[47] J. M. Ni, Y. Y. Huang, E. J. Cheng, Y. J. Yu, B. L. Pan, Q. Li, L. M. Xu, Z. M. Tian, and S. Y. Li, Nature Communications **12**, 307 (2021).

[48] T. Uehara, T. Ohtsuki, M. Udagawa, S. Nakatsuji, and Y. Machida, Nature Communications **13**, 4604 (2022).

[49] R. Berman, F. E. Simon, and J. M. Ziman, Proceedings of the Royal Society of London. Series A, Mathematical and Physical Sciences. **220**, 171 (1953).

[50] Berman, R., Foster, E. L., and Ziman, J. M., Proceedings of the Royal Society of London. Series A, Mathematical and Physical Sciences. **231**, 130 (1955).

[51] S. Y. Li, J.-B. Bonnemaison, A. Payeur, P. Fournier, C. H. Wang, X. H. Chen, and L. Taillefer, Physical Review B **77**, 134501 (2008).

[52] P. G. Klemens (Academic Press, 1958) pp. 1–98.

[53] R. Berman, *Thermal conduction in solids*, Oxford studies in physics (Clarendon Press, Oxford, 1976).

[54] B. Gao, T. Chen, D. W. Tam, C.-L. Huang, K. Sasmal, D. T. Adroja, F. Ye, H. Cao, G. Sala, M. B. Stone, C. Baines, J. A. T. Verezhak, H. Hu, J.-H. Chung, X. Xu, S.-W. Cheong, M. Nallaiyan, S. Spagna, M. B. Maple, A. H. Nevidomskyy, E. Morosan, G. Chen, and P. Dai, Nature Physics **15**, 1052 (2019).

[55] J. Gaudet, E. Smith, J. Dudemaine, J. Beare, C. Buhariwalla, N. Butch, M. Stone, A. Kolesnikov, G. Xu, D. Yahne, K. Ross, C. Marjerrison, J. Garrett, G. Luke, A. Bianchi, and B. Gaulin, Physical Review Letters **122**, 187201 (2019).

[56] F. Pobell, *Matter and Methods at Low Temperatures*, 3rd ed. (Springer, 2007).

[57] J. R. Taylor, *An introduction to error analysis: the study of uncertainties in physical measurements*, 2nd ed. (University Science Books, Sausalito, California, 1997).

[58] D. Shoenberg, Mathematical Proceedings of the Cambridge Philosophical Society **31**, 265 (1935).

[59] L. Landau, Zeitschrift f ur Physik **64**, 629 (1930).

[60] W. J. de Haas and P. M. van Alphen, Proc. Netherlands Roy. Acad. Sci. **33**, 1106 (1930).

[61] L. Onsager, The London, Edinburgh, and Dublin Philosophical Magazine and Journal of Science **43**, 1006 (1952).

[62] N. Toyota, J. Müller, and M. Lang, in *Low-Dimensional Molecular Metals*, Springer Series in Solid-State Sciences (Springer, Berlin, Heidelberg, 2007) pp. 99–140.

[63] Z. Fisk, J. L. Sarrao, S. L. Cooper, P. Nyhus, G. S. Boebinger, A. Passner, and P. C. Canfield, Physica B: Condensed Matter Proceedings of the International Conference on Strongly Correlated Electron Systems, **223-224**, 409 (1996).

[64] P. S. Riseborough, Physical Review B **45**, 13984 (1992).

[65] M. Dzero, K. Sun, V. Galitski, and P. Coleman, Physical Review Letters **104**, 106408 (2010).

[66] Z. Fisk, J. L. Sarrao, J. D. Thompson, D. Mandrus, M. F. Hundley, A. Miglori, B. Bucher, Z. Schlesinger, G. Aeppli, E. Bucher, J. F. DiTusa, C. S. Oglesby, H.-R. Ott, P. C. Canfield, and S. E. Brown, Physica B: Condensed Matter Proceedings of the International Conference on Strongly Correlated Electron Systems, **206-207**, 798 (1995).

[67] P. S. Riseborough and D. L. Mills, Physical Review B **21**, 5338 (1980).

[68] C. L. Kane and E. J. Mele, Physical Review Letters **95**, 226801 (2005).

[69] C. L. Kane and E. J. Mele, Physical Review Letters **95**, 146802 (2005).

[70] D. J. Thouless, M. Kohmoto, M. P. Nightingale, and M. den Nijs, Physical Review Letters **49**, 405 (1982).

[71] M. Schirber, Physics **9**, 116 (2016).

[72] M. Z. Hasan and C. L. Kane, Reviews of Modern Physics **82**, 3045 (2010).

[73] M. Z. Hasan and J. E. Moore, Annual Review of Condensed Matter Physics **2**, 55 (2011).

[74] L. Fu, C. L. Kane, and E. J. Mele, Physical Review Letters **98**, 106803 (2007).

[75] L. Fu and C. L. Kane, Physical Review B **76**, 045302 (2007).

[76] S. Souma, H. Kumigashira, T. Ito, T. Takahashi, and S. Kunii, Physica B: Condensed Matter The International Conference on Strongly Correlated Electron Systems, **312-313**, 329 (2002).

[77] R. L. Cohen, M. Eibschütz, and K. W. West, Physical Review Letters **24**, 383 (1970).

[78] A. Menth, E. Buehler, and T. H. Geballe, Physical Review Letters **22**, 295 (1969).

[79] J. C. Nickerson, R. M. White, K. N. Lee, R. Bachmann, T. H. Geballe, and G. W. Hull, Physical Review B **3**, 2030 (1971).

[80] C. M. Varma and Y. Yafet, Physical Review B **13**, 2950 (1976).

[81] L. M. Falicov and J. C. Kimball, Physical Review Letters **22**, 997 (1969).

[82] C. M. Varma, Reviews of Modern Physics **48**, 219 (1976).

[83] M. Mizumaki, S. Tsutsui, and F. Iga, Journal of Physics: Conference Series **176**, 012034 (2009).

[84] N. P. Butch, J. Paglione, P. Chow, Y. Xiao, C. A. Marianetti, C. H. Booth, and J. R. Jeffries, Physical Review Letters **116**, 156401 (2016).

[85] J. C. Cooley, M. C. Aronson, Z. Fisk, and P. C. Canfield, Physical Review Letters **74**, 1629 (1995).

[86] S. Wolgast, c. Kurdak, K. Sun, J. W. Allen, D.-J. Kim, and Z. Fisk, Physical Review B **88**, 180405 (2013).

[87] D. J. Kim, S. Thomas, T. Grant, J. Botimer, Z. Fisk, and J. Xia, Scientific Reports **3**, 3150 (2013).

[88] F. Lu, J. Zhao, H. Weng, Z. Fang, and X. Dai, Physical Review Letters **110**, 096401 (2013).

[89] N. Xu, P. K. Biswas, J. H. Dil, R. S. Dhaka, G. Landolt, S. Muff, C. E. Matt, X. Shi, N. C. Plumb, M. Radović, E. Pomjakushina, K. Conder, A. Amato, S. V. Borisenko, R. Yu, H.-M. Weng, Z. Fang, X. Dai, J. Mesot, H. Ding, and M. Shi, Nature Communications **5**, 4566 (2014).

[90] P. Hlawenka, K. Siemensmeyer, E. Weschke, A. Varykhalov, J. Sánchez-Barriga, N. Y. Shitsevalova, A. V. Dukhnenko, V. B. Filipov, S. Gabáni, K. Flachbart, O. Rader, and E. D. L. Rienks, Nature Communications **9**, 517 (2018).

[91] N. Xu, H. Ding, and M. Shi, Journal of Physics: Condensed Matter **28**, 363001 (2016).

[92] L. Li, K. Sun, C. Kurdak, and J. W. Allen, Nature Reviews Physics **2**, 463 (2020).

[93] J. Kim, C. Jang, X. Wang, J. Paglione, S. Hong, J. Lee, H. Choi, and D. Kim, Physical Review B **99**, 245148 (2019).

[94] Y. Xu, S. Cui, J. K. Dong, D. Zhao, T. Wu, X. H. Chen, K. Sun, H. Yao, and S. Y. Li, Physical Review Letters **116**, 246403 (2016).

[95] P. Syers, D. Kim, M. S. Fuhrer, and J. Paglione, Physical Review Letters **114**, 096601 (2015).

[96] K. Flachbart, M. Reiffers, v. Jánoš, Y. B. Paderno, V. I. Lazorenko, and E. S. Konovalova, Journal of the Less Common Metals **88**, L11 (1982).

[97] Z. Xiang, B. Lawson, T. Asaba, C. Tinsman, L. Chen, C. Shang, X. H. Chen, and L. Li, Phys. Rev. X **7**, 031054 (2017).

[98] S. Gabáni, K. Flachbart, E. Konovalova, M. Orendáč, Y. Paderno, V. Pavlık, and J. Šebek, Solid State Communications **117**, 641 (2001).

[99] K. Flachbart, S. Gabáni, K. Gloos, E. Konovalova, M. Orendáč, Y. Paderno, V. Pavlık, M. Reiffers, and P. Samuely, Physica B: Condensed Matter **312-313**, 379 (2002).

[100] K. Flachbart, S. Gabáni, K. Neumaier, Y. Paderno, V. Pavlík, E. Schuberth, and N. Shitsevalova, Physica B: Condensed Matter **378-380**, 610 (2006).

[101] W. A. Phelan, S. M. Koohpayeh, P. Cottingham, J. W. Freeland, J. C. Leiner, C. L. Broholm, and T. M. McQueen, Phys. Rev. X **4**, 031012 (2014).

[102] G. Li, Z. Xiang, F. Yu, T. Asaba, B. Lawson, P. Cai, C. Tinsman, A. Berkley, S. Wolgast, Y. S. Eo, D.-J. Kim, C. Kurdak, J. W. Allen, K. Sun, X. H. Chen, Y. Y. Wang, Z. Fisk, and L. Li, Science **346**, 1208 (2014).

[103] P. G. LaBarre, A. Rydh, J. Palmer-Fortune, J. A. Frothingham, S. T. Hannahs, A. P. Ramirez, and N. A. Fortune, Journal of Physics: Condensed Matter **34**, 36LT01 (2022).

[104] T. E. Millichamp, D. Billington, H. C. Robarts, J. Laverock, D. ONeill, M. C. Hatnean, G. Balakrishnan, J. A. Duffy, J. W. Taylor, S. R. Giblin, and S. B. Dugdale, "Direct measurement of a remnant Fermi surface in SmB_6," (2021).

[105] G. Baskaran, "Majorana Fermi Sea in Insulating SmB_6: A proposal and a Theory of Quantum Oscillations in Kondo Insulators," (2015).

[106] O. Erten, P.-Y. Chang, P. Coleman, and A. M. Tsvelik, Physical Review Letters **119**, 057603 (2017).

[107] D. Chowdhury, I. Sodemann, and T. Senthil, Nature Communications **9**, 1766 (2018).

[108] J. Knolle and N. R. Cooper, Physical Review Letters **118** (2017).

[109] J. Knolle and N. R. Cooper, Physical Review Letters **115**, 146401 (2015).

[110] L. Zhang, X.-Y. Song, and F. Wang, Physical Review Letters **116**, 046404 (2016).

[111] R. Peters, T. Yoshida, and N. Kawakami, Physical Review B **100**, 085124 (2019).

[112] S. Julian, Canadian Journal of Physics (2023).

[113] W. A. Phelan, S. M. Koohpayeh, P. Cottingham, J. A. Tutmaher, J. C. Leiner, M. D. Lumsden, C. M. Lavelle, X. P. Wang, C. Hoffmann, M. A. Siegler, N. Haldolaarachchige, D. P. Young, and T. M. McQueen, Scientific Reports **6**, 20860 (2016).

[114] P. S. Riseborough and Z. Fisk, Physical Review B **96**, 195122 (2017).

[115] N. Harrison, Physical Review Letters **121**, 026602 (2018).

[116] J. C. Souza, P. F. S. Rosa, J. Sichelschmidt, M. Carlone, P. A. Venegas, M. O. Malcolms, P. M. Menegasso, R. R. Urbano, Z. Fisk, and P. G. Pagliuso, Physical Review Research **2**, 043181 (2020).

[117] M. E. Valentine, S. Koohpayeh, W. A. Phelan, T. M. McQueen, P. F. S. Rosa, Z. Fisk, and N. Drichko, Physical Review B **94**, 075102 (2016).

[118] M. E. Valentine, S. Koohpayeh, W. A. Phelan, T. M. McQueen, P. F. Rosa, Z. Fisk, and N. Drichko, Physica B: Condensed Matter **536**, 60 (2018).

[119] B. Skinner, Physical Review Materials **3**, 104601 (2019).

[120] R. Zhang, B. Singh, C. Lane, J. Kidd, Y. Zhang, B. Barbiellini, R. S. Markiewicz, A. Bansil, and J. Sun, Physical Review B **105**, 195134 (2022).

[121] P. C. Canfield and Z. Fisk, Philosophical Magazine B **65**, 1117 (1992).

[122] G. Balakrishnan, M. R. Lees, and D. M. Paul, Journal of Crystal Growth **256**, 206 (2003).

[123] W. T. Fuhrman and P. Nikolić, Physical Review B **101** (2020).

[124] Y. S. Eo, S. Wolgast, A. Rakoski, D. Mihaliov, B. Y. Kang, M. S. Song, B. K. Cho, M. C. Hatnean, G. Balakrishnan, Z. Fisk, S. R. Saha, X. Wang, J. Paglione, and Ç. Kurdak, Physical Review B **101**, 155109 (2020).

[125] S. Sen, N. S. Vidhyadhiraja, E. Miranda, V. Dobrosavljević, and W. Ku, Physical Review Research **2**, 033370 (2020).

[126] W. T. Fuhrman, J. C. Leiner, J. W. Freeland, M. van Veenendaal, S. M. Koohpayeh, W. A. Phelan, T. M. McQueen, and C. Broholm, Physical Review B **99**, 020401 (2019).

[127] M. C. Hatnean, M. R. Lees, D. M. Paul, and G. Balakrishnan, Scientific Reports **3**, 3071 (2013).

[128] S. Otani, H. Nakagawa, Y. Nishi, and N. Kieda, Journal of Solid State Chemistry **154**, 238 (2000).

[129] S. Gabáni, M. Orendáč, G. Pristáš, E. Gažo, P. Diko, S. Piovarči, V. Glushkov, N. Sluchanko, A. Levchenko, N. Shitsevalova, and K. Flachbart, Philosophical Magazine **96**, 3274 (2016).

[130] M. Orendáč, S. Gabáni, G. Pristáš, E. Gažo, P. Diko, P. Farkašovský, A. Levchenko, N. Shitsevalova, and K. Flachbart, Physical Review B **96**, 115101 (2017).

[131] P. J. Robinson, J. Munarriz, M. E. Valentine, A. Granmoe, N. Drichko, J. R. Chamorro, P. F. Rosa, T. M. McQueen, and A. N. Alexandrova, Angewandte Chemie International Edition **59**, 10996 (2020).

[132] M. Shahrokhvand, S. Pezzini, M. R. van Delft, U. Zeitler, N. E. Hussey, and S. Wiedmann, Physical Review B **96**, 205125 (2017).

[133] C. Kittel, *Introduction to Solid State Physics*, 8th ed. (Wiley, 2004).

[134] P. Coleman, "Kondo insulators: Iconic forerunners of emergent quantum materials," (2022), APS March Meeting.

[135] D. W. Ruesink and J. M. Perz, Canadian Journal of Physics **61**, 177 (1983).

[136] S. Nakamura, T. Goto, M. Kasaya, and S. Kunii, Journal of the Physical Society of Japan **60**, 4311 (1991).

[137] P. W. Anderson, Physical Review **102**, 1008 (1956).

[138] M. Udagawa and L. Jaubert, eds., *Spin Ice*, Springer Series in Solid-State Sciences, Vol. 197 (Springer International Publishing, Cham, Switzerland, 2021).

[139] J. D. Bernal and R. H. Fowler, The Journal of Chemical Physics **1**, 515 (1933), publisher: American Institute of Physics.

[140] S. T. Bramwell, M. J. P. Gingras, and P. C. W. Holdsworth, in *Frustrated Spin Systems*, edited by H. T. Diep (World Scientific, 2020) 3rd ed., Chap. 7, pp. 397–486.

[141] M. J. P. Gingras, P. A. McClarty, and J. G. Rau, in *Spin Ice*, Springer Series in Solid-State Sciences, edited by M. Udagawa and L. Jaubert (Springer International Publishing, 2021) Chap. 1, pp. 1–18.

[142] R. Siddharthan, B. S. Shastry, A. P. Ramirez, A. Hayashi, R. J. Cava, and S. Rosenkranz, Physical Review Letters **83**, 1854 (1999).

[143] R. Moessner, Physical Review B **57**, R5587 (1998).

[144] R. G. Melko, B. C. den Hertog, and M. J. P. Gingras, Physical Review Letters **87**, 067203 (2001).

[145] R. G. Melko and M. J. P. Gingras, Journal of Physics: Condensed Matter **16**, R1277 (2004).

[146] J. S. Gardner, M. J. P. Gingras, and J. E. Greedan, Reviews of Modern Physics **82**, 53 (2010).

[147] C. Castelnovo, R. Moessner, and S. L. Sondhi, Physical Review B **84**, 144435 (2011).

[148] S. T. Bramwell and T. Fennell, in *Spin Ice*, Springer Series in Solid-State Sciences, edited by M. Udagawa and L. Jaubert (Springer International Publishing, 2021) Chap. 8, pp. 189–238.

[149] Henley, Christopher L., Annual Review of Condensed Matter Physics **1**, 179 (2010).

[150] T. Fennell, O. Petrenko, G. Balakrishnan, S. Bramwell, J. Champion, B. Føak, M. Harris, and D. Paul, Applied Physics A **74**, s889 (2002).

[151] Z. Hiroi, K. Matsuhira, and M. Ogata, Journal of the Physical Society of Japan **72**, 3045 (2003).

[152] K. Matsuhira, Z. Hiroi, T. Tayama, S. Takagi, and T. Sakakibara, Journal of Physics: Condensed Matter **14**, L559 (2002).

[153] R. Higashinaka, H. Fukazawa, and Y. Maeno, Physical Review B **68**, 014415 (2003).

[154] J. Snyder, J. S. Slusky, R. J. Cava, and P. Schiffer, Nature **413**, 48 (2001).

[155] A. M. Samarakoon, A. Sokolowski, B. Klemke, R. Feyerherm, M. Meissner, R. A. Borzi, F. Ye, Q. Zhang, Z. Dun, H. Zhou, T. Egami, J. N. Hallén, L. Jaubert, C. Castelnovo, R. Moessner, S. A. Grigera, and D. A. Tennant, Physical Review Research **4**, 033159 (2022).

[156] T. Fennell, O. A. Petrenko, B. Fåk, S. T. Bramwell, M. Enjalran, T. Yavors'kii, M. J. P. Gingras, R. G. Melko, and G. Balakrishnan, Physical Review B **70**, 134408 (2004).

[157] T. Fennell, P. P. Deen, A. R. Wildes, K. Schmalzl, D. Prabhakaran, A. T. Boothroyd, R. J. Aldus, D. F. McMorrow, and S. T. Bramwell, Science **326**, 415 (2009).

[158] D. J. P. Morris, D. A. Tennant, S. A. Grigera, B. Klemke, C. Castelnovo, R. Moessner, C. Czternasty, M. Meissner, K. C. Rule, J.-U. Hoffmann, K. Kiefer, S. Gerischer, D. Slobinsky, and R. S. Perry, Science **326**, 411 (2009).

[159] B. Klemke, M. Meissner, P. Strehlow, K. Kiefer, S. A. Grigera, and D. A. Tennant, Journal of Low Temperature Physics **163**, 345 (2011).

[160] G. Kolland, O. Breunig, M. Valldor, M. Hiertz, J. Frielingsdorf, and T. Lorenz, Physical Review B **86**, 060402 (2012).

[161] G. Kolland, M. Valldor, M. Hiertz, J. Frielingsdorf, and T. Lorenz, Physical Review B **88**, 054406 (2013).

[162] C. Fan, Z. Y. Zhao, H. D. Zhou, X. M. Wang, Q. J. Li, F. B. Zhang, X. Zhao, and X. F. Sun, Physical Review B **87**, 144404 (2013).

[163] S. Scharffe, G. Kolland, M. Valldor, V. Cho, J. F. Welter, and T. Lorenz, Journal of Magnetism and Magnetic Materials Selected papers from the sixth Moscow International Symposium on Magnetism (MISM-2014), **383**, 83 (2015).

[164] C. Broholm, R. J. Cava, S. A. Kivelson, D. G. Nocera, M. R. Norman, and T. Senthil, Science **367** (2020).

[165] J. Knolle and R. Moessner, Annual Review of Condensed Matter Physics **10**, 451 (2019).

[166] M. Hermele, M. P. A. Fisher, and L. Balents, Physical Review B **69**, 064404 (2004).

[167] H. R. Molavian, M. J. P. Gingras, and B. Canals, Physical Review Letters **98**, 157204 (2007).

[168] K. A. Ross, L. Savary, B. D. Gaulin, and L. Balents, Physical Review X **1**, 021002 (2011).

[169] S. Lee, S. Onoda, and L. Balents, Physical Review B **86**, 104412 (2012).

[170] S. Lee and E.-G. Moon, Physical Review B **99**, 014412 (2019).

[171] J. M. D. Coey, *Magnetism and Magnetic Materials* (Cambridge University Press, 2009) Chap. 4, p. 633.

[172] Jensen, Jens and Mackintosh, Allan R., *Rare Earth Magnetism: Structures and Excitations* (Clarendon Press, Oxford, 1991).

[173] R. M. White, *Quantum theory of magnetism: magnetic properties of materials*, 3rd ed., Springer series in solid-state sciences (Springer, Berlin ; New York, 2007).

[174] S. Onoda and Y. Tanaka, Physical Review B **83**, 094411 (2011).

[175] S. Onoda, Journal of Physics: Conference Series **320**, 012065 (2011).

[176] L. Savary and L. Balents, Physical Review Letters **108**, 037202 (2012).

[177] O. Benton, O. Sikora, and N. Shannon, Physical Review B **86**, 075154 (2012).

[178] L. Savary and L. Balents, Physical Review Letters **118**, 087203 (2017).

[179] J. S. Gardner, B. D. Gaulin, A. J. Berlinsky, P. Waldron, S. R. Dunsiger, N. P. Raju, and J. E. Greedan, Physical Review B **64**, 224416 (2001).

[180] A. P. Sazonov, A. Gukasov, and I. Mirebeau, Journal of Physics: Condensed Matter **23**, 164221 (2011).

[181] T. Fennell, M. Kenzelmann, B. Roessli, H. Mutka, J. Ollivier, M. Ruminy, U. Stuhr, O. Zaharko, L. Bovo, A. Cervellino, M. K. Haas, and R. J. Cava, Physical Review Letters **112**, 017203 (2014).

[182] M. Hirschberger, J. W. Krizan, R. J. Cava, and N. P. Ong, Science **348**, 106 (2015).

[183] Y. Hirokane, Y. Nii, Y. Tomioka, and Y. Onose, Physical Review B **99**, 134419 (2019).

[184] T. Taniguchi, H. Kadowaki, H. Takatsu, B. Fåk, J. Ollivier, T. Yamazaki, T. J. Sato, H. Yoshizawa, Y. Shimura, T. Sakakibara, T. Hong, K. Goto, L. R. Yaraskavitch, and J. B. Kycia, Physical Review B **87**, 060408 (2013).

[185] Y. Gritsenko, S. Mombetsu, P. T. Cong, T. Stöter, E. L. Green, C. S. Mejia, J. Wosnitza, M. Ruminy, T. Fennell, A. A. Zvyagin, S. Zherlitsyn, and M. Kenzelmann, Physical Review B **102**, 060403 (2020).

[186] Y. Nii, Y. Hirokane, S. Nakamura, N. Kabeya, S. Kimura, Y. Tomioka, T. Nojima, and Y. Onose, Physical Review B **105**, 094414 (2022).

[187] K. Kimura, S. Nakatsuji, J.-J. Wen, C. Broholm, M. B. Stone, E. Nishibori, and H. Sawa, Nature Communications **4**, 1934 (2013).

[188] K. Kimura, S. Nakatsuji, and A. A. Nugroho, Journal of the Korean Physical Society **63**, 719 (2013).

[189] A. L. Cornelius and J. S. Gardner, Physical Review B **64**, 060406 (2001).

[190] D. J. Flood, Journal of Applied Physics **45**, 4041 (1974).

[191] K. Matsuhira, C. Sekine, C. Paulsen, M. Wakeshima, Y. Hinatsu, T. Kitazawa, Y. Kiuchi, Z. Hiroi, and S. Takagi, Journal of Physics: Conference Series **145**, 012031 (2009).

[192] J. Alam, Y. M. Jana, and A. A. Biswas, Journal of Magnetism and Magnetic Materials **416**, 391 (2016).

[193] A. V. Guskov, P. G. Gagarin, V. N. Guskov, A. V. Tyurin, and K. S. Gavrichev, Russian Journal of Inorganic Chemistry **67**, 201 (2022).

[194] P. Bonville, S. Guitteny, A. Gukasov, I. Mirebeau, S. Petit, C. Decorse, M. C. Hatnean, and G. Balakrishnan, Physical Review B **94**, 134428 (2016).

[195] B. A. Trump, S. M. Koohpayeh, K. J. T. Livi, J.-J. Wen, K. E. Arpino, Q. M. Ramasse, R. Brydson, M. Feygenson, H. Takeda, M. Takigawa, K. Kimura, S. Nakatsuji, C. L. Broholm, and T. M. McQueen, Nature Communications **9**, 2619 (2018).

[196] N. Martin, P. Bonville, E. Lhotel, S. Guitteny, A. Wildes, C. Decorse, M. Ciomaga Hatnean, G. Balakrishnan, I. Mirebeau, and S. Petit, Physical Review X **7**, 041028 (2017).

[197] J. Röchner, L. Balents, and K. P. Schmidt, Physical Review B **94**, 201111 (2016).

[198] K. Behnia, Annalen der Physik **534**, 2100588 (2022).

[199] R. Sibille, E. Lhotel, M. C. Hatnean, G. Balakrishnan, B. Fåk, N. Gauthier, T. Fennell, and M. Kenzelmann, Physical Review B **94**, 024436 (2016).

[200] A. Samartzis, *Magnetic Investigation of Effective Spin-1/2 Magnetic Insulators Based on 3d and 4f Magnetic Ions*, Ph.D., Technische Universitaet Berlin (Germany), Germany (2020).

[201] R. D. Shannon and A. W. Sleight, Inorganic Chemistry **7**, 1649 (1968).

[202] R. D. Shannon, Acta Crystallographica Section A **32**, 751 (1976).

[203] D. Prabhakaran, in *Spin Ice*, Springer Series in Solid-State Sciences, edited by M. Udagawa and L. Jaubert (Springer International Publishing, 2021) Chap. 2, pp. 19–35.

[204] C. Karthik, T. J. Anderson, D. Gout, and R. Ubic, Journal of Solid State Chemistry **194**, 168 (2012).

[205] P. E. R. Blanchard, S. Liu, B. J. Kennedy, C. D. Ling, M. Avdeev, J. B. Aitken, B. C. C. Cowie, and A. Tadich, The Journal of Physical Chemistry C **117**, 2266 (2013).

[206] V. Anand, A. Islam, A. Samartzis, J. Xu, N. Casati, and B. Lake, Journal of Crystal Growth **498**, 124 (2018).

[207] M. Yamashita, Journal of the Physical Society of Japan **88**, 083702 (2019).

[208] Y. Xu, J. Zhang, Y. S. Li, Y. J. Yu, X. C. Hong, Q. M. Zhang, and S. Y. Li, Physical Review Letters **117**, 267202 (2016).

[209] M. C. Runyan and W. C. Jones, Cryogenics **48**, 448 (2008).

[210] V. K. Anand, A. K. Bera, J. Xu, T. Herrmannsdörfer, C. Ritter, and B. Lake, Physical Review B **92**, 184418 (2015).

[211] R. Orbach, Physical Review Letters **8**, 393 (1962).

[212] J. P. Harrison, J. P. Hessler, and D. R. Taylor, Physical Review B **14**, 2979 (1976).

[213] J. T. Folinsbee, J. P. Harrison, D. B. McColl, and D. R. Taylor, Journal of Physics C: Solid State Physics **10**, 743 (1977).

[214] D. R. Taylor, J. P. Harrison, and D. B. McColl, Physica B+C **86-88**, 1164 (1977).

[215] R. O. Pohl, Physical Review Letters **8**, 481 (1962).

[216] S. J. Li, Z. Y. Zhao, C. Fan, B. Tong, F. B. Zhang, J. Shi, J. C. Wu, X. G. Liu, H. D. Zhou, X. Zhao, and X. F. Sun, Physical Review B **92**, 094408 (2015).

[217] A. F. May, M. A. McGuire, J. E. Mitchell, A. S. Sefat, and B. C. Sales, Physical Review B **88**, 064502 (2013).

[218] Y. J. Yu, Y. Xu, K. J. Ran, J. M. Ni, Y. Y. Huang, J. H. Wang, J. S. Wen, and S. Y. Li, Physical Review Letters **120**, 067202 (2018).

[219] Y. Y. Huang, Y. Xu, L. Wang, C. C. Zhao, C. P. Tu, J. M. Ni, L. S. Wang, B. L. Pan, Y. Fu, Z. Hao, C. Liu, J.-W. Mei, and S. Y. Li, Phys. Rev. Lett. **127**, 267202 (2021).

[220] G. A. Toombs and F. W. Sheard, Journal of Physics C: Solid State Physics **6**, 1467 (1973).

[221] R. J. Elliott and J. B. Parkinson, Proceedings of the Physical Society **92**, 1024 (1967).

[222] L. J. Challis, M. A. McConachie, and D. J. Williams, Proceedings of the Royal Society of London. Series A, Mathematical and Physical Sciences **310**, 493 (1969).

[223] J. R. Fletcher and K. W. H. Stevens, Journal of Physics C: Solid State Physics **2**, 444 (1969).

[224] M. Mori, A. Spencer-Smith, O. P. Sushkov, and S. Maekawa, Physical Review Letters **113**, 265901 (2014).

[225] S. Onoda and Y. Tanaka, Physical Review Letters **105**, 047201 (2010).

[226] Z. Xiang, Y. Kasahara, T. Asaba, B. Lawson, C. Tinsman, L. Chen, K. Sugimoto, S. Kawaguchi, Y. Sato, G. Li, S. Yao, Y. L. Chen, F. Iga, J. Singleton, Y. Matsuda, and L. Li, Science **362**, 65 (2018).

[227] Y. Sato, Z. Xiang, Y. Kasahara, T. Taniguchi, S. Kasahara, L. Chen, T. Asaba, C. Tinsman, H. Murayama, O. Tanaka, Y. Mizukami, T. Shibauchi, F. Iga, J. Singleton, L. Li, and Y. Matsuda, Nature Physics **15**, 954 (2019).

[228] Z. Xiang, L. Chen, K.-W. Chen, C. Tinsman, Y. Sato, T. Asaba, H. Lu, Y. Kasahara, M. Jaime, F. Balakirev, F. Iga, Y. Matsuda, J. Singleton, and L. Li, Nature Physics (2021).

[229] N. W. Ashcroft and N. D. Mermin, *Solid State Physics* (Holt, Rinehart and Winston, 1976).

[230] J. M. Ziman, *Principles of the theory of solids*, Second ed. (Cambridge University Press, Cambridge, 1972).

[231] H. B. G. Casimir, Physica **5**, 495 (1938).

[232] G. K. White and P. J. Meeson, "Heat capacity," in *Experimental techniques in low-temperature physics* (Clarendon Press, Oxford, 2002) 4th ed.

[233] O. L. Anderson, Journal of Physics and Chemistry of Solids **24**, 909 (1963).

[234] T. Klitsner, J. E. VanCleve, H. E. Fischer, and R. O. Pohl, Physical Review B **38**, 7576 (1988).

[235] W. S. Hurst and D. R. Frankl, Physical Review **186**, 801 (1969).

[236] J. M. Ziman, *Electrons and phonons* (Clarendon Press, Oxford, 1960).

[237] E. Swartz and R. Pohl, Reviews of Modern Physics **61**, 605 (1989).

[238] J. Callaway, Physical Review **113**, 1046 (1959).

[239] M. G. Holland, Physical Review **132**, 2461 (1963).

[240] P. G. Klemens, Proceedings of the Physical Society. Section A **68**, 1113 (1955).

Appendices

Appendix A

Thermal transport theory

A.1 Kinetic theory

Thermal conductivity has contributions from mobile excitations. Conventionally, contributions include phonons from lattice vibrations and mobile electrons in metals. In order to analyse thermal conductivity results, it is important to differentiate between contributions from these different excitations. In particular, we can separate out conventional phonons and electrons from novel quasiparticles by treating them as mobile gas particles and using the kinetic theory formulation.

The thermal current $\boldsymbol{j}$ is estimated for a temperature gradient along the x-axis by taking an expectation value over all solid angles of the product of the energy density $u(x)$ at position $x_0 - \ell\cos(\theta)$ and the x-component of the velocity, $v_s\cos\theta$ [229]:

$$\boldsymbol{j} = \langle v_s \cos\theta u(x_0 - \ell\cos\theta)\rangle_\theta. \tag{A.1}$$

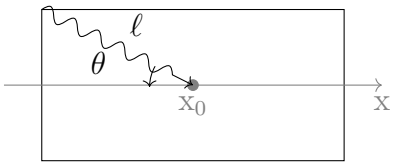


Figure A.1: Visualization of phonon transport using kinetic theory along the x direction. The thermal current at x_0 last scattered a distance ℓ from the point at an angle θ from the x-axis and travelled at speed v_s.

Integration over the solid angle produces the expression, to linear order, of thermal current $\boldsymbol{j} = \kappa\left(-\frac{\partial T}{\partial x}\right)$, where the phonon thermal conductivity κ_{ph} depends on the lattice specific heat capacity per unit volume $C = \frac{\partial u}{\partial T}$ as [133, 229]

$$\kappa_{\text{ph}} = \frac{1}{3} C v_s \ell. \tag{A.2}$$

The distance ℓ is also referred to as the "mean free path", or the mean distance of travel prior to a scattering event. Due to the similar assumptions surrounding electrons behaving as gas particles, the kinetic theory approach derives an equivalent expression for thermal conduction by electrons in metals using the electronic specific heat capacity C_{el}, Fermi velocity v_F and electron mean free path ℓ:

$$\kappa_{\text{el}} = \frac{1}{3} C_{\text{el}} v_F \ell. \tag{A.3}$$

A.2 Thermal conductivity of metals

In the case of thermal conduction by electrons in metals, the collision time $\tau = \ell / v_F$ is also related to the charge conduction. By Drude theory, the electrical conductivity σ of metals is

$$\sigma = \frac{n e^2 \tau}{m_e} \tag{A.4}$$

and the heat capacity per unit volume for a Fermi gas is

$$C_{\text{el}} = \frac{\pi^2}{2} n k_{\text{B}} \frac{T}{T_F} \tag{A.5}$$

for number density of free electrons $n = N/V$ and Fermi temperature $T_F = \epsilon_F / k_{\text{B}}$ [133, 230]. Then, using equation (A.3) and the Fermi energy $\epsilon_F = \frac{m v_F^2}{2}$, we obtain the Wiedemann-Franz law relating the electron thermal conductivity κ_{el} to the electrical conductivity σ and temperature T as

$$\kappa_{\text{el}} = \frac{\pi^2}{3} \left(\frac{k_{\text{B}}}{e}\right)^2 \sigma T. \tag{A.6}$$

The ratio $\frac{\pi^2}{3}\left(\frac{k_B}{e}\right)^2$ is also known as the "Lorentz ratio" L_0, such that the expectation for the ratio between the electron thermal conductivity and electrical conductivity in the region where the Wiedemann-Franz law is valid is $\kappa_{el}/\sigma = L_0 T$. The region of validity for this ratio is where the assumption of elastic scattering is valid, such as, for metals, the lowest temperatures where the electronic thermal conductivity increases linearly with temperature and the residual resistivity depends on elastic scattering from sample impurities [230].

A.3 Phonon thermal conductivity

A.3.1 Boundary-limited thermal conductivity

The expected maximum phonon thermal conductivity at low temperatures can be calculated using the kinetic theory expression, Equation (A.2). In this limit, the phonon mean free path is proportional to the sample cross-sectional area. Casimir shows that this geometrical relation is apparent in the treatment of phonons scattering events similar to non-interacting gas particles or electromagnetic radiation in an empty space [231]. The phonon scattering behaviour is assumed to be perfectly elastic such that all of the thermal energy applied to the heat source end of the sample travels to the other end, resulting in an independence of this limit from sample length. Moreover, at the lowest temperatures, the phonon wavelength is long enough that phonon-phonon interactions can be neglected. In the limit of a sufficiently long, disorder-free cylindrical sample with a perfectly periodic lattice, the scattering events are simply at the circular walls with distance equal to the sample diameter D between events. Casimir's more formal approach involving integration over all paths arrives at the conclusion that for a cylinder-shaped sample with diameter of the cross-sectional area D, the Casimir estimate of the mean free path is $\ell_C = D$, whereas for a rectangular cross-sectional area, the geometric mean gives

$$\ell_C = \sqrt{4A/\pi} \tag{A.7}$$

for cross-sectional area A. We can calculate an estimate for the phonon thermal conductivity at low temperatures in the limit of the mean free path equal to ℓ_C. In this limit, the specific heat capacity can be treated with the Debye model where the phonon dispersion is linear. Then the specific heat integral over all phonon modes is given as

$$C = 9nk_B\left(\frac{T}{\Theta_D}\right)^3 \int_0^{\Theta_D/T} \frac{x^4 e^x dx}{(e^x-1)^2} \tag{A.8}$$

and the integral can be evaluated in the limit of $T \ll \Theta_{\mathrm{D}}$ to give a lattice specific heat capacity per unit volume (see for example [229, 232]):

$$C = \frac{12\pi^4}{5} n k_{\mathrm{B}} \left(\frac{T}{\Theta_{\mathrm{D}}}\right)^3 . \tag{A.9}$$

The speed of sound v_s can be calculated as [229, 232, 233]

$$v_s = \Theta_{\mathrm{D}} \frac{k_{\mathrm{B}}}{h} \left(\frac{4\pi V}{3qZ}\right)^{1/3} \tag{A.10}$$

with number of atoms per formula unit q, number of formula units per unit cell Z, unit cell volume V, Planck constant h, and Boltzmann constant k_{B}. Then with gas constant R, the coefficient of the lattice specific heat β ($C = \beta T^3$) is

$$\beta = \frac{12\pi^4}{5} q R \left(\frac{1}{\Theta_{\mathrm{D}}}\right)^3 . \tag{A.11}$$

Moreover, v_s can be derived from ultrasonic experiments as [232, 233],

$$v_s = \left[\frac{1}{3}\left(\frac{2}{v_t^3} + \frac{1}{v_l^3}\right)\right]^{-1/3} \tag{A.12}$$

where v_t and v_l are the averaged transverse and longitudinal sound velocities, respectively.

For non-metallic materials with phonons dominating thermal conduction, typically at low temperatures the thermal conductivity is dominated by boundary scattering. Any additional scattering reduces the thermal conductivity. Then the maximum estimate for the thermal conductivity is

$$\kappa_{\mathrm{ph}} = \frac{1}{3} \beta v_s \ell_C T^3 \tag{A.13}$$

where ℓ_C is the Casimir limit of the mean free path.

A.3.2 Finite boundaries

The Casimir expression for the boundary-limited phonon mean free path [Eq. (A.7)] is motivated with the assumption of an infinite sample length with diffusive scattering at sample boundaries. For a finite sample length or for surfaces with specular reflection, Berman, Siman and Ziman (BSZ) [49] motivate a phonon mean free path $\ell = \alpha \ell_C = \alpha 2R$ for a constant α. They derive this expression using the same approach as Casimir, but allow for additional phonon scattering at the ends of the sample lengths or by specular reflection at sample surfaces [49, 234–236]. Their results for the mean free path as well as thermal conductivity are shown in Figures A.2a and A.2n respectively. In these figures, the results are reported as a function of the ratio of the effective radius $R = \ell_C/2$ with the actual sample length L, and diffuse scattering fraction f that is equal to 1 in the limit of perfectly diffuse phonon scattering. Generally, when specular reflections are a significant portion of scattering, $1 - f > 0$ or when the ratio $\ell_C/(2L)$ is finite, and the ratio $\ell/\ell_C = \alpha \neq 1$. The net effect is to increase the ratio such that $\alpha > 1$ when specular reflection is more than $\sim 20\%$ of the total reflections. Berman *et al.* [49] also observe a similar increase in thermal conductivity from the Casimir expectation on sapphire crystals with smooth surfaces, which is consistent with the expectations from this theory.

Specular reflection effects may also impact the power law of thermal conductivity. Li *et al.* [51] demonstrate this effect in the cuprate Nd_2CuO_4 (Fig. A.3). Rather than observing a correction to the Casimir mean free path that is constant in temperature as expected by the BSZ expression [49], the authors observe a temperature dependence in the phonon mean free path below ~ 0.15 K. They report that specular reflection results in a temperature dependence of thermal conductivity that is closer to $\kappa \sim T^2$ rather than the typical cubic temperature dependence observed for the roughened sample above ~ 0.15 K in addition to reporting the aforementioned phenomenon of the phonon mean free path rising above the geometric mean in the limit of perfectly reflective surfaces. It's possible that the increase in thermal conduction in reflective samples at temperatures below ~ 0.15 K is related to an acoustic mismatch model at the interface between the sample and its metallic contacts due to poor heat transmission at an interface with reflective contacts [237].

A.3.3 Phonon scattering with disorder

In the analysis of phonon boundary scattering, the phonon mean free path is assumed to be a constant that depends on sample geometries. In imperfect crystals, phonons also scatter with sample disorder. Unlike the boundary scattering process, scattering with sample

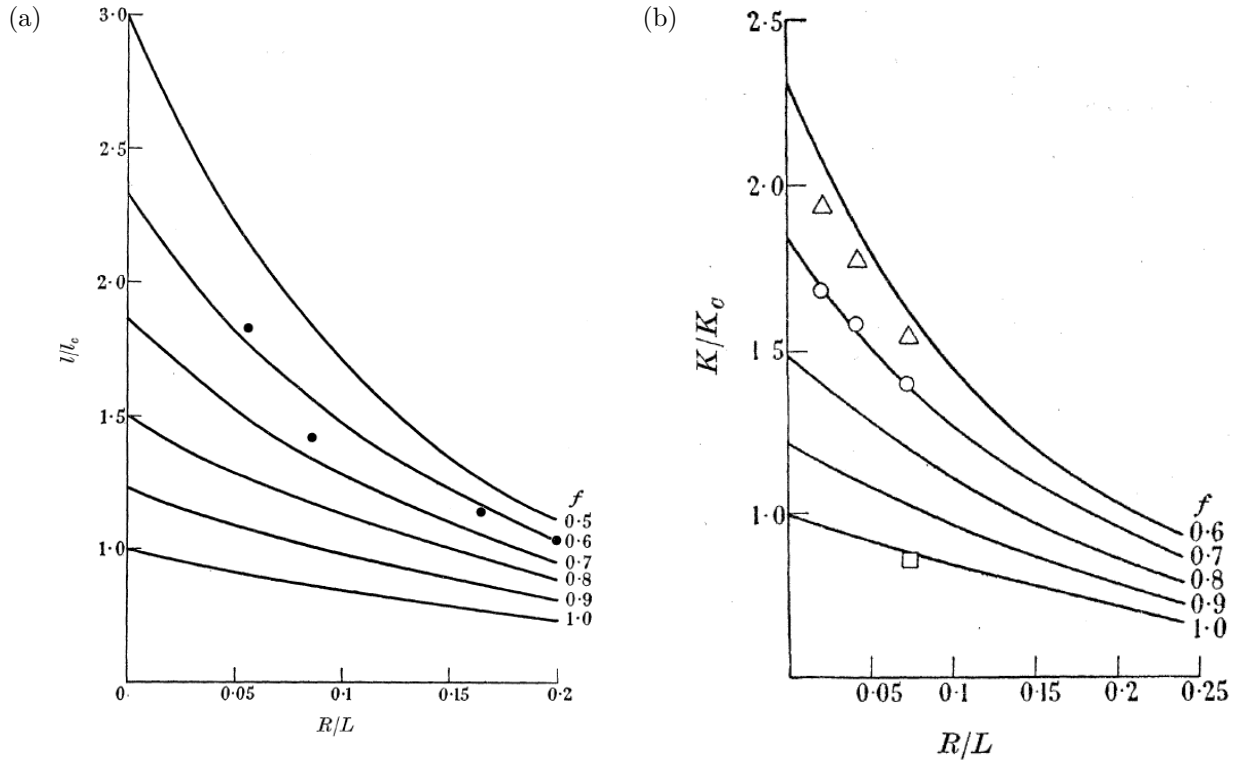


Figure A.2: (a) Calculated ratios of the phonon mean free path in the boundary scattering limit ℓ normalized by the Casimir value ℓ_c for different proportions of diffuse scattering f and sample proportions R/L. The black dots are observed values of ℓ/ℓ_C for four different sample geometries, Image and data from Berman *et al.* [49]. (b) Calculated ratios of phonon thermal conductivity K to the Casmir expectation K_c for different values of f and R/L. □ rough sapphire crystal, ○ and △ smooth crystal at 5.9 and 4.5 K. Image from Berman *et al.* [50]

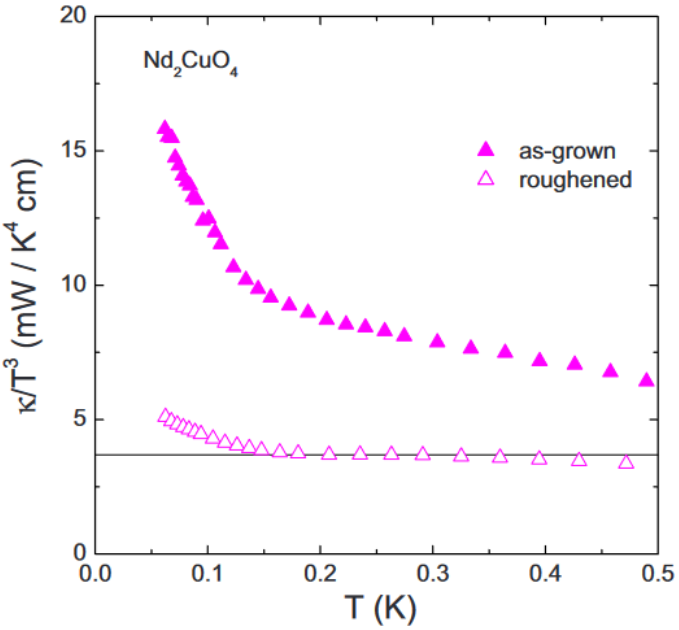


Figure A.3: The thermal conductivity plotted as κ/T^3 versus T of Nd_2CuO_4 with as-grown (smooth) and roughened sample boundaries. The black line indicates the theoretical expectation for phonon conduction limited by sample boundaries with a mean free path proportional to the geometric mean of the sample cross-sectional area. *Reprinted with permission from* [51]. *Copyright 2008 by the American Physical Society.*

disorder is typically dependent on the phonon frequency and therefore has a temperature-dependent behaviour. The total scattering adds using Matthiessen's rule

$$\tau_{\text{tot}}^{-1}(\omega) = \sum_i \tau_i^{-1}(\omega). \tag{A.14}$$

Due to the temperature-dependent scattering from disorder in the denominator of the kinetic theory formula, the thermal conductivity has a temperature dependence that is less than cubic with disorder. In real crystals, at lowest temperatures, phonon conductivity $\kappa \sim T^\alpha$ with $\alpha \lesssim 3$ and a lower exponent associated with stronger temperature-dependent scattering.

The temperature-dependence of phonon dispersion influences the dominant scattering mechanisms. The dominant scattering process(es) in Equation (A.14) at a particular tem-

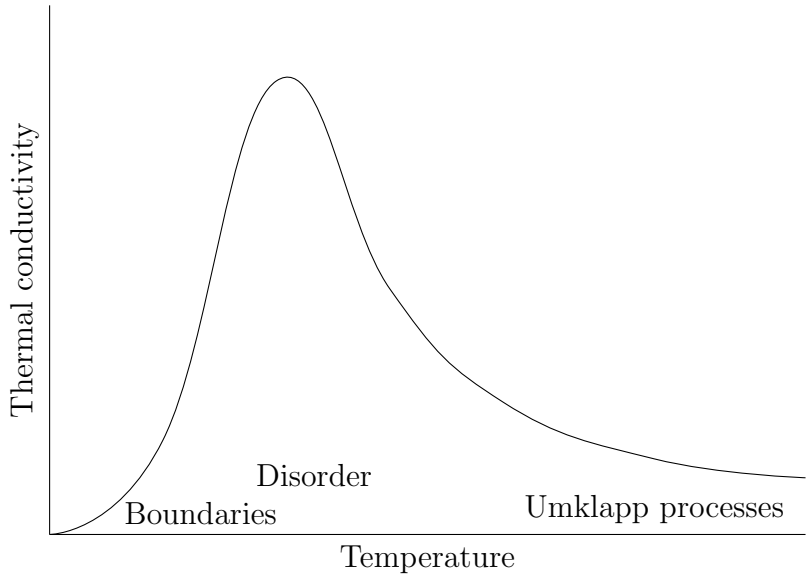


Figure A.4: Typical thermal conductivity for a non-metallic crystal as a function of temperature [52, 53]. Qualitatively, the phonon-dominated thermal conductivity is limited by sample boundaries at the lowest temperatures, reaches a peak at intermediate temperatures ($\sim \Theta_D/30$ [53]) with a height suppressed by sample disorder, and Umklapp (phonon-phonon) scattering dominating at higher temperatures.

perature depend on the value of ω determined by the phonon dispersion. As a result, the thermal conductivity of non-magnetic crystals, in which phonon conduction dominates, tends to follow a common structure. Figure A.4 shows a typical qualitative structure of thermal conduction as temperature increases from the milliKelvin regime. At the lowest temperatures, the phonon wavelength is at its longest and hence phonon conduction is typically mainly limited by the sample geometry with scattering behaviour. This wavelength decreases with increasing temperature, until the phonons interact with the aperiodicity in the lattice introduced by sample disorder, limiting the thermal conductivity's maximal value. This thermal conductivity peak is lower for samples with higher concentrations of disorder. Finally, the phonon wavelength is small enough such that phonons predominantly scatter with other phonons within the Brillouin zone. At higher temperatures, the thermal conductivity levels off to a material-dependent limit that is independent of sample disorder and geometry.

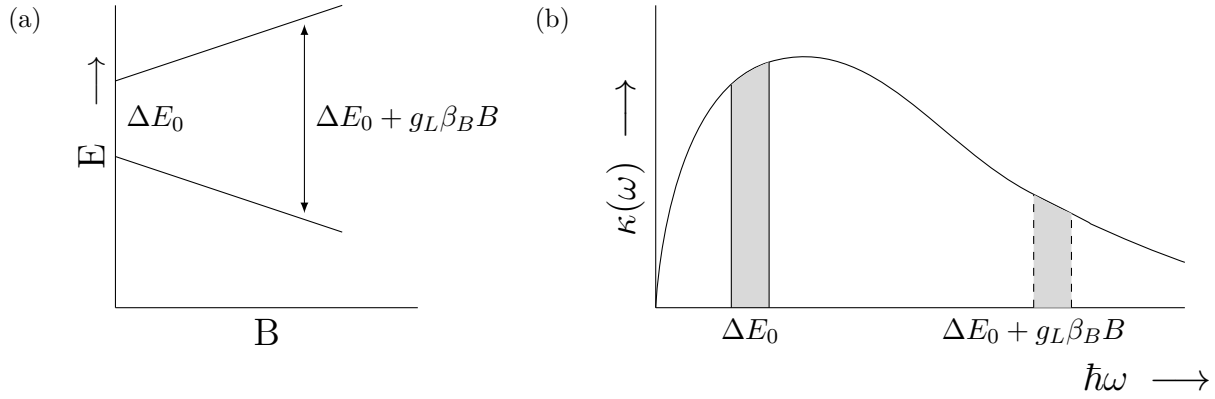


Figure A.5: Reproduced from Berman [53]. (a) Energy gap of a splitting in zero field ΔE_0 and increase in the energy gap in applied field B. (b) A band of phonons scatter resonantly, removing the contributions of these phonons to thermal conductivity for a band of phonons that is centered around the energy gap.

A.3.4 Resonance scattering in paramagnetic crystals

Phonons can also interact with distortions in the crystal field through resonance scattering. They get absorbed and re-emitted at a different frequency. Figure A.5 shows the energy levels of this mechanism. The separation of the crystal distortion increases with the application of a magnetic field according to the Zeeman energy. This increases the contribution to thermal conductivity by phonons at lower energies by increasing the energy required for this resonant interaction [53].

A.4 Callaway model fitting

A.4.1 Callaway model

The thermal conductivity of high quality, insulating crystals is dominated by phonons with a cubic specific heat capacity in the boundary scattering limit at the lowest temperatures. Other scattering mechanisms τ_i^{-1} simply reduce the phonon thermal conductivity. Callaway developed expression to integrate over phonon frequency ω in Debye approximation with Debye temperature $\Theta_\mathrm{D} = \frac{\hbar c k_\mathrm{D}}{k_\mathrm{B}}$ and Debye frequency k_D [238, 239]. After replacing phonon frequency with the dimensionless variable $x \equiv \hbar\omega/k_\mathrm{B}T$, this results in the expression

$$\kappa = \frac{k_B}{2\pi^2 v_s}\left(\frac{k_B}{\hbar}\right)^3 T^3 \int_0^{\Theta_D/T} \frac{x^4 e^x}{\sum_i \tau_i^{-1}(e^x-1)^2} dx \tag{A.15}$$

which is equivalent to Equation (A.2) using Equation (A.8) and using the relation $n = k_D^3/(6\pi^2)$. This expression allows consideration of the change in phonon scattering strength as the wavevector changes with temperature. It assumes an isotropic, dispersionless phonon spectrum in a three-dimensional material.

A.4.2 Scattering with sample disorder

In imperfect crystals, phonons scatter with lattice disorder including point defects, stacking faults, and dislocations as they break the periodicity of the lattice [52]. The rate of scattering with such imperfections depends on the phonon frequency. The scattering rates for these static imperfections are as follows.

A point defect is an isolated or randomly distributed impurity that is of much smaller dimension than the phonon wavelength, such as randomly distributed vacancies or insertions from off-stoichiometry. The scattering rate of phonons due to the mass difference introduced by point defects is [52, 53, 240]

$$\tau_{pd}^{-1} = \frac{c_p a^3 \omega^4}{4\pi v_s^3}\left(\frac{\Delta M}{M}\right)^2 \tag{A.16}$$

where the point defect's mass is $M + \Delta M$ given a mass of the correct atom M, and the defects are distributed across the sample in concentration c_p. In reality, the defect also affects force constants and nearest-neighbour distances which are especially apparent in the calculation when the mass difference is small, however the estimated total scattering rate accounting for such factors is still proportional to ω^4.

For defects with a larger size than an isolated defect, the scattering is proportional to a lower power law than ω^4 [53]. Depending on the geometry of a dislocation defect, it can have a scattering power law $\propto \omega^3$ or ω, where the former is for core dislocations and the latter is for the strain field of a dislocation.

A screw dislocation is a line of defects arranged in a cylindrical pattern, resulting in phonon scattering by dislocations oriented perpendicular to the temperature gradient of the form [52, 240]

$$\tau_{\mathrm{sd}}^{-1} = \frac{2^{3/2}}{3^{7/2}} N_d b^2 \gamma^2 \omega \tag{A.17}$$

for the number of dislocation lines per unit area N_d, Burgers vector magnitude b [1], and Grüneisen parameter γ. If the dislocation line is parallel to the phonon wavevector then the scattering rate vanishes, and if it is randomly oriented, then the scattering rate of Equation (A.17) is still valid once multiplied by a factor equal to 0.55 to account for the scattering probability of the different orientations [240].

A.4.3 Fitting

To fit Callaway model, we developed a code for C++ stochastic gradient descent with backtracking. This code needs starting parameters for the total scattering rate $\sum_i \tau_i^{-1}$ and a global function that is the integrand expression of Equation (A.15). For a data set with n data points $\{\kappa_j, T_j\}$ for $j = 1...n$, the algorithm first calculates the result of Equation (A.15) for each temperature data point by integration, finding a thermal conductivity estimate for the input function and parameters at the given temperature equal to

$$\kappa_j' = \frac{k_{\mathrm{B}}}{2\pi^2 v_s} \left(\frac{k_{\mathrm{B}}}{\hbar}\right)^3 T_j^3 \int_0^{\Theta_{\mathrm{D}}/T_j} \frac{x^4 e^x}{\sum_i \{\tau_i(T_j)\}^{-1} (e^x - 1)^2} dx \tag{A.18}$$

and calculates an error

$$\sum_{j=1}^{n} \frac{(\kappa_j' - \kappa_j)^2}{(\kappa_j - \bar{\kappa})^2} \tag{A.19}$$

where the denominator normalizes the data point by the difference between that point and the average thermal conductivity of the data set $\bar{\kappa} = \frac{1}{n}\sum_{j=1}^{n} \kappa_j$ in order to skew the algorithm towards minimizing the error difference at the average value of the data set instead of towards the regions with smallest thermal conductivity.

[1] Burgers vector

Appendix B

YbB_{12} thermal conductivity

In Chapter 5, we discussed samples SmB_6 FZ1 and FZ2 as being in the low disorder limit. This gives us confidence that the observed in-field increase in the thermal conductivity cannot be attributed to a reduction in phonon scattering. In contrast, our preliminary results for the thermal conductivity of TKI candidate YbB_{12} are well below the limit expected for high quality samples and our observed increase with applied field is marginal. Therefore our measurements are inconclusive regarding evidence of field-enhanced quasiparticle excitations.

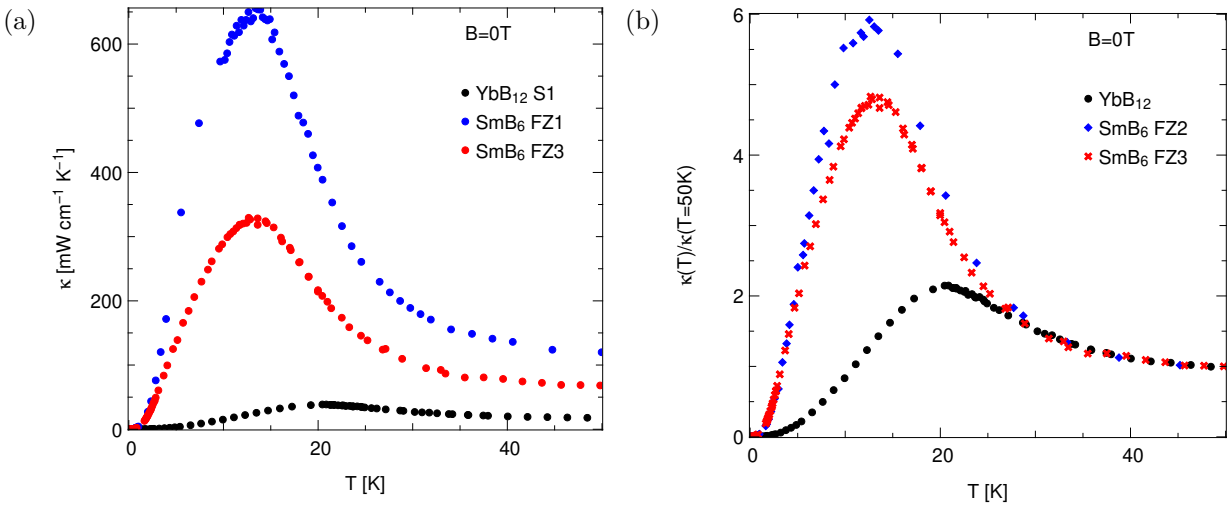


Figure B.1: (a) Thermal conductivity of YbB_{12} S1 in zero field and temperatures up to 50 K compared to the thermal conductivity in this range for SmB_6 samples FZ1 and FZ3. (b) Same but with the thermal conductivity normalized by the 50 K value to account for sample-dependent effects.

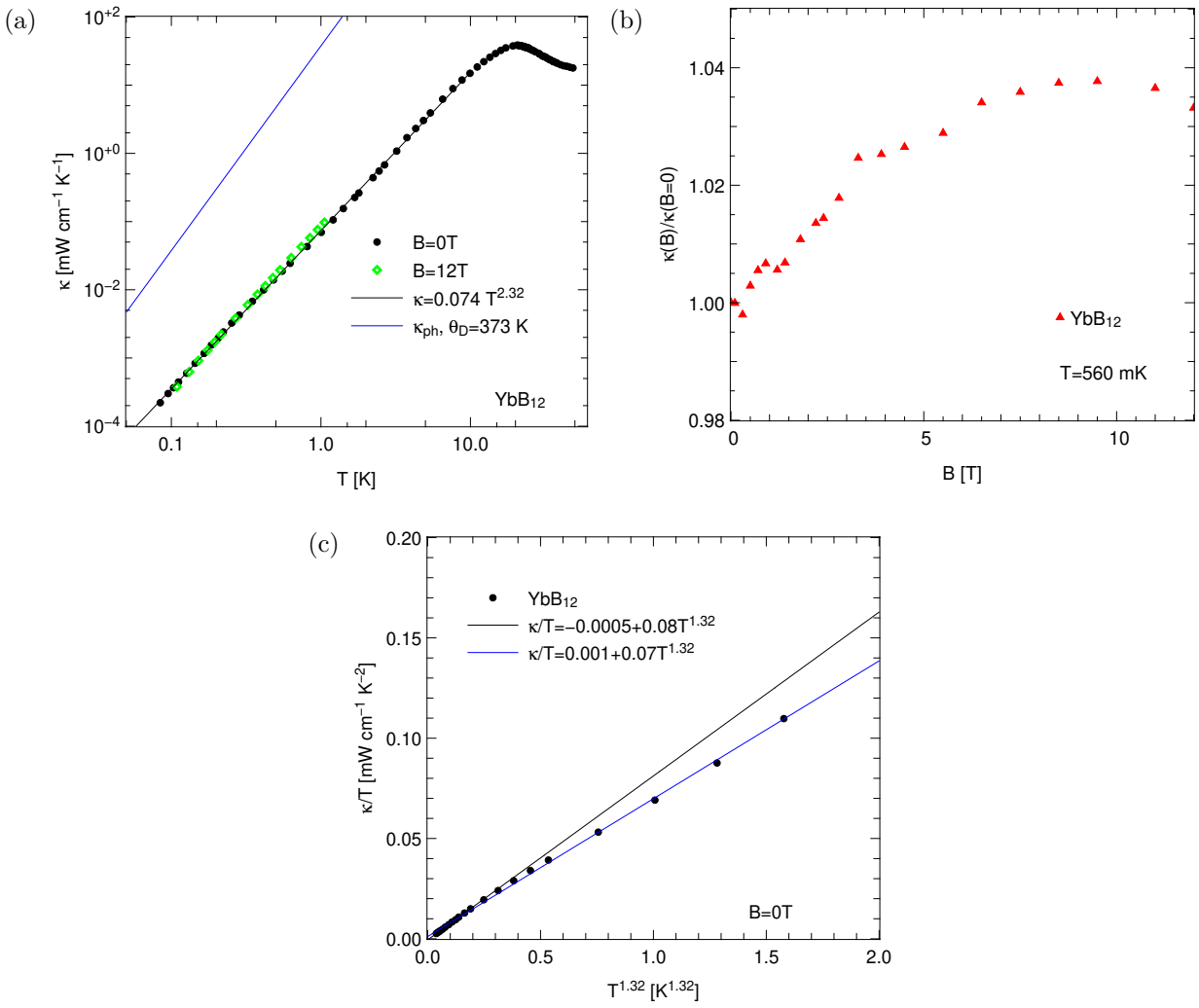


Figure B.2: (a) Low temperature thermal conductivity of YbB_{12} sample in zero field and 12 T field on a log-log plot. Black line is a fit to $\kappa = AT^{\alpha}$ and blue line is the estimated maximum phonon thermal conductivity from the sample geometry and a Debye temperature $\Theta_D = 373$ K. (b) Ratio of thermal conductivity in applied field to zero field value as a function of applied field and at an average temperature of 560 mK. (c) Thermal conductivity in zero field plotted as κ/T versus $T^{1.32}$. Lines are fits to $\kappa/T = A + BT^{1.32}$.